BULGARIAN CHEMICAL COMMUNICATIONS

2026 Volume 58 / Number 4

Journal of the Chemical Institutes
of the Bulgarian Academy of Sciences
and of the Union of Chemists in Bulgaria

Bulgarian Chemical Communications, Volume 58, Issue 4 (pp. 421-430) 2026 *DOI: 10.34049/bcc.58.4.5713*

Comparing odor-active compounds of South Indian mangoes by odor uproot blend analysis and the natural aroma instantaneous input to the sniffing port method for evaluating odor interactions

S. Suthagar [1], K. S. Tamilselvan [2]*
[1]Department of Electronics and Communication Engineering, Kongu Engineering College, Erode, Tamil Nadu, 638060 India
[2]Department of Biomedical Engineering, KPR Institute of Engineering and Technology, Arasur, Uthupalayam, Tamil Nadu, 641407 India

Received: July 03 2025; Revised: June 12, 2026

This research work identifies odor-active components of four South Indian mangoes. Volatile compounds in the South Indian mangoes Malgova, Alphonso, Senthuram, and Banganapalli, which belong to the *Mangifera Indica* family, were investigated using odor uproot blend analysis (OUBA) and natural aroma instantaneous input to the sniffing port (NAIIS). The evaluation of odor interactions—the connections between a naturally occurring scent and volatile substances extracted using gas chromatography was done using the NAIIS and OUBA approaches. This led to detecting 28 odor-active chemicals, 25 of which were identified. For the first time, three volatile chemicals were found in South Indian mangoes: γ-undecalactone, cis-3-hexenol, and cis-3-hexenyl acetate. The flavor dilution (FD) factor for γ-undecalactone of Malgova, Alphonso, Senthuram, and Banganapalli mangoes was 20542, 10254, 55261, and 49527 by OUBA and 65251, 75681, 82641, and 54216 by NAIIS, respectively. The FD factor for cis-3-hexenol of Malgova, Alphonso, Senthuram, and Banganapalli mangoes was 521, 815, 621, and 115 by OUBA and 2541, 1026, 3521, and 925 by NAIIS, respectively. The FD factor for cis-3-hexenyl acetate of Malgova, Alphonso, Senthuram, and Banganapalli mangoes was 10256, 13254, 18761, 16841 by OUBA and 8256, 9215, 11523, 12145 by NAIIS, respectively. Furthermore, OUBA classified cis-3-hexenyl acetate as green whereas NAIIS defined it as fruity.

Keywords: South Indian mangoes, odor-active components, OUBA, NAIIS, flavor dilution (FD) factor

INTRODUCTION

One of the world's most widely consumed tropical fruits, particularly in India, is the mango (*Mangifera Indica L.*). South Indian mangoes are very special for Indian people and favor people who need enriching foods. However, due to poor maintenance and non-technical approach, the average amount of wasted mango fruit ranges from 30% to 50%, 24% of which is wasted during distribution. The preliminary step of identifying the volatile odor component of such mangoes will help apply a technology to reduce waste and provide it to needy people.

The top four mango varieties from South India are Banganapalli, Alphonso, Senthuram, and Malgova. The village of Banganapalli in Andhra Pradesh, India, is the origin of the Banganapalli mango, sometimes referred to as Benishan or Baneshan [1]. This variety has an unusually sweet flavor, is large and rectangular, and has thin skin. It is exported to many countries and is frequently used to make mango pulp. Over time, the popularity and cultivation of various mango kinds have changed, and each variety has become linked with certain places recognized for their distinct mango features.

Mango farming has a strong cultural and agricultural legacy in India, where these kinds significantly add to the country's vast diversity of mangoes. The Ratnagiri area of Maharashtra, India, is thought to be the birthplace of the variety Alphonso, often known as Hapus [2]. It is well-known for its unique sweetness, taste, and scent. It is regarded as one of the most excellent mango kinds in the world, featuring brilliant yellow skin when mature. Only mangoes from this region may be marketed under the Alphonso name thanks to the geographical indication (GI) certification, which safeguards the brand. The Senthuram mango is a local or regional variety [3] having restricted origin. Local variations can have distinct sizes, tastes, and looks. Senthuram's qualities vary depending on the area and local farming customs. The Malgova mango is thought to originate from Tamil Nadu, India's Salem area [4]. It is distinguished by an

* To whom all correspondence should be sent:
E-mail: *susjou@gmail.com*

© 2026 Bulgarian Academy of Sciences, Union of Chemists in Bulgaria

enormous size, elongated form, silky skin, and sweet flavor. It is well-liked for both export and domestic use. The Malgova mango is grown using conventional techniques, including budding and grafting. Over time, horticulturists and farmers strive to enhance the cultivar.

Solid phase extraction and gas chromatography-mass spectrometry were employed to determine the components of air fresheners thought to be a likely source of volatile organic compounds [5]. Using the wet-digestion method and microwave plasma-atomic emission spectroscopy, the amounts of macro and trace metals in *Rubus steudneri Schweinf* fruit were ascertained [6]. OUBA and NAIIS were used to identify strong odor components in different varieties of mango [7]. The interactions between natural odors and the chemicals extracted from aroma concentrates by GC may be assessed using NAIIS. It has been found that some volatile substances have an effect on one another, even at quantities below the odor threshold [8, 9]. Some of the most significant features of the smell of natural goods are the odor interactions, about which a great deal of study has been published in various sectors, particularly wine [10-13].

Thus, the purpose of this work was to use odor uproot blend analysis (OUBA) and natural aroma instantaneous input to the sniffing port (NAIIS) to clarify the powerful volatile chemicals of four types of South Indian mangoes that have distinct smells. Once the odor-active components present in the south Indian mangoes are determined, they can be used to choose the corresponding odor detection sensor to design an embedded system. Such an embedded system can be utilized for determining and classifying the ripening stages of South Indian mangoes. By doing so, mangoes after post-harvest can be delivered to customers on time as per customer or consumer requirement, which avoids wastage of fruit before reaching the consumer.

EXPERIMENTAL

Materials

- *Chemicals and reagents.* All chemicals and reagents used in the present work were of analytical grade quality, including dichloromethane (Merck India), magnesium sulfate (Merck India), nitrogen gas (Linde India Ltd), ethanol (Merck India), ascorbic acid (Merck India), helium (Linde India Ltd), TC-WAX column (Restek India) and hydrogen gas (Linde India Ltd).

Apparatus and instruments

- *Blender* (model: Vitamix 5200; Vitamix India): The Vitamix 5200 is a high-power laboratory mixing/homogenizing system powered by a 1.2–1.38 kW variable speed motor, and a 1.9 L processing vessel. The unit offers shear rates adjustable from 10 discreet speed settings for efficient homogenization, dispersion, emulsification and particle-size reduction of liquid and semi-solid samples. The high-speed blade assembly provides for high mechanical shear for quick processing of heterogeneous materials to homogeneous suspensions. The system also has a self-cleaning mechanism, resulting in less downtime between processing cycles and higher system efficiency.
- *Centrifuge* (model: Eppendorf 5804R; Eppendorf India Pvt. Ltd): The Eppendorf 5804R Refrigerated Centrifuge features a benchtop design and has a refrigeration capacity of up to 20°C. It operates at speeds between 200 and 14,000 rpm and reaches a maximum RCF of 20,913 × g. It fits up to four tubes of 250 mL or two microplates and works in the temperature range of –9°C to +40°C. The unit automatically recognizes the rotor and detects imbalance, provides the user with 35 programmable settings, 10 acceleration/deceleration profiles, low noise operation (<58 dB), and is compatible with fixed-angle and swing-bucket rotors for a wide range of laboratory uses.
- *Rotary evaporator* (model: Buchi R-300; Buchi India Pvt. Ltd.): It is an innovative modular rotary evaporator for solvent evaporation, concentration, distillation and drying. The key specifications are: evaporating flask capacity 50 mL-5 L, flask load to 3kg, evaporation rotation speed 10-280 rpm, heating bath temperature range 20-220°C, manual or automatic lift, up to 8 condensation patterns. Automated distillation, remote monitoring with BUCHI software/cloud services, SOP programming, vacuum integration, modular system expansion for R&D, pharmaceutical, chemical, food and academic laboratories.
- *Nitrogen gas cylinder* (Linde India Ltd): Linde India nitrogen cylinders store nitrogen gas at high pressure (47L cylinders of high-pressure steel 150–300 bar) with high purity (99.9–99.999%) in high-pressure steel cylinders and result in about 7–14 m^3 of gas. The non-flammable, inert (UN 1066, Class 2.2) gas is used for purging, blanketing, welding, electronics, pharma, and food packaging applications. It should be stored vented to prevent risk of oxygen displacement.

- *GC-olfactometry system* (model: 7890 GC, 5975B MS; Agilent Technologies India): The Agilent 7890 GC is capable of simultaneous instrumental and human sensory analysis of volatiles with the addition of an olfactory detection port (GC-O) for the Agilent 5975B MSD. The 7890 GC is capable of high-resolution capillary separation with programmable temperature control, and the 5975B quadrupole MS performs the mass spectrum, identification (m/z 35-600) under EI (70 eV) conditions. Odor event detection is performed by the sniffing port, while the effluent post-column is divided for chromatographic data collection and spectral data collection for the correlation and confirmation of aroma-active compounds.
- *Sniffing port* (model: Gerstel olfactometer; Gerstel India Pvt. Ltd.): Gerstel GC-O sniffing port is operated with a heated transfer line at approximately 150-250 °C with adjustable effluent split ratios of about 1:1 to 1:4 (nose: detector). Typically, the flow of carrier/make-up gas is 20-60 mL/min. The port supplies almost 100% relative humidity to the nose, so that it doesn't get dry. With sniff port pressure at atmospheric level, the event detection of the odor can be obtained with sub-second to ~1 s time resolution, which allows correlation with the GC retention time.
- *Air pump* (KNF Neuberger India): It is an oil-free gas transfer, polytetrafluoroethylene-coated membrane, polyphenylene sulfide head, fully fluorinated polymer elastomer material (FFPM) valves; flow ~20 – 50 L/min, vacuum up to ~2 mbar abs, pressure up to 0.5 bar. Low maintenance, corrosion resistant, for lab vacuum, distillation and filtration.

Experimental procedure

The ripening stages of mango fruit are broadly classified into three stages: unripe stage (initial stage 1), ripe (stage 2), and overripe stage (stage 3) [14]. In the unripe stage, the fruit is hard and slightly yellow or green; in the ripening stage, the fruit is slightly softer, and the color changes from green to full yellow; and during the overripe stage, the fruit is very soft, full yellow with dark brown spotsas shown in Fig. 1.

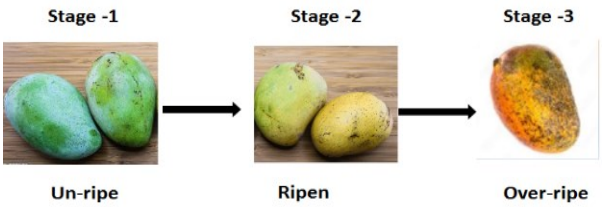


Fig. 1. Ripening stages of mango with its firmness and color

The ripened mango fruit samples of Malgova, Alphonso, Senthuram, and Banganapalli were purchased from a mango farm located in the Salem district in the state of Tamil Nadu, India, and stored at 6°C. Steps were followed to prepare aroma concentrations for the four categories of mangoes:

Step 1: Each category's fresh, ripe mangoes were peeled, and their seeds were removed individually.

Step 2: Mango extracts of Banganapalli, Alphonso, Senthuram, and Malgova were made by blending 1.1 kg of mango pulp at 25 °C for 20 min in each category, using a different blender for each kind of mango flesh.

Step 3: After centrifugation (6000 × g, 4 °C, 20 min), the dichloromethane layer was separated and distilled using a solvent-assisted flavor evaporation process (SAFE) to generate volatile fragrance concentrates.

Step 4: The aroma distillates were dried to about 2 mL using a rotary evaporation set at 40 °C and 600 mm Hg, with an excess of magnesium sulfate added.

Step 5: Finally, a light stream of nitrogen gas was used to prepare 100 µL of the aroma concentrate.

GC-olfactometry investigations were conducted using a 7890 GC system with a 5975B mass spectrometer and a sniffing port equipped with a TC-WAX column specification of 30 m × 0.32 mm and film thickness of 0.50 µm. Helium was employed as a carrier gas at a 1 mL/min rate. The splitless mode was used to inject the samples (0.2 µL) at a temperature of 250 °C. At 70 eV, the mass spectrometer was operated in electron impact (EI) mode. At a pace of 5 °C per min, the oven temperature was increased from 60 to 250 °C. The mass spectrometer and sniffer port shared the effluent at the capillary column's end. By comparing the mass spectra, linear retention indices (RI), and olfactory properties of volatile substances with reference compounds from our lab, two experienced panelists performed GC-olfactometry testing. The n-alkane retention durations were used to calculate the compounds' relative intensities (RIs).

Analytical method

- *Odor uproot blend analysis.* The flavor dilution (FD) factors were determined for the odor-active compounds. Each odor-active chemical in the aroma concentrates has an FD factor, the highest dilution factor that gas chromatography-olfactometry can detect [15]. The more the component contributes to the sample's scent, the higher is the FD factor. Ethanol was used to

progressively dilute the mango scent concentrations, resulting in dilution ratios between 1:31 and 1:310 for all mango categories. Using the TC-WAX column, gas chromatography-olfactometry was used to examine each dilution.

Natural aroma instantaneous input to the sniffing port

Odor-active components interacting with the mango odor were examined for all the mango categories using NAIIS. This technique is based on odor uproot blend analysis and gas chromatography-olfactometry. 10 g of a 1% ascorbic acid solution was added to a 100-g portion of fresh mangoes of each category cage that had been cut into ~2 cm cubes. The mangoes were kept in a glass container at 25 ºC, and 100 mL per min of air was used to release the mango's natural scent into the sniffing port. NAIIS was carried out by combining sensory mango odor detection with gas chromatography-olfactometry analysis. The odor uproot mix study mentioned that the mango scent was accentuated in serial dilutions. The NAIIS-derived FD factors show how much each chemical contributes to the odor of mangos under each mango category.

RESULTS AND DISCUSSION

Four panelists assessed the aroma of freshly cut pieces of Banganapalli, Malgova, Alphonso, and Senthuram mangoes. Results showed milky, tropical, fruity, green, hop, fiber-like, fatty, honey, floral, rose, lactone, sweet, coconut, peach, butter, vanilla, sulfur, and plastic-like odor for Malgova mango; tropical, fruity, green, bamboo, terpeny, fiber-like, fatty, honey, floral, rose, lactone, sweet, coconut, peach, butter, vanilla, sulfur, and plastic odor for Alphonso mango; tropical, fruity, green, hop, terpeny, fiber-like, fatty, honey, floral, rose, lactone, sweet, coconut, peach, butter, vanilla, sulfur, and plastic odor for Senthuram mango and milky, tropical, fruity, green, hop, bamboo, terpeny, fiber-like, fatty, honey, floral, rose, lactone, sweet, coconut, peach, butter, vanilla, sulfur, and plastic-like odor for Banganapalli mango. Using the solvent-assisted flavor evaporation method, the volatile aroma concentrations in each category were determined [16].

Table 1. OUBA: Determined odor compounds for Malgova, Alphonso, Senthuram, and Banganapalli mangoes.

S.No	RI	*Compound	#Odor quality	FD factor			
	TC-WAX			Malgova	Alphonso	Senthuram	Banganapalli
1.	975	2,3-butanedione	milky	3	-	-	3
2.	1024	α-pinene	green, tropical	557	763	251	324
3.	1049	ethyl butanoate	fruity	62	84	26	72
4.	1079	ethyl 3-methylbutanoate	fruity	62	84	26	72
5.	1087	hexanal	green		5	5	1
6.	1150	(Z)-3-hexenal	green	33251	29512	31265	24156
7.	1155	cis-3-hexenol	fresh, green	521	815	621	115
8.	1165	β-myrcene	green, hop	61		3	12
9.	1379	(Z)-3-hexenol	green, fiber-like	1524	2103	976	1065
10.	1399	unknown	sulfur	2513	25	41	7
11.	1455	3-carene oxide	plastic	19602	2561	10213	5201
12.	1549	(E)-2-nonenal	green, fatty	162	281	91	201
13.	1830	(E)-β-damascenone	honey, floral	240	251	243	249
14.	1837	geraniol	floral, rose	2051	2150	2165	2230
15.	1920	γ-octalactone	lactone, sweet, coconut	50269	42510	41568	52143
16.	1920	γ-undecalactone	sweet, fruity	20542	10254	55261	49527
17.	1925	cis-3-hexenyl acetate	green	10256	13254	18761	16841
18.	1934	unknown	sweet	251	251	251	251

19.	1954	δ-octalactone	lactone, fatty, sweet, coconut	36521	42751	3220	7162
20.	1992	4-acetoxy-2,5-dimethyl-3(*2h*)-furanone	sweet	62512	81254	65412	76524
21.	2016	γ-nonalactone	lactone, sweet	35216	41524	51264	49527
22.	2017	4-hydroxy-2,5-dimethyl-3(2H)-furanone (HDMF)	sweet	59049	61254	36524	59049
23.	2059	p-cresol	animal	19683	881	19683	2564
24.	2128	γ-decalactone	lactone, peach	51246	33216	45621	32564
25.	2234	(Z)-7-decen-5-olide	lactone, butter	723	25	625	381
26.	2405	unknown	bamboo, terpeny	-	12	-	51
27.	2535	vanillin	sweet, vanilla	50212	45621	44152	48521
28.	2550	(*Z*)-6-dodecen-4-olide	lactone	1025	11265	10224	1654

*Expert agreement was used to identify each odor's active component and assess its mass spectrum, retention index, and odor quality in relation to the standard reference compounds. # Quality of odor as perceived at the sniffing port.

Table 2. NAIIS: Determined odor compounds for Malgova, Alphonso, Senthuram, and Banganapalli mangoes.

S.No	RI	*Compound	#Odor quality	FD factor			
	TC-WAX			Malgova	Alphonso	Senthuram	Banganapalli
1.	975	2,3-butanedione	milky	1	-	1	-
2.	1024	α-pinene	green, fresh	2193	2193	2193	2193
3.	1049	ethyl butanoate	fruity	1	2	1	1
4.	1079	ethyl 3-methylbutanoate	fruity	7	-	7	7
5.	1087	hexanal	green	1	-	1	1
6.	1150	(Z)-3-hexenal	green, fresh	2185	2185	2187	2185
7.	1155	cis-3-hexenol	fresh, green	2541	1026	3521	925
8.	1165	β-myrcene	green		2	1	1
9.	1379	(Z)-3-hexenol	green, fresh	253	253	253	251
10.	1399	unknown	sulfur	59049	25	41	7
11.	1455	3-carene oxide	plastic	20652	23561	19254	54261
12.	1549	(E)-2-nonenal	green	71	3	5	5
13.	1830	(E)-β-damascenone	honey, floral, potato	4	-	3	3
14.	1837	geraniol	floral, rose	5	5	51	27
15.	1920	γ-octalactone	body, sweet	19652	11211	53261	5283
16.	1920	γ-undecalactone	sweet, fruity	65251	75681	82641	54216
17.	1925	cis-3-hexenyl acetate	fruity	8256	9215	11523	12145
18.	1934	unknown	fruity	25561	42561	65821	21560
19.	1954	δ-octalactone	body, sweet	52481	21652	8562	561
20.	1992	4-acetoxy-2,5-dimethyl-3(*2H*)-furanone	sweet	65214	65843	26851	35462
21.	2016	γ-nonalactone	lactone, sweet	17658	2561	215	3126
22.	2017	4-hydroxy-2,5-dimethyl-3(2H)-furanone (HDMF)	sweet, sugar	64523	42541	51026	21565
23.	2059	p-cresol	ripe, animal	651	2591	21	3651
24.	2128	γ-decalactone	fruity	62514	71256	50202	91562

25.	2234	(Z)-7-decen-5-olide	sweet, fatty	6524	5231	9691	10230
26.	2234	(*Z*)-6-dodecen-4-olide	lactone	12897	19876	32684	41562
27.	2405	unknown	ripe	251	-	-	27
28.	2535	vanillin	sweet	59049	20158	14652	62150

*Expert agreement was used to identify each odor's active component and assess its mass spectrum, retention index, and odor quality to the standard reference compounds. # Quality of odor as perceived at the sniffing port.

After analyzing the aroma concentrates for each of the four categories of mango using OUBA and NAIIS, 28 odor-active chemicals were found, as indicated in Tables 1 and 2. These odor compounds' structures were determined by comparing their mass spectra, RIs, and olfactory characteristics to standard reference compounds in our laboratory. Three newly found compounds (γ-undecalactone, cis-3-hexenol, and cis-3-hexenyl acetate) were among the twenty-eight detected compounds that were identified. Furthermore, previous research indicated that the volatile compounds δ-3-carene and α-terpinolene were plentiful in Malgova mango, but not in OUBA or NAIIS [17]. Accordingly, it was suggested that volatile substances with low odor thresholds can be found by gas chromatography-olfactometry but not by gas chromatography [18].

Table 1 displays the outcomes of the OUBA. 4-Acetoxy-2,5-dimethyl-3(2H)-furanone (FD: 62512), 4-hydroxy-2,5-dimethyl-3(2H)-furanone (HDMF) (FD: 59049), and γ-octa lactone (FD: 51246) exhibit the top three FD factors, while ethyl butanoate (FD: 62), ethyl 3-methylbutanoate (FD: 62), β-myrcene (FD: 61), and 2,3-butanedione (FD: 3) appear to have the least three values for Malgova mango. 4-Acetoxy-2,5-dimethyl-3(2H)-furanone (FD: 81254), 4-hydroxy-2,5-dimethyl-3(2H)-furanone (HDMF) (FD: 61254), and vanillin (FD: 45621) exhibit the top three FD factors, while (Z)-7-decen-5-olide (FD: 25), unknown (FD: 12), and hexanal (FD: 5) appear to have the least three values for Alphonso mango. 4-Acetoxy-2,5-dimethyl-3(2H)-furanone (FD: 65412), γ-undecalactone (FD: 55261), and γ-nonalactone (FD: 51264) exhibit the top three FD factors, while ethyl 3-methyl butanoate (FD: 26), ethyl butanoate (FD: 26), hexanal (FD: 5), and β-myrcene (FD: 3) appear to have the least three values for Senthuram mango. 4-Acetoxy-2,5-dimethyl-3(2H)-furanone (FD: 76524), 4-hydroxy-2,5-dimethyl-3(2H)-furanone (HDMF) (FD: 59049), and γ-octalactone (FD: 52143) exhibit the top three FD factors, while β-myrcene (FD: 12), 2,3-butanedione (FD: 3), and hexanal (FD: 1) appear to have the least three values for Banganapalli mango. β-Myrcene appeared in Malgova, Senthuram, and Banganapalli mangoes with FD factors of 61, 3, and 12, but was missing in Alphonso mango. 2,3-Butanedione appeared in Malgova and Banganapalli mango with FD factors of 3 and 3 but was missing in Senthuram and Alphonso mangoes. Hexanal appeared in Senthuram, Banganapalli, and Alphonso mangoes with FD factors of 5, 5, and 1, but was missing in Malgova mango. γ-Undecalactone, cis-3-hexenyl acetate, and cis-3-hexenol appeared for the first time in South Indian mangoes with a high FD factor. The FD factors of γ-undecalactone in Malgova, Alphonso, Senthuram, and Banganapalli are 20542, 10254, 55261, and 49527, respectively. The FD factors of cis-3-hexenyl acetate in Malgova, Alphonso, Senthuram, and Banganapalli are 10256, 13254, 18761, and 16841, respectively. The FD factors of cis-3-hexenyl acetate in Malgova, Alphonso, Senthuram, and Banganapalli are 10256, 13254, 18761, and 16841, respectively. The FD factors of cis-3-hexanol in Malgova, Alphonso, Senthuram, and Banganapalli are 521, 815, 621, and 115, respectively.

In summary, OUBA found chemicals with low and high odor offsets in each mango category. In general, it is known that interactions between components with low olfactory thresholds and powerful fragrances affect the odors of natural products.

According to a study on beer aromas, none of the odorants alone was responsible for any of the collective characteristics of beer signature odor [19]. Instead, the odor of the beer was mostly influenced by the combined synergistic effects of many odorants. Stated differently, the unique, harmonious aroma of beer results from the interaction and balancing of several odorants. In this study, NAIIS extracted distinct odor components from the four mango category fragrance isolates, combining them with the preexisting mango odor.

The results of NAIIS are shown in Table 2. Generally, NAIIS permits the assessment of these compounds' interactions with the natural flavors, whereas gas chromatography-olfactometry and OUBA permit the evaluation of the odor characteristics of isolated compounds [20]. The flavor dilution factors and odor characteristics of the compound found in NAIIS differed from those in OUBA because of odor interactions. γ-Undecalactone (FD: 62512), 4-acetoxy-2,5-dimethyl-3(2H)-furanone (FD: 65214), and 4-hydroxy-2,5-dimethyl-3(2H)-furanone (HDMF) (FD: 64523) exhibit the top three FD factors, while asgeraniol (FD: 5), (E)-β-damascenone (FD: 4), 2,3-butanedione (FD: 1), ethyl butanoate (FD: 1), hexanal (FD: 1), and 2,3-butanedione (FD: 3) appear to have the least three values for Malgova mango. γ-Undecalactone (FD: 75681), γ-decalactone (FD: 71256), and 4-acetoxy-2,5-dimethyl-3(2H)-furanone (FD: 65843) exhibit the top three FD factors, while (E)-2-nonenal (FD: 3), ethyl butanoate (FD: 2), and β-myrcene (FD: 2) appear to have the least three values for Alphonso mango. γ-Undecalactone (FD: 82641), unknown (FD: 65821), and γ-octalactone (FD: 53261) exhibit the top three FD factors, while (E)-2-nonenal (FD: 5), (E)-β-damascenone (FD: 3), ethyl butanoate (FD: 1), 2,3-butanedione (FD: 1), and β-myrcene (FD: 1) appear to have the least three values for Senthuram mango. γ-Decalactone (FD: 91652), vanillin (FD: 62150), and 3-carene oxide (54261) exhibit the top three FD factors. At the same time (E)-2-nonenal (FD: 5), (E)-β-damascenone (FD: 3), ethyl butanoate (FD: 1), hexanol (FD: 1), and β-myrcene

(FD: 1) appear to have the least three values for Banganapalli mango. Ethyl 3-methyl butanoate appears in Malgova, Senthuram, and Banganapalli mangoes with FD factors of 7, 7, and 7 but was missing in Alphonso mangoes.

(E)-β-damascenone appears in Malgova, Senthuram and Banganapalli mangoes with FD factor of 4, 3, and 3 but is missing in Alphonso mango. β-Myrcene appears in Alphonso, Senthuram and Banganapalli mangoes with FD factors of 2, 1, and 1 but is missing in Malgova mango. Hexanal appears in Malgova, Senthuram and Banganapalli mangoes with FD factors of 1, 1, and 1, but is missing in Alphonso mangoes. 2,3-Butanedione appears in Malgova, and Senthuram mangoes with FD factors of 1 and 1, but is missing in Alphonso and Banganapalli mangoes. Figures 2, 3, 4 and 5 depict the comparison of the FD factors for Malgova, Alphonso, Senthuram, and Banganapalli mangoes by OUBA and NAIIS analyses.

OUBA and NAIIS have their own advantages and disadvantages with different categories of mangoes and odor-active components. Both analyses produce distinct odor-active components which play an important role in effectively differentiating mangoes and their ripening stages. As a result of the analysis, utilizing both methods as the hybrid method for classification would result in excellent performance. According to national and international standards, the weight, size, and color grade system for Indian mangoes are used to determine the ripening phases of the fruit. Internal and exterior quality factors: mangoes can be classified as unripe, early ripe, partially ripe, ripe, or overripe [21]. However, the proposed system uses the odor as the parameter to determine different categories of mango and its ripening stages. The novelty of the proposed work scientifically shows the massive difference in the classification of mangoes and their ripening stages.

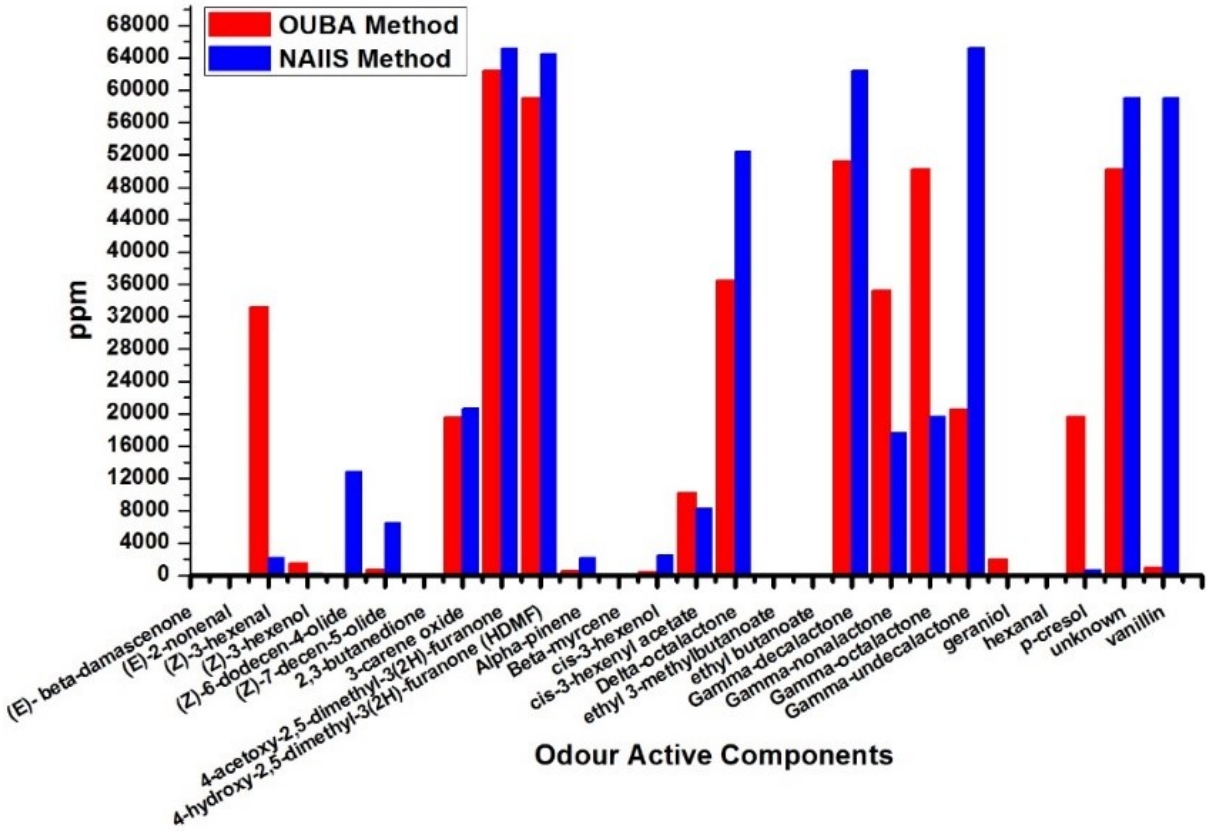


Fig. 2. The FD factor for Malgova mango compared using OUBA and NAIIS analyses.

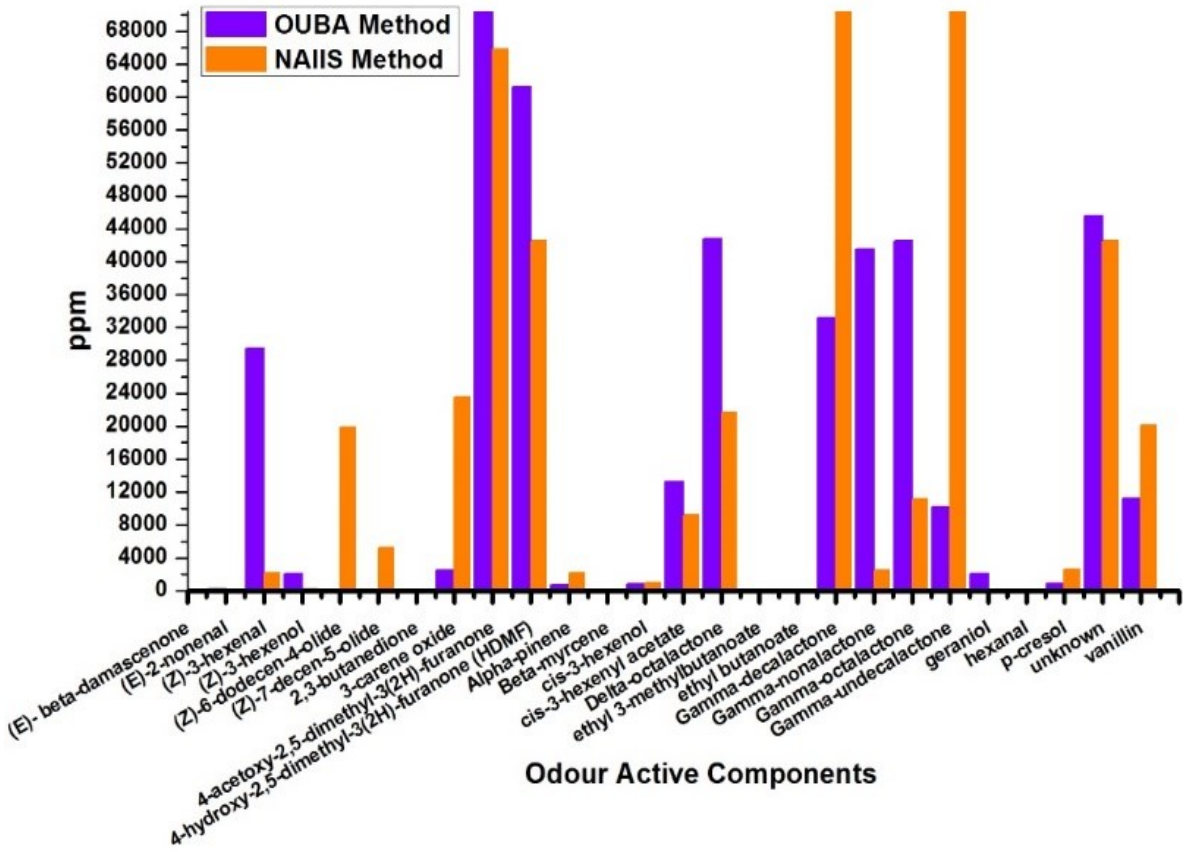


Fig. 3. The FD factor for Alphonso mango compared using OUBA and NAIIS analyses.

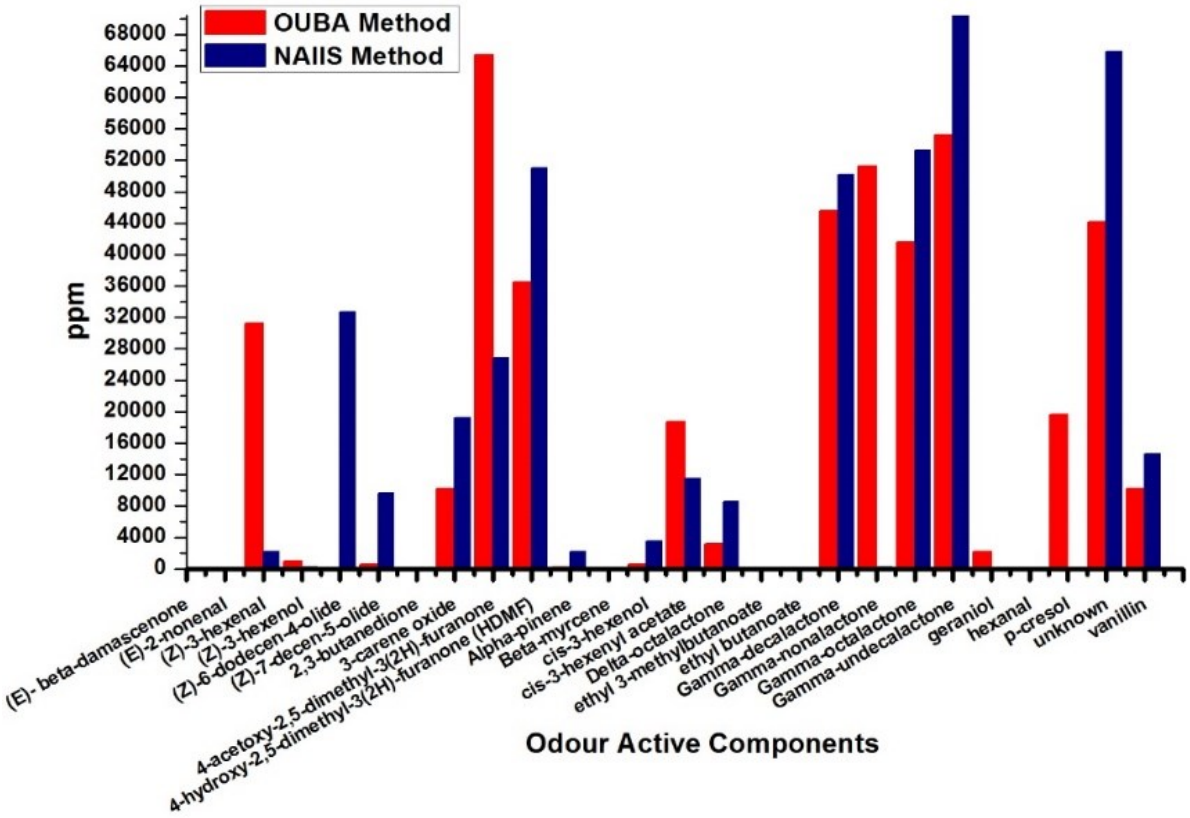


Fig. 4. The FD factor for Senthuram mango compared by OUBA and NAIIS analyses.

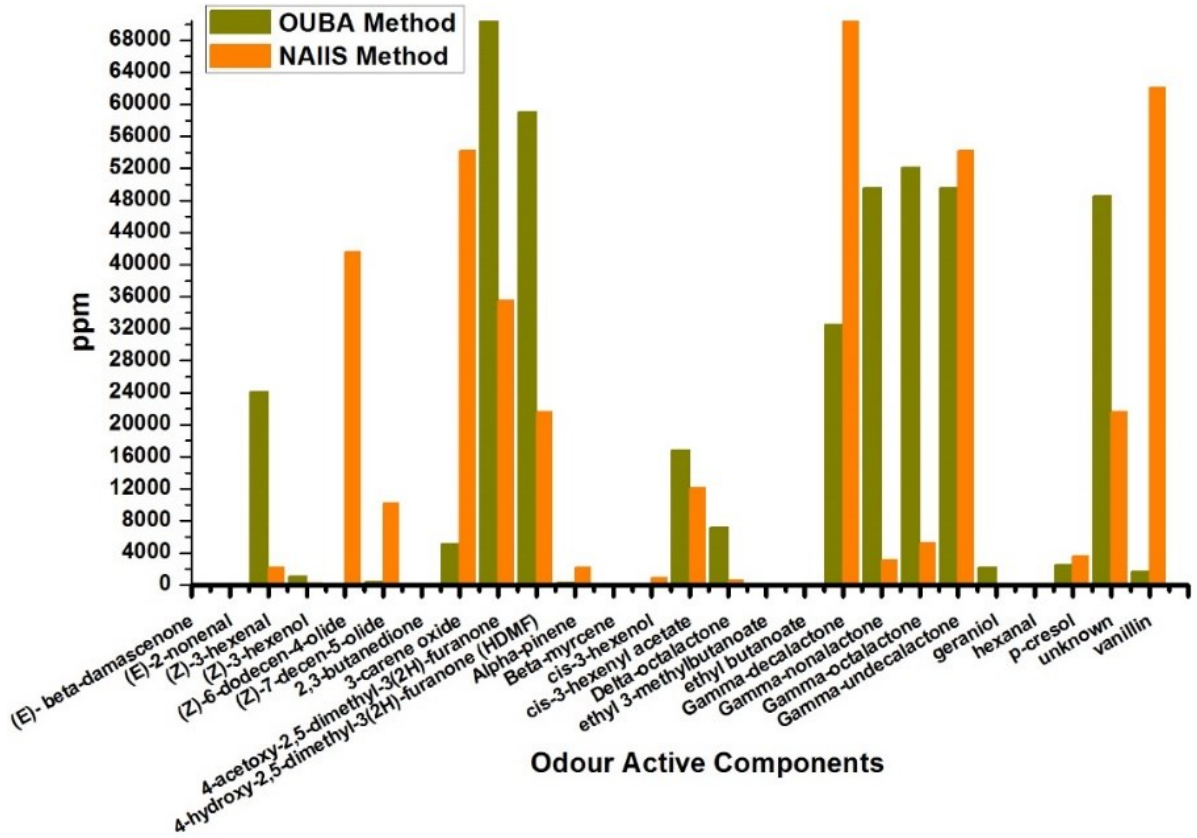


Fig. 5. The FD factor for Banganapalli mango compared using OUBA and NAIIS analyses.

OUBA and NAIIS methods gave FD factors for all 28 odor-active components of Malgova mango, where the percent error is zero. For Alphonso mango, the OUBA method determined the FD factor for 27 components, and the NAIIS method determined the FD factor for 22 components out of 28, which leads to a percent error of 3.57% and 21.42%, respectively. The OUBA method determined the FD factor for 26 components, and the NAIIS method determined the FD factor for 27 components out of 28, which leads to a percent error of 7.14% and 3.57%, respectively, for Senthuram mango. Similarly, for Banganapalli mango, the OUBA method determined the FD factor for 28 components, and the NAIIS method determined the FD factor for 27 components out of 28, which leads to a percent error of 0% and 3.57%, respectively. Therefore, the average percent error for determining the odor active component using OUBA and NAIIS are 2.66% and 7.14% based on the FD factor.

CONCLUSIONS

Odor uproot blend analysis (OUBA) and NAIIS (natural aroma instantaneous input to the sniffing port) identify 25 odor-active components and three unknown components of top four categories of South Indian mangoes. The odor-active components such as γ-undecalactone, cis-3-hexenol, cis-3-hexenyl acetate, β-myrcene, 2,3-butanedione, β-myrcene, (E)-β-damascenone, and hexanal can be utilized to differentiate between these four categories of South Indian mangoes. These identified odor-active components can be used to design an odor sensor specially for these categories of mangoes, which can be implemented in automated systems in mango export and related product production factories. Further, it will also be helpful to identify the ripening stages of all these categories of mangoes so that mango fruit can be delivered on time for consumers and avoid fruit wastage, which is essential for human beings who need it.

Acknowledgement: *We would like to acknowledge Kongu Engineering College, Erode, India and KPR Institute of Engineering and Technology for providing laboratory support for this research project.*

Funding statement: *The authors received no financial support for the research, authorship, and/or publication of this article.*

Data availability statement: *The data generated and analyzed during this study are available from the corresponding author on reasonable request.*

REFERENCES

1. D. V. Rao Sudhakar, C. K. Narayana, Emerging Technologies for Shelf-Life Enhancement of Fruits, B. S. Dar, S. A. Mir (eds.), Taylor and Francis, 2020, p. 313.
2. P. R. Kiran, I. Mani, R. A. Parrey, M. Srivastav, *Environ. Conserv. J.,* **24**, 64 (2023). https://doi.org/10.36953/ECJ.20472555

3. S. Anusha, N. Indra, R. Kannan, P, Geetha, C. Sh. Rahale, *Int. J. Plant Soil Sci.,* **35**, 1291 (2023).
4. Th. Thanaraj, S. Landahl, L. A. Terry, *J. Agric. Food Res.,* 100053 (2020). https://doi.org/10.1016/j.jafr.2020.100053
5. H. M. Ali, M. R. Khan, A. A. Essawy, A. El Aziz. A. Nayl, H. Ibrahim, H. Gomaa, M. Gamal, Y. H. Alruwaili, Gh. B. Al Rwilly, T. H. A. Hasanin, *Bull. Chem. Soc. Ethiop.,* **38** 1543 (2024). https://dx.doi.org/10.4314/bcse.v38i6.4
6. Z. Pawlos, Bh. Singh, Ch. Y. Weldegebriel, A. Embiale, *Bull. Chem. Soc. Ethiop*., **35**, 217 (2021). https://dx.doi.org/10.4314/bcse.v35i2.1
7. T. Wang, Zh. Wang, L. Guo, J. Zhang, W. Li, H. He, R. Zong, D. Wang, Zh. Jia, Y. Wen, *Agric. Syst.,* **193**, 103220 (2021), https://doi.org/10.1016/j.agsy.2021.103220
8. N. Baldovini, A. Chaintreau, *Nat. Prod. Rep*., **37**, 1589 (2020). https://doi.org/10.1039/D0NP00020E
9. T. Tang, Zh. Min,Bh. Bhesh, *Foods,* **12**, 1263 (2023), https://doi.org/10.3390/foods12061263
10. A. de la Fuente-Blanco, M.-P. Sáenz-Navajas, J. Ballester, *Int. Viti. and Enol. Soc. ,***57** (2023). https://doi.org/10.20870%2Foeno-one.2023.57.2.7089
11. P. Duchamp-Viret, N. Kuczewski, Ch. Baly, *In Flavor*, *Woodhead Publishing,* **2**, 149 (2023) https://doi.org/10.1016/B978-0-323-89903-1.00007-4
12. Ferreira, V. M.-P. Sáenz-Navajas, E. Campo, P. Herrero, A. de la Fuente, P. Fernández-Zurbano, *Food Chem*. **199,** 447 (2016). https://doi.org/10.1016/j.foodchem.2015.12.048
13. V. Ferreira, A. de la Fuente-Blanco, M.-P. Sáenz-Navajas, *Foods*, **10,** 1627 (2021). https://doi.org/10.3390/foods10071627
14. R. K. Shakibur, M. Mirazus, S. Rituporna, R. Joyashree, Bh. Swarna, Md. Rakibul, I. Rakib, Ch. K. Saha, A. Rahman, *Smart Agric. Technol.,* **9**, 100558 (2024). https://doi.org/10.1016/j.atech.2024.100558
15. Ch. Chen, Zh. Liu, H. Yu, Zh. Xu, H. Tian, *Food Chem.*, **368,** 130736 (2022). https://doi.org/10.1016/j.foodchem. 2021.130736
16. Z. Feng, X. Yang, C. Zou, J. Yin, *J. Vis. Exp.,* **26**, 65522 (2023).
17. D. M. Saleem, Bh. B. Dholakia, S. A. Punekar, V. S. Gupta, A. P. Giri, *India Section B: Biological Sciences*, **93**,659 (2023). https://doi.org/10.1007/s40011-023-01455-6
18. C. Fisher, T. R. Scott, Food flavours, biology and chemistry, Royal Society of Chemistry, 2020.
19. J. A. Piornos, D. P. Balagiannis, L. Methven, E. Koussissi, E. Brouwer, J. K. Parker, *J. Agric. Food Chem.,* **68,** 10088 (2020).
20. Y. Niu, P. Wang, Q. Xiao, Z. Xiao, H. Mao, J. Zhang, *Molecules,* **25**, 1083 (2020). https://doi.org/10.3390/molecules25051083
21. V. Namb, Eyarkai, K. Thangavel, D. Manohar Jesudas, *Sci. Hortic.,* **193**, 90 (2015). https://doi.org/10.1016/j.scienta.2015 05.031

Bulgarian Chemical Communications, Volume 58, Issue 4 (pp. 431-435) 2026 *DOI: 10.34049/bcc.58.4.5728*

UV-Vis spectrometer from scratch: a budget do-it-yourself solution to a growing problem

N. Stamenov[1,2], I. I. Lozanov[1*]

[1]*Faculty of Chemistry and Pharmacy, Sofia University 'St. Kliment Ohridski', 1 James Bourchier Blvd., 1164 Sofia, Bulgaria*
[2]*National High School for Mathematics and Science 'Acad. Lyubomir Chakalov', 52 Bigla Str., Sofia, Bulgaria*

Received: October 28, 2025: Revised: June 22, 2026

UV-Vis spectrophotometry is one of the most commonly applied spectral methods for quantitative analysis. Its concept, meaning and applicability are an important part of the specialized chemistry course *Methods for control and compound analysis*. As most schools lack UV-Vis spectrophotometers, there is a tendency to skip the laboratory exercises dedicated to this topic. Our work presents a simple and practical way to remedy the present problem. A methodology is proposed that allows students to perform simple spectrophotometric experiments using low-cost equipment. A sample experimental protocol for conducting a successful lab exercise is developed and further data processing is demonstrated. The results are promising, showing that UV-Vis spectrophotometry can be successfully taught in practice with low cost, minimal preparatory time and without specialized equipment.

Keywords: low-cost spectrophotometric teaching equipment; inquiry-based learning; self-led exercise, chemistry education.

INTRODUCTION

In the past years, the Bulgarian curriculum and high-school system were changed in a way that allows students to choose and pick up to four specialized subjects during their last two years of education, called second high-school level (similar to A level). Those who choose chemistry are taught in much more detail including aspects of applied science, which broadens their knowledge and prepares them for further scientific work and academia. The curriculum in chemistry is divided into four separate parts that are taught in the following order:

1. Theoretical foundations of chemistry (11th grade)
2. Inorganic chemistry (11th grade)
3. Organic chemistry (12th grade)
4. Methods for control and compound analysis (12th grade)

The present work focuses on the fourth, last part, because it appears to be the most challenging one for high-school teachers. Common reasons why they face difficulties are: (i) reduced number of hours due to the shorter semester for 12th-graders; (ii) insufficient time for preparation and conducting laboratory exercises; (iii) lack of equipment for students to conduct any spectroscopic analysis.

This article presents a simple and low-cost, yet effective experiment for quantitative analysis of colored aqueous solutions. The analysis is quite suitable for a 2- or 3-h laboratory exercise, as outlined in the Experimental part. Its main advantage is that students can experiment almost without any input from the teacher (self-led exercise). The presented approach for quantitative analysis has already given excellent results among other students worldwide [1-8] with simple 3d printed devices and use of smartphones, moreover, such low-cost approach has merit in real life applications [9]. While the experimental setup suggested in this work does not significantly differ from other examples, the mathematical methods for data processing do. Depending on the students' mathematical knowledge, one of two approaches should be utilized to process experimental data (e.g., excluding or including logarithms).

Aims and research purpose

This article suggests a low-cost, multi-aspect, practical lab experiment dedicated to quantitative UV-Vis spectroscopic analysis. It could be easily conducted by high-school students during their chemistry lessons. The authors aim to prove that including a reliable and accurate spectroscopic experiment at school is achievable even provided limited financial and material resources.

Problem statement

The current task is to analyze two sets of freshly prepared standard solutions of copper (II) sulfate ($CuSO_4$) and nickel (II) sulfate ($NiSO_4$), as well as

* To whom all correspondence should be sent:
Email: *ivoil@uni-sofia.bg*

© 2026 Bulgarian Academy of Sciences, Union of Chemists in Bulgaria

to derive calibration curves (Beer's law). Additionally, the results obtained with the presented spectrometer are compared to those measured with a reference PASCO spectrometer. The questions to be answered are; - is the accuracy of our measurement tool comparable to that of a professional spectrometer, and how to best process the obtained experimental data.

EXPERIMENTAL

Setup

The experimental setup includes the following:

- Small cardboard box;
- Duct tape, glue, ruler and scissors;
- Aluminum foil;
- Cuvette;
- Two smartphones (or a smartphone and a laptop);
- Purified water and standard solutions of Cu(II); and Ni(II) (chosen because their absorbance is in the visible spectrum);
- Weighting scale Kern TGD 50-3C;
- PASCO PS-2600A spectrometer (used as reference).

A small 50×50 mm box is made of cardboard (box size could be modified). A circular hole is made on one side of the box so it can accommodate a smartphone camera. Then, another bigger rectangular hole is made on the opposite side to place a smartphone or laptop screen as a red-green-blue (RGB) light source. A small square hole is made at the top of the box so that a standard cuvette could be placed inside (Figures 1, 2). The outside of the constructed spectrometer is covered with aluminum foil, so it blocks light entering the box thus reducing error.

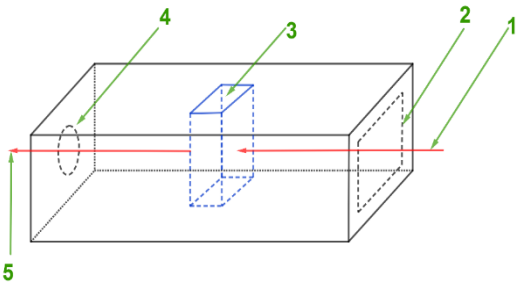


Fig. 1. Sample scheme of the constructed spectrometer: 1 – input light ray; 2 – rectangular hole for the light source; 3 – cuvette space; 4 – small circular hole for a camera; 5 – output light ray

Procedure

A set of $CuSO_4$ aqueous solutions with concentrations of 0.025 M; 0.050 M; 0.10 M; 0.20 M and 0.30 M are prepared by weighing an exact mass of stock $CuSO_4.5H_2O$ and dissolving it with purified water in a 100 mL volumetric flask. The mixture is homogenized, then an aliquot is taken and diluted with water in a 50 mL volumetric flask. The procedure is then repeated to prepare the rest of the solutions. All aliquots are measured with a burette to ensure that exact volumes are transferred to the volumetric flasks. The solutions of $CuSO_4$ should be measured at a wavelength $\boldsymbol{\lambda_{max}} \sim 635$ nm ($\varepsilon = 2.8\ \mathrm{L \cdot mol^{-1} \cdot cm^{-1}}$) [10, 11] and the solutions of $NiSO_4$ - at $\boldsymbol{\lambda_{max}} = 393$ nm ($\varepsilon = 5.1\ \mathrm{L \cdot mol^{-1} \cdot cm^{-1}}$) [12]. Given the educational focus of this work, our aim is to emphasize the key aspects of spectrophotometry, as well as to facilitate the experiment itself and make it more suitable for students. Therefore, analyte solutions with higher concentration are preferred, which justifies the choice of the absorption bands for $CuSO_4$ and $NiSO_4$ corresponding to low intensity $d \rightarrow d$ transitions. Light sources with continuous spectra allow a free choice of wavelength. However, students do not often come to school with such light emitters. In contrast, they never miss the opportunity to bring their smartphones and laptops to school every day. So, the main question is: can they use digital screens as light sources, given the obstruction that they only emit a linear RGB spectrum? The answer is — yes, however, a slight change in results interpretation is required. Digital screens emit red, green, and blue light, and thus each sample is measured by the color it absorbs the most. For example — blue samples like $CuSO_4$ and methylene blue absorb most intensely red light. Red compounds like Co(II) salts or the $[Fe(SCN)_6]^{3-}$ complex absorb mostly in blue. Therefore, the classic concept for absorption at a fixed wavelength is substituted by absorbing red, green, or blue light.

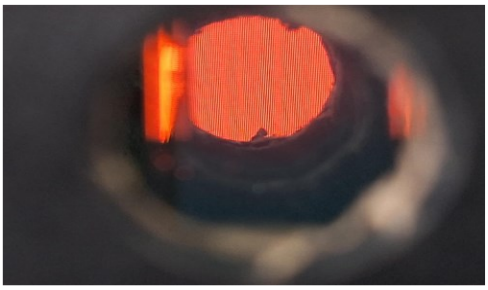


Fig. 2. Picture made with a smartphone camera placed in front of the spectrometer circular hole

RESULTS AND DISCUSSION

Although professional spectrophotometers directly display the absorbance A of a sample at certain λ, the presented tool can only measure RGB light components. For green and blue solutions, the most significantcomponent is $[R]$ while for red

solutions it is the green one [G] [13]. It is essential to note the correlation between numerical values for [R] light and sample concentration c. Suppose a purely red screen is a light source, the measured [R] should be proportional to the light intensity I passed through the cuvette. Although each smartphone camera introduces transformations to the measured light, for this article's aims the correlation between [R] and I could be assumed linear without an intercept: $I = \alpha \cdot [\mathrm{R}]$, where α is a coefficient specific for each camera and depends on the surrounding light, screen brightness and parameters that are specific for each individual measurement set. The constructed educational measurement tool should be calibrated before changing the surrounding light, the sample color, the screen/its brightness and the detecting camera. Given all the assumptions are requirements, we do not propose, nor do we claim that this is a universal calibration protocol. The calibration of the spectrometer only consists of obtaining a linear correlation between the sample concentration and the specific function of [R], representing the absorbance A. Thus, for concentrations in the linear section of Beer's law, the following relation is obtained:

$$A = \lg\left(\frac{I_0}{I}\right) \sim \lg\left(\frac{[R]_0}{[R]}\right),$$

where $[R]_0$ is the absolute [R] value of the red screen. Ideally, $[R]_0 = 2^8 = 256$. Given that we work with line light spectrum, no wavelength could be specified. At first glance, this might seem to be a limitation, however the entire spectral analysis regards only one of the spectral components present in the emitted light – [R], [G] or [B] [14, 15]. Therefore, samples are analyzed, based on their general sensitivity to red, green, or blue light.



Fig. 3. Front view of the constructed spectrometer

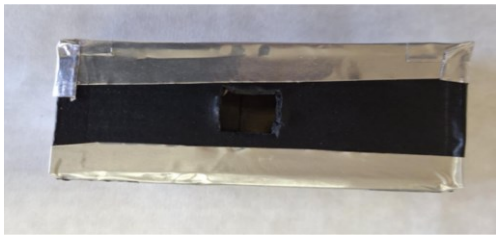


Fig. 4. Top view of the constructed spectrometer

The working protocol presented below is followed. It is useful, but not the only one, so it could be optimized depending on the teacher's goals and the students' preparation level.

Protocol

1. Samples preparation;
2. Spectrometer calibration against purified or distilled water;
3. Measurements with the constructed spectrometer;
   Data processing as:
   a. [R] *vs.* c plot and $c = \alpha[R]$ fit;
   b. lg [R] *vs.* c plot and $c = \beta - \alpha.\lg[R]$ fit;
4. Comparison between both methods and data analysis methods.

Analysis with reference PASCO spectrometer

For each solution set, all samples are analyzed starting from the most dilute one. The spectrometer is calibrated using its built-in functions against a cuvette filled with purified water. Samples are then transferred to the cuvette, and the absorbance is read and written down. All data gathered for both compounds are summarized in Table 1.

Table 1. Experimental data for the absorbance A of all samples obtained with the reference PASCO spectrometer

№	c_1($CuSO_4$), M	A_1, -	c_2($NiSO_4$), M	A_2, -
1	0.025	0.06 ± 0.02	0.019	0.03 ± 0.02
2	0.050	0.09 ± 0.02	0.038	0.10 ± 0.02
3	0.100	0.21 ± 0.02	0.075	0.21 ± 0.02
4	0.200	0.43 ± 0.02	0.150	0.43 ± 0.02
5	0.300	0.70 ± 0.02	0.300	0.93 ± 0.02

The absorbance is plotted against solution concentration – $A(c)$, and correlation coefficients R^2 of 0.9990 and 0.9959 are obtained.

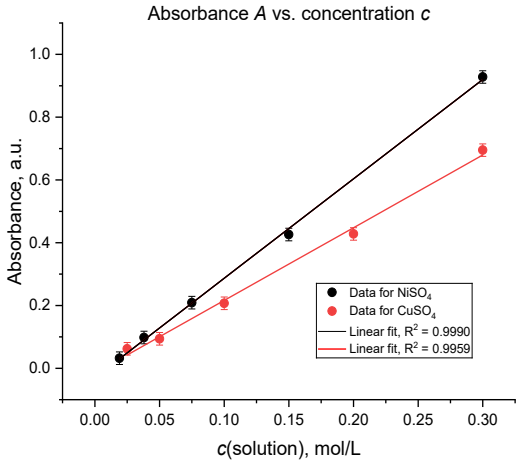


Fig. 5. Absorbance results for both sets of analyzed solutions using the PASCO spectrometer

Analysis with the constructed spectrometer and the linear data model

New samples from the already prepared standard solutions are taken and analyzed against a bright laptop screen which emits light in the discrete RGB range of the spectrum. The measurement procedure is the following: a laptop screen is set on a specific color and is put right next to the large rectangular hole of the constructed spectrometer. A cuvette containing a colored sample is put in the spectrometer, and then a smartphone is used to take a picture of the sample through the smaller circular hole. Preferably, the pictures should focus in the cuvette's center. All pictures are carefully analyzed using *Color Analyzer* mobile app. Its main advantage is that it displays RGB values both quickly and accurately. In addition, RGB values are available for each point of the analyzed picture. That means one could easily specify the desired spot for investigation and could potentially conduct multiple sample analyses if more samples are present in the picture.

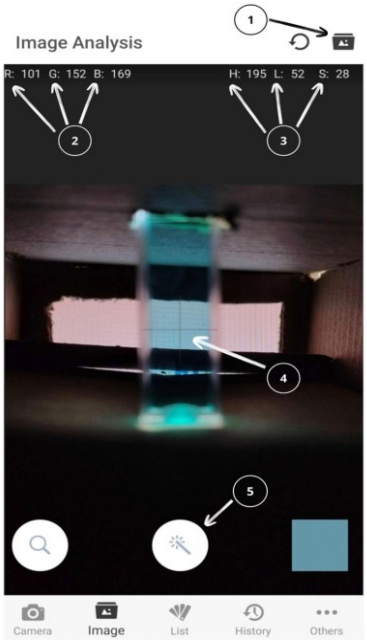


Fig. 6. Screenshot showing the interface of the RGB analyzing software

Main criteria for linearity of the results is assumed to be the numerical value of the correlation coefficient R^2. The obtained experimental data are summarized in Table 2. The results in Figure 7 confirm the hypothesis that a linear correlation analogous to Beer's law can be derived for a certain RGB spectral component.

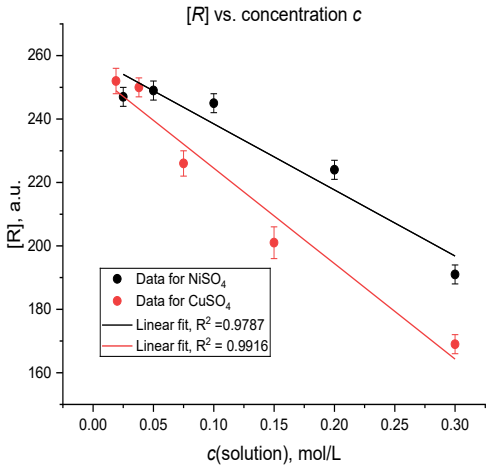


Fig. 7. Experimental results for all samples + spectrophotometer + linear data model

Table 2. Absolute [*R*] spectral value vs. samples concentration *c* for measurements with the constructed spectrometer

№	c_1(CuSO4), M	[*R*], -	c_2(NiSO4), M	[*R*], -
1	0.025	247 ± 3	0.019	252 ± 4
2	0.050	249 ± 3	0.038	250 ± 3
3	0.100	245 ± 3	0.075	226 ± 4
4	0.200	224 ± 3	0.150	201 ± 5
5	0.300	191 ± 3	0.300	169 ± 3

Analysis with constructed spectrometer and logarithmic model

The previously gathered data for [*R*] are logarithmized, and a linear regression is fitted.

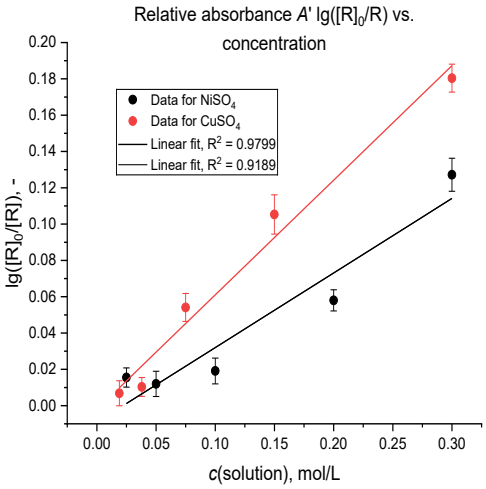


Fig. 8. Experimental results for all samples + spectrophotometer + logarithmic data model

Table 3. Logarithmized [*R*] spectral value *vs*. concentration *c* for measurements with the constructed spectrometer

№	$c_1(CuSO_4)$, M	$\lg([R]_0/[R])$, -	$c_2(NiSO_4)$, M	$\lg([R]_0/[R])$, -
1	0.025	0.016 ± 0.005	0.019	0.007 ± 0.005
2	0.050	0.012 ± 0.007	0.038	0.010 ± 0.005
3	0.100	0.019 ± 0.007	0.075	0.054 ± 0.008
4	0.200	0.058 ± 0.006	0.150	0.105 ± 0.011
5	0.300	0.127 ± 0.009	0.300	0.180 ± 0.008

CONCLUSION

Although the proposed spectrometer does not reach the same precision as a professional instrument, its accuracy is fully adequate for educational use. Moreover, the do-it-yourself version is very low-cost, easy to construct and flexible in its operation. It succeeds in demonstrating key spectroscopic phenomena and measurement techniques, which makes it a powerful tool for teaching. In this sense, the advantages of the proposed instrument far outweigh its small loss of accuracy.

Author contributions: ***NS****: Conceptualization, methodology, investigation, data curation, Writing - editing and review;* ***IL****: Methodology, investigation, data curation, original draft – writing.*

Acknowledgement: *Margarita Stefanova from the Faculty of Chemistry and Pharmacy, Sofia University 'St. Kliment Ohridski' is acknowledged for her assistance in constructing the spectrometer.*

REFERENCES

1. U. Jarujareet, G. Pichayawaytin, P. Sripetch, N. Doljirapisit, S. Sumriddetchkajorn, P. Prempree, K. Chaitavon, P. Punpetch, R. Amarit, *Journal of Chemical Education*, **100**, 546 (2023).
2. B. Bruininks, L. B. F. Juurlink, *Journal of Chemical Education*, **99**, 2168 (2022).
3. A. Khandelwal, T. K. Leong, Y. Yang, L. K. Wee, F. J. Garcia Clemente, T. Venkatesan, H. Jani, *The Physics Educator*, **04**, 2250003 (2022).
4. S. Shidiq, A. Permanasari, H. Hernani, *Proceedings of the 4th Asian Education Symposium (AES 2019)*, 150 (2020).
5. M. A. Lema, E. M. Aljinovic, M. E. Lozano, *Biochemistry and Molecular Biology Education*, **30**, 106 (2002).
6. P. V. Kolesnichenko, A. Eriksson, L. Lindh, D. Zigmantas, J. Uhlig, *Journal of Chemical Education*, **100**, 1128 (2023).
7. V. Santos, W. Oliveira, J. P. de Almeida, M. Foguel, W. Suarez, J. de Oliveira, *Quimica Nova*, **46** (2023).
8. E. K. Grasse, M. H. Torcasio, A.W. Smith, *Journal of Chemical Education*, **93**, 146 (2016).
9. J. B. Santiago, F. B. Sevilla, *Microchemical Journal*, **172**, 106952 (2022).
10. Kafle, B. Pokhrel, R. Gyawali, A. Kafle, T. Shrestha, R. Shrestha, R. Adhikari, *International Journal of Materials Science and Applications*, **4**, 314 (2014).
11. S. Rahardjo, T. Saraswati, A. Masykur, N. Finantrena, H. Syaima, *IOP Conference Series*: *Materials Science and Engineering*, **349**, 012056 (2018).
12. H. Syaima, S. B. Rahardjo, N. Amanati, *Journal of Physics: Conference Series*, **1022**, 012028 (2018).
13. M. Paristiowati, M. Moersilah, M. Nurjayadi, A. N. Fitria, *Journal of Physics: Conference Series*, **1869**, 012064 (2021).
14. J.-S. Kim, A.-H. Kim, H.-B. Oh, B.-J. Goh, E.-S. Lee, J.-S. Kim, G.-I. Jung, J.-Y. Baek, J.-H. Jun, *Bio-Medical Materials and Engineering*, **26**, 1773 (2015).
15. E. Cha, H. Lee, *Journal of International Research in Medical and Pharmaceutical Sciences*, **19**, 24 (2014).

Bulgarian Chemical Communications, Volume 58, Issue 4 (pp. 436-441) 2026 *DOI: 10.34049/bcc.58.4.5739*

Design and biological evolution of La_2O_3-ZnO mixed metal oxide nanomaterials for anticancer activity against MCF-7 cell lines

A. R. Padol[1], M. E. Navgire[2], M. A. Raut[3]*

[1]*Dr. Rafiq Zakaria College for Women, Chh. Sambhajinagar, 431003 India*
[2]*Jijamata College of Science and Arts, Bhende Bk. Ahilyanagar, India*
[3]*Pratisthan Mahavidyalaya, Paithan, Chh. Sambhajinagar, India*

Received: December 14, 2025; Revised: May 25, 2026

Nanotechnology-based mixed metal oxide nanocomposites have gained significant attention in biomedical applications owing to their enhanced physicochemical and therapeutic properties. In the present study, La_2O_3–ZnO mixed oxide nanoparticles were synthesized by a co-precipitation method and evaluated for their *in-vitro* anticancer activity against MCF-7 human breast cancer cells. Structural and morphological characterization was carried out using XRD, UV-DRS, FTIR and SEM techniques. The XRD analysis confirmed the crystalline nature of the synthesized nanocomposite with an average crystallite size of 30.79 nm. The UV-DRS analysis revealed optical band gap energy of 3.21 eV for the La_2O_3-ZnO nanocomposite. FTIR spectra confirmed the formation of La–O and Zn–O bonds while SEM images demonstrated a porous nanocrystalline morphology. Cytotoxicity study using the MTT assay showed a dose-dependent reduction in MCF-7 cell viability which decreased from 97.11 ± 6.54% to 17.04 ± 1.22% with increasing nanoparticle concentration (1–50 µg/mL). Morphological studies further confirmed cellular deformation and apoptotic changes after nanoparticle treatment. The obtained results indicate that La_2O_3–ZnO mixed oxide nanoparticles exhibit promising anticancer potential and may serve as effective alternative nanotherapeutic agents for breast cancer treatment.

Keywords: La_2O_3–ZnO nanocomposite; anticancer activity; MCF-7 cells; mixed metal oxide; nanotechnology

INTRODUCTION

In the recent years considerable attention is paid to the field of nanoscience and nanotechnology. A variety of applications in the field of material sciences, medicine, computer sciences and environmental studies such as pollution was studied. The synthesis of nanomaterial-based anticancer and antimicrobial agents has gained considerable attention owing to their fundamental, distinctive physico-chemical and biological properties resulting from the small size and large surface area. Anticancer agents synthesized from nanomaterials and nanocomposites have shown much better stability under different physical conditions such as temperature, pressure and mass-to-volume ratio compared to organic-based anticancer agents [1-5]. In the past few years a variety of studies has been performed to investigate the anticancer activity of metal oxides, mixed metal oxides and their composites [6-13].

A number of research papers on cytotoxic (anticancer) activity is focused on mixed metal oxides [14-17]. Mixed nanocomposite materials, along with surface-active agents such as cetyltrimethyl ammonium bromide (CTAB), PEG and others, are investigated for their cytotoxic effect and anticancer activities, giving a considerable contribution to the development of alternate anticancer agents for the control of cancerous cells. Transition metals, with their important properties such as high melting point, high mass-to-volume ratio, high thermal conductivity and good physico-chemical properties due to their 4f orbital electrons, have been applied in electronic, medicinal, and agricultural studies [18, 19].

Nanotechnology is an emerging research field with agro-industrial, pharmaceutical and medicinal applications [20]. Nanomaterials can disrupt the generation of free radicals through different mechanisms due to their capacity to mimic the activity of enzymes or to donate electrons [21].

Rare earth nanoparticles are used in human healthcare for drug delivery in tumor therapy, bio imaging and diagnosis [22]. The development of this type of nanomaterials can include the use of essential trace elements such as Zn^{2+} which is a safe material exploited for nano biotechnologies due to its optical, biological, mechanical, catalytic and intrinsic therapeutic properties and its easy manipulation in the synthesis of doped nanostructures, e.g. lanthanum doped with zinc [23-29].

In therapeutic applications, zinc-doped nano-particles have been reported to target neurological diseases and to possess biocompatibility with treatment regimens such as chemotherapy and radiotherapy [30, 31]. As compared to other

* To whom all correspondence should be sent:
E-mail: *mahanandaraut@yahoo.in*

© 2026 Bulgarian Academy of Sciences, Union of Chemists in Bulgaria

lanthanide series elements, lanthanum oxide (La_2O_3) is applied to fabricate nanostructures through different physical and chemical methods. Lanthanum is recognized for its important biomedical uses due to its genotoxicity, presence of 4f shielded electrons, biocompatibility, magnetic features and redox switching capacity [32].

This study aims to synthesize and characterize lanthanum-zinc mixed oxide nanoparticles and evaluate their anticancer potential against the MCF-7 breast cancer cell line. The nanoparticles were synthesized by a co-precipitation method, and their cytotoxicity was evaluated using MTT assay, with DOXO serving as the standard reference drug.

MATERIALS AND METHODS

Chemicals and materials

Zinc nitrate, lanthanum nitrate, and ammonia were purchased from Sigma Aldrich. All chemicals were of analytical grade and were used as received.

Synthesis of lanthanum-zinc mixed oxide materials

The synthesis was made using deionized water and 500 ml of precursor salt solution prepared by mixing individual solutions of the two salts such as to contain an overall metal concentration of 0.5 mole l^{-1} and lanthanum-to-zinc molar ratio of 1:4. This solution mixture was slowly added in a beaker under continuous magnetic stirring. At a flow rate of 9 ml min^{-1} ammonia (1:1) was added to keep the pH value of the medium at 10±0.2. An initial volume of 25 ml of water was placed in the beaker before dropping of metallic salts mixture and ammonia solution. After addition of reactants, the solution mixture was aged at ambient temperature for 40 min under continuous stirring. Subsequently, the mixture was ultrasonicated at 40 °C for 30 min. After cooling, the product was centrifuged (10 min at 4000 rpm). Then the product was washed three times with distilled water and dried at 80 °C for 24 h. Synthesized sample was calcined at 650 °C for about 3 h.

Characterizations

- *X-ray diffraction (XRD) analysis.* XRD analysis confirmed that the synthesized La_2O_3-doped ZnO nanocomposite material was crystalline in nature (see Fig. 1). The diffraction of peaks of pure ZnO, shown in Fig. 1(a) with 2θ (°) values of 32.135, 35.083, 37.095, 47.734, 56.75, 63.07 and 70.187 corresponds to (100), (002), (101), (102), (110), (103), and (201) planes, and perfectly match JCPDS card no. 79-0205 with hexagonal phase [33]. Similarly, Fig. 1(b) shows the diffraction peaks of pure La_2O_3 with 2θ (°) values of 22.861, 29.614, 30.960, 44.547 and 54.549, corresponding to (221), (321), (400), (440) and (631) planes, respectively, and perfectly matching JCPDS card no. 04-0856 with cubic phase [34].

Figure 1(c) illustrates the formation of the mixed phase of the La_2O_3-ZnO nanocomposite material. The planes that have (hkl) values of (221), (321), and (440) correspond to La_2O_3 while remaining planes, which have (hkl) values of (100), (002), (101), (102), (110), (103) and (201) correspond to ZnO material. By using Debye-Scherrer equation, the crystallite size of the synthesized nanocomposite material was calculated (Table 1).

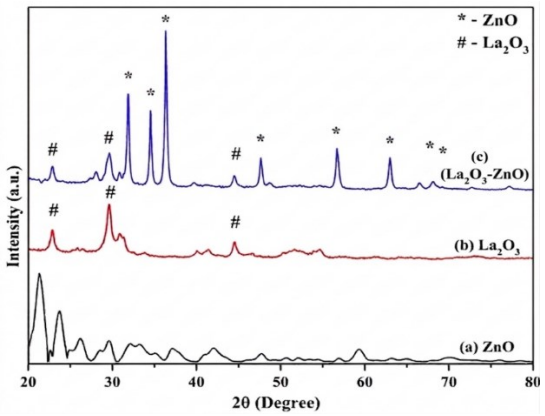


Figure 1. XRD analysis of (a) ZnO, (b) La_2O_3 and (c) La_2O_3-ZnO nanocomposite

Table 1. Crystallite size of synthesized nanocomposite materials.

S. No.	Material	2θ (°)	FWHM (°)	Crystallite size (nm)
1	La_2O_3	29.614	0.8399	10.23
2	ZnO	21.401	0.9741	8.67
3	La_2O_3 -ZnO	36.365	0.2838	30.79

- *Ultraviolet diffuse reflectance spectroscopy (UV-DRS) analysis.* The optical study of the synthesized material was done by UV-DRS analysis, as shown in Fig. 2. The band gap energy was calculated using Kubelka-Munk function [35] with $(F(R)h\vartheta)^2$ $(eV(cm^{-1}))^2$ *versus* energy ($h\vartheta$) shown in Fig. 2. The material shows band gap energy of 3.21 eV for mixed La_2O_3-ZnO nanocomposite material [36].

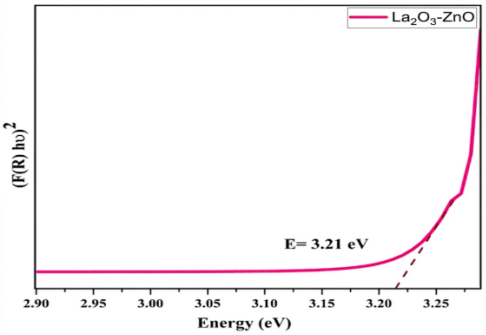


Figure 2. UV-DRS spectrum of La_2O_3-ZnO nanocomposite

- *Fourier transform infrared spectroscopy (FTIR) analysis.* The FTIR spectra of ZnO, La_2O_3 and La_2O_3-ZnO nanocomposite were recorded in the range of 4000–450 cm^{-1} (see Figure 3(a-c)). The sharp peak at 612 cm^{-1} is characteristic of the presence of Zn–O stretching vibrations. The peaks at 1070 and 1429 cm^{-1} are due to C-O stretching vibration and adsorbed carbonate groups, respectively, as shown in Fig. 3(a) [37-40]. The stretching frequencies at 854 and 645 cm^{-1} are primarily due to La-O stretching and bending vibrations, respectively, as shown in Fig. 3(b) [41].

Figure 3(c) shows the FTIR spectrum of La_2O_3-ZnO with characteristic Zn-O stretching vibrations at 499 cm^{-1} and La-O stretching and bending vibrations at 672 and 851 cm^{-1}, which confirms the formation of nanocomposite material [42].

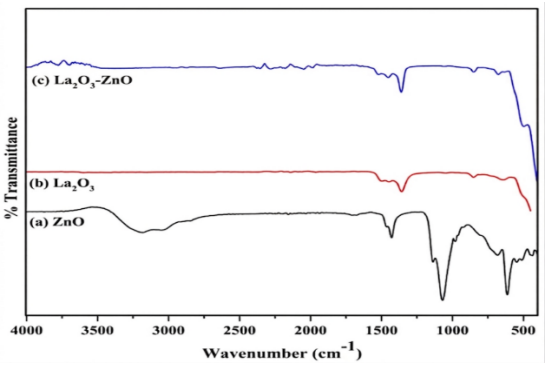


Figure 3. FTIR spectra of (a) ZnO, (b) La_2O_3 and (c) La_2O_3-ZnO nanocomposite

- *Scanning electron microscopy (SEM) analysis.* The surface morphology of La_2O_3-ZnO nanocomposite was tested by SEM analysis to find out the dispersion of the active species on the support. Figure 4 shows SEM images with different resolution, which demonstrate the nanocrystalline structure of the composite material. The increasing porosity and improved morphology of the material is clearly seen.

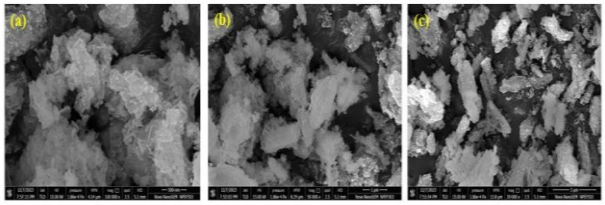


Figure 4. SEM micrographs of (a) ZnO, (b) La_2O_3, and (c) La_2O_3-ZnO nanocomposite

Application for anticancer activity

- *Cytotoxicity against MCF-7 cells using MTT assay.* The MTT cell viability test is a simple, sensitive, quantitative and efficient procedure for counting the number of viable cells in a given culture. This homogeneous colorimetric evaluation works by converting MTT, a pale-yellow substrate, to formazan, a purple dye. This cellular reduction requires the pyridine nucleotide cofactors NADH/NADPH and is only catalyzed by live cells. The formazan product has limited water solubility and appears as purple crystals. Dissolving the resultant formazan in a solubilization buffer allows for easy measurement of its production. The intensity of the product color, measured between 550 and 620 nm, is associated with the number of living cells in the culture. The test kit's reagents were carefully developed and adjusted for sensitivity, assay robustness and automation.
- *Morphological studies.* MCF-7 human breast cancer cell lines were cultured in 25 cm^2-Corning canted neck flasks using DMEM-F12 medium enriched with 20% FBS and 3 mM L-glutamine. This was further supplemented with an antibiotic mixture containing 500 µg/mL of penicillin, 500 µg/mL of streptomycin and 1.25 µg/mL of amphotericin-B to prevent bacterial infections. The cultures were kept in 5% CO_2 humidified atmosphere at 37 °C. For passaging, cells were detached using 0.25% trypsin-1mM EDTA and reseeded in 75 cm^2-flasks at 2.3×10^4 cells/cm^2, with the medium refreshed every two days. Cell confluence of 80% was microscopically verified before conducting experiments 24 h after seeding to avoid cell differentiation. Et-16 and Et-20 refer to synthetic anti-neoplastic ether lipids (specifically, alkyl-lysophospholipid analogues) treatments were applied at their IC_{50} concentrations 24 h post-seeding, with observations and imaging done 24 h post-treatment using an Axiovert 200M phase contrast microscope at 10× magnification utilizing Axiovision Rel.4.2 software for image capture.

DOXO sample was used as positive control. IC_{50} of La_2O_3-ZnO nanocomposite against MCF-7 was calculated based on a non-linear regression method. At least three individual experiments were

conducted. Results are shown as mean ± SD in Table 2, Figs. 5 and 6. By using one-way ANOVA, statistical significance was determined.

Table 2. Determination of MCF-7 cell viability over the treatment of test La_2O_3-ZnO nanocomposite

Conc. (µg/mL)	% Cell viability at 48 h	
	La_2O_3-ZnO	DOXO
1	97.11 ± 6.54	87.02 ± 7.04
5	90.58 ± 7.21	69.52 ± 5.74
10	81.89 ± 8.04	45.12 ± 3.11
20	65.12 ± 5.78	18.32 ± 1.63
30	47.12 ± 3.15	8.24 ± 1.01
40	31.11 ± 2.15	3.02 ± 0.47
50	17.04 ± 1.22	0.21 ± 0.05

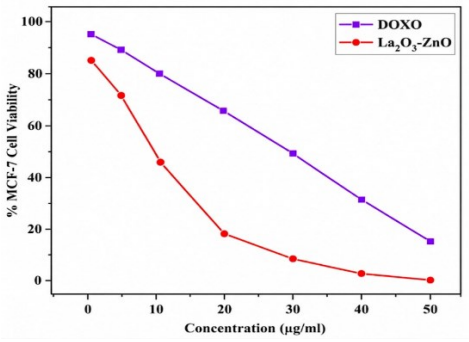


Figure 5. MCF-7 cell viability over the treatment test with La_2O_3-ZnO nanocomposite

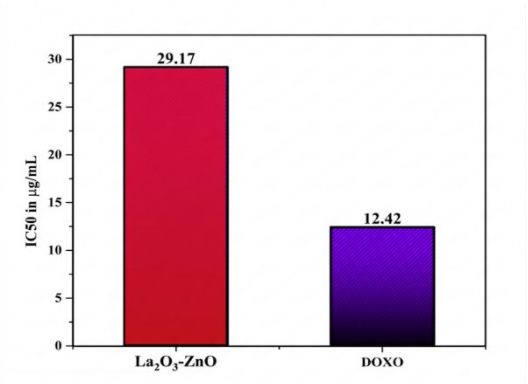


Figure 6. % Viability of MCF-7 over the treatment with La_2O_3-ZnO nanocomposite

RESULTS AND DISCUSSION

Consistent with the cytotoxicity results obtained from the MTT assay, both the synthesized La_2O_3-ZnO nanocomposite (lanthanum–zinc mixed oxide) and the reference drug DOXO caused noticeable morphological changes in MCF-7 cells, as shown in Figure 7. The analysis revealed that the La_2O_3-ZnO nanocomposite caused comparatively less morphological deformation in MCF-7 cells than that observed with DOXO treatment. Exposure to the lanthanum–zinc mixed oxide induced subtle morphological alterations, where the initially elongated spindle-shaped cells gradually became rounded and the intercellular spacing increased. In addition, increased cellular refraction was observed after treatment with the nanocomposite material.

.

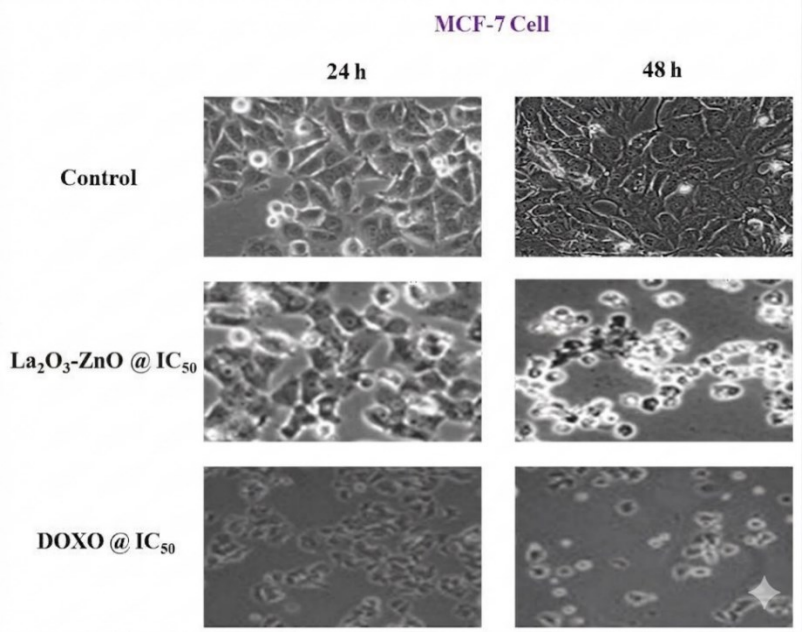


Figure 7. Morphological screening of MCF-7 cells over the treatment with La_2O_3-ZnO nanoparticles

The synthesized nanoparticles were further evaluated for their anticancer efficacy against the MCF-7 breast cancer cell line. Figure 7 illustrates the *in-vitro* activity profile and demonstrates the dose-dependent relationship between the synthesized lanthanum–zinc mixed oxide and anticancer activity. The study confirmed that the nanocomposite material produced comparatively moderate morphological distortion of MCF-7 cells relative to the severe cellular damage caused by DOXO. Specifically, treatment with the lanthanum–zinc mixed oxide resulted in gradual morphological modifications, including the transformation of spindle-shaped cells into rounded structures along with increased spacing between cells. The MTT assay results indicated that the synthesized nanoparticles exhibited moderate to good antiproliferative activity against MCF-7 breast cancer cells.

CONCLUSION

La_2O_3–ZnO mixed oxide nanoparticles were successfully synthesized using a simple co-precipitation technique. XRD analysis confirmed the crystalline nature of the nanocomposite with an average crystallite size of 30.79 nm, while UV-DRS analysis revealed band gap energy of 3.21 eV. FT-IR and SEM studies verified the formation of mixed metal oxide nanoparticles with porous nanocrystalline morphology. Cytotoxicity analysis demonstrated significant dose-dependent anticancer activity, the MCF-7 cell viability decreasing from 97.11 ± 6.54% at 1 µg/mL to 17.04 ± 1.22% at 50 µg/mL concentration. Morphological observations revealed cellular shrinkage, rounding, and structural deformation after nanoparticle treatment. The findings suggest that La_2O_3–ZnO nanocomposite possesses promising anticancer efficacy and may be considered as potential nanotherapeutic candidate for breast cancer treatment. Further investigations involving mechanistic studies, apoptosis pathway analysis, and *in-vivo* evaluations are recommended to establish its biomedical applicability and safety.

Acknowledgement: *The authors gratefully acknowledge Dr. Rafiq Zakaria, College for Women Aurangabad, Maharashtra, India for providing all required facilities for the research work. Authors also thank the Principal and Head of the Department of Chemistry, Jijamata College of Science and Arts, Bhende, Maharashtra, India for providing analysis facilities for the research work.*

Funding Support: *First author A. R. Padol heartily acknowledges for providing financial support from SARATHI, Maharashtra, India (Award No. 701/2022).*

Conflict of interest*: All authors hereby declare no conflict of interest.*

REFERENCES

1. D. Yuvaraj, R. Kaushik, K. Narasimha Rao, *ACS Applied Materials & Interfaces*, **2** (4), 1019 (2010), doi: 10.1021/am900792k.
2. Y. Wu, W. Jia, Q. An, Y. Liu, J. Chen, G. Li, *Nanotechnology*, **20** (24), 245101 (2009), doi: 10.1088/0957-4484/20/24/245101.
3. Y. Wang *et al.*, *Advanced Functional Materials*, **18** (7), 1131 (2008), doi: 10.1002/adfm.200701120.
4. W. K. Son, J. H. Youk, W. H. Park, *Carbohydrate Polymers*, **65** (4), 430 (2006), doi: 10.1016/j.carbpol.2006.01.037.
5. J.-P. Mosnier *et al.*, *Science and Technology of Advanced Materials*, **10** (4), 045003 (2009), doi: 10.1088/1468-6996/10/4/045003.
6. W. Jiang, H. Mashayekhi, B. Xing, *Environmental Pollution*, **157** (5), 1619 (2009), doi: 10.1016/j.envpol.2008.12.025.
7. Q. Li *et al.*, *Water Res,* **42** (18), 4591 (2008), doi: 10.1016/j.watres.2008.08.015.
8. M. Diao, M. Yao, *Water Res.,* **43** (20), 5243 (2009), doi: 10.1016/j.watres.2009.08.051.
9. A. Sharma et al., *Mater. Sci. Eng. C*, **165**, 115432 (2024).
10. S. Verma, P. Singh, *J. Alloys Compd.*, **987**, 178945 (2025).
11. M. Al-Harbi et al., *Ceram. Int.*, **51** (4), 11220 (2025).
12. R. K. Patel et al., *Nano-Struct. Nano-Objects*, **39**, 101245 (2024).
13. Y. Chen et al., *J. Nanobiotechology*, **24**, 55 (2026).
14. J. S. Kim *et al.*, *Nanomed.: Nanotechnol. Biol. Med.*, **3** (1), 95 (2007), doi: 10.1016/j.nano.2006.12.001.
15. Z. Huang *et al.*, *Langmuir*, **24** (8), 4140 (2008), doi: 10.1021/la7035949.
16. K. H. Tam *et al.*, *Thin Solid Films*, **516** (18), 6167 (2008), doi: 10.1016/j.tsf.2007.11.081.
17. E. Bae *et al.*, *Environ. Toxicol. Chem.*, **29** (10), 2154 (2009), doi: 10.1002/etc.278.
18. P. Huang *et al.*, *Environ. Toxicol. Pharmacol.* **31** (1), 25 (2011), doi: 10.1016/j.etap.2010.09.001.
19. G. A. H. Mekhemer, *Phys. Chem. Chem. Phys.*, **4** (21), 5400 (2002), doi: 10.1039/B204056P.
20. R. He *et al.*, *Nano Today*, **48**, 101694 (2023), doi: 10.1016/j.nantod.2022.101694.
21. B. Omran, K.-H. Baek, *Molecules*, **26** (22), 7031, (2021), doi: 10.3390/molecules26227031.
22. Q. Fan, X. Cui, H. Guo, Y. Xu, G. Zhang, and B. Peng, *J. Biomater. Appl.*, **35** (2), 237 (2020), doi: 10.1177/0885328220924540.
23. S. Keerthana, A. Kumar, *Crit. Rev. Toxicol.*, **50** (1), 47 (2020), doi: 10.1080/10408444.2020.1726282.
24. C. Picasso *et al.*, *Nanomater.*, **12** (13), 2265 (2022), doi: 10.3390/nano12132265.
25. Y. Mongy, T. Shalaby, et al., *Sci. Rep*., **14**, 13470 (2024). doi.org/10.1038/s41598-024-63258-7
26. S. A. Bhat, V. Kumar, D. S. Dhanjal, et al., *Discover Nano*, **19**, 121 (2024). https://doi.org/10.1186/

s11671-024-04072-y
27. J. B. Oehler, W. Rajapaksha, H. J.Albrecht, *Pers. Med,* **14**, (7), 723 (2024). https://doi.org/ 10.3390/jpm14070723
28. G. Ferro-Flores, A. Ancira-Cortez, B. Ocampo-García, L. Meléndez-Alafort, *Nanomater*., **14** (3), 296 (2024). https://doi.org/10.3390/nano14030296
29. S. Chandramohan, A. P. Francis, S. Pajaniradje, R. Rajagopalan, *Part. Sci. Technol*., **42** (7), 1155 (2024). https://doi.org/10.1080/ 02726351.2024.2364859
30. Z. Luo, Z. Yi, X. Liu, *Acc. Chem. Res.*, **56** (4), 425 (2023), doi: 10.1021/acs. accounts. 2c00681.
31. H. Wei *et al.*, *Adv. Opt. Mater.*, **11**, 11 (2023), doi: 10.1002/adom.202370037.
32. H. E. A. Mohamed *et al.*, *Appl. Organomet. Chem.,* **37** (6) (2023), doi: 10.1002/aoc.7091.
33. A. C. Albertsson, J., S. C. Abrahams, A. Kvick, *Acta Cryst.* B, **45**, 34 (1989), https://doi.org/10.1107/ S0108768188010109
34. Z. Lohberg, *Phys. Chem.,* **28**, 402 (1935).
35. H. Jamil *et al.*, *Thin Solid Films*, **732**, 138796 (2021), doi: 10.1016/j.tsf.2021.138796.
36. Z. N. Kayani, B. Amir, S. Riaz, S. Naseem, *Opt. Mater.*, **109**, 110287 (2020), doi: 10.1016/j.optmat. 2020.110287.
37. D. E. Navarro-López *et al.*, *Mater. Sci. Eng. C,* **123**, 112004 (2021), doi: 10.1016/j.msec.2021.112004.
38. P. Somu, H. D. Khanal, L. A. Gomez, R. Vinaykumar, J.-J. Shim, Y. R. Lee, *Biomass Conv. Bioref.* **15**, 22041 (2025), doi: 10.1007/s13399-022-03474-1.
39. R. L. Danhalilu, A. I. Kankara, S. M. Batagarawa, *Curr. J. Appl. Sci. Technol.,* **32** (2), 1 (2019), doi: 10.9734/CJAST/2019/46052.
40. M. I. Alahmdi *et al.*, *J. Inorg. Organomet. Polym. Mater.*, **32** (6), 2146 (2022), doi: 10.1007/s10904-022-02263-7.
41. A. A. Pathan, K. R. Desai, S. Vajapara, C. P. Bhasin, *Adv. Nanoparticles*, **07** (01), 28 (2018), doi: 10.4236/anp.2018.71003.
42. J. Mohanta, B. Dey, S. Dey, *ACS Omega*, **5** (27), 16510 (2020), doi: 10.1021/acsomega.0c00999.

Bulgarian Chemical Communications, Volume 58, Issue 4 (pp. 442-450) 2026 *DOI: 10.34049/bcc.58.4.5740*

Photocatalytic degradation of azo dye (Congo red) using aluminum-doped cadmium oxide nanoparticles

M. S. Deshpande[1], D. V. Sonawane[1*], S. S. Deshmukh[1], A. E. Athare[2]

[1]*Department of Chemistry, Pemraj Sarda College, Ahilyanagar, (MS), India*
[2]*New Art's Commerce and Science College, Ahilyanagar, (MS), 414001, India*

Received: December 26, 2025; Revised: June 25, 2026

In this work, cadmium oxide (CdO) nanoparticles doped with aluminum (Al) at various amounts (0.002, 0.004, 0.006, and 0.008 g) were made by sol-gel citrate synthesis. X-ray diffraction (XRD), Fourier transform infrared spectroscopy (FTIR), ultraviolet-visible (UV-Vis) spectroscopy, scanning electron microscopy (SEM), and energy-dispersive X-ray spectroscopy (EDS) were used for chemical and elemental characterization. The organic dye was degraded using Al-doped CdO NPs, and the catalysis was assessed by UV-Vis absorption spectrometry. Finally, it was proven that these nano-catalysts destroyed the organic dye at an amount of 0.008 g with 93% degradation efficiency in 90 min. Al-doped CdO NPs may therefore be employed as catalysts to remediate industrial effluents.

Keywords: cadmium oxide nanoparticles, aluminum, EDS, SEM, azo dye.

INTRODUCTION

A variety of methods including coagulation, flocculation, membrane filtration, photo-catalytic degradation, etc., have been used to remove colored contaminants from textile, food, paper, cosmetics, and other industries releasing toxic contaminants into the environment. The textile industry's discharged wastewater is mostly polluted with dyes that deplete oxygen and harm aquatic life [1]. Congo red (CR) is an extensively used synthetic dye. It is a crucial model contaminant for assessing how well nanotechnology works to clean wastewater. Furthermore, researchers employ CR as a dopant to improve the catalytic, thermal, and optical characteristics of particular host nanoparticles. CR acts as a target for nanoparticle adsorption and degradation [2]. The development of nanoscience and nanotechnology has made it possible to produce nanoparticles using a variety of methods. Researchers have looked into numerous semiconductors that use visible light to break down a lot of resistant chemicals in aqueous systems; in fact, nano-sized metal oxide semiconductor materials are now widely acknowledged as the best substances for water purification [3]. Many metal oxide semiconductors including ZnO [4], SnO_2 [5], TiO_2 [6], metal particles such as Ag [7], Au [8], Pd [9], Pt [10], and a few doped metal oxides [11] have been extensively utilized to break down organic contaminants, e.g. methylene blue [12]. La-doped ZnO nanoflowers [13], Ag-doped CdO nanocomposite [14], and polyaniline CdO nanocomposite [15]. To the best of our knowledge, however, no reports have yet been made on the synthesis of Al-doped CdO nanoparticles and their particle size-related photo-catalytic activity in the photo-degradation of CR. Therefore, the goal of the current work was to investigate the photo-catalytic degradation of CR dye using an Al-doped CdO photo-catalyst produced by the chemical co-precipitation approach using the sol-gel citrate method.

Materials and methods

Al-doped CdO nanoparticles were produced by chemical co-precipitation using the sol-gel citrate method. For this purpose, citric acid, ethylene glycol, muffle furnace, aluminum nitrate hexahydrate [(Al $(NO_3)_2.6H_2O$)] and cadmium nitrate tetrahydrate [Cd $(NO_3)_2.4H_2O$] were used. All chemicals were of analytical grade.

A scanning electron microscope (SEM), JEOL JSM-5910 was used to examine the morphology of CdO nanoparticles (NPs). Energy-dispersive X-ray (EDX) spectroscope model INCA 200 was used to examine the elemental composition of the synthesized Al-doped CdO nanoparticles. The particle size and the group frequencies of the latter were examined using XRD (DW-XRD-Y3000) and FTIR (Bruker ALPHA II Compact FTIR) technique from Savitribai Phule, Pune University.

* To whom all correspondence should be sent: Email: *dvsonawane011@gmail.com*

© 2026 Bulgarian Academy of Sciences, Union of Chemists in Bulgaria

Synthesis of Al-doped CdO nanoparticles

Nanocrystalline pure and Al-doped CdO nanoparticles were synthesized by employing the sol-gel citrate technique. A stoichiometric mixture of cadmium nitrate tetrahydrate (Cd $(NO_3)_2.4H_2O$) with citric acid and ethylene glycol was appropriately blended. The mixture was agitated on a magnetic stirrer at 80°C for 3 h to obtain a homogenous transparent solution. To create a gel, the mixture was further heated in a pressure vessel at 130° C for almost 12 h. Then the gel was exposed to heat treatment at 350°C in a muffle furnace to get a fine dry powder of pure CdO nanoparticles. The same procedure was performed for Al-doped CdO nanoparticles using aluminum nitrate hexahydrate, [(Al $(NO_3)_2.6H_2O$)] to create $Al_xCd_{1-x}O$ nanoparticles.

RESULTS AND DISCUSSION

Characterization and structural analysis of the synthesized Al-doped CdO NPs were performed by XRD, FTIR, UV, SEM, and EDX analysis discussed below.

Structural analysis

XRD analysis: The generated Al-doped CdO nanoparticles of varied concentration were characterized using X-ray diffraction to gather information on crystal structure, crystallite size and purity. XRD patterns of the produced cadmium oxide and doped cadmium oxide were obtained at ambient temperature. The scanning angle 2θ was adjusted in the range of 20-80°. X-ray diffraction data were acquired by employing Cu Kα radiation (1.5406 Å). The full width at half maximum of the peaks was used to calculate the crystallite size of the generated pure CdO and Al-doped CdO nanostructures using the Scherrer formula [16].

$$d = \frac{K\lambda}{\beta \mathrm{Cos}\theta} \qquad (1)$$

where d is the average crystallite grain size; β is the full width half maximum in radian; θ is the Bragg angle; λ is the wavelength of X-rays (0.15406 nm for Cu target Kα radiation); K is a shape factor.

Two distinctive peaks are visible in the XRD patterns shown in Figures 1a and 1b. The peaks in Figure 1a are regarded as fingerprints for a highly polycrystalline pure CdO compound without visible presence of aluminum oxide. The use of a very tiny quantity of Al as a dopant is the reason for the lack of aluminum oxide peaks. The (111) and (200) planes contain the Al: CdO film's highest intensity peaks. As a result, these crystallographic planes have the ideal orientation for crystal formation. The degree of crystallization for the plane (111) is slightly higher. The increased crystallinity can be attributed to the films being on the hot plate for a few hours following deposition (annealing process), which eliminates the internal tensions caused by alternate spraying. The typical XRD spectra of pure and doped CdO nanoparticles at 650° C are shown in Figures 1a and 1b, respectively. The produced single-phase CdO nanoparticles show a rock salt-like cubic crystal structure with unit cell parameters, a = b = c = 4.6990 Å and α = β = γ = 90°. The corresponding reflection peaks of (hkl) are seen at (111), (200), (220), (311), and (222). The XRD peaks in the (111) crystallographic plane of CdO nanoparticles are crisp, confirming the nanoparticles' crystalline structure [17]. The crystallinity of the doped nanoparticles decreases with rise in the doping %, as shown in Table 1.

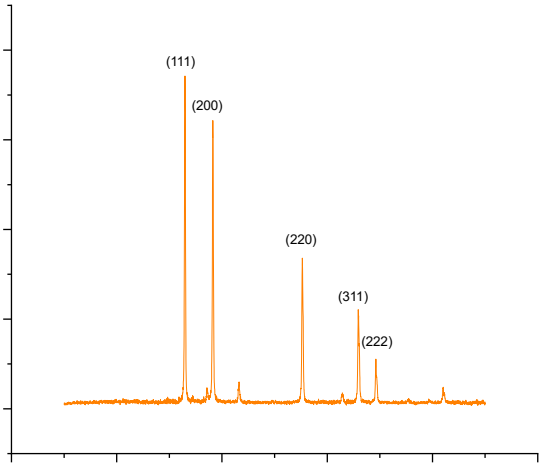


Figure 1a. XRD spectrum of undoped CdO NPs.

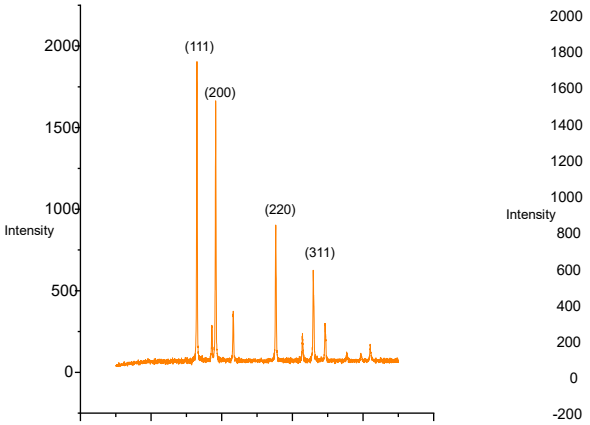


Figure 1b. XRD spectrum of Al-doped CdO NPs.

Table 1. Particle sizes in Al-doped CdO nanoparticles.

Samples	Particle size (nm)	Lattice parameter (Å)
CdO: nanoparticles	38.20	4.7990
CdO: Al (0.2%)	40.9	4.2786
CdO: Al (0.4%)	36.0	4.2771
CdO: Al (0.6%)	31.15	4.7446

Fourier transform infrared spectroscopy (FTIR) analysis

The spectra of pure and Al-doped CdO nanoparticles were measured in the range from 500 to 4000 cm^{-1}. It was noticed that owing to atmospheric moisture, the O-H stretching vibrations occurred around 3742.90 cm^{-1}. The CdO stretching was corroborated by the absorption peak at 2408 cm^{-1} and that at 2356 cm^{-1} was assigned to asymmetric CH_2 stretching frequency. FTIR also reveals the presence of O-H and Cd-O vibrations, as seen in Figures 2a and 2b [18].

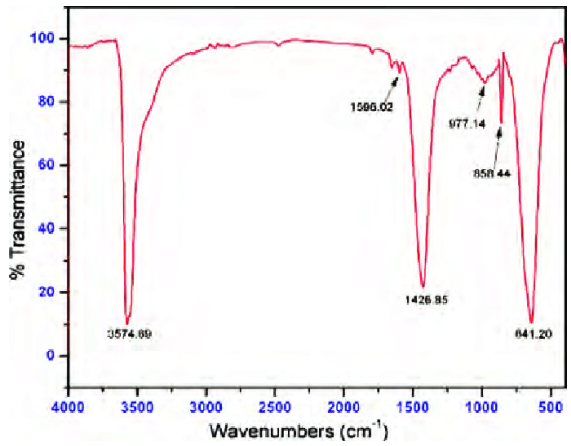


Figure 2a. FTIR spectrum of undoped CdO NPs.

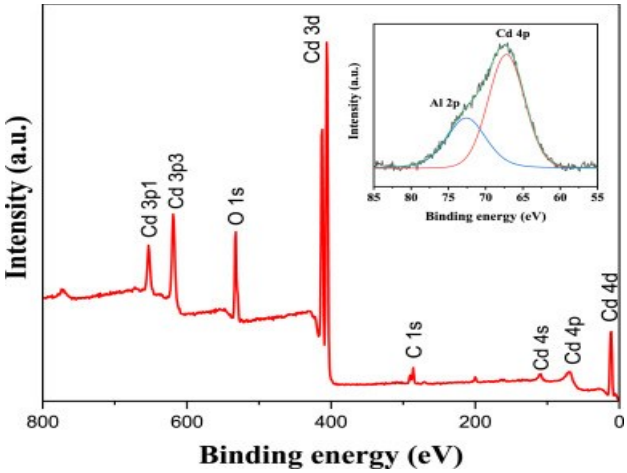


Figure 2b. FTIR spectrum of Al-doped CdO NPs.

UV- visible spectroscopy analysis

The band gap of Al-doped CdO nanoparticles is usually wider than that of undoped CdO. Undoped CdO is an n-type semiconductor with an intrinsic direct band gap spanning between 2.2 eV and 2.5 eV, as shown in Figure 3a. When doped with Al, the band gap changes upward depending on the dopant concentration, generally reaching between 2.5 eV and 3.0 eV. Two events are the main causes of the band gap difference between undoped and Al-doped CdO NPs. The absorption spectrum of Al-doped CdO NPs demonstrates that CdO NPs absorb in the range of 250-500 nm, which suggests that the CdO sample absorbs light in the visible range. The absorption spectrum at around 280 nm which is related to the electronic transition suggests that the CdO NPs were correctly synthesized [19]. The result is presented in Figure 3b.

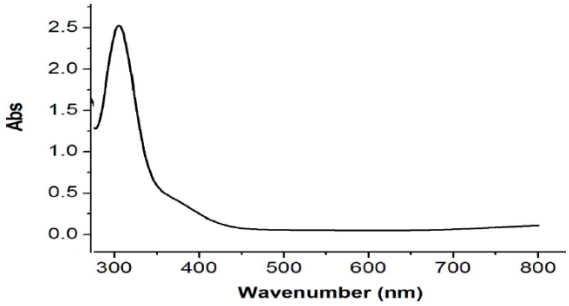


Figure 3a. UV-Vis spectrum of pure CdO NPs.

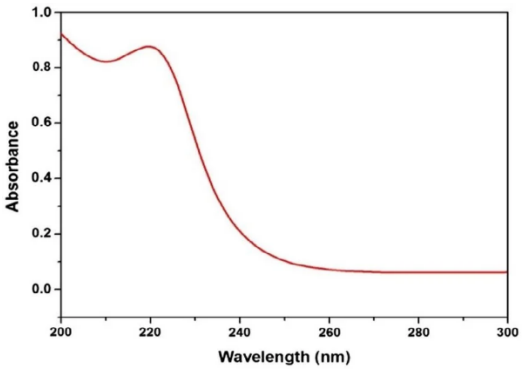


Figure 3b. UV-Vis spectrum of Al-doped CdO NPs.

Causes for the increase in band gap

Burstein-Moss (BM) effect: Aluminum functions as n-type donor in cadmium oxide because it is a trivalent metal. By substituting Cd, Al adds more free electrons to the conduction band. This effectively increases the optical band gap by filling the lowest accessible energy levels in the conduction band and making electrons need higher energies to migrate from the valence band.

Quantum confinement effect: Doping frequently inhibits nanoparticle development, resulting in reduced crystallite sizes. Spatial confinement of charge carriers results in a blue-shift in the

absorption spectra below a crucial threshold, which increases the band gap.

SEM analysis

The surface morphology of the samples was investigated using scanning electron microscopy. Figure 4a depicts the morphology of undoped CdO samples, which suggests that there is a spherical grain aggregation while Al-doped CdO nanoparticles have a somewhat corn-like nanorod shape shown in Figure 4b [20]. SEM images reveal that pure CdO is more crystalline and has ball-like structure. By Al-doping, the structure becomes nanowire and the diameter decreases with the increase in Al concentration, as seen in Figure 4b.



Figure 4a. SEM image of pure CdO NPs.

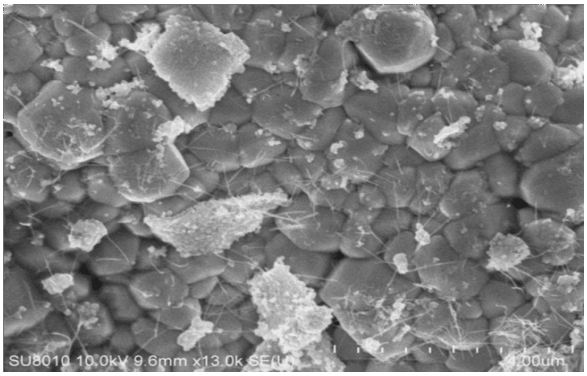


Figure 4b. SEM image of Al-doped CdO NPs.

EDS analysis

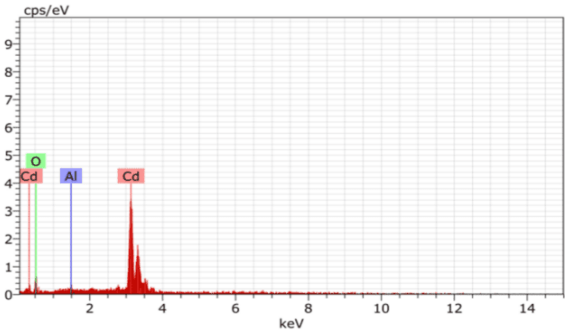


Figure 5. EDS image of Al-doped CdO NPs.

The EDS image of Al-doped CdO NPs reveals the presence of Al and no other impurities. Numerous distinct peaks related to Al, O, and Cd are visible in the EDX spectrum. The absence of additional impurity-related peaks in the spectrum further verifies that the produced nanoparticles are of Al-doped CdO, as shown in Figure 5 [21].

Photocatalytic degradation of Congo red dye

CR dye was catalytically degraded in aqueous media under UV irradiation to evaluate the photo-catalytic activity of the Al-doped CdO nanoparticles created in this investigation. Photographs of a CR dye solution taken at different time intervals (15, 30, 45, 60, 75, and 90 min, see Figure 6a) were used to visualize the degradation process. The color shifts seen in the images offer a tangible proof of the CR dye's gradual photo-degradation. In particular, a discernible rise in dye degradation is correlated with a progressive increase in irradiation time. CR distinctive color is more noticeable at the earlier time points, suggesting a larger dye concentration in the solution.

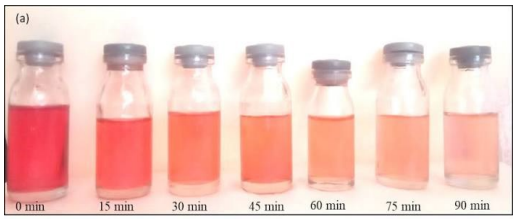


Figure 6a. CR dye degradation in solution taken at different time intervals.

The photo-catalytic system's effectiveness over prolonged irradiation times is highlighted by these visual observations, which are consistent with the quantitative analysis of the photo-catalytic degradation process and confirm that the synthesized Al-doped CdO NPs show a time-dependent enhancement of their ability to degrade CR dye [22]. By tracking the relative intensity of the UV-Vis spectral peak linked to CR, the photo-degradation of CR was evaluated at 497 nm (see Figure 6b). The proportion of CR dye degradation over time is shown in Figure 6c. The graph clearly shows that degradation is slowing with time. In particular, the following percentages of dye degradation are noted: 33% at 15 min, 50% at 30 min, 66% at 45 min, 83% at 60 min, 86% at 75 min, and 93% at 90 min. These findings imply that the photo-degradation of CR is a time-dependent process, where a longer duration results in more significant dye degradation [23].

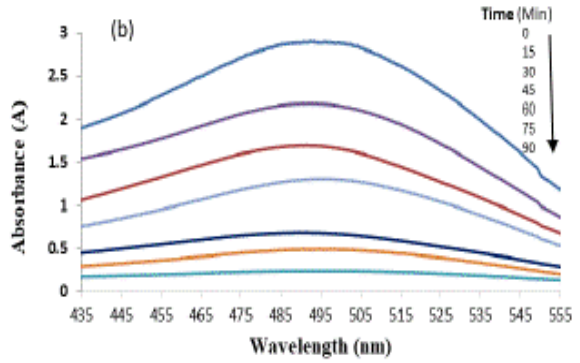


Figure 6b. UV-Vis spectral peak of CR dye solution.

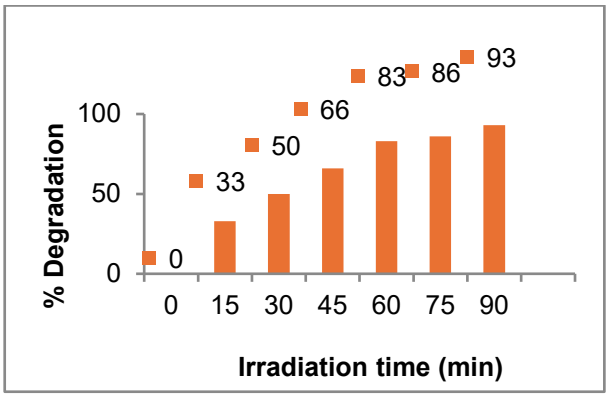


Figure 6c. Proportion of CR dye degradation over time.

Effect of dye concentration on photocatalytic degradation

The effect of dye concentration on the photo-catalytic degradation was investigated by keeping the amount of catalyst constant for 20 min. When the concentration of dye increased, the photo-degradation decreased, as shown in Figure 7a. The Beer-Lambert law which states that increased dye concentrations cause entering photons to travel a shorter distance, can be used to explain this tendency. As a result, there is less photon adsorption on the catalyst surface, which lowers the possibility of photo-degradation. The percentage of CR dye degradation is shown in Figure 7b, which shows a decrease as the dye concentration increases. For dye solutions containing 70, 80, and 90 parts per million of dye, the percent degradation during a 20-min period is 50%, 33%, and 11%, respectively (see Figure 7c). This result highlights the inverse relationship between dye concentration and photo-catalytic degradation efficiency, offering important information about how to maximize dye removal conditions [24].

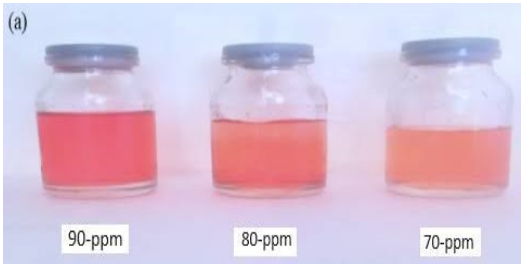


Figure 7a. Effect of dye concentration in solution on photo-catalytic degradation of CR dye.

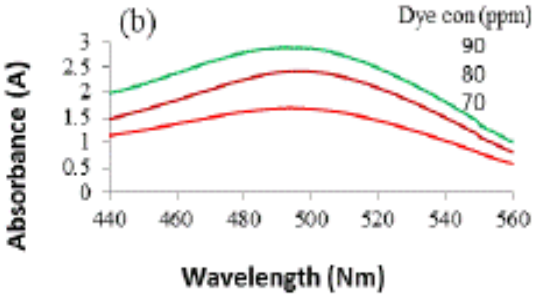


Figure 7b. Validity of Beer's law in CR dye degradation.

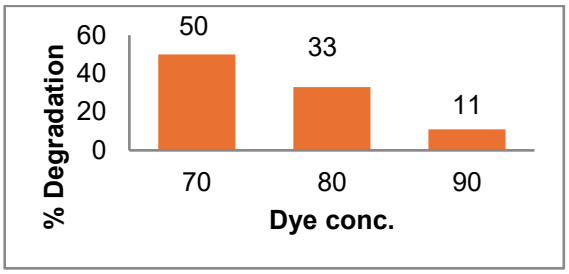


Figure 7c. Percent degradation of CR dye.

Effect of pH on the photo-degradation

Considering the variety of pH levels at which industrial effluents, especially those from industries like dyes, paints, and textiles, are usually released, the impact of pH on the photo-degradation of CR becomes an important issue. A thorough investigation of how pH affects the photo-degradation process is required due to the fluctuation in pH values in these effluents. The photo-degradation rates of CR dye show a clear dependence on pH of the medium, as seen in Figure 8. This relationship emphasizes how important pH is in determining the production of hydroxyl radicals and the overall photo-degradation effectiveness. The graph shows a positive correlation between pH and the rate of photo-catalytic degradation, with a discernible rise in degradation as the pH increases. Higher pH values cause an increase in the production of active hydroxyl radicals (•OH), which accelerates the pace of breakdown. The graphs in Figure 8 show that as pH rises, the percent deterioration proportionally increases. In particular, the percent degradation at

pH 4, 7, and 10 after 45 min is 46%, 60%, and 80%, respectively. The effect of pH on the production of hydroxyl radicals is responsible for the reported pH-dependent enhancement in the photo-degradation process. A more effective breakdown of the CR dye is made possible by the increased availability of hydroxyl radicals at higher pH values. This knowledge is essential for developing customized and efficient wastewater treatment methods by adjusting the photo-degradation process according to the unique pH conditions of industrial effluents [24, 25].

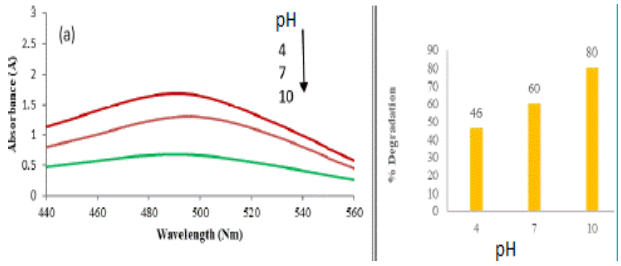


Figure 8. Positive correlation between pH and the rate of photo-catalytic degradation of CR dye.

Effect of the catalyst dosage on the photo-degradation

At a constant period of 20 min, the effect of catalyst dosage on the photo-degradation rate of CR dye was examined over a range of catalyst amounts, from 0.002 g to a maximum of 0.008 g per 20 mL of dye solution, as presented in Figure 9a. To explore the quantitative aspect, the percent UV degradation of CR dye during a 15-min period using varying concentrations of the photo-catalyst is presented in Figure 9b. The evolution of CR degradation in aqueous media with varying catalyst concentrations is graphically depicted in Figure 9c. For catalyst quantities of 0.002 g, 0.004 g, 0.006 g, and 0.008 g, the corresponding percent degradation values are 33%, 46%, 64%, and 75%, respectively. Higher catalyst amounts may result in better treatment outcomes, since this data supports the positive link between catalyst dosage and the effectiveness of CR dye degradation [26].



Figure 9a. Effect of catalyst dosage on CR dye degradation.

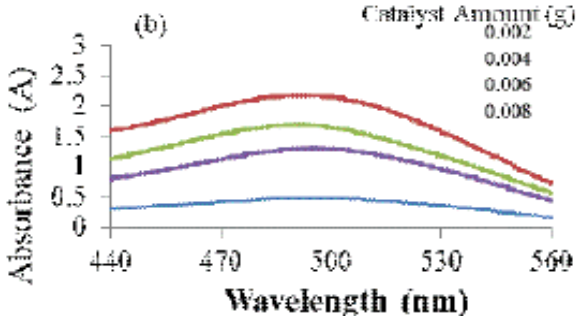


Figure 9b. Percent UV degradation of CR dye.

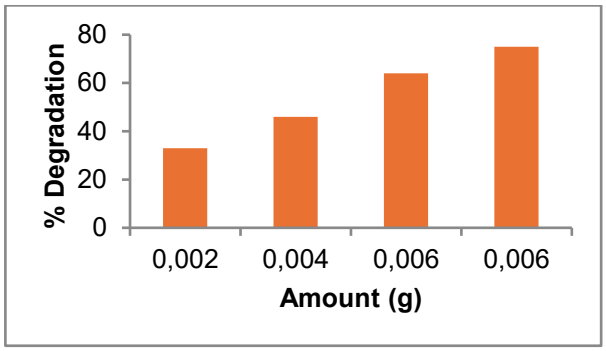


Figure 9c. Effect of catalyst dosage on the photo-degradation of CR dye.

Effect of the recovered catalyst on photo-degradation

The study highlights how the recovery procedure affects the catalyst photo-degradation activity. Recovery is important for cost-effectiveness and sustainability and is also critical to carefully analyze the change in catalyst performance. The observed decrease in photo-degradation efficiency emphasizes the necessity for additional recovery method improvement to preserve or improve the catalyst effectiveness in later applications. In order to evaluate the efficacy of recovered catalysts, the photo-degradation performance of the catalyst was investigated under standard experimental conditions. To guarantee that any adsorbed dye on the catalyst was removed, the recovery process required many washings with deionized water. The recovered catalyst showed a significant decrease in activity when compared to the original catalyst, even though it had a great capacity to degrade CR dye. The possible blockage of active sites on the photo-catalyst surface is responsible for the observed decrease in the recovered catalyst's photo-degradation efficacy, as shown in Figure 10a. The accumulation of photosensitive hydroxides during the heating process is the cause of this obstacle. These hydroxides may accumulate on the catalyst surface, impairing its capacity to effectively start photo-degradation reactions. The percent degradation of

CR dye by the original and the recovered photo-catalyst is graphically shown in Figure 10b. It is seen that during the 90-min experiment, the original catalyst accomplished amazing 93% dye degradation. The restored catalyst performed worse, degrading 82% of the dye for the same duration. The recovered catalyst's decreased activity is caused by a number of circumstances. Although washing procedures are necessary to remove adsorbed dye, they may unintentionally change the catalyst's surface characteristics and structural integrity. Furthermore, the catalyst's photo-degradation efficacy may be impacted by residual impurities or compositional changes that occur throughout the recovery process [27, 28].

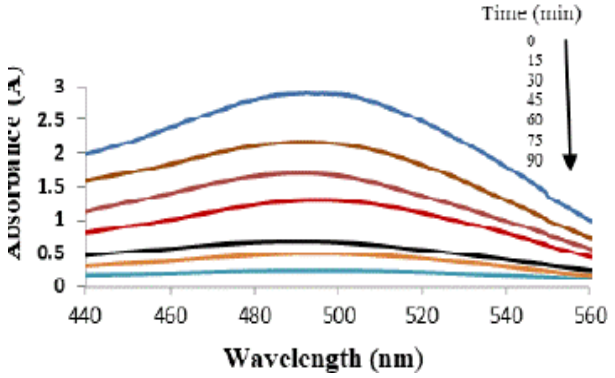


Figure 10a. Effect of the recovered catalyst on the photo-degradation of CR dye.

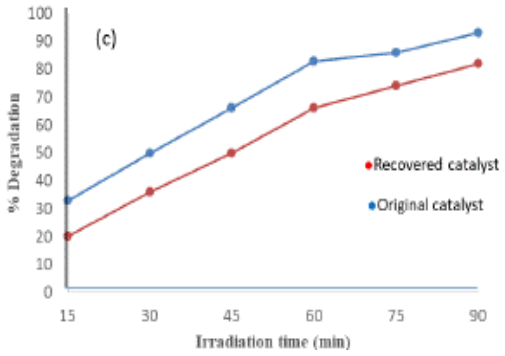


Figure 10b. Percent degradation of CR dye.

Mechanism of photocatalytic degradation and analysis of band gap energy

The suggested process of photo-catalytic degradation of the targeted CR dye is shown in Figure 11. The following mechanism underlies the photo-catalytic degradation of dyes: an electron-hole pair is created when the catalyst is activated by UV light, moving electrons from the valence band to the conduction band.

$$\text{Catalysts (NPs)} + h \rightarrow \text{NPs } (e^- + h^+) \quad (2)$$

The electron in the conduction band is represented by e^-, and the positive hole in the valence band is represented by h^+. These two species move to the catalyst surface, where they engage with other organic species. Because of its high oxidative potential, the positive hole can either directly oxidize the dye molecule or combine with water molecules to form hydroxyl radicals. Superoxide radicals, which are extremely reactive and aid in the deterioration of dyes, are created when electrons in the conduction band react with oxygen molecules [29]. The following equations provide a summary of the potential reactions.

$$\text{NPs} + h\nu \rightarrow \text{NPs } (h^+ + e^-) \quad (3)$$

$$h^+ + \text{dye} \rightarrow \text{oxidation of the dye molecules} \quad (4)$$

$$h^+ + OH^- \rightarrow \cdot OH \quad (5)$$

$$e^- + O_2 \rightarrow \cdot O_2 \quad (6)$$

$$\cdot OH + \cdot O^{2-} + \text{dye} \rightarrow \text{degradable/less toxic species} \quad (7)$$

An important consideration in the context of photo-catalysis is the band gap. Electrons in the valence band may be stimulated to the conduction band when a material is exposed to light, particularly in the visible light spectrum, resulting in the creation of electron-hole pairs. Numerous applications, including photo-catalysis, depend on this mechanism. With a band gap of 2.7 eV [29], metal oxides are implied to absorb light mostly in the UV region, which limits their efficiency in using visible light for photo-catalysis. However, the material becomes more sensitive to visible light when doped with Al, which causes the band gap to drop to 1.3 eV.The Burstein-Moss effect usually causes the band gap energy of Al-doped CdO nanoparticles to increase, although structural flaws or strain might cause it to decrease at higher doping concentrations. In conclusion, Al-doping of CdO nanoparticles results in a decrease in band gap values, which improves visible light utilization, increases electron-hole pair creation, and eventually enhances the metal oxide nanoparticles' photo-catalytic performance, as shown in Figure 12 [9].

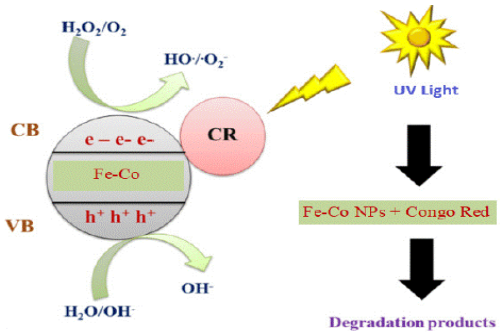


Figure 11. Mechanism of the photo-catalytic degradation of CR dye.

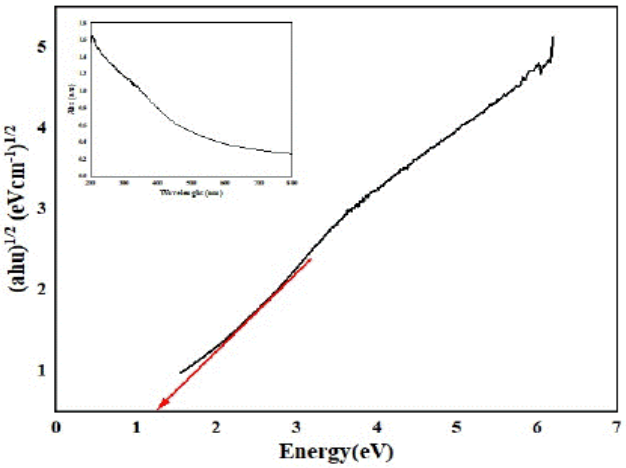


Figure 12. Band gap energy of Al-doped CdO NPs.

CONCLUSION

The results indicate that Al-doped CdO nanoparticles exhibit a notable level of photo-catalytic activity, particularly in the process of degrading Congo red dye through photo-degradation. Impressively, within a span of 90 min, a substantial 93% of the dye was successfully degraded. Notably, the observed trend reveals that as the duration of exposure increases, there is a corresponding augmentation in the photo-degradation of the dye. Furthermore, the study highlights the influence of the catalyst's quantity on the photo-degradation process. It was evident that an escalation in the amount of catalyst positively correlated with the degradation efficiency. For instance, utilizing 0.002 g of the photo-catalyst resulted in the degradation of 66% of the dye within a 45-min time frame. The impact of the medium's pH on the degradation process was also investigated. The findings illustrated a direct relationship between pH levels and dye degradation. Specifically, at pH 10, an impressive 80% of the dye underwent degradation within a relatively short span of 45 min, indicating the significance of the medium's alkalinity in enhancing the degradation efficiency. However, an intriguing observation emerged concerning the concentration of the dye. Surprisingly, the research demonstrated that as the concentration of the dye increased, the rate of photo-degradation exhibited a counter-intuitive decrease. This suggests a nuanced relationship between the dye concentration and the efficacy of the photo-degradation process.

Acknowledgement: *Authors are thankful to the Management and Principal of New Art's, Commerce and Science College, Ahilyanagar, for providing necessary facilities to the Department to carry out this work. Authors are also thankful to the Department of Physics Savitribai Phule Pune University, for characterization of samples.*

REFERENCES

1. K. A. Vijayalakshmi, N. Kartthikeyan, *Inorganic and Nano-Metal Chemistry,* ***55*****(6),** 657 (2024).
2. S. Krishnaraj, R. Anitha, *Journal of Advanced Scientific Research,* **12**(1), 0976-9595, 75 (2021).
3. H. Munawaroh, S. Wahyuningsih, A. H. Ramelan, *Materials Science and Engineering***, 176,** 012049, 1 (2017).
4. S. Sivakumar, N. Pallavi, S. Surendiran, P. Sangeetha, B. Karthikeyan, C. T. Manikandan. B. Sangeetha, E. B. Bharathi, *AIP Advances,* **16,** 045124, 1 (2026).
5. Sh. Mathur, R. Jain, *International Journal of Latest Technology in Engineering, Management and Applied Science (IJLTEMAS),* **8(12),** 28 (2019).
6. S. A. Muhammed, N. K. Abbas, *Baghdad Science Journal,* **20(5),** 2411 (2023).
7. N. H. Harb, H. Y. Hammod, S. T. Mohmmed, B. H. Adil, *Journal of Physical Science*, **35(3),** 17 (2024).
8. Sh. N. Matussin, F. Khan, M. H. Harunsani, Y.-M. Kim, M. M. Khan, *Catalysts,* **13(96),** 2 (2023).
9. F. Shan, L. Panariello, G. Wu, A. Gavriilidis, H. H. Fielding, I. P. Parkin, *RSC Adv.,* **11,** 17694 (2021).
10. A. Tabriz, N. Shahzad, S. Nadeem, S. Mehmood, N. Iqbal, G. Ali, M. I. Shahzad, *Mater. Proc.,* **17(9),** 2 (2024).
11. V. Aherkar, A. A. Mohammed, A. A. Al-shimary, R. M. Ovhal, Sh. Pawar, G. Kamblee, P. A. Ubale, *RSC Adv.,* **16,** 16253 (2026).
12. T. Alemu, G. Taye, G. Asefa, L. B. Merga, *Heliyon*, **8,** e11608 (2022).
13. E. S. Al-Farraj, E. A. Abdelrahman, *ACS Omega,* **9,** 4870 (2024).
14. M. S. Deshpande, D. V. Sonawane, Sh. S. Deshmukh, A. E. Athare, *Current Science,* **6(1),** 5846 (2026).
15. M. S. Deshpande, D. V. Sonawane, S. S. Deshmukh, and A. E. Athare, *International Journal of Scientific Research in Science, Engineering, and Technology*, **12(6),** 225 (2025).
16. D. V. Sonawane, *Science, Technology and Development*, **11(5),** 0950-0707, 388 (2022).
17. M. S. Deshpande, D. V. Sonawane, Sh. S. Deshmukh, A. E. Athare, *Journal of Scientific Research and Report,* **32(4),** 176 (2026).
18. H. H. Darwoysh, A. A. Yousif, K. A. Aadim, *International Journal of Scientific Research in Science and Technology,* **10(3),** 310 (2023).
19. R. A. Jassim, A. S. Abbas, *Iraqi Journal of Chemical and Petroleum Engineering*, **26(2),** 83 (2025).
20. S. Arul, T. Senthilnathan, *Rasayan J. Chem.,* **12(2),** 891 (2019).
21. L. K. Gaur, P. Gairola, S. P. Gairola, M. Ch. Mathpal, P. Kumar, S. Kumar, D. Kushavah, V. Agrahari, F. F. H. Aragon, M. A. G. Soler, H. C. Swart, *J. Alloys Compd.,* **868,** 159189 (2021).

22. D. T. Sponza, *American Journal of Surgery and Clinical Case Reports,* **6(16),** 1 (2023).
23. A. A. Manda, Q. A. Drmosh, Kh. A. Elsayed, A. L. Al-Alotaibi, I. O. Alade, S. A. Onaizi, H. D. M. Dafalla, A. Elhassan, *Arab. J. Chem.,* **15(8),** 104004 (2022).
24. S. Mondal, B. Bhattacharjee, *J. Water Environ. Nanotechnol.*, **9(4),** 415 (2024).
25. J. Panwar, L. Joshi, R. Ameta, D. Soni, *Rasayan J. Chem.,* **16(3),** 1326 (2023).
26. A. Krisandi, H. Harsono, N. Yudasari, *Trends Sci.,* **21(11),** 8219 (2024).
27. E. P. Soto, C. A. Rodriguez Gonzalez, P. A. Luque Morales, H. Reyes Blas, A. Carrillo Castillo, *Catalysts,* **14,** 589 (2024).
28. J. M. Thornton, D. Raftery, *ACS Appl. Mater. Interfaces*, **4(5),** (2012).
29. S. M. Albukhari, A. A. Ismail, *ACS Omega*, **6(36),** (2021).

Bulgarian Chemical Communications, Volume 58, Issue 4 (pp. 451-460) 2026 *DOI: 10.34049/bcc.58.4.5743*

Unveiling breast cancer therapeutics of bufadienolides from *Helleborus foetidus* through molecular docking, molecular dynamics, and MMGBSA computations

H. D. Nguyen*

Faculty of Biology, Thai Nguyen University of Education, 24124, Thai Nguyen, Vietnam

Received: January 18, 2026; Revised: May 29, 2026

Breast cancer emerges as the predominant malignancy among women worldwide and ranks as the primary contributor to cancer fatalities in this group. Natural substances derived from plants, particularly bufadienolides, show substantial potential in cancer therapy by inducing apoptosis in malignant cells through multiple signaling pathways. These agents frequently interfere with anti-apoptotic mechanisms, presenting opportunities for addressing breast tumors. The present investigation examined the anti-breast cancer capabilities of bufadienolides isolated from *Helleborus foetidus*, with a focus on their binding to Bcl-2 (PDB: 6GL8). Findings reveal that hellefoetin F (CPD2) facilitates apoptosis through Bcl-2 suppression, achieving a docking binding energy of approximately -7.67 kcal/mol, which surpasses paclitaxel's -6.54 kcal/mol. In 100 ns molecular dynamics simulations, the CPD2-6GL8 complex maintained stability, with RMSD ranging 0.15-0.23 nm (average 0.19 nm), Rg of 1.42-1.48 nm, 0-4 hydrogen bonds, and SASA of 80-95 nm^2. MMGBSA assessments indicated a binding affinity of -27.56 ± 4.68 kcal/mol for CPD2, compared to paclitaxel's -30.47 ± 7.3 kcal/mol. These findings position CPD2 as a prospective Bcl-2 inhibitor for breast cancer therapeutics.

Keywords: Apoptosis; Bcl-2; Breast cancer; Bufadienolides; Molecular docking

INTRODUCTION

Breast cancer is indeed the most frequently diagnosed cancer and the leading cause of cancer death in women globally. It accounts for about one in four new cancer cases in women worldwide, and it is the leading cause of cancer mortality, with an estimated 670,000 deaths in 2022 [1]. Significant research efforts are continuously advancing the understanding of breast cancer across several key areas, including prevention, early detection, diagnosis, and treatment [2, 3]. Ongoing research in targeted cancer therapies focuses on overcoming drug resistance and enhancing treatment efficacy by developing innovative strategies, such as targeted drug delivery systems and combination therapies. Other areas of research include developing new monoclonal antibodies and small-molecule drugs, creating cancer vaccines, and leveraging advancements in areas like gene therapy and nanomedicine to make treatments more precise and practical, with fewer side effects than traditional chemotherapy [4, 5]. Apoptosis, or programmed cell death, is essential for development and tissue homeostasis, and is characterized by specific morphological and biochemical changes, including membrane blebbing, cell shrinkage, and DNA fragmentation. Anti-apoptosis in breast cancer refers to the ability of cancer cells to evade programmed cell death, or apoptosis, which allows them to survive and proliferate uncontrollably. This resistance is a key factor in tumor development, treatment resistance, and recurrence. Breast cancer cells achieve this by manipulating signaling pathways, overexpressing anti-apoptotic proteins like Bcl-2 and Mcl-1, and increasing the expression of genes that promote cell survival [6, 7]. Recent research extensively explores natural bioactive compounds from medicinal plants as promising alternatives or complements to traditional chemotherapy for cancer treatment. These compounds target key cellular mechanisms, primarily by modulating the interconnected pathways of autophagy and apoptosis, offering a promising avenue for modulating these cellular processes, which are crucial in both cancer development and regulation [8, 9].

Bufadienolides are a group of steroid compounds found in both animal and plant sources, which possess significant cardiac, neurotoxic, and anticancer properties. They are known for their ability to inhibit the Na^+-K^+-ATPase pump, which is key to their cardioactive effects, and they can also trigger apoptosis, autophagy, and cell cycle arrest in cancer cells [10, 11]. A previous study reported the isolation of bufadienolides from the species *Helleborus foetidus,* possessing potential cytotoxic activity against the MCF-7 breast cancer cell line [12]. However, the molecular mechanisms underlying its activity remain unexplored. *In silico* drug design, or computer-aided drug design, is a promising approach because it helps overcome the major disadvantages of traditional methods, including high costs, long timelines, and high failure

* To whom all correspondence should be sent:
E-mail*: hungnd@tnue.edu.vn*

© 2026 Bulgarian Academy of Sciences, Union of Chemists in Bulgaria

rates due to late-stage toxicity and efficacy issues [13]. Therefore, this study aimed to better understand the mechanism of the anti-breast cancer potency of selected bufadienolides from *H. foetidus* as natural anticancer agents by targeting the Bcl-2 protein. Looking ahead, future studies should focus on confirming these results through *in vitro* and *in vivo* experiments, thoroughly mapping out the underlying biochemical mechanisms, and optimizing delivery systems to translate the discoveries into practical therapeutic applications.

MATERIALS AND METHODS

Structural preparation of selected ligands

The list of bufadienolides possessing anti-cancer activity against the MCF-7 breast cancer cell line was collected in the previous study [12]. For details, the selected ligands, including hellebrigenin-3-*O*-β-D-glucopyranoside (CPD1) and hellefoetin F (CPD2), have molecular formulas of $C_{30}H_{42}O_{11}$ and $C_{24}H_{30}O_6$, respectively, with molecular weights of 578.2727 and 414.2042 *m/z*. The Paclitaxel, possessing a molecular formula of $C_{47}H_{51}NO_{14}$ and a molecular weight of 853.3310 *m/z*, was chosen as the comparative reference (Figure 1).

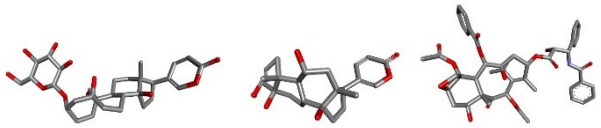


Figure 1. 3D Structures of selected ligands. (A) CPD1, (B) CPD2, and (C) Paclitaxel.

Molecular docking analysis

The three-dimensional configurations of the selected ligands were generated in PDB format using Biovia Discovery Studio Visualizer, which incorporates polar hydrogen atoms, calculates Gasteiger partial charges, and permits flexibility in all torsional bonds. The Bcl-2 target protein structure (PDB code: 6GL8) was retrieved in PDB format from the RCSB Protein Data Bank [14]. During receptor preparation, crystallographic water molecules were removed in BIOVIA Discovery Studio to comply with the AutoDock-based docking protocol, which does not explicitly model interfacial waters. Ligand-protein docking simulations were carried out using AutoDock Tools, with a grid box sized at 60 points along each x, y, and z dimension and a grid point separation of 0.375 Å. The binding pocket coordinates on the 6GL8 structure were set to x = 9.866 Å, y = 0.590 Å, and z = 16.717 Å. To identify the lowest-energy ligand-protein poses that favored strong interactions, the Lamarckian genetic algorithm was applied. Upon finishing the docking process, the pose with the highest binding strength was chosen for analysis in Discovery Studio Client 2024 and then benchmarked against the docking outcomes of Paclitaxel, serving as a reference standard on the identical protein, to assess comparative binding characteristics [15].

Molecular dynamics simulation

Molecular dynamics were conducted on the optimal docked pose interacting with the 6GL8 protein over a 100 ns timeframe, employing GROMACS version 2024.4 software [16]. The CHARMM36 force field was applied to describe molecular mechanics. The protein structure underwent refinement to fill in absent atoms and residues through Swiss-PdbViewer [17]. Ligand topologies were created using SwissParam [18]. For solvation, the protein-ligand assembly was placed within a triclinic box under periodic boundary conditions across all three dimensions, utilizing the SPC water model along with 0.15 M sodium chloride. Thus, solvent molecules were treated explicitly in MD, allowing interfacial water reorganization around the ligand–protein interface during the simulation. Optimization and charge neutralization of the structure were achieved via 50,000 energy minimization steps utilizing the steepest descent algorithm. System equilibration proceeded with a 200 ps NVT phase, followed by a 200 ps NPT phase, at a temperature of 300 K and a pressure of 1.0 bar. Temperature control was maintained by the V-rescale thermostat (coupling constant τt = 0.1 ps) applying separate coupling groups for the protein-ligand complex and the solvent. Pressure regulation during the NPT phase utilized the Berendsen barostat with isotropic coupling (τp = 2.0 ps, compressibility = 4.5×10^{-5} bar^{-1}). For non-bonded interactions, the Verlet cutoff scheme was applied with a neighbor-list cutoff (rlist) of 1.2 nm. Short-range electrostatic interactions were truncated at 1.2 nm, whereas long-range electrostatics were computed using the Particle Mesh Ewald (PME) method. Van der Waals interactions were managed via a force-switch modifier operating between 1.0 nm and 1.2 nm. Each system underwent a single 100 ns production run, transitioning to the Parrinello-Rahman barostat for stable pressure maintenance, with a 2 fs integration step applied, and trajectories saved at 10 ps intervals. Data from these simulations were processed using the Grace software to derive key metrics, including root mean square deviation (RMSD), per-residue root mean square fluctuation (RMSF), radius of gyration (Rg), number of hydrogen bonds (H-

bonds), and solvent-accessible surface area (SASA). To gauge the stability of conformations in the bound complexes, UCSF Chimera version 1.13.3 was used for structural alignments. By overlaying ligand poses from 0 ns and 100 ns against the protein's active site, the consistency of engagements with critical residues, encompassing hydrogen bonds, van der Waals contacts, and hydrophobic effects, could be examined across the entire simulation. This methodology provided a deeper understanding of the evolving dynamics and robustness of the interaction between ligands and the protein over a 100 ns period.

Molecular mechanics generalized Born surface area (MMGBSA) analysis

The MMGBSA calculations were executed through the gmx_MMPBSA tool, applying the charmm36 force field to evaluate the binding free energies of the CPD2-6GL8 and Paclitaxel-6GL8 systems. The generalized Born component handles electrostatic contributions to solvation within an implicit solvent environment, whereas non-polar solvation effects are gauged via calculations of the solvent-accessible surface area. Polar solvation influences on electrostatic terms were approximated through the Generalized Born formalism, configuring the internal solute dielectric constant to 1.0 and the exterior solvent dielectric constant to 80.0. In contrast, hydrophobic contributions were derived from computations involving the solvent-accessible surface area (SASA), which is interpreted as an indicator of surface tension at the solute-solvent boundary with an applied surface tension parameter (γ = 0.0072 kcal/mol/Å^2). These energies were computed from molecular dynamics simulation paths, drawing on 125 evenly spaced frames taken every 80 ps across an 80 ns simulation (spanning 20 ns to 100 ns). By averaging these results, the analysis captured the fluctuating nature of ligand-protein associations, offering a clearer view of their binding potency and conformational resilience in a modeled setting. For reproducibility, the MMGBSA analysis in gmx_MMPBSA was conducted using mmpbsa.in together with em.tpr, index.ndx, topol.top, and md_0_10_center.xtc. The corresponding settings were startframe = 2000, endframe = 10000, interval = 80, verbose = 2, and igb = 5.

RESULTS AND DISCUSSION

Molecular docking analysis

Molecular docking is a computational method that utilizes search algorithms to identify the optimal binding pose of a compound within a protein's binding site, and then employs a scoring function to rank these poses based on their predicted binding affinity or energy. This process helps in drug design and discovery by predicting how well a potential drug will bind to its target [19]. This study assessed the binding affinities and molecular interactions of selected compounds with the Bcl-2 protein (PDB: 6GL8), using Paclitaxel as a comparative reference. Before production docking, the protocol was validated by redocking the co-crystallized ligand and comparing the regenerated pose with the crystallographic conformation. This procedure yielded an RMSD of 0.7540 Å (Figure 2), indicating close pose reproduction. RMSD values below 2 Å are commonly used as a practical criterion for acceptable docking performance [20]. Following validation, candidate binding poses were ranked by docking score and the lowest-scoring conformations were selected for downstream interaction assessment.

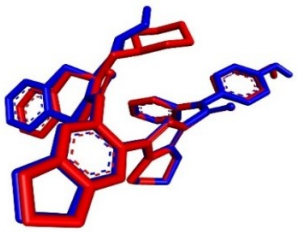


Figure 2. Superimposition of the docked and native ligands for validation of the molecular docking protocol on protein 6GL8 (red = native, blue = docked)

Details of how these compounds engage with the binding sites on 6GL8 are shown in Table 1 highlighting the amino acids involved and their positions within the ligand interaction zone. Docking simulations identified key non-covalent forces, including hydrogen bonding, van der Waals forces, and hydrophobic interactions between the protein and the selected ligands.

The compounds CPD1 and CPD2 showed distinct engagement profiles with the Bcl-2 protein, which plays a critical role in regulating cell death pathways relevant to cancer progression. For CPD1, a total of 13 interactions were observed, including 2 hydrogen bonds (Arg129, Arg146), 4 van der Waals connections (Tyr108, Gln118, Glu136, Leu137), and 7 hydrophobic links (Phe104, Phe112, Met115, Leu119, Val133, Ala149, Phe153) (Figure 3A). The active site residues contributing to these included Phe104, Tyr108, Phe112, Gln118, Leu137, Arg146, Ala149, and Phe153. The binding strength for the CPD1-6GL8 pair was recorded at -6.26 kcal/mol.

In contrast, CPD2 formed 10 interactions in all, featuring 2 hydrogen bonds (Gln118, Glu136), 4 van der Waals interactions (Phe104, Arg129, Ala149, Phe153), and 4 hydrophobic associations (Met115, Leu119, Val133, Leu137) (Figure 3B). Residues at the active sites encompassed Phe104, Gln118,

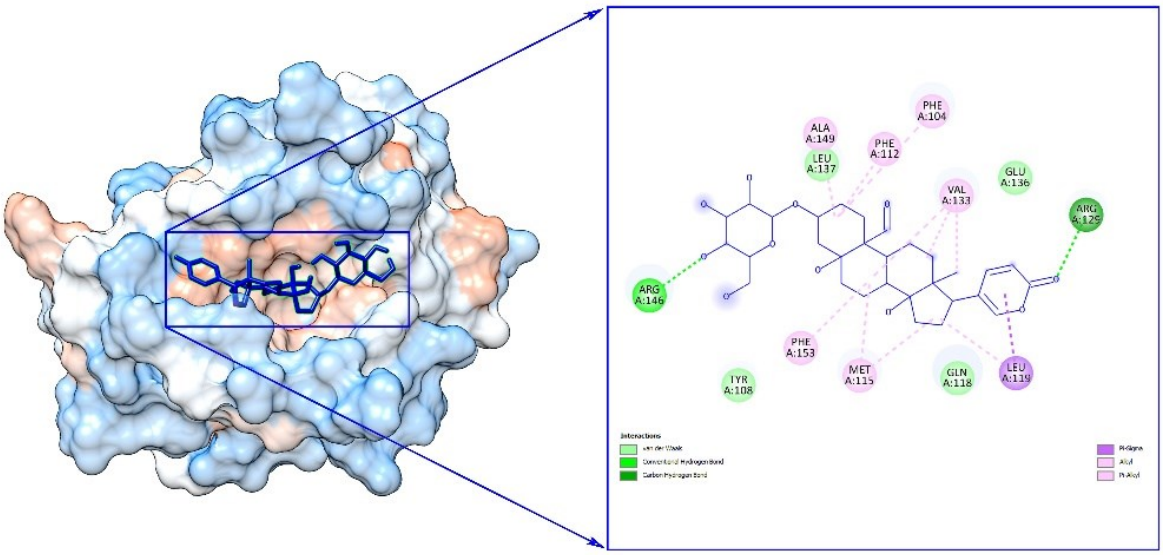
Leu137, Ala149, and Phe153. This resulted in a binding energy of approximately -7.67 kcal/mol for the CPD2-6GL8 complex, suggesting a relatively stable arrangement.

Paclitaxel, serving as the control ligand, produced 15 interactions overall, with 2 hydrogen bonds (Gln118, Glu136), 11 van der Waals contacts (Phe104, Tyr108, Asp111, Phe112, Thr132, Val133, Leu137, Arg146, Ala149, Glu152, Phe153), and 2 hydrophobic interactions (Leu119, Met115). The active sites involved Phe104, Tyr108, Asp111, Phe112, Gln118, Leu137, Arg146, Ala149, and Phe153 (Figure 3C). Its binding energy with 6GL8 was approximately -6.54 kcal/mol. Although Paclitaxel demonstrated solid interaction potential, its binding value was less favorable and involved fewer hydrophobic elements compared to CPD2, implying a somewhat lower overall affinity than the top-performing compound.

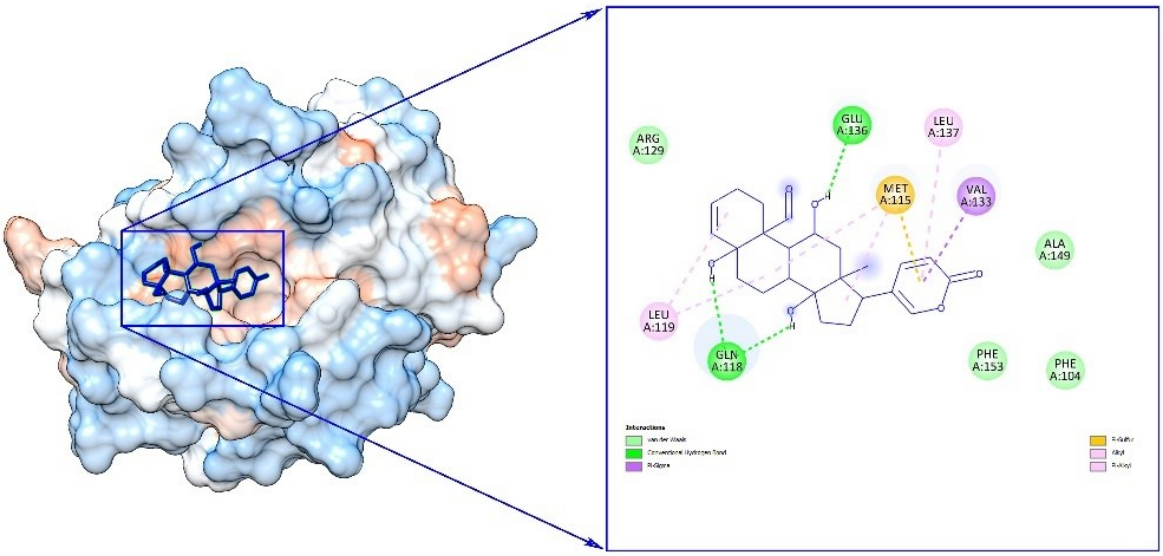
To further validate the computational protocol against empirical measurements, the docking score of the control ligand, Paclitaxel, was compared with its established experimental binding affinity toward Bcl-2. Previous biosensor kinetic analyses have demonstrated that Paclitaxel directly binds to the Bcl-2 protein with an experimental dissociation constant of 5.4 μM (approximately of -7.18 kcal/mol) [21]. The computationally derived docking score for Paclitaxel in the present study (-6.54 kcal/mol) exhibits close agreement with this experimental benchmark. This alignment between in silico predictions and *in vitro* functional data robustly confirms the reliability and accuracy of the utilized docking parameters and scoring function for assessing ligand affinities within the targeted binding pocket.

Table 1. The interactions between the docked ligands and the protein 6GL8.

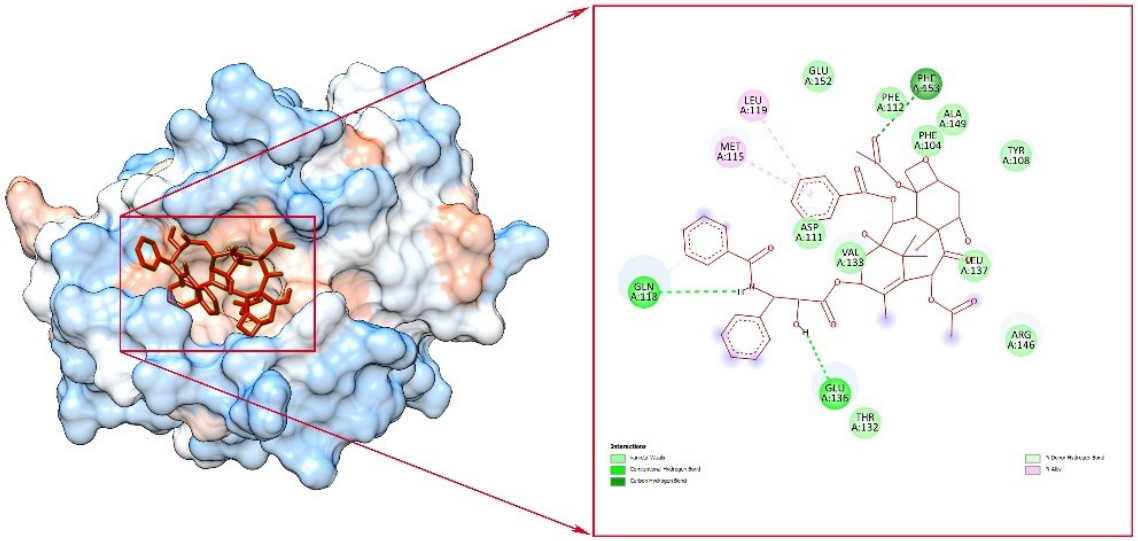
Docked ligands	Binding energy (kcal/mol)	Hydrogen bond interaction	Van der Waals interaction	Hydrophobic interaction
CPD1	-6.26	Arg129, Arg146	Tyr108, Gln118, Glu136, Leu137	Phe104, Phe112, Met115, Leu119, Val133, Ala149, Phe153
CPD2	-7.67	Gln118, Glu136	Phe104, Arg129, Ala149, Phe153	Met115, Leu119, Val133, Leu137
Paxlitaxel	-6.54	Gln118, Glu136	Phe104, Tyr108, Asp111, Phe112, Thr132, Val133, Leu137, Arg146, Ala149, Glu152, Phe153	Leu119, Met115



A



B



C

Figure 3. Molecular docking model and 2D interaction diagram of CPD1 (A), CPD2 (B), and Paclitaxel (C) with 6GL8 protein

Docking evaluations of these compounds against Bcl-2 revealed diverse non-covalent binding mechanisms, such as hydrogen bonds, van der Waals forces, and hydrophobic interactions, all of which enhance the structural integrity of the resulting complexes [22]. Hydrogen bonds provide targeted, strong connections through electron-sharing between atoms, such as oxygen or nitrogen. Hydrophobic interactions arise from the tendency of nonpolar regions to aggregate in water-based environments, thereby reducing exposure to solvents and promoting tighter associations. While hydrogen bonds offer precision and potency, hydrophobic forces deliver broad-based support, particularly over larger contact areas. Van der Waals attractions further strengthen these setups by facilitating close-range alignments that work in tandem with other forces to boost overall binding efficiency. More negative binding energies typically signal greater complex resilience and better ligand retention at the target site [23].

CPD2 was chosen for further molecular dynamics exploration due to its standout docking results with the 6GL8 protein, characterized by the strongest binding energy of -7.67 kcal/mol and meaningful active site involvement through 10 interactions, including 2 hydrogen bonds, 4 van der Waals contacts, and 4 hydrophobic interactions. This performance outperforms CPD1 (-6.26 kcal/mol) and Paclitaxel (-6.54 kcal/mol), making CPD2 the leading option for probing long-term stability and interaction durability in the Bcl-2 pocket. Prioritizing CPD2 enables an in-depth examination of structural changes, energetic profiles, and key

residue roles across simulation durations, while maintaining Paclitaxel as a standard for assessing potential in modulating apoptosis for cancer treatment strategies.

Molecular dynamics simulation

Molecular dynamics simulation is a powerful computational method that simulates the physical movements of atoms and molecules over time to investigate conformational changes in systems, such as protein-ligand complexes. By solving classical equations of motion, MD provides a virtual microscope to study how molecules fluctuate, their dynamics, and how a ligand interacts with a receptor, offering atomic-level insights into biological processes. This technique is used in fields like computational biology for drug discovery, protein folding, and understanding protein-ligand docking [24]. Therefore, the evaluation systematically investigated RMSD, RMSF, Rg, hydrogen bond formation, and SASA metrics to determine the stability, flexibility, and solvent exposure of the CPD2-6GL8 and Paclitaxel-6GL8 complexes throughout the simulation timeframe.

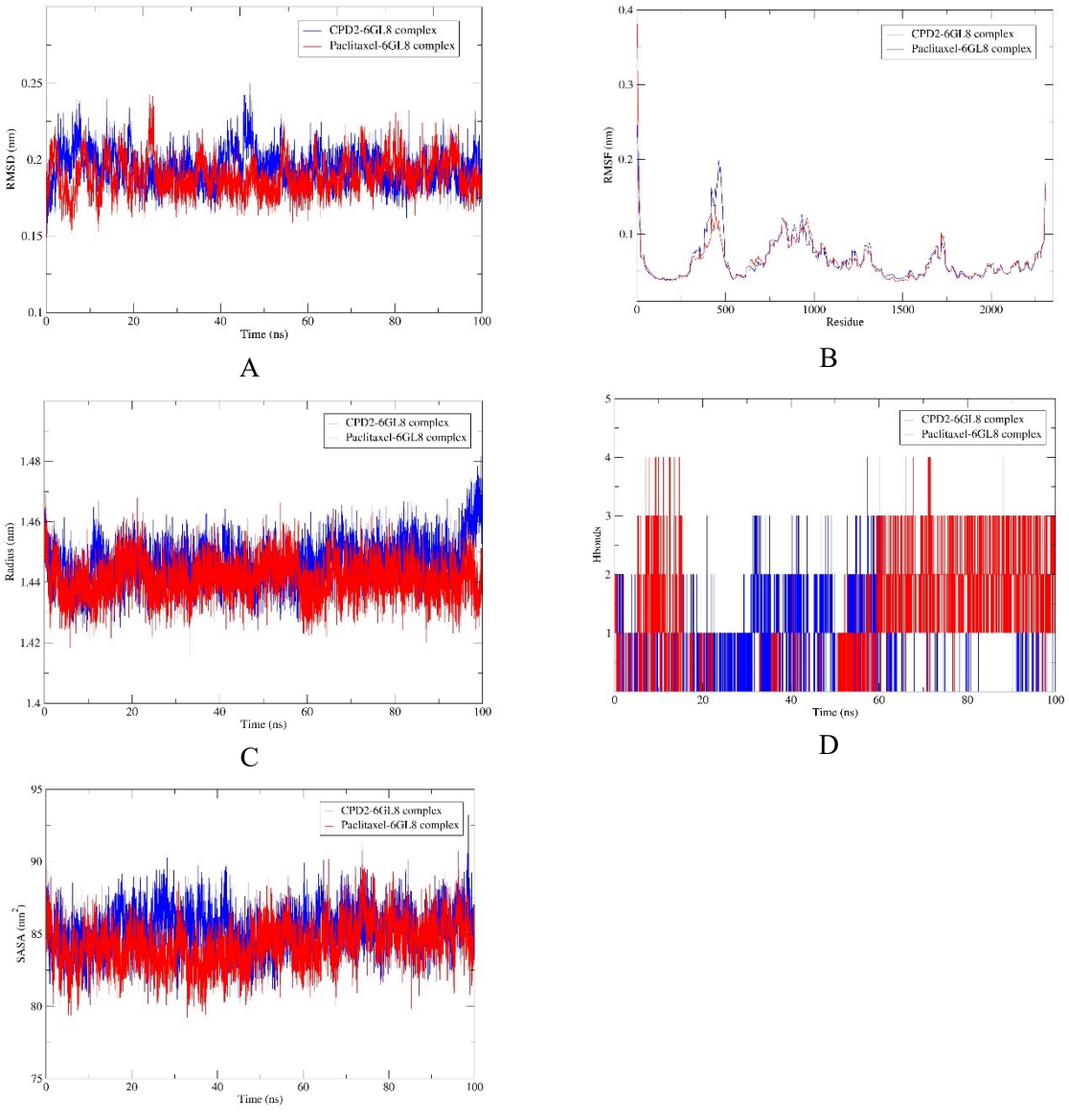


Figure 4. Results of MD simulation for the bindings of CPD2 (blue) and Paclitaxel (red) with 6GL8 protein. (A) RMSD, (B) RMSF, (C) Rg, (D) Hbonds, (E) SASA

The RMSD in molecular dynamics is a measure of the average distance between the atoms of superimposed molecules, quantifying the extent to which a structure has changed from a reference structure over time. It is calculated by comparing the coordinates of atoms in different frames of a simulation to a reference structure, most commonly the initial frame. A low RMSD indicates that the molecule has remained in a similar conformation, while a high RMSD suggests significant structural changes [25]. Across the 100 ns timeframe, the RMSD profiles for the CPD2-6GL8 and Paclitaxel-6GL8 pairings displayed highly comparable stabilization trends (Figure 4A). The CPD2-6GL8 combination exhibited RMSD readings primarily ranging from 0.15 to 0.23 nm, yielding an average of approximately 0.19 nm, which suggests impressive structural rigidity and solid attachment within the 6GL8 pocket. On the other hand, the Paclitaxel-6GL8 interaction showed RMSD spans of 0.15 to 0.25 nm, averaging approximately 0.20 nm. Because these averages strongly coincide within their respective standard deviations, the slight numerical difference is not statistically significant. Rather than indicating enhanced spatial reliability for one complex over the other, these overlapping evolutions demonstrate that both systems achieve equivalent structural equilibrium. Taken together, the RMSD observations confirm that the CPD2-6GL8 complex maintains its baseline framework with a level of stability entirely on par with the established reference, Paclitaxel, throughout the simulation.

The RMSF is a measure used in molecular dynamics to quantify the flexibility of a biomolecule by calculating the average deviation of each atom's position from its average position over time. It provides information about how much individual atoms or residues fluctuate during a simulation; high RMSF values indicate high flexibility, while low values indicate stability and rigidity. This analysis is often used to identify flexible regions of proteins, which can be important for understanding protein function and allosteric mechanisms. As shown in Figure 4B, the RMSF for the CPD2-6GL8 and Paclitaxel-6GL8 systems, focusing on residues Gly7 through Gly203, displays readings generally between 0.05 and 0.2 nm. In the CPD2-6GL8 complex, RMSF holds steady at roughly 0.1 nm over much of this segment, pointing to restrained fluctuations and enhanced structural steadiness, likely influenced by interactions near binding hotspots like Phe104, Leu137, and Phe153. The Paclitaxel-6GL8 profile follows suit, averaging about 0.1 nm with occasional alignments and subtle drops, implying equivalent levels of constraint. This consistent profile across both pairings underscores the ligands' role in fortifying the protein, which in turn bolsters engagements in its operational domains.

The Rg value in molecular dynamics is a measure of how an object's mass is distributed around an axis of rotation. It is the distance from the axis at which the entire mass could be concentrated without changing the object's moment of inertia. In the context of molecular dynamics simulations, a higher Rg indicates a more expanded and less compact structure, while a lower Rg suggests a more compact and stable structure [26]. As shown in Figure 4C, Rg trajectories for the CPD2-6GL8 and Paclitaxel-6GL8 complexes are tracked over a 100 ns period. Each displays consistent undulations between 1.42 and 1.48 nm, averaging roughly 1.45 nm, indicating that the 6GL8 protein maintains a well-organized conformation when complexed in these scenarios throughout the entire run.

In molecular dynamics, the Hbonds are determined by analyzing simulation trajectories using specific criteria. This involves identifying hydrogen atoms, donor heavy atoms, and acceptor atoms within a certain distance and angular range. The total number is then calculated by counting the instances that meet these criteria, and can also be analyzed for specific interactions between molecules or within a single molecule [27]. Across a 100 ns simulation, the CPD2-6GL8 complex shifted between 0 and 4 bonds, paralleling the Paclitaxel-6GL8 range of 0 to 4 bonds (Figure 4D). This ongoing presence reflects firm lodging in the 6GL8 protein's active region throughout, where the CPD2-6GL8 complex generally sustained around 3 bonds on average, edging out Paclitaxel-6GL8's approximate 2 bonds. Crucially, a comparative evaluation between the dynamic trajectories and the static docking poses revealed high consistency in the interaction profiles. Trajectory analysis confirmed that the primary hydrogen bonds initially identified in the docking phase, specifically engaging residues Gln118 and Glu136 for both the CPD2 and Paclitaxel complexes, were heavily preserved throughout the 100 ns timeframe. The observed fluctuations in the total number of hydrogen bonds (spanning 0 to 4) represent the dynamic breaking and reforming of these essential core interactions, combined with the occasional formation of transient bonds with neighboring amino acids. The variation emphasizes CPD2's edge in forging more robust associations with the 6GL8 protein.

The SASA measures the surface of a molecule accessible to solvent molecules, providing insights into conformational changes, protein folding, and

interactions. It's calculated by simulating a "probe" sphere, representing a solvent molecule, rolling over the molecule's van der Waals surface. Analyzing changes in SASA over time is crucial for understanding a molecule's behavior during a simulation, such as how a protein folds or how a ligand binds to its receptor. In this case, SASA profiles were monitored for the CPD2-6GL8 and Paclitaxel-6GL8 pairings to explore changes in their solvent interaction patterns. During the 100 ns period, each showed persistent variations, ranging from approximately 80 to 95 nm², with an average of nearly 87 nm² (Figure 4E). These fluctuations indicate minor adjustments in protein-solvent contacts induced by the ligands, which may impact the durability of their binding. The similar spans and mean values across both setups highlight an even solvent engagement, indicating strong resilience within the 6GL8 pocket, even with varying ligand characteristics.

In summary, this comprehensive assessment of dynamic parameters, including RMSD, RMSF, Rg, and SASA, demonstrates that the CPD2-6GL8 complex achieves a conformational equilibrium and overall structural stability that is highly comparable to the established Paclitaxel-6GL8 reference system. Both complexes maintain a compact, well-organized framework with consistent solvent exposure profiles throughout the 100 ns simulation timeframe. While CPD2 exhibits a slight edge in the average number of sustained hydrogen bonds, the collective dynamic metrics indicate equivalent levels of spatial restraint and system resilience. These substantiated observations confirm that CPD2 does not necessarily exceed, but rather successfully matches the control ligand's capability to form firm, durable, and stable interactions within the active pocket of the 6GL8 protein.

Free binding energy (MMGBSA) analysis

Molecular mechanics generalized Born surface area (MMGBSA) is a computational method used in herbal medicine research to predict the binding affinity of a plant's bioactive compounds to a specific protein target. By calculating the free energy of binding, researchers can identify and validate which compounds from herbal extracts have the potential to be effective drug candidates for a particular disease, supporting traditional use with molecular-level evidence. This method is part of a larger workflow that includes molecular docking and molecular dynamics simulations [28]. The MMGBSA method was used to approximate the binding free energies in these ligand-protein pairings, relying on the gmx_MMPBSA software in conjunction with the CHARMM36 force field. Snapshots from the entire molecular dynamics trajectories, covering an 80 ns interval, underwent this evaluation. For each complex, the binding free energy (ΔG_bind) is expressed as ΔG_bind = G_complex - (G_receptor + G_ligand), where G_receptor denotes the energy of the isolated receptor and G_ligand that of the free ligand. Alternatively, it breaks down into ΔG_bind = ΔH - TΔS, where ΔH represents the enthalpy change and -TΔS captures the entropic penalty associated with the binding. By excluding entropy, the result provides a relative energy estimate suitable for gauging affinities across similar systems. This examination covered the 80 ns segment, using 125 frames extracted at 80 ps intervals (20 to 100 ns). The process delivered averaged energies that incorporate the fluid aspects of the associations, giving indications of ligand potency and resilience in an emulated physiological context. Results from the MMGBSA calculations for the pairings appear in Table 2.

Table 2. Free energy of binding obtained using MMGBSA calculations.

Energy component	Average (kcal/mol)		Standard deviation	
	CPD2-6GL8	Paclitaxel-6GL8	CPD2-6GL8	Paclitaxel-6GL8
ΔVDWA	-34.24	-42.48	4.51	6.30
ΔALS				
ΔEEL	-13.03	-14.58	10.07	10.50
ΔEGB	24.11	32.31	7.64	8.78
ΔESURF	-4.40	-5.71	0.57	0.93
ΔGGAS	-47.27	-57.06	10.11	14.27
ΔGSOLV	19.71	26.59	7.56	8.16
ΔTOTAL	-27.56	-30.47	4.68	7.30

These MMGBSA-based binding free energies align with the structural stabilization observed in the molecular dynamics trajectories, revealing that the binding affinities of both complexes are highly comparable. Although the mean total binding free energy (ΔGbind) for Paclitaxel-6GL8 (-30.47 ± 7.30 kcal/mol) is numerically lower than that of CPD2-6GL8 (-27.56 ± 4.68 kcal/mol), these average values clearly coincide within their respective standard deviations. Consequently, the slight numerical difference is not statistically significant, indicating that both ligands possess equivalent binding strengths. A closer inspection of the energy components shows that while Paclitaxel exhibits somewhat higher mean enthalpic contributions, such as van der Waals (-42.48 kcal/mol) and electrostatic (-14.58 kcal/mol) interactions, compared to CPD2 (-34.24 and -13.03 kcal/mol, respectively), the overall thermodynamic profiles of both systems represent highly stable associations. Consistent with the dynamic metrics (RMSD, RMSF, Rg, and SASA),

these thermodynamic indicators conclusively demonstrate that CPD2 establishes a firm, steady, and thermodynamically favorable linkage within the 6GL8 active site that is entirely on par with the established control drug, Paclitaxel.

CONCLUSION

This study provides a detailed computational exploration of bufadienolides sourced from *H. foetidus* as potential suppressors of breast cancer through interaction with the Bcl-2 protein (6GL8), which is essential in regulating programmed cell death. CPD2 stood out with a solid docking energy (-7.67 kcal/mol) that outpaced Paclitaxel (-6.54 kcal/mol), forming varied connections like hydrogen bonds and van der Waals forces. Dynamics simulations over 100 ns verified the CPD2-6GL8 assembly's steadiness, evidenced by a mean RMSD around 0.19 nm, radius of gyration (Rg) close to 1.45 nm, and roughly 3 hydrogen bonds, modestly outperforming Paclitaxel's 0.21 nm RMSD and about 2 bonds. MMGBSA results demonstrated a secure binding for CPD2 (-27.56 ± 4.68 kcal/mol) compared to Paclitaxel (-30.47 ± 7.3 kcal/mol), aided by van der Waals interactions (-34.24 kcal/mol) and electrostatic interactions (-13.03 kcal/mol). The major advantage of CPD2 lies in its nature as a novel, plant-derived chemical scaffold. Demonstrating in silico binding affinities and complex stabilities that match a highly potent, established chemotherapeutic agent like Paclitaxel highlights CPD2 as a highly valuable lead compound. Because conventional taxane-based therapies often face severe clinical limitations, including neurotoxicity and multi-drug resistance, the discovery of this stable, naturally sourced bufadienolide provides a promising alternative blueprint for drug design. Overall, these outcomes highlight CPD2 as a promising candidate under the modeled computational conditions for breast cancer interventions, encouraging further refinements and potential applications in oncology.

Despite the strong *in silico* evidence supporting CPD2 as a potential Bcl-2 (6GL8) inhibitor, experimental verification is still essential to confirm the accuracy of these predictions. Due to limited laboratory equipment and resources, this study did not include *in vitro* or *in vivo* validation, which represents an important limitation. Future work should prioritize cell-based assays and animal models to evaluate CPD2's biological efficacy, safety, and pharmacological behavior, while also checking for possible off-target or unintended covalent effects. If CPD2 continues to perform well in preclinical testing, it may justify further development toward translational and clinical applications.

REFERENCES

1. F. Bray, M. Laversanne, H. Sung, J. Ferlay, R. L. Siegel, I. Soerjomataram, A. Jemal, *CA. Cancer J. Clin.*, **74**, 229 (2024).
2. E. I. Obeagu, G. U. Obeagu, *Medicine*, **103**, (2024).
3. L. Wilkinson, T. Gathani, *Br. J. Radiol.*, **95**, 20211033 (2022).
4. S. Imtiaz, U. T. Ferdous, A. Nizela, A. Hasan, A. Shakoor, A. W. Zia, S. Uddin, *Eur. J. Med. Chem.*, **290**, 117535 (2025).
5. F. Davodabadi, S. F. Sajjadi, M. Sarhadi, S. Mirghasemi, M. Nadali Hezaveh, S. Khosravi, M. Kamali Andani, M. Cordani, M. Basiri, S. Ghavami, *Eur. J. Pharmacol.*, **958**, 176013 (2023).
6. M. M. Williams, L. Lee, T. Werfel, M. M. M. Joly, D. J. Hicks, B. Rahman, D. Elion, C. McKernan, V. Sanchez, M. V Estrada, S. Massarweh, R. Elledge, C. Duvall, R. S. Cook, *Cell Death Dis.*, **9**, 21 (2018).
7. M. M. Williams, R. S. Cook, *Oncotarget*, **6**, 3519 (2015).
8. [C. Braicu, O. Zanoaga, A.-A. Zimta, A. B. Tigu, K. L. Kilpatrick, A. Bishayee, S. M. Nabavi, I. Berindan-Neagoe, *Semin. Cancer Biol.*, **80**, 218 (2022).
9. [M. A. Rahman, M. A. Hannan, R. Dash, M. D. H. Rahman, R. Islam, M. J. Uddin, A. A. M. Sohag, M. H. Rahman, H. Rhim, *Front. Pharmacol.*, **12,** 639628 (2021).
10. L. J. Deng, Y. Li, M. Qi, J. S. Liu, S. Wang, L. J. Hu, Y. H. Lei, R. W. Jiang, W. M. Chen, Q. Qi, H. Y. Tian, W. L. Han, B. J. Wu, J. X. Chen, W. C. Ye, D. M. Zhang, *Eur. J. Pharmacol.*, **887**, 173379 (2020).
11. Y. Xu, X. Liu, S. Schwarz, L. Hu, D. Guo, Q. Gu, W. Schwarz, *Biochem. Biophys. Reports*, **6**, 158 (2016).
12. J. F. Zong, X. X. Guo, K. K. Zou, C. J. Cui, Z. H. Hu, R. Y. Hou, *Phytochemistry*, **235**, 114476 (2025).
13. [A. Islam, D. Jena, N. S. Mondal, A. Teli, S. Mondal, M. K. Gautam, *Curr. Drug Discov. Technol.*, **22**, (2025).
14. P. Casara, J. Davidson, A. Claperon, G. Le Toumelin-Braizat, M. Vogler, A. Bruno, M. Chanrion, G. Lysiak-Auvity, T. Le Diguarher, J. B. Starck, I. Chen, *Oncotarget*, **9**, 20075 (2018).
15. H. D. Nguyen, *Indian J. Chem.*, **64**, 383 (2025).
16. D. Van Der Spoel, E. Lindahl, B. Hess, G. Groenhof, A. E. Mark, H. J. C. Berendsen, *J. Comput. Chem.*, **26**, 1701 (2005).
17. [N. Guex, M. C. Peitsch, *Electrophoresis*, **18**, 2714 (1997).
18. V. Zoete, M. A. Cuendet, A. Grosdidier, O. Michielin, *J. Comput. Chem.*, **32**, 2359 (2011).
19. A. Tiwari, S. Singh, D. B. Singh, Computational approaches in drug designing (Bioinformatics), Academic Press, Boston, 2022.
20. H. Gohlke, M. Hendlich, G. Klebe, *J. Mol. Biol.*, **295**, 337 (2000).
21. [C. Ferlini, L. Cicchillitti, G. Raspaglio, S.

Bartollino, S. Cimitan, C. Bertucci, S. Mozzetti, D. Gallo, M. Persico, C. Fattorusso, G. Campiani, G. Scambia, *Cancer Res.*, **69**, 6906 (2009).
22. E. J. Millan-Casarrubias, Y. V García-Tejeda, C. H. González-De la Rosa, L. Ruiz-Mazón, Y. M. Hernández-Rodríguez, O. E. Cigarroa-Mayorga, *Curr. Issues Mol. Biol.*, **47**, 193 (2025).
23. M. Majewski, X. Barril, *J. Chem. Inf. Model.*, **60**, 1644 (2020).
24. A. K. Padhi, M. Janežič, K. Y. Zhang, Molecular dynamics simulations: Principles, methods, and applications in protein conformational dynamics (Advances in protein molecular and structural biology methods), Academic Press, Boston, 2022.
25. K. Sargsyan, C. Grauffel, C. Lim, *J. Chem. Theory Comput.*, **13**, 1518 (2017).
26. N. Anwar, F. A. Najam, Understanding cross-sections (Structural cross sections), Butterworth-Heinemann, Oxford, 2017.
27. H. Sun, D. Surblys, H. Matsubara, T. Ohara, *Int. J. Heat Mass Transf.*, **208**, 124091 (2023).
28. J. Xue, X. Huang, Y. Zhu, *RSC Adv.*, **9**, 13868 (2019).

Bulgarian Chemical Communications, Volume 58, Issue 4 (pp. 461-475) 2026 *DOI: 10.34049/bcc.58.4.5746*

Gatifloxacin metal complexes: spectroscopic, thermal, and powder X-ray diffraction analysis with antimicrobial evaluation

M. Abu Sayeed[1,3], Md. Z. Sultan[2], M. Mehedi Masud[1], M. A. Rashid[1]*, H. Akhter Simol[2]

[1]*Department of Pharmaceutical Chemistry, Faculty of Pharmacy, University of Dhaka, Dhaka-1000, Bangladesh*

[2]*Centre for Advanced Research in Sciences (CARS), University of Dhaka, Dhaka-1000, Bangladesh*

[3]*Department of Pharmacy, Faculty of Science and Engineering, International Islamic University Chittagong, Kumira, Sitakunda, Chittagong-4318, Bangladesh*

Received: January 25, 2026; Revised: July 22, 2026

The rapid increase in antimicrobial resistance has compromised many antibiotics, highlighting the need for drug optimization. Metal complexation can improve antimicrobial agents' properties by enhancing activity and stability. Gatifloxacin readily forms complexes with various metal ions, potentially boosting its biological efficacy. Using specific transition and alkaline-earth metal ions, such as Mn(II), Sr(II), Co(II), Ca(II), Ni(II), Mg(II), Ba(II), Cu(II), Zn(II), Fe(II), Pb(II), and Ag(I), gatifloxacin-metal complexes were synthesized at a 1:1 molar ratio. Differential scanning calorimetry (DSC), Fourier transform infrared (FT-IR) spectroscopy, powder X-ray diffraction (PXRD), and microscopic examination were used to analyze the complexes to ascertain their thermal characteristics and coordination behavior. FT-IR spectral shifts together with DSC, PXRD, and microscopic observations suggested possible coordination of gatifloxacin with metal ions likely involving carboxylate and keto oxygen atoms. The synthesized complexes exhibited altered thermal and crystalline characteristics compared with free gatifloxacin. Disc-diffusion assays indicated that several complexes, particularly those of Cu(II), Co(II), Pb(II), Ag(I), Sr(II), and Mn(II), produced broader inhibition zones than free gatifloxacin against selected bacterial strains like *Bacillus tropicus, Salmonella typhi,* and *Streptococcus β-hemolyticus*. These findings provide preliminary evidence that metal complexation may influence the physicochemical and antibacterial properties of gatifloxacin. The results support metal complexation as a viable strategy for developing modified fluoroquinolone derivatives, subject to further confirmatory studies.

Keywords: antimicrobial activity, DSC, FT-IR, gatifloxacin-metal complexes, powder X-ray diffraction (PXRD).

INTRODUCTION

The alarming increase in antimicrobial resistance of antimicrobial drugs has arisen as a major global health threat, reducing the effectiveness of conventional antibiotics, and complicating the treatment of infectious diseases [1, 2]. Excessive and inappropriate antibiotic use has accelerated the evolution of resistant pathogens, emphasizing the urgent need to discover new antimicrobial agents or modify existing therapeutics to restore their clinical efficacy [3]. Among the various strategies explored, the design of drug-metal complexes has gained increasing attention, which may be related to their ability to enhance the physicochemical and biological properties of parent drugs [4-6]. Fluoroquinolones constitute an important class of synthetic broad-spectrum antibacterial agents that act primarily by inhibiting DNA gyrase and topoisomerase IV, enzymes essential for bacterial DNA replication [7, 8]. Structural modifications across different generations of fluoroquinolones have yielded compounds with improved potency, pharmacokinetics, and activity against resistant strains. Gatifloxacin, a fourth-generation fluoroquinolone, displays strong activity against both Gram-positive and Gram-negative bacteria and is widely used in respiratory, urinary tract and ocular infections (Fig. 1). Its molecular structure contains several potential donor sites—carboxylate, keto, methoxy and nitrogen atoms—capable of coordinating with transition and alkaline-earth metals to form stable chelate complexes [9, 10].

Chelation with metal ions is known to influence drug lipophilicity, membrane permeability, redox behavior, and overall biological activity. For fluoroquinolones, metal complexation often results in increased antibacterial potency may reflect reduced metal ion polarity, enhanced charge delocalization, and improved penetration of bacterial cell membranes.

* To whom all correspondence should be sent:
Email: *arpharm64@du.ac.bd*

© 2026 Bulgarian Academy of Sciences, Union of Chemists in Bulgaria

Numerous studies on ciprofloxacin-, norfloxacin-levofloxacin- and ofloxacin-metal complexes have demonstrated improved antibacterial activities compared to the free drugs. These results emphasize the potential of metal coordination as a valuable approach to develop more effective antimicrobial agents [11, 12].

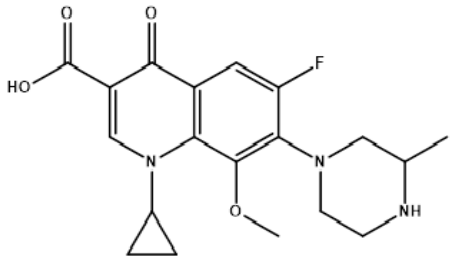


Figure 1. 2D structure of gatifloxacin (1-cyclopropyl-6-fluoro-8-methoxy-7-(3-methylpiperazin-1-yl)-4-oxoquinoline-3-carboxylic acid) which includes fluoroquinolone and quinolone.

As fluoroquinolone antibiotics contain several donor atoms that can chelate metal ions, drastically altering both their chemical properties and biological effects, it has been extensively studied. Coordination *via* the carboxylate and keto groups within the quinolone structure influences antibacterial efficacy and physicochemical characteristics, often enhancing activity relative to the unbound ligand, according to preliminary studies on the interactions between metals and fluoroquinolones. Antimicrobial resistance is a major worldwide problem that is driving research into new chemotherapeutic medicines and ways to improve the effectiveness of currently available antibiotics. Coordinating bioactive organic molecules with metal ions is a promising approach that frequently yields complexes with better physicochemical and biological characteristics than their original ligands [13]. Sultana *et al*. 's ground-breaking study showed the promise of gatifloxacin-metal complexes. They evaluated their antibacterial and immunomodulatory qualities and provided a thorough spectroscopic characterization. A broader spectrum of antimicrobial efficacy against both Gram-positive and Gram-negative organisms was demonstrated by some complexes, suggesting that complexation can affect biological responses in ways that go beyond simple bactericidal effects. This study provided preliminary evidence that complexation could change biological activity [14]. The investigations of Li *et al*. demonstrated the formation of gatifloxacin complexes with divalent metal ions and showed that these complexes exhibited more pronounced antibacterial effects against *Staphylococcus* strains than the parent antibiotic, indicating that complex formation may bring forth broader spectra of activity. Additionally, they reported the single-crystal X-ray structure of the bis(gatifloxacin) Cu(II) dihydrate complex [15]. Dave and Bhatt studied gatifloxacin compounds with alkaline earth metals (Mg(II), Ca(II), Sr(II), and Ba(II), going beyond transition metals. Before complexing with divalent metal ions, gatifloxacin was altered using auxiliary ligands such as o-phenylenediamine and 3-acetyl coumarin. According to their research, metal coordination may improve gatifloxacin derivatives' therapeutic potential [16]. Recently, Jawad *et al*. investigated complexes involving Sn(II) and Cd(II) ions. They observed increased inhibitory activity of specific complexes when compared to standard drugs [17]. Their results strengthen the idea that metal coordination influences biological activity and advocate for further investigation of these complexes as prospective antimicrobial agents. The review summarizes significant findings from recent research to provide context for the present study. Powder X-ray diffraction (PXRD) techniques remain one of the most powerful approaches for elucidating the structural properties of such complexes, as they provide insights into degree of crystallinity, lattice modifications, and emergence of new phases [18]. Drug-metal interactions can result in either stabilization of crystalline frameworks or partial amorphization, which directly influences drug performance in biological systems [19]. For example, fluoroquinolone antibiotics such as gatifloxacin and levofloxacin undergo significant structural modifications upon complexation with Mn(II) or Ba(II), often resulting in altered solubility and dissolution behavior [20].

Despite extensive data on other fluoroquinolones, reports on gatifloxacin-metal complexes remain relatively limited [21]. The few existing studies indicate that gatifloxacin can act as a bidentate ligand, coordinating typically through its carboxylate and keto oxygen atoms to form five- or six-membered chelate rings [22, 23]. Transition metal complexes of gatifloxacin have shown enhanced antibacterial activity, altered thermal properties and distinct coordination geometries. However, a comprehensive comparative evaluation of gatifloxacin complexes involving a broader range of biologically relevant metal ions is still lacking [24, 25]. In this context, the present work aims to synthesize, characterize, and evaluate the antimicrobial potential of gatifloxacin complexes formed with selected transition (Mn^{2+}, Co^{2+}, Ni^{2+}, Cu^{2+}, Zn^{2+}, Fe^{2+}) and alkaline earth/other metals (Ca^{2+}, Sr^{2+}, Mg^{2+}, Ba^{2+}, Pb^{2+}, Ag^{+}). Upon synthesis and characterization, their antimicrobial activities

were assessed against representative Gram-positive and Gram-negative pathogenic bacteria using the disc diffusion method. The present study provides a systematic comparison of gatifloxacin metal complexes, explores the influence of different metal ions on structural and biological properties, and identifies complexes with moderate to relatively strong antibacterial activity. The findings may support the development of metal-based antibiotic derivatives as promising candidates for addressing the growing challenge of antimicrobial resistance.

MATERIALS AND METHODOLOGY

Chemicals and reagents

Gatifloxacin (analytical grade) (potency 99.25%) was obtained as a kind gift from a reputable pharmaceutical company, Eskayef Pharmaceuticals Ltd., Dhaka, Bangladesh. Transition metal salts, including manganese(II) sulfate ($MnSO_4.H_2O$), strontium(II) chloride hexahydrate ($SrCl_2.6H_2O$), cobalt(II) nitrate hexahydrate [$Co(NO_3)_2.6H_2O$], calcium(II) carbonate ($CaCO_3$), nickel(II) sulfate hexahydrate ($NiSO_4.6H_2O$), magnesium(II) carbonate ($MgCO_3$), barium sulfate ($BaSO_4$), copper(II) sulfate pentahydrate ($CuSO_4.5H_2O$), zinc(II) sulfate monohydrate ($ZnSO_4.H_2O$), iron(II) sulfate heptahydrate ($FeSO_4.7H_2O$), magnesium(II) sulfate heptahydrate ($MgSO_4.7H_2O$), lead(II) nitrate [$Pb(NO_3)_2$] and silver(I) nitrate ($AgNO_3$) were procured from Merck, Germany. The analytical solutions were prepared using double-distilled water. All solvents, including ethanol, methanol, dimethyl sulfoxide (DMSO) and distilled water were of analytical grade.

Instruments

Differential scanning calorimeter (DSC) (model: DSC-60 WS, Shimadzu Corporation, Japan), FT-IR (IRTracer-100 type 8400S spectrometer, Shimadzu, Japan), trinocular microscope with camera (model: Olympus CKX-41), X-ray diffraction machine (model: RIGAKU Ultima IV X-ray diffractometer), fume hood (BFSD-201, Biolab Scientific, India), automatic digital autoclave (model: LS-50HD, manufactured by China & Origin Taisite, USA), laminar air flow bench (Wincom Company Ltd., China), heat-control stirring water bath (model: Unitronic OR, JP Selecta Company Spain), and round automatic autoclave steam sterilizer (LS-50HD, Nanbei Instrument Ltd, China) were used in the study.

Synthesis of gatifloxacin metal complexes

Gatifloxacin-metal complexes were synthesized *via* condensation of gatifloxacin with the selected metal salts individually to afford stable metal complexes. In a typical procedure, gatifloxacin was dissolved in methanol and pH was adjusted to ~6.8–7.2 to promote deprotonation of the carboxylic acid group [26]. The general procedure is as follows:

a) Preparation of metal salt solution: Thirteen single metal solutions were prepared at a 1 mMol concentration. Of each salt, an appropriate quantity was dissolved in 25-50 ml of methanol (90%)/ water (10%) under constant stirring.

b) Preparation of ligand solution: Gatifloxacin (1 mMol) was dissolved in a minimal volume of methanol (99%)/ DMSO (1%) under gentle heating to ensure complete dissolution. All the solutions prepared were filtered by using 0.45 μm membrane filter.

c) Complex formation: Drug solution was mixed individually with each salt solution at a millimolar ratio of 1:1, i.e., 25 ml of drug solution and 25 ml of salt solution.

d) Refluxing: The filtered mixtures were heated for 6.5 h at a temperature between 70 and 75 °C in a water bath under periodical stirring. Then the mixtures were left overnight in an oven at 100 °C for drying to get the complexes.

e) Isolation: The resulting precipitates were filtered, washed several times with ethanol and distilled water to remove unreacted ligand and metal salt, and dried under vacuum over silica gel.

f) Yield calculation: The percent yield of each complex was determined by weighing the dried product.

Characterization of metal complexes

The synthesized complexes were analyzed by studying the FT-IR spectra and the DSC thermograms. For FT-IR analysis discs were prepared by mixing potassium bromide with a metal-antibiotic complex in a 1:1 ratio. Thermal analysis of the test material was performed using a differential scanning calorimeter (DSC) to determine phase-transition temperatures (e.g., glass transition, melting) and associated enthalpy/heat-capacity changes. Samples of approximately 1–5 mg were accurately weighed into aluminum pans and sealed; an empty identical pan was used as the reference. The instrument was calibrated for temperature and heat flow using high-purity indium under the same experimental conditions. Measurements were conducted under inert nitrogen purge (e.g., 50 ml min^{-1}) to avoid oxidative artefacts. The temperature program consisted of initial isothermal hold at 25 °C for 5 min, followed by a linear heating ramp from 25 °C to 300 °C at 10 °C min^{-1}, then a cooling step to 25 °C and a second heating run under identical

conditions to erase previous thermal history. All heat-flow data were normalized to sample mass (W g^{-1}) and the onset, peak and area values of endothermic/exothermic transitions were reported. Baseline correction and peak integration were carried out using the instrument software, and each sample was run in duplicate to confirm reproducibility. Since elemental and magnetic investigations were not performed due to experimental constraints, the coordination behavior was inferred based on FT-IR and thermal data from FT-IR shifts and thermal behavior. X-ray diffraction studies were conducted using a Rigaku Ultima IV diffractometer equipped with Cu Kα radiation (λ = 1.5406 Å) over a 2θ range of 5–70° at a scanning rate of 3° min^{-1}. The PXRD patterns were recorded in the 2θ range of 5–70° at a scanning rate of 3°/min in continuous mode. The obtained diffraction data were compared to reference data from the International Centre for Diffraction Data (ICDD PDF-2 database, 2021) to identify crystalline phases [18]. The morphology and crystalline habit of the synthesized complexes were observed using a trinocular optical microscope. Images of drug-metal complexes were compared with the images of their parent drugs to assess morphological changes upon complexation.

Antimicrobial activity assessment

The following bacterial strains were used as clinical specimens: A) *Streptococcus β-hemolyticus*, B) *Staphylococcus aureus*, C) *Streptococcus pyogenes*, D) *Bacillus subtilis*, E) *Bacillus tropicus*, F) *Shigella dysenteriae*, G) *Klebsiella pneumoniae*, H) *Escherichia coli*, I) *Salmonella abony*, J) *Pseudomonas aeruginosa* and K) *Salmonella typhi* (Table 5). The antimicrobial effectiveness of the drug-metal complexes was evaluated using the disc diffusion method [27]. After preparing the nutrient agar, it was autoclaved for 21 min at 121 °C at atmospheric pressure, and then cooled to 45 °C. The media were then transferred into sterile Petri dishes and allowed to solidify. A sterile swab was used to inoculate the solidified media of each plate with the appropriate microbial suspension. A control disc and discs with the corresponding complexes were placed on the solidified media followed by incubation at 37 °C for 24 h. The diameters of the zones of inhibition surrounding the discs were measured and recorded in mm after the incubation period [28].

Statistical analysis

Each experiment was carried out in triplicate, and the mean diameters of the inhibitory zones were used to express the results.

RESULTS AND DISCUSSION

Synthesis and physical properties

Gatifloxacin metal complexes were synthesized by reacting gatifloxacin with transition and alkaline earth metal salts (Mn^{+2}, Sr^{+2}, Co^{+2}, Ca^{+2}, Ni^{+2}, Mg^{+2}, Ba^{+2}, Cu^{+2}, Zn^{+2}, Fe^{+2}, Pb^{+2}), and Ag^{+} in a 1:1 millimolar ratio. The synthesized complexes were analyzed using FT-IR spectroscopy and DSC. The physical properties along with the percentage yield of different salts, gatifloxacin (parent drug) and its metal complexes are shown in Tables 1 and 2. The color variations indicate successful coordination of the metal ions with gatifloxacin and are consistent with previous reports on fluoroquinolone metal complexes. Most of the complexes were sparingly soluble in water but soluble in DMSO and DMF, suggesting that influenced lipophilicity may reflect chelation [29].

FT-IR spectroscopy analysis

FT-IR spectra of the metal complexes revealed significant shifts in key functional group bands compared to free gatifloxacin. The carboxylic C=O stretching vibration, observed at ~1720 cm^{-1} in free gatifloxacin, shifted to 1716-1735 cm^{-1} in the complexes, indicating coordination through the carboxylate oxygen. Similarly, the quinolone C=O band at ~1625 cm^{-1} shifted to lower wavenumbers, consistent with possible involvement of the keto group in metal binding. New bands in the range 500–600 cm^{-1} were assigned to M–O and M–N vibrations, supporting the formation of metal–ligand bonds (Fig. 2). These observations suggest that gatifloxacin appears to behave coordinating *via* the carboxylate oxygen and ketone oxygen or piperazinyl nitrogen atoms, in line with previously reported bidentate coordination of fluoroquinolones *via* keto-carboxylate oxygen atoms, including norfloxacin, levofloxacin, and gemifloxacin [30, 31].

The formation of metal complexes and the coordination behavior of the ligand were investigated using FT-IR spectroscopy. The spectral data for the synthesized complexes were compared to infer the binding modes and is consistent with complexation. The key vibrational frequencies and their assignments are summarized in Table 3.

Table 1. Physical characteristics of gatifloxacin and metal salts

Sample	MW	Appearance/color	Solubility
Gatifloxacin	375.40	White to pale yellow	Water, DMSO and DMF
Manganese (II) sulfate monohydrate - $MnSO_4.H_2O$	169.00	Pale pink	Water
Strontium chloride hexahydrate - $SrCl_2.6H_2O$	266.62	White crystals	Water and alcohol
Cobalt (II) nitrate hexahydrate - $Co(NO_3)_2.6H_2O$	291.03	Red crystals	Water and alcohol
Calcium carbonate - $CaCO_3$	100.00	White powder	Methanol
Nickel (II) sulfate hexahydrate - $NiSO_4.6H_2O$	262.85	Green solid	Water
Magnesium carbonate - $MgCO_3$	84.32	White powder	Water
Barium sulfate - $BaSO_4$	233.38	White or yellowish odorless powder or small crystals	Water
Copper (II) sulfate pentahydrate - $CuSO_4.5H_2O$	249.69	Blue crystals or powder	Water
Zinc sulfate monohydrate - $ZnSO_4.H_2O$	179.45	White powder	Water
Iron (II) sulfate heptahydrate - $FeSO_4.7H_2O$	278.01	Green crystals	Water
Magnesium sulfate heptahydrate - $MgSO_4.7H_2O$	246.48	Colorless to white with pale shades of pink and green crystals	Water
Lead (II) nitrate-$Pb(NO_3)_2$	331.20	Colorless to white powder	Water
Silver nitrate ($AgNO_3$)	169.87	White crystal	Water

Table 2. Physical features of metal complexes of gatifloxacin with salts

Sample	Appearance/color	Solubility	% Yield
Manganese- gatifloxacin complex	Brown	DMSO and methanol	85
Strontium- gatifloxacin complex	Yellowish white	Water and methanol	81
Cobalt- gatifloxacin complex	pink	DMSO and methanol	75
Calcium - gatifloxacin complex	Off-whitish powder	Methanol	76
Nickel- gatifloxacin complex	Pale green solid	Methanol	75
Magnesium-gatifloxacin A complex*	White powder	Methanol, DMF	80
Barium- gatifloxacin complex	Yellowish-white powder	Methanol and DMSO	82
Copper (II) - gatifloxacin complex	Greenish-blue powder	Water	75
Zinc - gatifloxacin complex	White powder	DMSO	80
Iron (II) - gatifloxacin complex	Brown powder	DMF	75
Magnesium – gatifloxacin B complex*	White	Methanol	82
Lead - gatifloxacin complex	White powder	Water	85
Silver- gatifloxacin complex	Reddish-brown	Water, methanol	72

*Magnesium-gatifloxacin A and magnesium-gatifloxacin B complexes formed by interaction with magnesium carbonate- $MgCO_3$ and magnesium sulfate- $MgSO_4.7H_2O$, respectively.

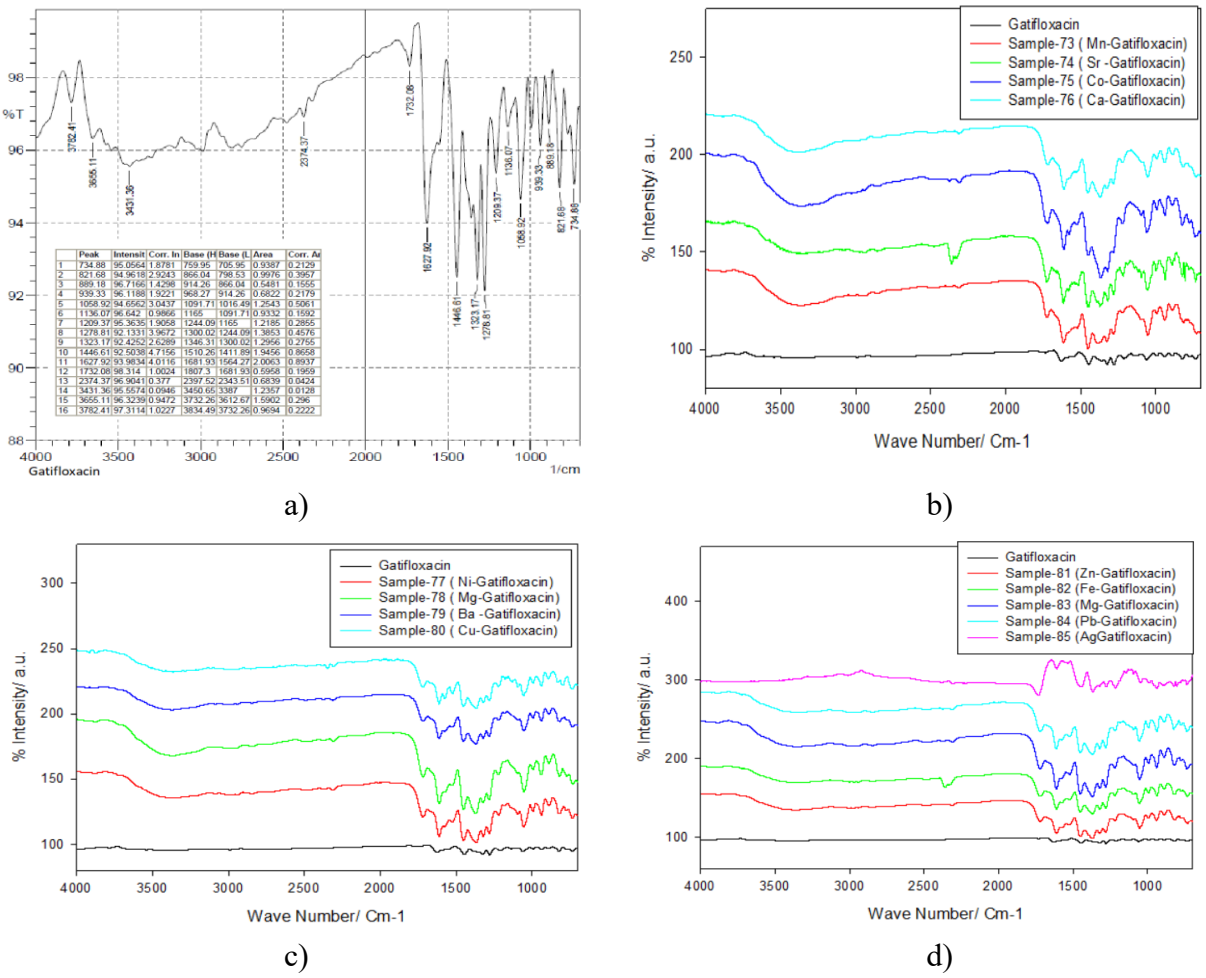


Figure 2. (a) FT-IR spectra of gatifloxacin; (b) Overlaying FT-IR spectra of gatifloxacin and complexes of Mn, Sr, Co and Ca; (c) Overlaying FT-IR spectra of gatifloxacin and complexes of Ni, Mg, Ba and Cu; (d) Overlaying FT-IR spectra of gatifloxacin and complexes of Zn, Fe, Mg, Pb and Ag.

Table 3. Characteristic FT-IR spectral data (cm^{-1}) for the synthesized complexes

Sample	Carboxylic /C=O stretch (Region I)	Quinolone /aromatic C=O (Region II)	M–O /M–N vibrations. 500-600 (New bands)
Manganese- gatifloxacin complex	1724.96	1625.66	Yes
Strontium- gatifloxacin complex	1726.29	1620.21	Yes
Cobalt- gatifloxacin complex	1720.5	1612.49	Yes
Calcium - gatifloxacin complex	1718.56, 1718.58	1622.49	Yes
Nickel- gatifloxacin complex	1716.66	1612.49	Yes
Magnesium- gatifloxacin A complex	1718.58	1610.56	Yes
Barium- gatifloxacin complex	1716.58	1610.56	Yes
Copper (II) - gatifloxacin complex	1716.86	1612.49	Yes
Zinc – gatifloxacin complex	1720.5	1610.56	Yes
Iron (II) - gatifloxacin complex	1720.5	1612.49	Yes
Magnesium - gatifloxacin B complex	1718.5	1610.56	Yes
Lead - gatifloxacin complex	1718.98	1612.49	Yes
Silver- gatifloxacin complex	1735.17	1609.62	Yes

The most significant evidence for complex formation is the shifting of key functional group vibrations associated with the ligand's potential donor atoms.

a) Carboxylate coordination: The stretching vibration for the carboxylic acid (C=O) group, which typically appears as a strong band above 1700 cm^{-1} in the free ligand, is observed in the range of approximately 1716-1727 cm^{-1} for most of the complexes. This shift, while present, is less pronounced than in some classical complexes, suggesting a specific coordination environment or hydrogen bonding network that influences the carbonyl frequency. A notable exception is the silver- gatifloxacin complex, which shows a distinct band at 1735 cm^{-1}, potentially indicating a different protonation state or weaker interaction with the metal center.

b) Ketone carbonyl coordination: A more consistent indication of possible coordination is the behavior of the quinolone ketone carbonyl band. In the spectra of the complexes, this vibration, which is expected near 1625 cm^{-1} for the free ligand, is systematically shifted to lower wavenumbers, appearing in the range of ~1610 - 1622 cm^{-1} across all complexes. This consistent redshift supports the possible involvement of the keto oxygen atom in coordination to the metal center.

c) Metal-ligand bond formation: The appearance of new, weak-to-medium intensity bands in the low-frequency region of 500-600 cm^{-1} (explicitly noted for the manganese-gatifloxacin complex) is a characteristic feature frequently associated with metal complexation. These bands are absent in the free ligand and are assigned to ν(M–O) and ν(M–N) vibrational modes, supporting the formation of coordinate covalent bonds between the metal ions and the ligand donor atoms. While not explicitly listed in every sample's peak table, the consistent shifts in the carbonyl regions imply the presence of these metal-ligand vibrations across the series.

The collective spectroscopic observations suggest with a possible bidentate coordination mode involving the carboxylate and keto oxygen atoms of gatifloxacin. However, without complementary techniques such as elemental analysis or magnetic susceptibility measurements, the exact coordination geometry (e.g., octahedral vs. tetrahedral) remains speculative. The structures in Fig. 3 are therefore proposed as plausible models rather than confirmed assignments.

The proposed structure of the metal–gatifloxacin complex shows bidentate coordination *via* the carboxylate and keto oxygen atoms, forming a six-membered chelate ring. M represents divalent metal ions. A suggested coordination structure for the gatifloxacin-metal complexes, shown in Fig. 3, is based on the shifts seen in the FT-IR spectra and is supported by previous research on fluoroquinolone-metal complexes.

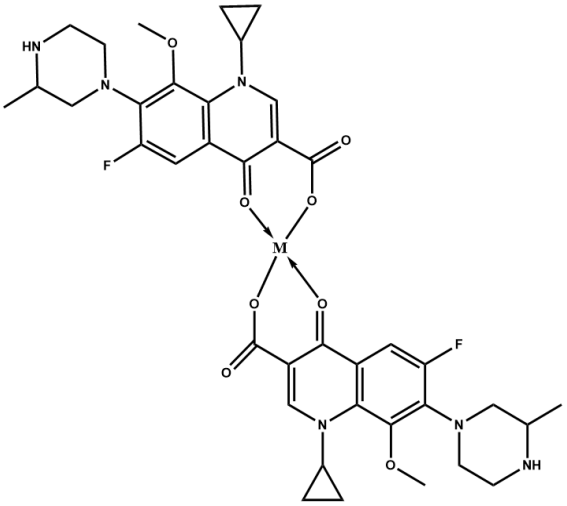


Figure 3. Plausible coordination model based on FT-IR, DSC, and PXRD observations together with previously reported fluoroquinolone coordination patterns.

By connecting through the oxygen atoms of the keto group at position 4 and the carboxylate group at position 3 of the quinolone ring, the ligand acts as a bidentate chelating agent. A stable six-membered chelate ring is formed with the metal ion because of this interaction. The complexes are anticipated to exhibit a proposed coordination mode, which is contingent upon the characteristics of the metal ion, and may necessitate further coordination with solvent molecules such as water. This suggested structure is consistent with fluoroquinolone antibiotic coordination modalities that have been previously reported.

The most plausible coordination mode involves the oxygen atoms of the carboxylate and the pyridone ketone group, forming a stable six-membered chelate ring with the metal center. This binding mode is consistent with the well-established coordination chemistry of fluoroquinolone antibiotics. The spectral variations observed across the formed complexes likely reflect subtle differences in the metal center, coordination geometry, or counterions, which can influence the precise vibrational frequencies. Apart from gatifloxacin, several fluoroquinolone antibiotics have been shown to act as bidentate ligands *via* the carboxylate ($–COO^–$) and keto (C=O) oxygen atoms. For instance, when norfloxacin forms stable chelate complexes with transition metal ions like Cu(II), Ni(II), and Zn(II), coordination occurs through the

3-carboxylate and 4-keto groups, resulting in the creation of six-membered chelate rings [10, 11]. Similarly, the FT-IR spectrum shifts, and the X-ray crystallographic investigations showed that levofloxacin coordinates with metal ions in a bidentate manner, indicating the involvement of the pyridone oxygen and carboxylate moiety [31, 32]. Similar coordination behavior is also shown in gemifloxacin, which forms stable metal complexes with enhanced biological activity when the ligand interacts with the quinolone core's oxygen donor atoms [29]. The coordination mode suggested for gatifloxacin in the current work is supported by these combined results, which demonstrate that bidentate coordination *via* keto-carboxylate groups is a distinguishing feature of fluoroquinolone drugs.

Differential scanning calorimetry (DSC) analysis

DSC thermograms of the pure drugs showed sharp endothermic peaks corresponding to their melting points, reflecting stability. Gatifloxacin exhibited a sharp melting transition around 190.13 °C. Based on the expanded DSC analysis of gatifloxacin-metal complexes, the Sr–gatifloxacin complex remains the most thermally stable one, exhibiting a significant endothermic event at 240.34 °C which is likely associated with melting or decomposition. In comparison, the Co–gatifloxacin complex shows a single thermal event at 138.19 °C, suggesting phase transition or dehydration. The Mn–gatifloxacin complex displays two mid-temperature events at 129.65 °C and 181.68 °C, which may correspond to successive dehydration steps or structural rearrangements. The Mg–gatifloxacin complex, with low-temperature events at 51.25 °C and 112.16 °C, appears to be the least stable, likely related to hydration or weaker metal coordination. Notably, the Ba–gatifloxacin complex shows no distinct thermal events up to 300 °C, indicating high thermal stability, possibly even higher than that of the Sr complex. These variations highlight the significant role of the metal ion in modulating the thermal behavior of gatifloxacin complexes, with larger metal ions like Sr^{2+} and Ba^{2+} conferring higher stability compared to transition metals like Mn^{2+} and Co^{2+}, or the smaller Mg^{2+} ion (Fig. 4). These variations in thermal behavior reflect the influence of the metal ion on the complex's crystallinity, stability, and hydration state, the Sr-complex being the most robust under thermal stress.

X-ray diffraction studies

The study of crystal structures of drug-metal complexes provides valuable insight into their stability, binding orientation, and physicochemical properties.

Metal ions often modulate the pharmacological activity of drugs through coordination, leading to altered solubility, crystallinity, and bioavailability. PXRD is one of the most powerful analytical techniques for characterizing crystalline phases, as it reveals both the molecular arrangement and the degree of order/disorder in solid-state materials. In this investigation, the crystalline structures of gatifloxacin-metal complexes were investigated using PXRD techniques.

- *Gatifloxacin and its Mn(II) complex*

The PXRD spectra for both pure gatifloxacin and its Mn(II) complex were obtained within a 2θ range of 5–70°. The pure gatifloxacin (form-Y) displayed distinct diffraction peaks at 2θ values of 5.1, 6.2, 7.8, 9.1, 9.8, 10.4, 12.9, 13.6, 14.3, 17.3, 17.7, 18.3, 18.8, 19.6, 20.7, 21.1, 23.4, 23.9, 24.4, 25.4, 25.9, and 26.6 ± 0.2°, which align with the previously documented crystalline data for gatifloxacin form-Y [33].

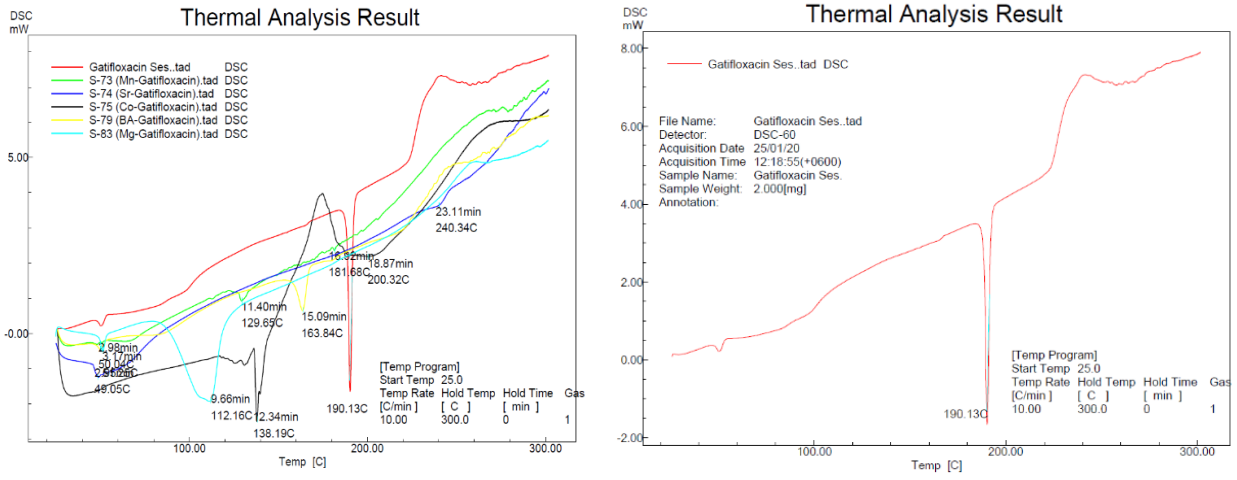


Figure 4. DSC spectra of different drug-metal complexes and gatifloxacin.

Upon interaction with $MnSO_4 \cdot H_2O$ (PDF Card No. 00-003-0370), the resulting diffractogram revealed additional peaks, alongside a decrease in intensity, broadening of peaks, and an increase in background noise when compared to pure gatifloxacin (https://trea.com/information/crystalline-forms-of-gatifloxacin/patentgrant/7a18a46e-c8f3-45ca-aea1-d4dccf0bdec6, accessed on 25th August 2025). These findings may suggest a partial disruption of the original crystalline lattice and the emergence of mixed amorphous–crystalline domains. Variations in peak position, intensity, and the appearance or disappearance of peaks in relation to the parent materials further imply the development of a modified crystalline phase or a change in solid-state organization following interaction with Mn(II) (Fig. 5).

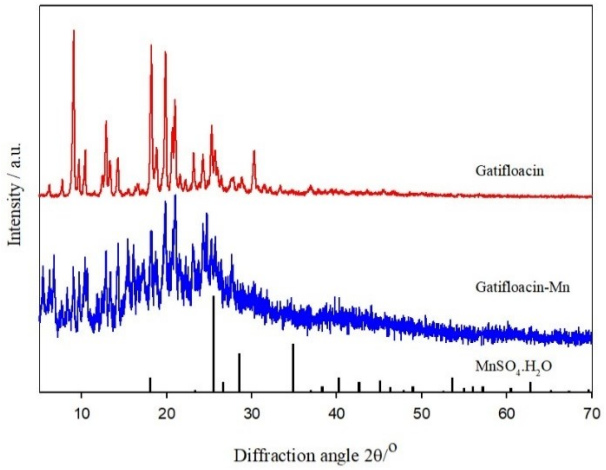


Figure 5. PXRD pattern of gatifloxacin-Mn complex.

- *Gatifloxacin and its Ba(II) complex*

Fig. 6 shows the PXRD pattern of (i) gatifloxacin and (ii) the gatifloxacin-Ba complex. The PXRD pattern of the gatifloxacin-Ba complex reveals a distinct alteration compared to pure gatifloxacin. The crystalline form of gatifloxacin (form-Y) has PXRD-peaks at 5.1, 6.2, 7.8, 9.1, 9.8, 10.4, 12.9, 13.6, 14.3, 17.3, 17.7, 18.3, 18.8, 19.6, 20.7, 21.1, 23.4, 23.9, 24.4, 25.4, 25.9, and 26.6 ± 0.2 degrees, which are consistent with experimental data (Table 4). (https://trea.com/information/crystalline-forms-of-gatifloxacin/patentgrant/7a18a46e-c8f3-45ca-aea1-d4dccf0bdec6, Accessed on 25th August 2025).

The diffraction peaks matched with ICDD PDF number 00-005-0448, corresponding to barite ($BaSO_4$) with an orthorhombic crystal structure. The PXRD pattern suggests the formation of a modified crystalline phase associated with the presence of Ba(II). These observations are consistent with possible structural modification following interaction between Ba(II) and gatifloxacin.

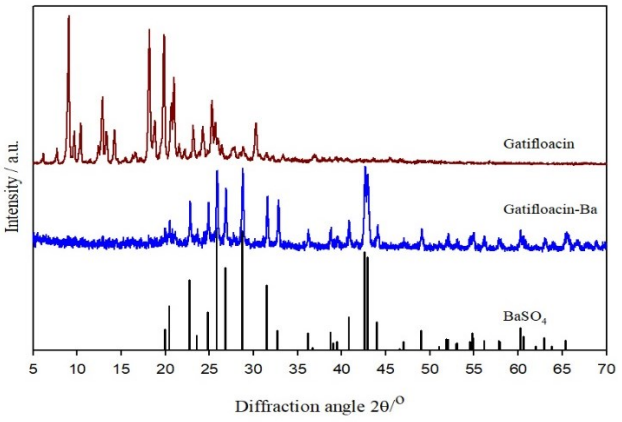
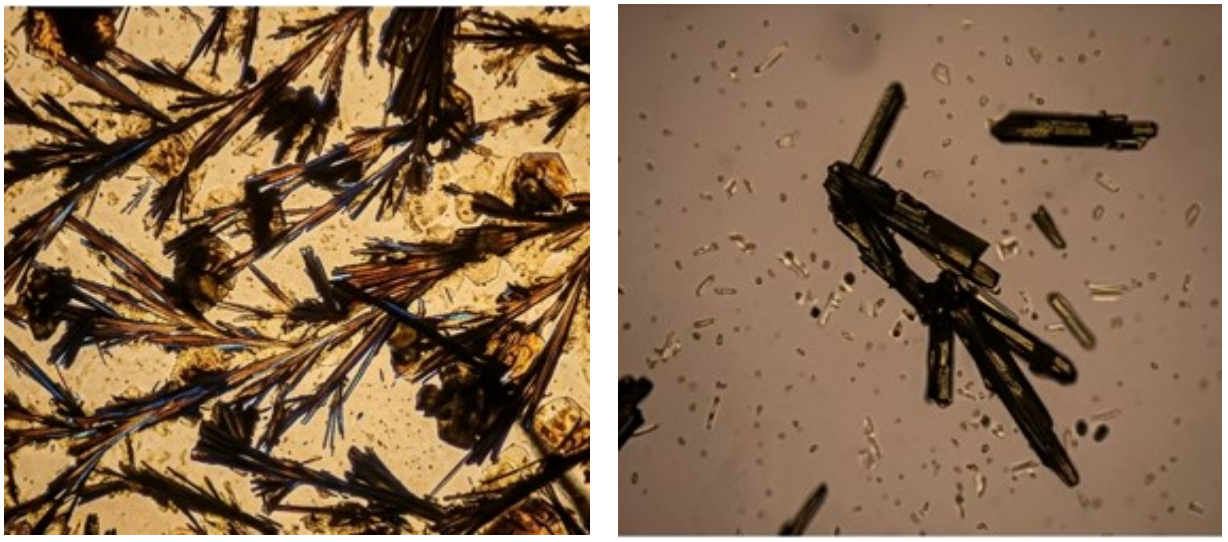


Figure 6. PXRD pattern of gatifloxacin-Ba complex.

Table 4. Characteristic 2θ peaks, observed crystalline phases, and structural interpretations for each drug-metal complex

Drug/ complex	Characteristic 2θ peaks (°)	Observed phase/structure
Gatifloxacin	5.1, 6.2, 7.8, 9.1, 9.8, 10.4, 12.9, 13.6, 14.3, 17.3–26.6	Crystalline (form-Y, consistent with literature)
Gatifloxacin-Mn	6.2, 7.9, 10.2, 13.8, 17.5, 18.7, 20.5, 23.5, 25.7	Mixed amorphous–crystalline (Mn incorporated, disrupted lattice)
Gatifloxacin-Ba	5.2, 7.0, 9.2, 14.0, 18.5, 21.0, 23.8, 26.5	Orthorhombic $BaSO_4$ phase (barite-like)

Partial loss of long-range order and presence of both crystalline and amorphous domains are indicated by the observed rise in background noise and the broadening of peaks in the complexes' diffractograms. This behavior is commonly observed in pharmaceutical solid dispersions and drug-metal coordination systems [34, 35]. It is significant that PXRD was only used as a qualitative tool for phase identification and crystallinity assessment. Since single-crystal X-ray diffraction data were not gathered, no thorough crystal structure solution or refinement was attempted. Pharmaceutical and coordination chemistry research are two areas where PXRD is widely used to confirm phase purity, lattice changes, and solid-state transitions [36-38].



(A) (B)

Figure 7. Trinocular microscopic images illustrating the crystal morphology of the synthesized metal–drug complexes. Distinct needle- and rod-shaped crystalline aggregates are observed for (A) Gatifloxacin–Mn(II) and (B) Gatifloxacin–Ba(II), indicating differences in crystal habit following complex formation.

Crystal habit observations

Microscopic examination under a trinocular microscope revealed that the synthesized complexes formed well-defined crystalline aggregates (Fig. 7).

Representative images of gatifloxacin-Mn, and gatifloxacin-Ba showed differences in morphology compared to the parent drugs. These morphological variations suggested significant interaction between drug molecules and metal ions, thereby justifying subsequent PXRD investigations. This analysis highlighted significant modifications in the crystalline framework of the investigated drugs upon metal incorporation. Gatifloxacin-Mn displayed a mixed amorphous–crystalline phase, whereas gatifloxacin–Ba exhibited a highly ordered orthorhombic lattice. These results are consistent with earlier studies that demonstrated the ability of divalent cations to disrupt or stabilize fluoroquinolone crystal lattices depending on their ionic radius and coordination geometry [39].

Antimicrobial activity

The antimicrobial activity of the synthesized gatifloxacin-metal complexes was evaluated against Gram-positive and Gram-negative pathogenic bacterial strains using the disc diffusion method (30 µg/disc). The inhibition zones were compared with a standard gatifloxacin disc (30 µg/disc). The results are summarized in Table 5.

Most complexes exhibited significant inhibitory effects against Gram-positive organisms, including *Streptococcus β-hemolyticus*, *Staphylococcus aureus*, *S. pyogenes*, *Bacillus subtilis* and *B. tropicus*. The Mn(II) complex demonstrated the highest activity, showing inhibition zones of 47.67 ± 0.67 mm and 41.0 ± 0.58 mm against *S. β-hemolyticus* and *S. pyogenes*, respectively. Similarly, Sr(II) and Co(II) complexes exhibited strong activity, particularly against *S. aureus* (46.0 ± 0.58 mm) and *B. tropicus* (50.0 ± 0.58 mm), surpassing the standard ciprofloxacin zone (39–42 mm). The Cu(II) complex also displayed broad-spectrum efficacy with inhibition zones up to 44.67 ± 0.33 mm. In contrast, Ni(II) and Fe(II) complexes showed lower activity, which may be attributed to reduced solubility or steric hindrance around the metal center that limits diffusion through the agar medium. The results in Table 6 suggest that coordination with transition metals may enhance the antimicrobial efficiency of gatifloxacin through chelation, facilitating drug penetration into bacterial membranes [40, 41]. Mn, Sr, Co, Cu, Pb, and Ag complexes of gatifloxacin show comparable or moderate to relatively strong activity to gatifloxacin. The pronounced activity of Cu(II), Pb(II), and Ag(I) complexes may arise from synergistic effects between gatifloxacin and metal ions, where the metal centers stabilize the quinolone's enolate oxygen, enhancing bacterial DNA-gyrase inhibition.

Silver's well-known antimicrobial effect related to Ag^+ ion release further contributes to its relatively higher activity [42]. Cu, Mg, Pb, Ag, and Sr complexes show higher zone of inhibition against standard gatifloxacin. Gatifloxacin shows consistent zones of ~39–46 mm, serving as an effective reference. Several complexes, notably Cu, Pb, Ag, Mn, and Sr, exhibit equal or relatively higher activity, suggesting enhanced chelation-based antimicrobial potential. Chelation-related effects on physicochemical properties may contribute to the observed differences in antibacterial activity. Some (e.g., Fe, Zn, Ni) show decreased activity, possibly attributed to low solubility or poor complexation.

Table 5. Antimicrobial screening of complexes formed by gatifloxacin and metal interactions against Gram-positive and Gram-negative pathogenic bacteria

-	Inhibition zones (mm)										
	Gram-positive pathogenic bacteria					Gram-negative pathogenic bacteria					
	(A)	*(B)*	*(C)*	*(D)*	*(E)*	*(F)*	*(G)*	*(H)*	*(I)*	*(J)*	*(K)*
Gat-30	37.33± 0.33	39.0 ± 1.0	41.67± 0.88	38.0 ± 0.58	39.67± 1.2	41.33 ±0.33	46.0± 0.58	40.67± 0.67	39.67± 0.67	39.0±0 .58	42.67± 1.33
Manganese-gatifloxacin complex	47.67± 0.67	24.67 ± 0.33	41.0±0. 58	21.33 ± 1.33	22.0± 1.0	36.67 ±0.33	34.33 ±1.33	12.33 ± 0.30	12.33 ±1.10	25.67± 0.33	28.0± 1.0
Strontium-gatifloxacin complex	41.67± 1.2	46.0 ± 0.58	44.33± 0.88	25.33 ± 1.2	39.67± 1.2	46.33 ±0.33	38.0± 1.0	44.0±1 .0	13.33 ± 0.23	28.67± 0.88	42.33± 0.33
Cobalt-gatifloxacin complex	45.67± 1.33	26.0 ± 1.0	45.0±0. 58	20.67 ± 0.33	21.67± 1.2	50.0± 0.58	41.0± 0.58	45.0±1 .0	13.33 ± 1.12	35.67± 0.88	41.0 ± 0.0
Calcium - gatifloxacin complex	43.33± 1.2	11.33 ± 1.33	28.33± 0.88	39.0 ± 0.58	24.67± 0.33	43.33 ±0.33	42.67 ±0.88	37.0±1 .0	11.33 ± 1.22	12.3 ± 1.33	45.0 ± 1.0
Nickel-gatifloxacin complex	44.33± 1.2	37.0 ± 0.58	12.67± 0.88	38.0 ± 1.15	28.0± 1.15	32.33 ±0.88	38.0± 0.58	36.67± 0.67	18.0±0 .58	10.23 ± 0.53	39.0 ± 1.0
Magnesium-gatifloxacin A complex	47.33± 0.88	15.33 ± 1.2	27.0±1. 0	39.0 ± 1.0	28.0± 1.15	14.33 ±0.67	42.67 ±0.67	45.33± 0.33	10.33 ± 0.3	24.33± 0.88	43.33± 0.33
Barium-gatifloxacin complex	42.67± 0.33	34.67 ± 0.88	43.67± 1.2	17.33 ± 0.33	32.0± 0.0	29.0 ±1.0	41.0± 0.58	42.0±0 .58	14.33 ± 0.35	38.0±0 .58	34.67 ± 1.2
Copper (II) - gatifloxacin complex	43.33± 0.67	41.67 ± 0.88	44.67± 0.33	28.0 ± 0.58	42.33± 0.88	43.33 ±1.2	10.33 ±0.88	10.33 ± 1.33	19.33± 0.33	38.0±0 .0	45.67± 0.88
Zinc - gatifloxacin complex	43.0± 0.0	19.0 ± 0.58	43.33± 0.88	26.0 ± 0.58	24.33± 1.33	29.67 ±0.33	29.0± 0.58	15.67± 0.67	15.33± 0.33	32.67± 1.33	26.0 ± 0.58
Iron (II) - gatifloxacin complex	41.33± 0.33	16.67 ± 1.2	10.33 ± 1.30	26.67 ± 0.67	25.33± 0.88	17.67 ±1.2	36.0± 1.0	10.33 ± 1.33	31.0± 0.58	31.33± 0.67	45.0 ± 0.0
Magnesium – gatifloxacin B complex	44.67± 1.33	34.33 ± 0.67	17.33± 0.88	30.0 ± 0.58	27.33± 0.88	37.33 ±1.2	42.0± 1.0	10.33 ± 1.33	38.67± 0.67	37.67± 0.88	47.33± 0.67
Lead - gatifloxacin complex	46.0±0. 58	33.33 ± 0.88	17.33± 0.88	30.0 ± 1.15	36.67± 0.67	34.67 ±0.88	39.33 ±0.88	10.33 ± 1.33	33.33± 0.33	24.67± 1.2	48.0 ± 1.0
Silver-gatifloxacin complex	37.67± 0.67	44.0 ± 0.58	12.33 ± 1.23	24.0 ± 0.58	33.67± 0.33	42.33 ±0.67	42.67± 1.2	10.33 ± 1.33	43.33± 0.33	47.33± 0.33	24.67 ± 1.2

Values are presented as mean inhibition zone diameters ((n=3). In each sample 30 μg/disc complex substance was applied and Gat-30 was the standard disc of gatifloxacin 30 µg/disc.

Table 6. Antimicrobial activity observed against Gram-positive bacteria of gatifloxacin-metal complexes.

Metal complex	Observations	Remarks
Manganese- gatifloxacin complex	Appreciable inhibition zones, especially *vs Streptococcus β-hemolyticus* (47.67 mm) and *S. pyogenes* (41.0 mm)	Mn complex shows broader inhibition profile.
Strontium- gatifloxacin complex	High activity, notably *vs S. aureus* (46 mm) and *Bacillus tropicus* (39.67 mm)	Sr enhances gatifloxacin's efficacy.
Cobalt- gatifloxacin complex	Strong effect on *Streptococcus β-hemolyticus (*45.67 mm), *Streptococcus pyogenes* (45 mm)	Cobalt complex exhibits good potency.
Calcium - gatifloxacin complex	Moderate to strong inhibition on *S. β-hemolyticus* (43.33 mm) and *Bacillus subtilis* (39 mm)	Calcium complex maintains good activity.
Nickel- gatifloxacin complex	High activity against *Streptococcus β-hemolyticus* (44.33 mm); lowest against *S. pyogenes* (12.67 mm)	Nickel reduces activity against most Gram-positive bacteria.
Magnesium- gatifloxacin A complex	Strong inhibition *vs S. β-hemolyticus* (47.33 mm), *Bacillus subtilis* (39 mm)	Magnesium complex retains broad efficacy.
Barium- gatifloxacin complex	Good inhibition, esp. *vs S. pyogenes* (43.67 mm)	Barium complex is active.
Copper (II) - gatifloxacin complex	Strong zones across many strains, e.g., *S. pyogenes* (44.67 mm)	Copper complex shows comperatively larger zone of inhibition.
Zinc - gatifloxacin complex	Good inhibition vs *S. β-hemolyticus* (47.33 mm), *Streptococcus pyogenes* (43 mm)	Zinc complex moderately effective.
Iron (II) - gatifloxacin complex	Weak to moderate, no inhibition against *S. pyogenes*.	Iron complex reduces drug efficacy.
Magnesium - gatifloxacin B complex	Good inhibition vs *S. β-hemolyticus* (44 mm)	Good Gram-positive performance.
Lead - gatifloxacin complex	Appreciable inhibition zones, *S. β-hemolyticus* (46 mm)	Lead complex surprisingly effective.
Silver- gatifloxacin complex	Very good activity against *S. aureus* (44 mm)	Silver complex shows enhanced activity.

The majority of the tested complexes demonstrated moderate to strong activity against Gram-negative bacteria (Table 7).

Table 7. Antimicrobial activity of gatifloxacin-metal complexes against Gram-negative bacteria

Metal complex	Observations	Remarks
Manganese- gatifloxacin complex	Low activity (12–36 mm range).	Less effective.
Strontium- gatifloxacin complex	Strong zones *vs Shigella dysenteriae (46.33 mm) and E. coli* (44 mm).	Dual-spectrum activity.
Cobalt- gatifloxacin complex	Strong zones *vs Shigella dysenteriae (50 mm) and E. coli* (45 mm).	Effective for both Gram classes.
Calcium - gatifloxacin complex	Strong against *S. dysenteriae* (43.33 mm).	Retains efficacy vs Gram-negative.
Nickel- gatifloxacin complex	Weak *vs S. abony* (18 mm).	Reduced effect on Gram-negative.
Magnesium- gatifloxacin A complex	Strong *vs E. coli* (45.33 mm) and *S. typhi* (43.33 mm).	Broader inhibition profile.
Barium- gatifloxacin complex	Active *vs E. coli* (42 mm).	Moderate overall.
Copper (II) - gatifloxacin complex	Strong *vs P. aeruginosa* (38 mm) and *S. typhi* (45.67 mm).	Among the most potent.
Zinc - gatifloxacin complex	Low activity (15–32 mm range).	Less effective.

Metal complex	Observations	Remarks
Iron (II) - gatifloxacin complex	Moderate *vs Salmonella typhi* (45 mm). Weak to moderate; inactive *vs* some strains.	Interferes with antibacterial action in most cases.
Magnesium - gatifloxacin B complex	High *vs S. typhi* (47.33 mm).	Broader Gram-negative inhibitor.
Lead - gatifloxacin complex	Strong *vs S. typhi* (48 mm).	Enhanced activity.
Silver- gatifloxacin complex	Very active *vs Salmonella abony* (43.33 mm) and *Pseudomonas aeruginosa* (47.33 mm).	Relatively strong activity, likely attributed to synergistic Ag^+ antimicrobial property.

The present study reveals that the antimicrobial activity of gatifloxacin is significantly influenced by metal complexation. Complexes with Cu(II), Pb(II), Ag(I), and Mn(II) ions exhibited relatively broader inhibitory activity within the tested panel. Meanwhile, Fe(II) and Ni(II) complexes were less effective, suggesting possible antagonistic interactions or stability issues. These findings suggest that such complexes may serve as promising candidates for further *in vivo* pharmacological studies and potential development of next-generation metal–antibiotic formulations [43, 44].

Statistical analysis

Mean inhibition zone diameters (mm) derived from triplicate measurements were used to express antimicrobial activity. The metal complexes and free gatifloxacin were qualitatively compared using the mean values. No inferential statistical analysis was done because of the study's preliminary nature and the small number of triplicates. As a result, antimicrobial efficacy was evaluated using observed variations in inhibition zone widths, a method frequently used in preliminary screening investigations of metal-drug complexes with the goal of detecting structure-activity patterns.

Limitation statement

Since elemental and magnetic tests were not carried out, the structural interpretations mostly relied on FT-IR, DSC, and PXRD evaluations. As such, the coordination mechanisms are to be considered as proposed. Similarly, the antimicrobial data were obtained *via* disc diffusion assays, providing qualitative comparisons; further studies involving MIC, MBC, and more statistical analyses are required to reach definitive conclusions.

CONCLUSION

Gatifloxacin complexes with several transition metal ions, alkaline-earth metal ions and Ag ion were synthesized and comparatively evaluated using FT-IR, DSC, PXRD, and microscopic techniques. Spectroscopic thermal analysis proposed the formation of bidentate metal-ligand complexes with possible coordination environments. The complexes showed larger inhibition zones, particularly Cu(II), Co(II), Pb(II), Ag(I), Sr(II), and Mn(II) derivatives, against tested bacterial strains, supporting further investigation of metal complexation approaches. These findings provide a foundation for further exploration of metal-based fluoroquinolone derivatives in combating multidrug-resistant pathogens. The differences observed in antimicrobial activity could be linked to modifications in physicochemical properties that occur after metal complexation, which may include changes in lipophilicity and interactions with membranes. Additionally, the potential synergistic effects arising from the coordinated metal ions should be acknowledged; however, these mechanisms were not explicitly assessed in this study and necessitate further experimental validation. These findings suggest a potential role of metal complexation in enhancing the activity by preliminary *in vitro* observations. PXRD analysis indicated that the Mn(II) complex displays a combination of amorphous and crystalline phases, while the Ba(II) complex has a stable orthorhombic structure akin to barite. X-ray diffraction demonstrated a degree of lattice disruption and a mixed amorphous–crystalline characteristic for the Mn(II) complex, in contrast to the Ba(II) complex, which resulted in a clearly defined orthorhombic crystalline phase. Overall, this work demonstrates that metal–gatifloxacin complexes represent promising candidates for developing new antimicrobial agents, especially in the context of combating multidrug-resistant pathogens. Future studies focusing on *in vitro* MIC/MBC and *in vivo* pharmacological evaluation, toxicity profiling, and structural optimization could further advance their potential as antimicrobial therapeutics.

Acknowledgement: *The authors gratefully acknowledge the Centre for Advanced Research in Sciences (CARS), University of Dhaka, Bangladesh, and the Laboratory of Pharmaceutical Microbiology, International Islamic University Chittagong, Bangladesh, for providing essential support, resources, and infrastructural facilities necessary for carrying out this research.*

Conflict of interest: *There are no conflicts to declare.*

Financing: *The work was carried out without financing.*

Contributions of authors*: Conception and design, or design of the research; or the acquisition, analysis, or interpretation of data: MAS, MZS, MAR, HAS. Drafting the manuscript or revising it critically for important intellectual content: MAS, MZS, MMM, MAR, HAS. Final approval of the version to be published: MAR. Agreement to be accountable for all aspects of the work in ensuring that questions related to the accuracy or integrity of any part of the work are appropriately investigated and resolved: MAR.*

REFERENCES

1. World Health Organization, Antimicrobial Resistance: A Manual for Developing National Action Plans, World Health Organization, Geneva, 2016, p. 1.
2. C. L. Ventola, *Pharm. Ther.*, **40**, 277 (2015).
3. G. D. Wright, *Nat. Prod. Rep.*, **34**, 694 (2017). DOI: 10.1039/C7NP00019G
4. Z. H. Chohan, C. T. Supuran, A. Scozzafava, *J. Enzyme Inhib. Med. Chem.*, **20**, 303 (2005). DOI: 10.1080/14756360310001624948
5. C. A. Akinremi, J. A. Obaleye, S. A. Amolegbe, J. F. Adediji, M. O. Bamigboye, *Int. J. Med. Biomed. Res.*, **1**, 24 (2012). DOI: 10.14194/ijmbr.115
6. V. E. Anderson N. Osheroff, *Curr. Pharm. Des.*, **7**, 337 (2001). DOI: 10.2174/1381612013398013
7. P. C. Appelbaum P. A. Hunter, *Int. J. Antimicrob. Agents*, **16**, 5 (2000). DOI: 10.1016/S0924-8579(00)00192-8
8. J. Anane, E. Owusu, G. Rivera,
9. D. Bandyopadhyay, *Int. J. Mol. Sci.*, **25**, 2263 (2024). DOI: 10.3390/ijms25042263
10. M. Ferreira, P. Gameiro, *Microorganisms*, **9**, 1506 (2021). DOI: 10.3390/microorganisms9071506
11. S. A. Sadeek, W. H. El-Shwiniy, *J. Mol. Struct.*, **977**, 243 (2010). DOI: 10.1016/j. molstruc.2010.05.041
12. I. Turel, *Coord. Chem. Rev.*, **232**, 27 (2002). DOI: 10.1016/S0010-8545(02)00027-9
13. A. Solanki, M. H. Sadhu, S. B. Kumar, P. Mitra, *J. Mol. Struct.*, **1076**, 475 (2014). DOI: 10.1016/j.molstruc.2014.07.082
14. N. Chavain, C. Biot, *Curr. Med. Chem.*, **17**, 2729 (2010). DOI: 10.2174/092986710791859306
15. N. Sultana, A. Naz, M. S. Arayne, M. A. Mesaik, *J. Mol. Struct.*, **969**, 17 (2010). DOI: 10.1016/j.molstruc.2010.01.036
16. Z. Q. Li, F. J. Wu, Y. Gong, C. W. Hu, Y. H. Zhang, M. Y. Gan, *Chin. J. Chem.*, **25**, 1809 (2007). DOI: 10.1002/cjoc.200790334
17. N. Dave, H. Bhatt, *Asian J. Chem. Sci.*, **10**, 98 (2021). DOI: 10.9734/ajocs/2021/v10i419109
18. H. A. Jawad, I. O. Alfatlawi, E. A. Alyasiry, S. Kadhim, *Afr. J. Biomed. Res.*, **28** (2025). DOI: 10.53555/AJBR.v28i3S.7766
19. M. K. Kumari, Spectroscopic Techniques in Pharmaceutical Analysis, in Pharmaceutical Analysis: A Comprehensive Guide, 2025, p. 154.
20. D. Dorniani, M. Z. Hussein, A. U. Kura, S. Fakurazi, A. H. Shaari, Z. Ahmad, *Int. J. Mol. Sci.*, **14**, 23639 (2013).
21. M. Ahmad, Ziaullah, N. U. Islam, M. Ali, S. Khan, *Chem. Afr.*, **7**, 4139 (2024). DOI: 10.1007/s42250-024-01059-1
22. P. Kumari, V. Lather, S. Khatri, P. Ahlawat, H. Sehrawat, S. P. Khatkar, V. B. Taxak, R. Kumar, *RSC Adv.*, **12**, 35827 (2022). DOI: 10.1039/D2RA05796D
23. S. P. Fricker, *Dalton Trans.*, **43**, 4903 (2007). DOI: 10.1039/b705551j.
24. C. L. Domínguez-Delgado, E. Fuentes-Prado, J. J. Escobar-Chávez, G. Vidal-Romero, I. M. Rodríguez-Cruz, R. Díaz-Torres, Chitosan and Pluronic® F-127*:* Pharmaceutical Applications, in: Encyclopedia of Biomedical Polymers and Polymeric Biomaterials, **11**, 1513 (2016). DOI: 10.1081/E-EBPP-120050057
25. J. M. Blondeau, *Surv. Ophthalmol.*, **49**, S73 (2004). DOI: 10.1016/j.survophthal.2004.01.005
26. S. Khatri, M. Kumar, R. Kumar, *Ann. Rom. Soc. Cell Biol.*, **25**, 396 (2021).
27. A. M. Shalash, H. I. Abu Ali, *Chem. Cent. J.*, **11**, 40 (2017). DOI: 10.1186/s13065-017-0268-2.
28. M. Z. Sultan, M. A. Sayeed, M. M. Masud, M. A. Rashid, *Indian J. Chem.*, **64**, 1089 (2025). DOI: 10.56042/ijc.v64i11.23368
29. S. Inouye, T. Takizawa, H. Yamaguchi, *J. Antimicrob. Chemother.*, **47**, 565 (2001). DOI: 10.1093/jac/47.5.565
30. N. E. El-Gamel, M. A. Zayed, *Spectrochim. Acta A Mol. Biomol. Spectrosc.*, **82**, 414 (2011). DOI: 10.1016/j.saa.2011.07.072
31. T. A. Hajam, H. Saleem, M. Syed Ali Padusha, K. K. Mohammed Ameen, *Polycycl. Aromat. Compd.*, **42**, 6662 (2022).
32. W. A. Zordok, *Spectrochim. Acta A Mol. Biomol. Spectrosc.*, **129**, 519 (2014).
33. M. S. Refat, *Spectrochim. Acta A Mol. Biomol. Spectrosc.*, **68**(5), 1393 (2007). DOI: 10.1016/j.saa.2006.12.078
34. S. S. Patil *et al*., Crystalline Forms of Gatifloxacin, US Pat., US20060270705A1 (2006).
35. H. G. Brittain, *Profiles Drug Subst., Excipients Relat. Methodol.*, **30**, 271 (2003). DOI: 10.1016/S0099-5428(03)30010-3
36. B. C. Hancock, G. Zografi, *J. Pharm. Sci.*, **86**, 1 (1997). DOI: 10.1021/js9601896

37. S. Gates-Rector, T. Blanton, *Powder Diffr.*, **34**, 352 (2019). DOI: 10.1017/S0885715619000812
38. B. D. Cullity, S. R. Stock, Elements of X-Ray Diffraction, 3rd edn., Prentice Hall, 2001.
39. P. Khadka, J. Ro, H. Kim, I. Kim, J. T. Kim, H. Kim *et al.*, *Asian J. Pharm. Sci.*, **9**, 304 (2014). DOI: 10.1016/j.ajps.2014.05.005
40. P. J. Sadler, *J. Inorg. Biochem.*, **67**, 4 (1997).
41. S. Khabnadideh, R. Mohamadi, A. Farrothroz, *Bioorg. Med. Chem.*, **13**(17), 2863 (2003).
42. A. N. Mustapha, N. P. Ndahi, B. B. Paul, M. B. Fugu, *J. Chem. Pharm. Res.*, **6**, 588 (2014).
43. N. Raman, A. Kulandaisamy, C. Thangaraja, P. Manisankar, S. Viswanathan, C. Vedhi, *Transition Met. Chem.*, **29**, 129 (2004). DOI: 10.1023/B:TMCH.0000019409.50574.0a
44. A. Rusu, G. Hancu, S. Imre, *Adv. Pharm. Bull.*, **8**, 181 (2018). DOI: 10.15171/apb.2018.022.
45. K. Ajay, *Int. J. Life Sci.*, **6**, 446 (2018).

Bulgarian Chemical Communications, Volume 58, Issue 4 (pp. 476-481) 2026 *DOI: 10.34049/bcc.58.4.5749*

Advancements in polylactic acid (PLA) biocomposites: a review on reinforcement, additive manufacturing, and prospects for a sustainable future

V. Dinesh Kumar[1*], P. Sammaiah[2], V. B. Hemadri[3]

[1] *Department of Mechanical Engineering, SR University, Warangal, Telengana, India*
[2]*Center for Materials and Manufacturing, Department of Mechanical Engineering, SR University, Warangal, Telengana, India*
[3]*Department of Mechanical Engineering, Dayananda Sagar University, Bengaluru, Karnataka, India*

Received: February 03, 2026; Revised: June 06, 2026

The environmental threat caused by non-biodegradable plastic wastes necessitates focusing on sustainable material alternatives. Polylactic acid (PLA), also known as polylactide, is a thermoplastic aliphatic polyester produced from renewable feedstocks such as corn starch, sugarcane, or other carbohydrate-rich biomass resources. Owing to its biodegradability, biocompatibility, mechanical strength, and low environmental impact, PLA has emerged as one of the most promising alternatives to conventional petroleum-derived polymers. It can be synthesized by two primary approaches: direct polycondensation of lactic acid monomers and ring-opening polymerization of cyclic lactide intermediates. However, the limitations of neat PLA including brittleness, and low thermal resistance hinder its widespread industrial application. These limitations can be addressed by infusing appropriate functional and natural fibers to PLA. The incorporation of such fibers and transforming them into complex components can be effectively achieved by a conventional additive manufacturing (AM) approach, primarily fused deposition modeling (FDM). This review paper outlines the recent research progress on PLA infused with biocomposites, with a focus on the influence of various natural fibers and nanofillers on its mechanical, thermal, and functional features. The correlation between the process parameters of FDM and the performance features of the printed parts is discussed. Furthermore, the paper explores the application, challenges, and process optimization of the hybrid composites.

Keywords: Non-biodegradable, biodegradable, polylactic acid, natural fibers, additive manufacturing

INTRODUCTION

In recent years, the primary environmental concerns are associated with waste plastic pollution. This consequence is due to the extensive use of petroleum-based polymers. Sustainable alternatives have to be developed to address this challenge [1]. Polylactic acid (PLA) was found to be one of the most sustainable biopolymers due to its biodegradability, and competitive mechanical properties [2]. PLA can be derived from renewable resources like corn starch or sugarcane, making it commercially viable. However, neat PLA suffers from several drawbacks, including inherent brittleness, low transition temperature, poor impact strength, low thermal stability, and slow crystallization rate. A widely adopted technique to improve the features of PLA is the infusion of appropriate reinforcements. Utilizing natural fibers as reinforcement agents is cost-effective; it also offers benefits including biodegradability and significant strength [3]. Furthermore, the integration of nanofillers or metal oxides can improve mechanical and thermal behavior [4]. The most commonly utilized additive manufacturing technology is the fused deposition modeling (FDM) because of its affordability, and capability to produce intricate patterns [5]. Owing to its compatibility, PLA is regarded as a prominent material in FDM. However, the mechanical characteristics of FDM-printed parts are highly anisotropic and highly dependent on process parameters [6]. The present review addresses the impacts of various reinforcements, the significance of FDM, the applications, and the challenges and prospects in this rapidly evolving sector.

Natural fiber reinforcement of polylactic acid

The focus on the development of sustainable materials has led to the incorporation of natural fibers into a biopolymer matrix such as polylactic acid (PLA). These natural reinforcements are typically classified based on their origin as blast fibers (flax and jute), leaf fibers (sisal), seed fibers (cotton), and grass fibers (bamboo). Bamboo fibers comprise a better strength-to-weight ratio. An overview of reinforcement materials in PLA biocomposites is summarized in Table 1.

* To whom all correspondence should be sent:
E-mail: *jv.dhinesh@yahoo.com*

© 2026 Bulgarian Academy of Sciences, Union of Chemists in Bulgaria

Table 1. Overview of reinforcement materials in PLA biocomposites

Reinforcement category	Primary function	Key contribution to sustainability
Natural plant fibers	Enhance stiffness, reduce cost and density	Biodegradability, renewable resource, waste valorization
Bio-derived nanofillers	Improve tensile/barrier properties, thermal stability	High performance from renewable bio-resources
Inorganic minerals	Increase stiffness, heat deflection temperature	Naturally abundant, can improve material efficiency
Synthetic/advanced fibers	Maximize strength and toughness for engineering uses	Promotes circular economy
Bio-based polymers	Enhance biodegradability or impact strength	Creates bio-based blends, compostability

Table 2. Impact of common natural fibers on PLA composite properties

Fiber type	Typical loading (% wt.)	Tensile strength	Tensile modulus	Impact strength	Key processing consideration
Flax/hemp	20-30	Significant increase	Excellent	Increase	High aspect ratio can cause clogging
Wood flour	20-40	Increase	Significant increase	Decrease	Low cost, but high viscosity and brittleness
Bamboo	15-25	Significant increase	Excellent	Increase/ decrease	Good strength-to-weight ratio; moisture sensitive
Recycled cellulose	10-20	Increase/ decrease	Increase	Decrease	Valorizes waste; properties depend on source and purity

Table 2 presents the impact of some typical natural fibers on the mechanical, thermal, and physical properties of PLA composites.

The outcomes of previous research revealed that bamboo fiber-PLA composites displayed significant tensile and flexural moduli, though a primary challenge is to achieve strong bonding between the naturally hydrophilic bamboo and the hydrophobic PLA. This challenge can be overcome by subjecting the composite to chemical treatment like alkalization [7, 8]. The blast fibers, when incorporated in PLA, enhance the stiffness and the thermal stability. The hybrid composites comprising PLA infused with jute and flax display better mechanical features than PLA reinforced with a single-fiber type [9]. The kenaf fiber, a prominent reinforcement material, when incorporated, provides substantial tensile strength and thermal resistance. Furthermore, fibers like sisal, elephant grass, and coir have the capability of improving impact resistance and rate of biodegradation. In contradiction, higher fiber content might lead to agglomeration and reduced tensile strength. The water resistance of the PLA matrix is a primary issue which restricts the reinforcement of hydrophilic natural fibers. However, this limitation can be addressed by chemical modifications including alkali, acetylation, and silane treatments, which significantly modify the fiber surface, facilitate interfacial adhesion, enable efficient stress transfer, and improve the overall mechanical properties of the composite [10].

Nanoscale functional fillers reinforcement of PLA

Though PLA is a biodegradable polymer, its functional features including; poor electrical conductivity, low thermal stability, and brittleness restrict its widespread application. The incorporation of nanoscale functional fillers helps to overcome these shortcomings without compromising its compostable nature. Typically, the nanoscale materials are derived from renewable resources; the most promising cellulosic nanomaterials are nanofibrillated cellulose (NFC) and cellulose nanocrystals (CNC). The exceptional mechanical properties including high stiffness and immense surface area make them ideal for reinforcing the PLA matrix. The PLA/NFC composites exhibit significantly improved tensile strength and stiffness. Lowering the agglomeration of the nanofibers makes them serve as stress concentrators and negatively influence toughness and impact strength. Carbon-based nanofillers like graphene (Gr) and carbon nanotubes (CNTs) are utilized in multiple applications. The tensile strength and modulus of PLA can be significantly increased by evenly distributed graphene reinforcement [11]. Furthermore, such reinforcement promotes properties including UV

shielding and electrical conductivity; makes it a viable candidate for applications in smart packaging and lightweight electronics. Metal and metal oxide nanoparticles are effective in imparting specific bioactive and protective functions. Studies have demonstrated that incorporating nanoparticles like zinc oxide (ZnO) and silver (Ag) can transform PLA films into active packaging materials. ZnO, when infused into PLA, enhances UV barrier properties and provides antibacterial activity [12]. Metal powders (Al, Cu), when employed as reinforcing materials, help to control thermal conductivity; infused milled carbon fibers increase the wear resistance. Moreover, recycled wastes such as spent ground coffee can alter composite properties and promote circular economy [13 – 15]. The key concept is that by meticulously selecting a filler, the characteristics of PLA can be precisely customized, transforming it into a useful material appropriate for specific applications.

Fused deposition modelling (FDM)

In recent years, FDM has become a viable processing technique for PLA biocomposites. The production of filament with superior quality is the primary challenge of this technique. Typically, it involves the use of a screw extruder to achieve homogeneous dispersion of the filler within the PLA matrix [16]. The flow index of the polymer undergoes a change in presence of fibers or particles, leading to nozzle clogging. The use of compatibilizer and plasticizers like polyethylene glycol (PEG) often facilitates smooth printing [17, 18]. The specific printing parameter has a significant influence on the mechanical and physical properties of parts manufactured through fused deposition modelling (FDM) [19, 20]. It is documented in previous studies that raster angle configurations of 0°/90° or ±45° and on-edge orientations result in higher tensile strength compared to other angles [21]. Furthermore, a smaller layer thickness increases the number of layers and the interlayer bonding area, which often enhances tensile strength at the cost of longer print times [22]. The infill density and pattern also play a significant role: higher infill density increases the mechanical strength, and the selection of patterns like cubic or gyroid can provide optimal balance between strength and material efficiency [23]. Furthermore, thermal parameters have significant impact on layer adhesion. The better layer adhesion relies on an optimum nozzle temperature whereas too high or too low nozzle temperatures might cause thermal degradation [24]. Therefore, optimizing these parameters is essential for mitigating the anisotropic nature of FDM particles and achieving performance suitable for functional applications. Table 3 summarizes the FDM processing parameters and their influence on quality and performance.

Table 3. FDM processing parameters and their optimization for PLA biocomposites

Processing parameter	Typical range for neat PLA	Effect of reinforcement	Recommended adjustment for composites
Nozzle temperature	190-220 °C	Fillers can increase melt viscosity	Increase by 5-15 °C to improve flow
Build plate temperature	50-70 °C	Often improves adhesion	Generally maintained or slightly increased
Print speed	40-80 mm/s	High filler content can hinder layer deposition	Reduce by 20-40% to ensure proper extrusion
Filament drying	Optional (recom-mended)	Natural fibers are highly hygroscopic	4-8 h at 50-60 °C before printing
Nozzle type	Brass	Abrasive fillers (e.g., carbon fiber, glass) cause rapid wear	Switch to hardened or stainless steel nozzle

Comparison of the mechanical property

PLA with incorporated fillers and reinforcements is compatible for a variety of applications due to strategic enhancement of properties. In common, PLA is ideal for low-stress applications; inducing reinforcements or filler materials can significantly alter its mechanical and thermal limitations. In particular, introducing micro-scale natural fibers typically increases material stiffness and thermal resistance with reduction in tensile strength and impact toughness. This is primarily attributed to concerns with adhesion between fiber and matrix. Moreover, by developing a better interfacial bond within the polymer matrix, synthetic fibers or nanoscale fillers like cellulose nanocrystals can facilitate a significant enhancement of strength, stiffness, and thermal stability, typically at lower loading levels. Integrating PLA with biodegradable polymers is a useful approach that enhances ductility and impact resistance rather than strength and rigidity, producing a harder, more flexible material. Choosing and incorporating an appropriate filler system customizes the property of the matrix to reach the customized ideal balance for its intended use. Table 4 compares the mechanical properties of PLA biocomposites developed for additive manufacturing.

Table 4. Comparison of the mechanical properties of PLA biocomposites for AM

Material formulation	Tensile strength (MPa)	Young's modulus (GPa)	Impact strength (J/m)	Heat deflection temp. (°C)
Neat PLA	50-70	3.0-3.5	20-30	55-60
PLA + 20% wood flour	45-55	4.0-5.0	15-20	60-65
PLA + 15% carbon fiber	80-100	7.0-9.0	35-45	100-110
PLA + 5% CNC	65-80	4.5-5.5	25-35	65-70
PLA/PHA blend	40-50	2.0-2.5	50-70	50-55

Applications of PLA biocomposites

Owing to the enhanced performance characteristics of PLA biocomposites, they are utilized for widespread industrial and commercial applications. PLA films reinforced with nanofillers such as ZnO reveal improved thermal barrier characteristics, making it compatible for sustainable applications [25, 26]. These materials are being used for non-structural interior parts due to their light weight and biodegradable benefits. PLA with the addition of hydroxyapatite (HAp) or Mg particles displays enhanced osteo conductivity and biodegradability, making it suitable for tissue engineering scaffolds, drug delivery and surgical systems, [27, 28]. The utilization of PLA biocomposites as a feedstock for FDM facilitates the production of functional prototypes, custom tools, and end-use parts [29, 30]. The extent of application continues to expand into construction, encompassing biodegradable products [31].

Challenges and future perspectives

Along with PLA significant advancements, there are certain limitations while utilizing biocomposites. The primary drawback is associated with achieving optimal and significant interfacial adhesion between the polymer matrix and the reinforcement, which is typically difficult with natural fibers. The recent research efforts will concentrate on developing novel, eco-friendly reinforcing agents and advanced surface modification techniques to address this limitation. Furthermore, printing of composite filaments necessitates precise parameter adjustment, a need for standardized procedures in manufacturing of filament and printing of component to ensure reproducibility and dependability [32]. PLA is biodegradable; therefore recycling PLA by chemical means saves materials and energy, [33]. The future research will be focused on using recycled PLA and waste materials, to make new composite filaments [34]. The future of FDM relies on 4D printing and multi-material printing. These enable PLA composites to be configured for modification in response to heat or moisture, forming a novel category of smart materials [35]. A promising approach is to develop hybrid composites which incorporate two or more filler materials, integrating natural fibers with nanoparticles. This approach intends to provide an integrated impact that addresses the drawbacks of distinct reinforcement systems and enables the exact modification of features for particular applications [36, 37]. Table 5 summarizes the functional applications of PLA biocomposites enabled by various additives. Table 6 outlines the current challenges associated with PLA biocomposites.

Table 5. Functional applications of PLA biocomposites enabled by additives

Target functionality	Typical additive	Mechanism	Potential application
Antimicrobial	Chitosan, silver nano-particles, zinc oxide	Disrupts microbial cell walls/ membranes	Medical implants, food packaging, hygienic devices
Electrical conductivity	Graphene, carbon nanotubes, carbon black	Forms a conductive percolation network	Static-dissipative packaging, sensors, flexible electronics
Flame retardancy	Aluminum tri-hydroxide, biobased phosphates	Endo-thermic decomposi-tion, char formation	Automotive interiors, electronics housings, building materials
Enhanced bio-degradation	Thermo-plastic starch	Increases hydrophili-city and microbial attack sites	Single-use agriculture products, compostable items

Table 6. Current challenges and future research directions in PLA biocomposites

Challenge category	Specific issue	Promising research direction
Material Performance	Poor interfacial adhesion between fiber and matrix	Development of novel bio-based coupling agents and surface treatments
Processability	Nozzle clogging and filament brittleness in FDM	Optimization of fiber aspect ratio and exploration of pellet-based 3D printing
Durability & aging	Hydrolytic degradation and UV sensitivity	Investigation of sustainable stabilizers and protective coatings
Standardization	Lack of material data and printing standards for composites	Establishing standardized test protocols and material databases for AM

CONCLUSION

This review points out that the primary limitations of neat PLA, which include brittleness and low thermal stability, can be significantly addressed by incorporating natural fibers and functional nanofillers, thereby customizing its properties for a wide range of applications. By addressing these constraints, PLA biocomposites can be able to make significant contributions to the transition from a conventional petroleum-based framework to a renewable, bio-based one. The use of polylactic acid (PLA) biocomposites is a significant and potent approach that successfully addresses the distinction between desirable engineering requirements and environmental sustainability. However, the associated challenges including interfacial adhesion necessitate advanced approaches. The introduction of biocomposites and additive manufacturing technologies, primarily FDM, facilitates the potential for creating complex, distinctive and lightweight components. Attaining significant interfacial adhesion between the water-resistant PLA matrix and the water-soluble natural fibers, maintaining optimum consistency in FDM and developing standardized procedures for reproducibility, are some of the primary obstacles. Future research should focus on developing novel, sustainable reinforcement agents, improving the features of composite for additive manufacturing, and integrating approaches using recycled PLA and recyclable waste fillers. PLA ensures the significant transition from a conventional, petroleum-centered economy to a renewable, bio-based approach. The research and development of PLA significantly contribute to sustainability in manufacturing and a more sustainable future.

REFERENCES

1. M. Hassan, A. K. Mohanty, M. Misra, *Materials and Design*, **237**, 112558 (2024). https://doi.org/10.1016/j.matdes.2023.112558
2. N. A. A. B. Taib, M. R. Rahman, D. Huda, K. K. Kuok, S. Hamdan, M. K. B. Bakri, A. Khan, *Polymer Bulletin,* **80** (2), 1179 (2023). https://doi.org/10.1007/s00289-022-04160-y
3. G. Rajeshkumar, S. Arvindh Seshadri, G. L. Devnani, M. R. Sanjay, S. Siengchin, J. Prakash Maran, A. R. Anuf, *Journal of Cleaner Production*, **310**, 127483 (2021). https://doi.org/10.1016/j.jclepro.2021.127483
4. J. Zhu, H. Sun, B.Yang, Y. Weng, *Materials*, **17**(2), 336 (2024). https://doi.org/10.3390/ma17020336
5. A. Cano-Vicent, M. M. Tambuwala, S. S. Hassan, D. Barh, A. A. A. Aljabali, M. Birkett, Á. Serrano-Aroca, *Additive Manufacturing*, **47**, 102378. (2021). https://doi.org/10.1016/j.addma.2021.102378
6. N. N. Ahmad, Y. H. Wong, N. N. N. Ghazali, *Soft Science*, **2** (3), 1 (2022). https://doi.org/10.20517/ss.2022.08
7. Y. Wang, J. Sultana, M. M. Rahman, A. Ahmed, A. Azam, R. T. Mushtaq, M. Rehman, *Fibers and Polymers*, **23** (12), 3299 (2022). https://doi.org/10.1007/s12221-022-4871-z
8. A. Khan, S. M. Sapuan, V. U. Siddiqui, E. S. Zainudin, M. Y. M. Zuhri, M. M. Harussani, *International Journal of Biological Macromolecules*, **253**, 127119 (2023). https://doi.org/10.1016/j.ijbiomac.2023.127119
9. A. Felix Sahayaraj, M. Muthukrishnan, M. Ramesh, *Polymer Composites*, **43** (5), 2854 (2022). https://doi.org/10.1002/pc.26581
10. R. A. Ilyas, M. Y. M. Zuhri, H. A. Aisyah, M. R. M. Asyraf, S. A. Hassan, E. S. Zainudin, N. H. Sari, *Polymers*, **14** (2), 202 (2022). https://doi.org/10.3390/polym14020202
11. K. H. Dehnou, G. S. Norouzi, M. Majidipour, *RSC Advances*, **13** (5), 1456 (2023). https://doi.org/10.1039/d2ra07011a
12. V. Salaris, I. San Félix García-Obregón, D. López, L. Peponi, *Nanomaterials*, **13** (15), 2236 (2023). https://doi.org/10.3390/nano13152236
13. C. Tosto, E. Pergolizzi, L. Vitiello, G. Filippone, G. Cicala, *Macromolecular Symposia*, **404** (1), 2100417 (2022). https://doi.org/10.1002/masy.202100417
14. M. V. Pavan, K. Balamurugan, V. Srinivasadesikan, S. L. Lee, *Arabian Journal for Science and Engineering*, **46** (12), 12709 (2021). https://doi.org/10.1007/s13369-021-05980-2
15. D. Deb, J. M. Jafferson, *Materials Today: Proceedings*, **46**, 1308 (2021). https://doi.org/10.1016/j.matpr.2021.02.397

16. C. H. Lee, F. N. B. M. Padzil, S. H. Lee, Z. M. A. Ainun, L. C. Abdullah, *Polymers*, **13** (9), 1407 (2021). https://doi.org/10.3390/polym13091407
17. E. O. Cisneros-López, A. K. Pal, A. U. Rodriguez, F. Wu, M. Misra, D. F. Mielewski, A. K. Mohanty, *Materials Today Sustainability*, **7–8**, 100027 (2020). https://doi.org/10.1016/j.mtsust.2019.100027
18. R. A. Ilyas, S. M. Sapuan, M. M. Harussani, M. Y. A. Y. Hakimi, M. Z. M. Haziq, M. S. N. Atikah, M. Asrofi, *Polymers*, **13** (8), 1326 (2021). https://doi.org/10.3390/polym13081326
19. K. Rajan, M. Samykano, K. Kadirgama, W. S. W. Harun, M. M. Rahman, *International Journal of Advanced Manufacturing Technology*, **120** (3–4), 1531 (2022). https://doi.org/10.1007/s00170-022-08860-7
20. M. H. Hsueh, C. J. Lai, S. H. Wang, Y. S. Zeng, C. H. Hsieh, C. Y. Pan, W. C. Huang, *Polymers*, **13** (11), 1758 (2021). https://doi.org/10.3390/polym13111758
21. M. M. Hanon, R. Marczis, L. Zsidai, *Periodica Polytechnica Mechanical Engineering*, **65** (1), 38–46 (2021). https://doi.org/10.3311/PPme.13683
22. K. Shergill, Y. Chen, S. Bull, *International Journal of Advanced Manufacturing Technology*, **126** (7–8), 3651 (2023). https://doi.org/10.1007/s00170-023-11270-y
23. M. Jasim, T. Abbas, A. Huayier, *Engineering and Technology Journal*, **40** (12), 1 (2022). https://doi.org/10.30684/etj.2021.131733.1054
24. G. Atakok, M. Kam, H. B. Koc, *Journal of Materials Research and Technology*, **18**, 1542 (2022). https://doi.org/10.1016/j.jmrt.2022.03.013
25. R. Sharma, S. M. Jafari, S. Sharma, *Food Control*, **112**, 107086 (2020). https://doi.org/10.1016/j.foodcont.2020.107086
26. M. Z. Mulla, M. R. T. Rahman, B. Marcos, B. Tiwari, S. Pathania, *Molecules*, **26** (7), 1967 (2021). https://doi.org/10.3390/molecules26071967
27. C. Pascual-González, C. Thompson, J. de la Vega, N. Biurrun Churruca, J. P. Fernández-Blázquez, I. Lizarralde, J. LLorca, *Rapid Prototyping Journal*, **28** (5), 884 (2022). https://doi.org/10.1108/RPJ-06-2021-0152
28. A. Grivet-Brancot, M. Boffito, G. Ciardelli, *Macromolecular Bioscience*, **22** (10), 2200039 (2022). https://doi.org/10.1002/mabi.202200039
29. E. H. Tumer, H. Y. Erbil, *Coatings*, **11** (4), 390 (2021). https://doi.org/10.3390/coatings11040390
30. V. H. M. Almeida, R. M. Jesus, G. M. Santana, T. B. Pereira, *Journal of Composites Science*, **8** (2), 67 (2024). https://doi.org/10.3390/jcs8020067
31. P. D. Jamadar, R. Sharma, H. K. Wagh, *AIP Conference Proceedings*, **2393**, 1 (2022). https://doi.org/10.1063/5.0074871
32. A. S. L. Rodrigues, A. C. B. Pires, P. A. Barbosa, Z. C. Silveira, *Polymer Composites*, (2024). https://doi.org/10.1002/pc.28269
33. P. Mc Keown, M. D. Jones, *Sustainable Chemistry*, **1** (1), 1 (2020). https://doi.org/10.3390/suschem1010001
34. K. Mikula, D. Skrzypczak, G. Izydorczyk, J. Warchoł, K. Moustakas, K. Chojnacka, A. Witek-Krowiak, *Environmental Science and Pollution Research*, **28** (10), 12321 (2021). https://doi.org/10.1007/s11356-020-10657-8
35. A. Kafle, E. Luis, R. Silwal, H. M. Pan, P. L. Shrestha, A. K. Bastola, *Polymers*, **13** (18), 3101 (2021). https://doi.org/10.3390/polym13183101
36. M. Nofar, R. Salehiyan, S. S. Ray, *Composites Part B: Engineering*, **215**, 108845 (2021). https://doi.org/10.1016/j.compositesb.2021.108845
37. S. Yaisun, T. Trongsatitkul, *Polymers*, **15** (20), 4106 (2023). https://doi.org/10.3390/polym15204106

Bulgarian Chemical Communications, Volume 58, Issue 4 (pp. 482-491) 2026 *DOI: 10.34049/bcc.58.4.5753*

Fitting and interpretation of equilibrium and kinetic models, and two-stage adsorber design of condensate-based adsorbents for methylene blue removal

T. F. Rahaman [1,2], F. Amran[1,2], M. A. A. Zaini[1,2*]

[1] *Faculty of Chemical & Energy Engineering, Universiti Teknologi Malaysia, 81310 UTM Johor Bahru, Johor, Malaysia*

[2] *Centre of Lipids Engineering and Applied Research (CLEAR), Ibnu-Sina Institute for Scientific and Industrial Research, Universiti Teknologi Malaysia, 81310 UTM Johor Bahru, Johor, Malaysia*

Received: February 13, 2026; Revised: June 17, 2026

The present work aims at evaluating the equilibrium and kinetic models, and traits of a two-stage adsorber in optimizing the mass of condensate-based adsorbents for methylene blue removal. Results show that CZ1.5 and CS0.5Z recorded high methylene blue capacities of 191 and 193 mg/g, respectively. The adsorption data obeyed the Langmuir model, while the kinetic data closely fitted a pseudo-second order model. In a two-stage adsorber design, to improve the removal efficiency from 80 % to 99 %, the total adsorbent mass has to be increased by 94.2 % due to strong liquid-phase mass transfer resistance and weak adsorbate-adsorbent affinity. Nonetheless, the mass required can be reduced by 54.8 % for treating any volumes of dye effluent. In the performance evaluation, the mass in stage-1 is higher than that in stage-2 for lessening the surface load to achieve equilibrium at minimum dosage. The two-stage adsorber aids to optimize the mass for different percentages of dye removal that are economically feasible for industrial applications.

Keywords: Palm oil condensate, adsorption, environmental engineering, methylene blue, wastewater treatment

INTRODUCTION

Textile printing and dyeing industry plays a vital role in modern society and is experiencing rapid advancement. The industry uses a large amount of water during wet processing and leads to a significant increase in the volume of wastewater heavily laden with dissolved dyes. The industry consumes around 1.6 million liters of water each day to produce approximately 8,000 kg of fabric [1]. There are more than 10,000 different dyes used in textile manufacturing, with nearly 70 % comprising azo dyes, which are synthetic and structurally complex [2]. Dyes are highly toxic, stable, highly visible in trace amounts, and not easily biodegradable [3]. Thus, the improper discharge of dye-containing wastewater without adequate treatment poses a significant threat, particularly to environment and aquatic ecosystems. During environmental migration, dyes may react with other substances, leading to the formation of hazardous compounds [4]. The compounds can cause teratogenic and neurotoxic effects in people who consume agricultural or aquatic products contaminated by them. Also, dye-containing wastewater can hinder sunlight penetration into water bodies, thereby interfering with the photosynthesis activity of aquatic plants [5]. Therefore, it is essential to eliminate the harmful dyes from wastewater prior to its discharge into the environment.

Several treatment methods have been employed for dye removal from wastewater, including coagulation/flocculation, precipitation, membrane filtration, reverse osmosis, ozonation, advanced oxidation processes, ion exchange and adsorption [6]. Adsorption remains one of the most effective methods, offering a simple procedure using abundant and low-cost adsorbents such as activated carbon [7], biochar [8], clays [9] and zeolites [10]. Activated carbon adsorption has proven to be able to achieve high removal efficiency of dye pollutants in many scientific publications [11, 12]. Activated carbon endows a large surface area, well-developed porous texture, and rich surface functional groups to improve interaction probabilities with dye molecules in water, thus enhancing the uptake capacity [13]. The physicochemical properties of activated carbon are highly dependent on the nature of the precursor used. The precursor should be a carbon-rich material that is locally available, abundant, and economically feasible.

Palm oil condensate is a liquid byproduct produced during the processing of oil palm fruits, which can be exploited as carbon feedstock. Not all of the steam is consumed in heating the fresh fruit bunch in palm oil processing, since about half of the steam might be lost as condensate and end up as palm oil mill effluent [14]. Malaysia ranks as the world's second-largest producer of palm oil, contributing significantly to global supply. Parveez

* To whom all correspondence should be sent:
Email: *abbas@cheme.utm.my*

© 2026 Bulgarian Academy of Sciences, Union of Chemists in Bulgaria

et al. [15] reported that the rise in Malaysia's palm oil production in 2023 is attributed to a 1.9 % increase in fresh fruit bunch yield per hectare and a 0.8 % improvement in the oil extraction rate. The sustainable palm oil industry has triggered quest to capitalize the condensate as activated carbon feedstock for wastewater treatment. Chemical activation is commonly used to convert precursor into activated carbon with highly developed pore structure, resulting in enhanced dye removal capacity [16].

The single-stage batch adsorber is widely recognized as a standard approach in adsorption research. However, it is inadequate for predicting high removal efficiency under optimal adsorbent dosage and contact time conditions when scaling up the process. Hence, a two-stage adsorber design has been proposed to reduce the adsorbent mass and contact time, making the dye adsorption process more cost-effective. A 14 % reduction in adsorbent mass is achieved through the use of a two-stage adsorber employing coffee residue-based activated carbon for phenol removal [17]. In a related work, the mass for malachite green adsorption is reduced by 44 % in a two-stage adsorber of date stone activated carbon [18]. This study uniquely integrates equilibrium and kinetic model interpretations with a two-stage adsorber design for methylene blue removal using condensate-based adsorbents. The novelty of this work lies in translating the adsorption behavior into a two-stage adsorption system to optimize the mass of activated carbon. The performance evaluation was discussed to broaden the knowledge towards sustainable industrial applications.

MATERIALS AND METHODS

Palm oil condensate was collected from palm oil milling in Johor state of Malaysia. Sulfuric acid (H_2SO_4) was purchased from R&M Chemicals. Zinc chloride ($ZnCl_2$) and potassium hydroxide (KOH) were purchased from Quality Reagent Chemicals (QReC), phosphoric acid (H_3PO_4) from JT Baker. Methylene blue (MW=319.85 g/mol) was supplied by HmBG Chemicals.

Preparation and characterization of adsorbents

A 1000 mL of palm oil condensate was oven-dried for two days until its volume was reduced to 800 mL. A 400 mL of the condensate was mixed with 200 mL of H_2SO_4 solution in a 0.5 ratio (v/v, H_2SO_4: palm oil condensate). Next, pyrolysis was performed in a muffle furnace at 400 °C for 2 h. The resultant sample was designated as CS0.5. Then, it was impregnated with $ZnCl_2$ solution at a ratio of 1 (w/w, $ZnCl_2$: CS0.5). The activation was conducted in a muffle furnace at 600 °C for 1 h. The adsorbent was refluxed with distilled water in a Soxhlet apparatus for 24 h to a constant pH. The same procedures were repeated for activation by KOH. The activated carbons were designated as CS0.5Z and CS0.5K, respectively.

The adsorbents were also prepared using dried palm oil condensate with different activators. The dried condensate or sludge was impregnated with H_3PO_4 solution in a 1.5 ratio (w/w, H_3PO_4: palm oil condensate). The activation was performed in a muffle furnace at 600 °C for 1.5 h. The same procedures were repeated for activation by $ZnCl_2$. The resultant materials, designated as CH1.5 and CZ1.5 were washed with distilled water to remove impurities and oven-dried prior to use. The condensate char, labelled as CC was prepared at the same temperature and holding time, but without activator for comparison.

The CZ1.5 was characterized for surface area and pore volume nitrogen adsorption at 77 K using Micromeritics ASAP 2020. The functional groups present on the adsorbent surface were identified using a FTIR spectrometer (Thermo Scientific, Nicolet iS10). The morphological surface structure was captured using a field emission scanning electron microscope.

Batch adsorption studies

A 20 mg portion of adsorbent was added into 20 mL of methylene blue solution at concentrations ranging from 10 to 350 mg/L. The adsorbent dose was fixed at 1 mg/mL to minimize volumetric variation that could nullify the mass balance assumption. The concentrations were selected to allow surface saturation of adsorbent at equilibrium. The mixture was left to equilibrate at room temperature of 27 °C for 72 h. The contact time of 72 h was judged from the kinetic data and considering the time taken to reach equilibrium if higher dye concentrations were used. The control solution was prepared to represent the initial concentration. The concentration of methylene blue was measured using a UV-vis spectrophotometer (DU-8200) at a wavelength of 620 nm. The capacity at equilibrium, q_e (mg/g) was calculated as

$$q_e = \frac{(C_o - C_e)V}{m} \quad (1)$$

where C_o (mg/L) is the initial dye concentration, C_e (mg/L) is the equilibrium dye concentration, V (L) is the solution volume and m (g) is the adsorbent mass. The adsorption data were analyzed using Langmuir,

Freundlich and Redlich-Peterson models, as expressed in equations (2), (3) and (4), respectively,

$$q_e = \frac{q_m K_L C_e}{1+K_L C_e} \quad (2)$$

$$q_e = K_f C_e^{\frac{1}{n}} \quad (3)$$

$$q_e = \frac{K_R C_e}{1+\alpha C_e^{\beta}} \quad (4)$$

where, q_m (mg/g) is the maximum capacity, K_L (L/mg) is the Langmuir constant, K_f and n are the Freundlich constants, and K_R and α are the Redlich-Peterson constants and β is an exponent that lies between 0 and 1.

Adsorbent (20 mg) was added into 20 mL of methylene blue solution at concentrations of 7.89 and 27.5 mg/L. The mixture was allowed to reach equilibrium at room temperature of 27 °C. Kinetics is often carried out at low initial concentrations to minimize concentration-dependent mass transfer limitations and to more clearly resolve intrinsic adsorption rate behavior without saturation effects. The concentration of methylene blue was measured at different time intervals. The adsorption capacity at any time, q_t (mg/g) was calculated as

$$q_t = \frac{(C_0 - C_t)V}{m} \quad (5)$$

where C_t (mg/L) is the dye concentration at time t. The kinetic data were analyzed using pseudo-first order, pseudo-second order and intraparticle diffusion models, as expressed in equations (6), (7) and (8), respectively:

$$q_t = q_e(1 - e^{-k_1 t}) \quad (6)$$

$$q_t = \frac{k_2 q_e^2 t}{1+k_2 q_e t} \quad (7)$$

$$q_t = k_d t^{\frac{1}{2}} + C \quad (8)$$

where t (h) is the contact time, k_1 (h^{-1}) is the pseudo-first order rate constant, k_2 (g/mg.h) is the pseudo-second order rate constant, k_d (mg/g.h) is the intraparticle diffusion rate constant, and C is the intercept of the intraparticle diffusion plot.

The selection of equilibrium and kinetic models was based on their established applicability in describing dye adsorption systems and to provide complementary insights into adsorption mechanisms. The Langmuir model, for example, assumes monolayer coverage onto a homogeneous surface, while the Freundlich model accounts for multilayer stacking over heterogeneous surface. The Redlich-Peterson presents the combined features of Langmuir and Freundlich models. In addition, kinetic models were employed to evaluate the adsorption rate and potential rate-controlling steps.

Two-stage adsorption

Adsorption data were used to model the two-stage adsorber. The simulation was performed using Microsoft Excel. Figure 1 visualizes the scheme of two-stage batch adsorber design. In a two-stage adsorber, the effluent volume V first passes through stage 1, where the adsorbent mass m_1 brings the system to equilibrium at concentration C_1. The partially treated effluent then flows into stage 2, where the additional mass m_2 further reduces the concentration to a final equilibrium concentration C_2. Fresh adsorbent is supplied to each stage to treat the same volume of dye solution, resulting in adsorption capacities q_1 and q_2, respectively. The initial adsorption capacity entering each stage q_o (mg/g) = 0. The overall process can be represented by mass balance as follows:

$$V(C_0 - C_1) = m_1(q_1 - q_0) \quad (9)$$

$$V(C_1 - C_2) = m_2(q_2 - q_0) \quad (10)$$

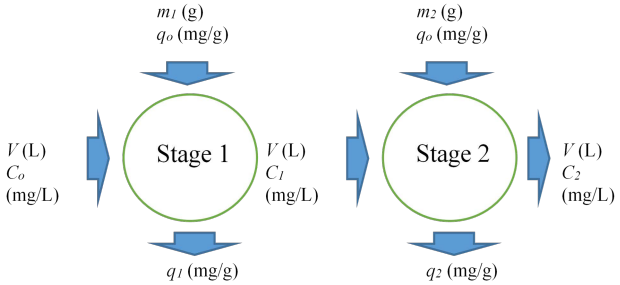


Figure 1. Two-stage adsorber design [19].

The design objective was to treat 100 mL of methylene blue solution at initial concentration C_o = 50 mg/L. A series of sorption system numbers for C_1 from 50 to 1.34 mg/L in a 2.5 mg/L step-size was considered [20]. For example, in sorption system number 1, the C_0 was reduced from 50 to 47.5 mg/L in stage-1. Similarly, in sorption system numbers 2, 3, and so on, the concentration values were reduced from 47.5 to 45.0 mg/L, 45.0 to 42.5 mg/L, and lastly down to 1.34 mg/L. While, in stage-2, the sorption system number 1 reduced the concentration from 47.5 to 1.34 mg/L. The volume was varied between 20 mL and 500 mL to observe its effect on optimum adsorbent mass. By substituting equation (2) into equation (9), the material balance as a function of Langmuir constants at each stage can be rewritten as

$$\frac{m_1}{V} = \frac{(C_0-C_1)(1+K_L C_1)}{q_m K_L C_1} \quad (11)$$

$$\frac{m_2}{V} = \frac{(C_1-C_2)(1+K_L C_2)}{q_m K_L C_2} \quad (12)$$

$$\frac{m_1+m_2}{V} = \frac{1}{q_m K_L}\left(\frac{(C_0-C_1)(1+K_L C_1)}{C_1} + \frac{(C_1-C_2)(1+K_L C_2)}{C_2}\right) \quad (13)$$

Equation (13) was differentiated against C_1, where $\frac{\mathrm{d}(m_1+m_2)/V}{\mathrm{d}C_1} = 0$ to yield

$$C_1 = (C_0 C_2)^{\frac{1}{2}} \quad (14)$$

The optimum mass for each stage can be computed by equations (13) and (14). Different removal rates (80 to 99 %) and final concentrations (0.5 to 10 mg/L) in the effluent were set to allow the performance evaluation of the two-stage adsorber. The removal percentage R was calculated by the following equation:

$$R = 100\left(\frac{C_o - C_2}{C_o}\right) \quad (15)$$

Figure 2 illustrates the overall flow of the study.

RESULTS AND DISCUSSION

Adsorption studies

Dye concentration plays a crucial role in the adsorption process. Figure 3 shows the equilibrium adsorption of methylene blue onto adsorbents. The adsorption capacity increased with dye concentration up to a point where maximum removal was achieved. At the point of surface saturation, any further increase in dye concentration may lead to a decline in removal efficiency. At low concentrations, the adsorption capacity was relatively low due to the limited number of dye molecules with respect to the active sites, indicating that the removal process is highly dependent on dye concentration. At high concentrations, the increased driving force helped to overcome mass transfer resistance and enhanced the interaction probabilities of the dye molecules with the adsorbent surface.

CZ1.5 showed a steeper adsorption gradient at low concentrations compared to other adsorbents, indicating a favorable removal of methylene blue. As the concentration increased, the removal of methylene blue by CZ1.5 began to level off at 191 mg/g, whereas CS0.5Z continued to show an upward trend, reaching a Langmuir capacity of 193 mg/g. Generally, the increase in dye removal is attributed to the higher surface area of the adsorbent, which provides more accessible adsorption sites for dye molecule uptake. During activation, dehydration of H_2SO_4 promotes the formation of internal pores by gasifying and combusting the carbon content of the precursor [21].



Figure 2. Overall flow of the study.

In addition, the second activation by $ZnCl_2$ at 600 °C provides adequate heat to release volatile matter and gas, thus causing the formation of more pores [22, 23]. Consequently, the double heating of CS0.5Z likely results in greater porosity, surface area, and adsorption capacity compared to the single-step treatment of CZ1.5. Also, the abundance of surface functional groups on the adsorbent surface enhances the adsorption capacity through several mechanisms, including electrostatic interactions, hydrogen bonding, π-π interactions, and hydrophobic interactions [24, 25]. However, CC exhibits the lowest adsorption capacity, probably due to its non-porous structure and low surface area.

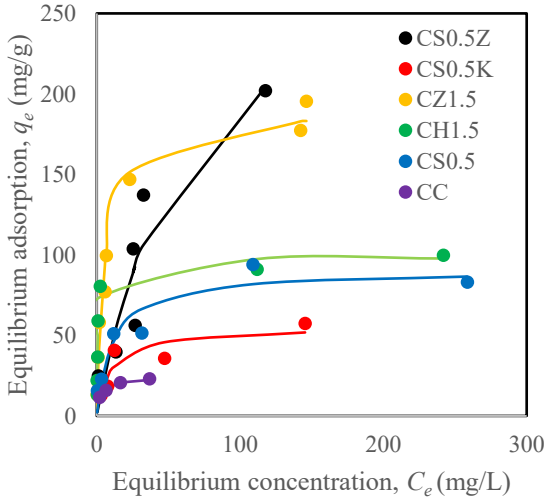


Figure 3 Adsorption of methylene blue onto adsorbents (Lines were predicted by Langmuir model).

The equilibrium distribution of dye molecules between the solid and liquid phases is described by an adsorption isotherm. Table 1 summarizes the isotherm constants for methylene blue adsorption onto adsorbents. The equilibrium data obeyed the Langmuir model with $R^2 > 0.891$, suggesting a single-layer coverage of dye molecules onto a homogeneous surface. An ideal adsorbent should possess both high maximum adsorption capacity and strong affinity K_L [26]. In this work, the affinity shows the favourable removal of methylene blue at low dye concentration, since there are more available binding sites on the adsorbent's surface relative to the amount of dye. The Redlich-Peterson model is a hybrid isotherm that incorporates characteristics of both the Langmuir and Freundlich models. The β values are close to 1, indicating that the Redlich-Peterson isotherm closely resembles the Langmuir isotherm.

Table 1. Isotherm constants for methylene blue adsorption onto adsorbents.

Adsorbent	CS0.5	CS0.5Z	CS0.5K	CZ1.5	CH1.5	CC
Q_{ex} (mg/g)	93.9	202	57.4	195	97.8	22.3
Langmuir						
Q_m (mg/g)	90.4	193	62.9	191	98.1	23.9
K_L (L/mg)	0.0880	0.0155	0.0903	0.168	1.28	0.390
SSE	602	3269	112	961	398	2.74
R^2	0.904	0.891	0.914	0.980	0.947	0.967
Freundlich						
K_f (mg/g) (L/mg)$^{1/n}$	24.0	15.0	13.4	49.0	45.0	10.2
n	4.07	1.82	3.37	3.61	6.55	4.29
SSE	601	3349	230	2260	1910	2.06
R^2	0.879	0.881	0.821	0.941	0.733	0.974
Redlich-Peterson						
K_R	15.7	95241	5.58	56.8	98.4	19.7
α	0.339	6360	0.0892	0.540	0.768	1.39
β	0.877	0.451	0.999	0.879	1.06	0.855
SSE	553	3349	112	579	326	0.719
R^2	0.899	0.881	0.913	0.984	0.954	0.991

Figure 4 shows the adsorption rate of methylene blue onto adsorbents at concentrations of 7.89 and 27.5 mg/L. CZ1.5 and CH1.5 exhibit a faster adsorption rate than CS0.5 and CS0.5Z, resulting in complete dye molecule adsorption more quickly. The transfer of dye molecules from the bulk solution to the boundary layer generally occurs rapidly, whereas their diffusion into the internal pores proceeds at a slower rate [27]. Thus, the larger pore size accounts for the faster adsorption rate by lowering mass transfer resistance and enabling dye molecules to reach active sites more rapidly [28]. Conversely, the slower adsorption rate may be due to the microporous structure of the adsorbent, which can partially restrict the diffusion of dye molecules into the pores [29]. The adsorption rate declined over time, as adsorption sites became progressively occupied, and the adsorbed dye layer induced electrostatic repulsion against the remaining dye molecules in the bulk solution. The decreased adsorption capacity of CS0.5 at 10 mg/L suggests dye molecule desorption, likely caused by weak binding energy with the solid surface. Generally, increasing the dye concentration results in a higher dye removal rate and requires a longer contact time to reach equilibrium. At high dye concentrations, the limited availability of adsorption sites restricts the adsorption process, causing the adsorption rate to decline gradually until it approaches zero.

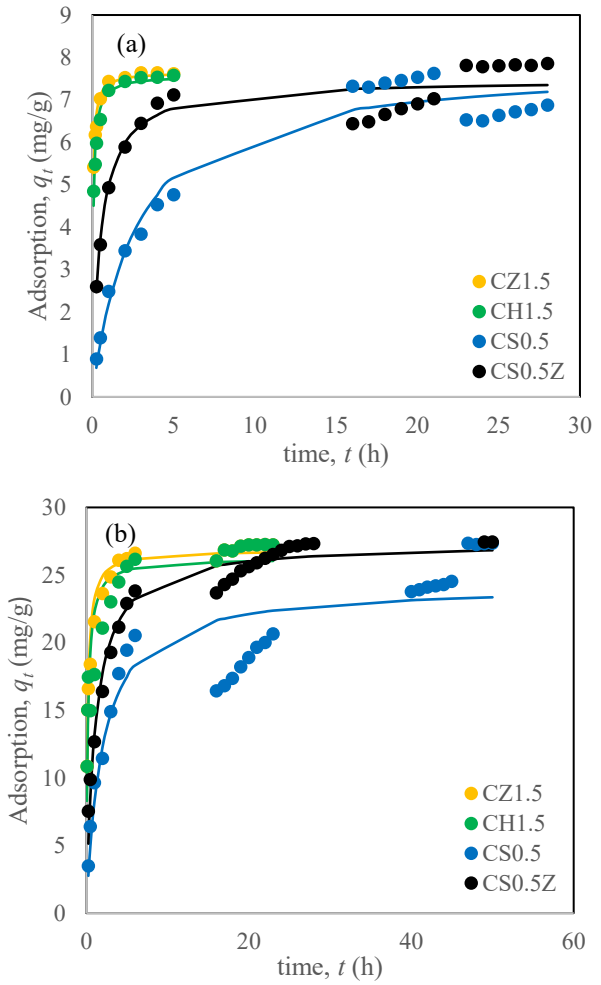


Figure 4. Rate of methylene blue adsorption at (a) 7.89 and (b) 27.5 mg/L onto adsorbents (lines were predicted by a pseudo-second order model).

Table 2 shows the kinetic constants for methylene blue adsorption onto adsorbents. The pseudo-second order model exhibits a higher R^2 value compared to the pseudo-first order model, indicating the applicability of the pseudo-second-order to describe the kinetic data. This suggests that the adsorption is governed by chemical adsorption, involving electron sharing or exchange between the dye molecules and the adsorbent surface [30]. Also, the calculated equilibrium adsorption capacities Q_e closely match the experimental values Q_{ex}, representing good model accuracy. Although the pseudo-second order model provided the best correlation with the experimental data, this alone is not sufficient to conclusively confirm a chemisorption mechanism; therefore, the results were interpreted in terms of adsorption kinetics and possible adsorbate-adsorbent interactions rather than a definitive mechanistic assignment. CZ1.5 exhibits the fastest rate, as reflected by its highest rate constant k_2, values. The increased dye concentration leads to a reduced k_2, thereby extending the time required to attain equilibrium. Nonetheless, the intraparticle diffusion rate constant k_d and C increased at higher dye concentration. The high k_d suggests that dye molecules diffuse into the adsorbent pores more rapidly through pore diffusion than through film diffusion. The high C indicates the increased adsorption rate and boundary layer thickness [16]. In this work, the Q_t *versus* $t^{1/2}$ plot did not pass through the origin, implying that intraparticle diffusion alone does not control the rate and that film diffusion may also be involved [31].

Table 2. Kinetic constants for methylene blue adsorption onto adsorbents.

Adsorbent	CS0.5		CS0.5Z		CZ1.5		CH1.5	
C_o (mg/L)	7.89	27.5	7.89	27.5	7.89	27.5	7.89	27.5
Q_{ex} (mg/g)	6.87	27.4	7.86	27.5	7.63	27.3	7.58	27.3
Pseudo-first order								
Q_e (mg/g)	7.04	22.3	7.17	25.9	7.36	26.0	7.23	25.1
k_1 (h^{-1})	0.289	0.417	1.24	0.557	13.3	4.19	9.98	4.05
SSE	3.63	266	5.40	66.8	1.27	66.1	1.93	170
R^2	0.964	0.743	0.867	0.941	0.773	0.866	0.796	0.679
Pseudo-second order								
Q_e (mg/g)	7.86	24.3	7.48	27.4	7.65	26.9	7.58	26.3
k_2 (g/mg.h)	0.0487	0.0212	0.264	0.0337	3.41	0.239	2.33	0.212
SSE	3.68	197	3.75	23.4	0.126	15.1	0.285	78.4
R^2	0.958	0.808	0.901	0.972	0.976	0.967	0.967	0.846
Intraparticle diffusion								
k_d (mg/g.h)	1.19	2.61	0.705	2.73	0.947	2.43	1.25	2.79
C	1.47	7.98	4.13	12.6	5.90	17.2	5.25	15.5
SSE	11.7	165	11.7	165	1.42	137	1.80	98.1
R^2	0.865	0.838	0.693	0.780	0.728	0.683	0.786	0.798

Characteristics of CZ1.5

Figure 5 shows the characteristics of CZ1.5. The N_2 adsorption-desorption profile exhibits a typical Type IV isotherm with H4 hysteresis, showing the volume adsorbed of 250 mmol/g at relative pressure → 1. The sample endows a surface area of 480 m^2/g with 72% mesopore content and average pore width of 2.91 nm, that is linked to the dehydrating effect of zinc chloride. The SEM image of CZ1.5 displays a rough and irregular surface with interconnected pores ranging from 1 to 10 μm. This implies a transition to mesoporous network with enhanced adsorptive potential for diffusion and surface interaction with dye molecules.

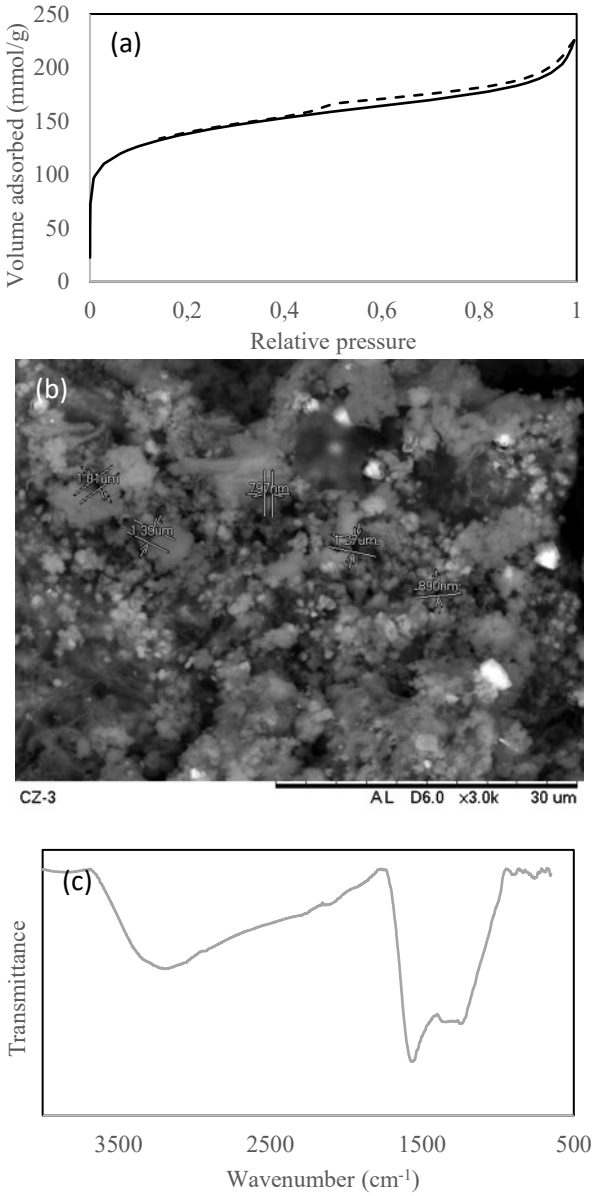


Figure 5. (a) N_2 adsorption-desorption profile (solid line: adsorption branch; dashed line: desorption branch), (b) SEM image and (c) FTIR spectrum of CZ1.5.

The FTIR spectrum shows a broad absorption band at 3500 cm^{-1} that represents O–H stretching vibrations of hydroxyl groups and physisorbed moisture. The peaks in the range of 3000 and 2800 cm^{-1} belong to C–H stretching vibrations of aliphatic hydrocarbon chains. A strong absorption band near 1700 cm^{-1} is attributed to C=O stretching vibrations, signifying the presence of carbonyl groups in CZ1.5. The presence of oxygenated functional groups, such as carboxylic and phenolic groups, at the edges of the carbon matrix is likely to enhance the removal of cationic molecules through electrostatic attraction, ion-exchange and surface complexation. The acidic functionalities increase the density of negatively charged active sites on the adsorbent surface, thereby promoting interactions and improving the adsorption performance.

Two-stage adsorber design

A two-stage adsorber design based on the Langmuir model was proposed for CZ1.5 to reduce the adsorbent mass needed for methylene blue removal. Figure 6(a) shows the profiles of adsorbent mass at different effluent volumes in a two-stage adsorber. The optimum mass of CZ1.5 increases as the volume of dye solution increases to meet 97.3 % removal of methylene blue. As the solution volume increases from 20 to 500 mL, the optimum mass of adsorbent increases from 0.012 to 0.292 g. The optimum mass is estimated at sorption number 18 for all effluent volumes. As the effluent volume increases, the mass gap between the one-stage adsorber (sorption system 1) and the two-stage adsorber (sorption system 18) becomes increasingly pronounced. Consequently, the adsorbent mass can be reduced by 54.8 % at all effluent volumes.

Figure 6(b) shows the mass profiles in each stage of the two-stage batch adsorber to treat 100 mL of methylene blue. In sorption system 18, stage-1 uses 0.042 g of mass, which is higher than the 0.016 g used in stage-2. Stage-1 bears the higher amount of adsorbent because of the high concentration gradient requirement to overcome mass transfer resistance, thereby reducing the amount of adsorbent needed in stage-2 [32].

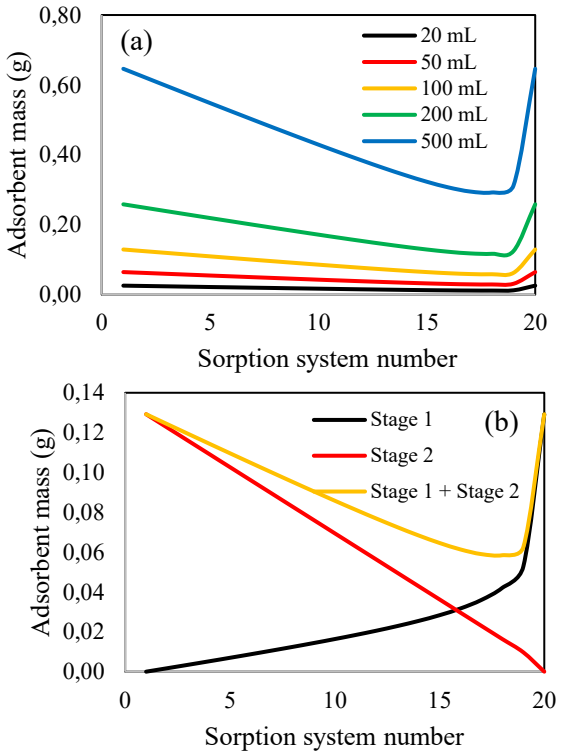
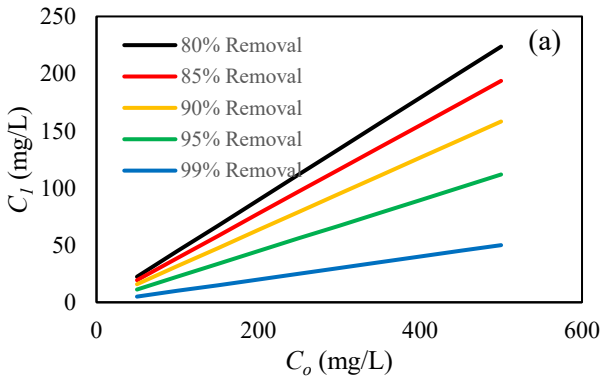


Figure 6. Profiles of adsorbent mass at (a) different effluent volumes and (b) each stage of a two-stage adsorber.

Figure 7 shows the effect of initial concentration C_o on intermediate concentration C_1 at different removal percentages and equilibrium concentrations C_2. From Figure 7(a), C_1 increased with rising C_o, however, as the removal percentage increases, C_1 decreases, indicating increased adsorption capacity. For 80 % removal, initial concentration of 50 mg/L decreased to $C_1 = 22.4$ mg/L, while achieving 99 % removal required a further reduction to $C_1 = 5$ mg/L. Similarly, C_1 is lower when $C_2 = 0.5$ mg/L and the value increases as C_2 increases. The lower C_1 signifies that larger adsorbent mass is applied in stage-1 to substantially decrease the dye concentration, allowing stage-2 to remove the remaining dye concentration at a lower equilibrium.



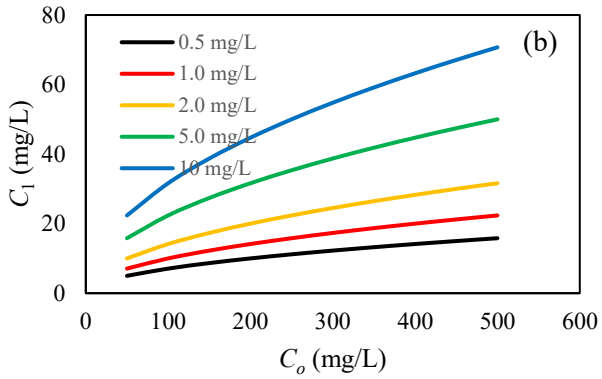
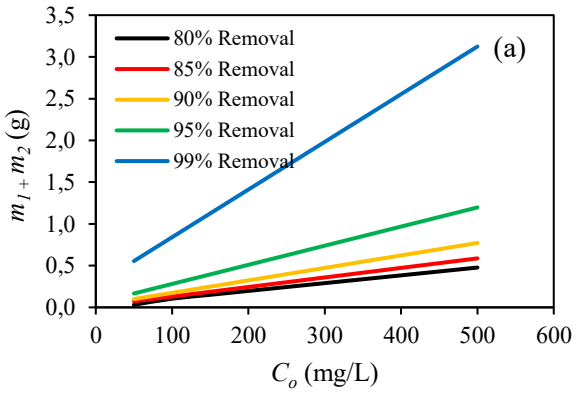


Figure 7. Effect of initial concentration C_o on intermediate concentration C_1 at different (a) removal percentages and (b) equilibrium concentrations C_2.

Figure 8 shows the effects of initial concentration C_o on the total adsorbent mass at different removal percentages and equilibrium concentrations C_2 in a two-stage adsorber. The total mass of adsorbent linearly increases with C_o for all dye removal as shown in Figure 8(a). It means that a larger amount of adsorbent is needed at higher initial concentration and removal percentage. The higher removal efficiency requires larger adsorbent mass to provide sufficient active sites for adsorbent-dye molecule interactions. At C_o = 50 mg/L, the total mass increased from 0.032 g for 80 % removal to 0.555 g for 99 % removal of methylene blue, yielding up to 94.2 % increase in total mass. Thus, the significant increase may be attributed to the weak affinity of the adsorbent surface towards methylene blue molecules [20,33]. The huge leap from 95 to 99 % removal suggests a pronounced effect of liquid-phase mass transfer resistance, which demands a considerably higher quantity of adsorbent to achieve complete dye removal. Likewise, Figure 8(b) shows that a lower C_2 requires more adsorbent mass.



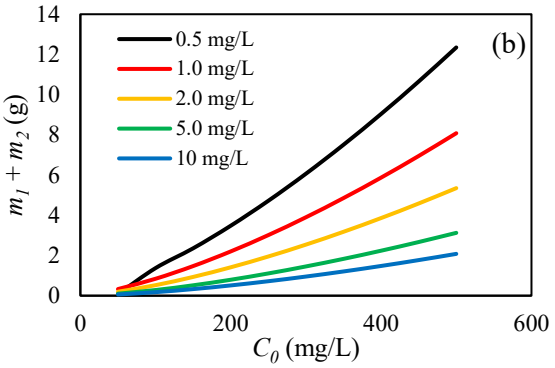


Figure 8. Effect of initial concentration C_o on total mass at different (a) removal percentages, (b) equilibrium concentrations C_2.

Figure 9(a) shows the efficiency of methylene blue removal at both stages for different removal percentages. For every targeted removal performance, the dye removal efficiency in stage-2 (C_1-C_2/m_2) is lower than that in stage-1 (C_o-C_1/m_2). This is due to the reduced dye concentration leaving stage-1 and entering stage-2. Figure 9(b) shows the efficiency of methylene blue removal at stage-2 for different equilibrium concentrations, C_2. Stage-2 efficiency increased with C_2, indicating a more substantial contribution to the overall performance of the two-stage system at elevated target C_2 values.

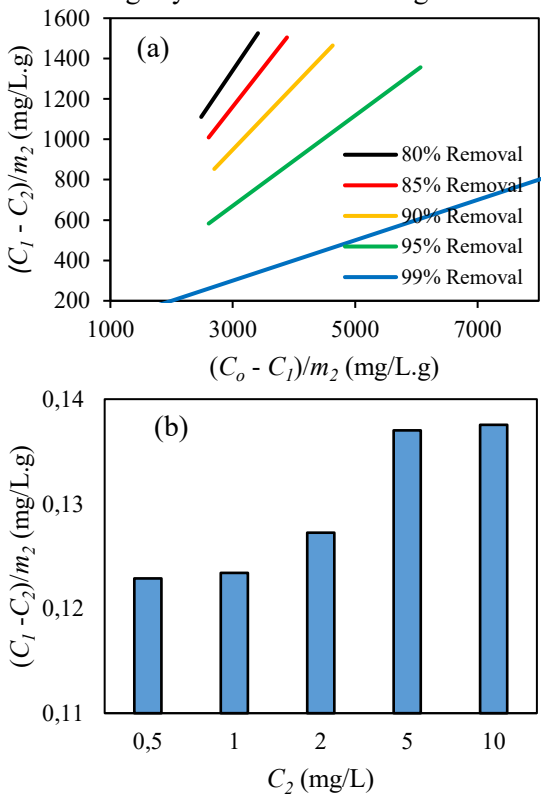


Figure 9. Methylene blue removal at (a) both stages for different removal percentages, and (b) stage-2 for different equilibrium concentrations C_2.

The proposed two-stage adsorber design was developed as a process-scale extension based on experimentally determined Langmuir constants obtained in this study. Although direct experimental validation is not included, the design itself is grounded on an established adsorption model and stage-wise mass balance calculations for preliminary adsorber design.

CONCLUSION

Palm oil condensate was converted into adsorbents *via* chemical activation for methylene blue removal. The removal efficiencies of adsorbents are in the order of CZ1.5 ≈ CS0.5Z > CH1.5 > CS0.5 > CS0.5K > CC. The activation of condensate using H_2SO_4 followed by $ZnCl_2$ activation may results in greater porosity and surface area. Nonetheless, its performance is comparable to the single-step treatment of CZ1.5. In a two-stage adsorber, the mass of CZ1.5 can be minimized to 54.8 % at any volumes, signifying the favorability of oil condensate as carbon feedstock for methylene blue removal. Thus, the two-stage adsorber enhances overall removal efficiency by optimizing carbon mass and lowering process costs.

Acknowledgement/Funding: *This work was supported by the Land and Survey Department of Sarawak through Kursi Premier Sarawak Grant No. 1R037.*

Data availability: *Data will be made available upon request.*

Ethical approval: *Not applicable.*

Competing interests: *All authors declare that they have no competing interests.*

REFERENCES

1. R. V. Khandare, S. P. Govindwar, *Biotechnol. Adv.*, **33** (8), 1697 (2015). http://dx.doi.org/10.1016/j.biotechadv.2015.09.003.
2. M. A. Hassaan, A. E. Nemr, *Am. J. Environ. Sci. Eng.*, **1** (3), 64 (2017). DOI:10.11648/j.ajese.20170103.11.
3. B. M. Adesanmi, Y. -T, Hung, H. H. Paul, C. R. Huhnke, *GSC Adv. Res. Rev.*, **10** (2), 126 (2022). https://doi.org/10.30574/gscarr.2022.10.2.0054.
4. Z. Liu, T. A. Khan, M. A. Islam, U. Tabrez, *Bioresour. Technol.*, **354**, 127168 (2022). https://doi.org/10.1016/j.biortech.2022.127168.
5. Y. Liu, J. Chen, D. Duan, Z. Zhang, C. Liu, W. Cai, Z. Zhao, *Sustainability*, **16**, 10867 (2024). https://doi.org/10.3390/su162410867.
6. Y. Song, L. Wang, X. Qiang, W. Gu, Z. Ma, G. Wang, *J. Water Process. Eng.*, **55**, 104242 (2023). https://doi.org/10.1016/j.jwpe.2023.104242.
7. F. Mbarki, T. Selmi, A. Kesraoui, M. Seffen, *Ind. Crops Prod.*, **178**, 114546 (2022). 10.1016/j.indcrop.2022.114546.

8. D. B. Pal, A. Singh, J. M. Jha, N. Srivastava, A. Hashem, M. A. Alakeel, E. F. Abd_Allah, V. K. Gupta, *Bioresour. Technol*., **339**, 125606 (2021). https://doi.org/10.1016/j.biortech.2021.125606.
9. S. Hamdi, A. Miguez-Gonzalez, R. Cela-Dablanca, A. Barreiro, M. J. Fernandez-Sanjurjo, A. Nunez-Delgado, E. Álvarez-Rodriguez, *J. Environ. Manage*., **368**, 122158 (2024). https://doi.org/10.1016/ j. jenvman.2024.122158.
10. L. Velarde, D. Nikjoo, E. Escalera, F. Akhtar, *Heliyon*, **10** (1), e24006 (2024). https://doi.org/10.1016/j.heliyon.2024.e24006.
11. J. Saleem, Z. K. B. Moghal, S. Pradhan, G. McKay, *RSC Adv*., **14** (46), 33797 (2024). doi: 10.1039/d4ra06287f.
12. M. Moheb, A. M. El-Wakila, F. S. Awad, *RSC Adv*., **15**, 674 (2025). DOI: 10.1039/D4RA07957D.
13. X. Zhang, L. Cheng, X. Wu, Y. Tang, Y. Wu, *J. Environ. Sci*., **33**, 97 (2015). https://doi.org/10.1016/j. jes.2015.01.014.
14. A. K. M. Omar, T. L. T. Norsalwani, M. S. Asmah, Z. Y. Badrulhisham, A. M. Easa, F. M. Omar, M. S. Hossain, M. H. Zuknik, N. A. N. Norulaini, *J. CO_2 Util.,* **25**, 205 (2018). https://doi.org/10.1016/j. jcou.2018.03.021.
15. G. K. A. Parveez, S. -S. Leow, N. N. Kamil, A. Z. Madihah, M. Ithnin, M. H. Ng, Y. A. Yusof, Z. Idris, *J. Oil Palm Res*., **36** (2), 171 (2024). https://doi.org/10.21894/jopr.2024.0037.
16. F. Amran, M. A. A. Zaini, *Surf. Interfaces,* **25**, 101277 (2021). https://doi.org/10.1016/j.surfin. 2021.101277F.
17. H. Palanisami, M. R. M. Azmi, M. A. A. Zaini, Z. A. Zakaria, M. N. H. Z. Alam, M. A. C. Yunus, *Water Pract. Technol*., **16** (3), 793 (2021). https://doi.org/10.2166/wpt.2021.034.
18. M. Hijab, P. Parthasarathy, H. R. Mackey, T. Al-Ansari, G. McKay, *Chem. Eng. Process: Process Intensif*., **167**, 108318 (2021). https://doi.org/10.1016/j.cep.2021.108318.
19. M. A. K. Anuar, N. Mahat, N. M. Rusli, M. N. H. Z. Alam, M. A. A. Zaini, *Int. J. Biomass Renew*., **10** (2), 1 (2021). DOI:10.61762/ijbrvol10iss2art12871.
20. S. A. H. Azaman, A. Afandi, B. H. Hameed, A. T. M. Din, *J. Appl. Sci. Eng*., **21** (3), 317 (2018). DOI:10.6180/jase.201809_21(3).0003.
21. N. Samghouli, I. Bencheikh, K. Azoulay, S. Jansson, S. E. Hajjaji, *Environ. Monit. Assess*., **197**, 259 (2025). https://doi.org/10.1007/s10661-025-13685-4.
22. P. E. Hock, M. A. A. Zaini, *Acta Chim. Slovaca*, **11** (2), 99 (2018). DOI: 10.2478/acs-2018-0015.
23. B. Li, J. Hu, H. Xiong, Y. Xiao, *ACS Omega*, **5**, 9398 (2020). https://dx.doi.org/10.1021/acsomega.0c00461.
24. T. K. Bui, L. T. Nguyen, T. M. Cao, V. V. Pham, *ACS Symp. Ser*., **1478**, 1 (2024). DOI: 10.1021/bk-2024-1478.ch001.
25. K. H. H. Aziz, N. M. Fatah, K. T. Muhammad, *R. Soc. Open Sci*., **11**, 232033 (2024). https://doi.org/10.1098/rsos.232033.
26. A. D. Sponza, N. J. Fernandez, D. Yang, K. A. Ortiz, A. E. Navarro, *Environments*, **2**, 388 (2015). DOI:10.3390/environments2030388.
27. B. An, *Processes*, **8**, 1194 (2020). DOI:10.3390/pr8091194.
28. S. Chen, X. Wang, W. Tong, J. Sun, X. Xu, J. Song, J. Gong, W. Chen, *Nanomaterials*, **11** (3), 799 (2021). https://doi.org/10.3390/nano11030799.
29. M. S. Musa, I. Rosazhar, F Amran, M. A. A. Zaini, *Chem. Afr*., **7**, 5577 (2024). https://doi.org/10.1007/s42250-024-01124-9.
30. M. I. Khan, S. Sufian, F. Hassan, R. Shamsuddin, M. Farooq, *RSC Adv*., **15**, 1989 (2025). https://doi.org/10.1039/D4RA05782A.
31. S. M. Nasser, M. Abbas, M. Trari, *Prog. React. Kinet. Mech*., **49**, 1 (2024). https://doi.org/10.1177/14686783241226858.
32. T. Sarawanan, N. Mahat, N. M. Rusli, M. A. A. Zaini, *Chem. Prod. Process Model*., **18** (3), 1 (2022). https://doi.org/10.1515/cppm-2022-0010.
33. Amran, N. F. Zainuddin, M. A. A. Zaini, *Malays. J. Fundam. Appl. Sci.,* 17**,** 768 (2021). DOI:10.11113/mjfas.v17n6.2303.

Bulgarian Chemical Communications, Volume 58, Issue 4 (pp. 492-503) 2026 *DOI: 10.34049/bcc.58.4.5756*

Integrated *in silico* discovery of anti-apoptotic sesquiterpenoid candidates from *Inula japonica* against hepatocarcinoma

H. D. Nguyen*

Faculty of Biology, Thai Nguyen University of Education, Thai Nguyen, 24124, Vietnam

Received: February 20, 2026; Revised: May 11, 2026

Hepatocellular carcinoma is a leading cause of cancer mortality, and resistance to programmed cell death remains a major barrier to durable therapeutic responses. Natural products from *Inula japonica*, particularly sesquiterpenoids, represent a chemically diverse source of anticancer scaffolds with potential to modulate anti-apoptotic signaling. An integrated *in silico* workflow evaluated nine reported sesquiterpenoids (CPD1-CPD9) against the anti-apoptotic target Myeloid Cell Leukemia 1 (Mcl-1) (PDB: 6B4U), using Simvastatin as a clinically used apoptosis-oriented comparative compound. Docking predicted consistently favorable affinities (-7.56 to -8.84 kcal/mol), with CPD9 (1-*O*-acetyl-6-*O*-isobutyrylbritannilactone) yielding the numerically most negative score among the screened sesquiterpenoids (-8.84 kcal/mol), which was essentially comparable to Simvastatin (-8.80 kcal/mol) and engaging the canonical groove largely through hydrophobic and van der Waals contacts. In 100 ns molecular dynamics simulations, both CPD9-6B4U and Simvastatin-6B4U complexes remained stable, while CPD9 showed comparatively reduced late-stage deviation and solvent exposure. MMGBSA (Molecular mechanics generalized Born surface area) analysis estimated stronger mean binding for Simvastatin than for CPD9, driven mainly by a more favorable van der Waals component. pkCSM profiling suggested improved modeled solubility and permeability for CPD9 but indicated an AMES-positive alert. DFT (Density Functional Theory) descriptors supported a harder, more electrophilic electronic profile for CPD9 relative to Simvastatin. These results nominate CPD9 a prioritized sesquiterpenoid scaffold for further optimization rather than a directly developable lead, particularly because its AMES-positive alert must be resolved before advancement.

Keywords: Anti-apoptosis; DFT; Hepatocarcinoma; Mcl-1; Molecular modeling; Sesquiterpenoids.

INTRODUCTION

Hepatocellular carcinoma (HCC) remains a major global health burden and one of the leading causes of cancer-related mortality [1]. Poor outcomes in advanced disease are partly driven by tumor adaptation to cytotoxic stress and impaired apoptosis regulation [2]. Among apoptosis-related pathways, anti-apoptotic B-cell lymphoma 2 (Bcl-2) family proteins promote survival by restraining mitochondrial outer membrane permeabilization through sequestration of pro-death BH3-only activators and effectors [3]. Myeloid cell leukemia 1 (Mcl-1) is a key pro-survival member of this family and has become an important target in BH3-mimetic discovery [4]. However, the physicochemical complexity of the Mcl-1 BH3-binding groove and safety-related concerns continue to complicate inhibitor development [5]. Recent studies further support Mcl-1 as a relevant but challenging anticancer target. In HCC models, dual inhibition of Mcl-1 and Bcl-2 using MIK665/S64315 and venetoclax synergistically induced intrinsic apoptotic cell death [6]. Other recent efforts, including first-in-human evaluation of AZD5991 and preclinical development of BRD-810, compound 26, and macrocyclic Mcl-1 inhibitors, highlight continued attempts to improve potency, selectivity, pharmacokinetics, and safety [7, 8]. Nevertheless, no Mcl-1 inhibitor has yet been approved for clinical use.

Natural products from medicinal plants provide structurally diverse scaffolds for modulating apoptosis-related targets [9]. *Inula japonica* (Asteraceae) is a source of sesquiterpenoids and sesquiterpene lactones with reported cytotoxic and apoptosis-associated activity against hepatocarcinoma cell lines, including HepG2 and SMMC-7721 [10, 11]. *In silico* workflows can accelerate early prioritization by integrating structure-based screening, conformational stability assessment in explicit solvent, end-point free-energy estimation, and developability-oriented profiling before resource-intensive experimentation. AutoDock-based docking has become a widely adopted approach for pose generation and interaction mapping. At the same time, molecular dynamics simulations with GROMACS enable time-resolved evaluation of binding-mode persistence under physiologically relevant conditions [12]. Complementary MMGBSA (Molecular mechanics generalised Born surface area) analysis supports comparative energetic ranking from ensemble

* To whom all correspondence should be sent:
E-mail*: hungnd@tnue.edu.vn*

© 2026 Bulgarian Academy of Sciences, Union of Chemists in Bulgaria

snapshots, and pkCSM provides rapid ADMET (Absorption, Distribution, Metabolism, Excretion, Toxicity) inference using graph-based molecular signatures [13, 14]. Quantum-chemical calculations with ORCA further inform electronic descriptors relevant to noncovalent recognition and reactivity trends at the lead-optimization stage [15]. Accordingly, this study evaluated reported sesquiterpenoids from *I. japonica* against Mcl-1 (PDB: 6B4U), using Simvastatin as a clinically used apoptosis-associated comparative compound to contextualize binding, stability, and developability within a unified computational approach.

MATERIALS AND METHODS

Structural preparation of selected ligands

The list of sesquiterpenoids possessing anti-cancer activity against the SMMC-7721 human hepatocarcinoma cell line was collected in the previous study [16]. For details, the selected ligands, including 1β-hydroxyalantolactone (CPD1), eupatolide (CPD2), deacetylovatifolin (CPD3), 2α-acetoxy-4β-hydroxy-pseudoguaia-11(13)-en-12,8α-olide (CPD4), deacetylbritanin (CPD5), 2α,6α-diacetoxy-4β-hydroxy-pseudoguaia-11(13)-en-12,8α-olide (CPD6), 6α-isovaleryloxy-4-oxo-4,5-seco-guaia-1(5),11(13)-dien-12,8β-olide (CPD7), 6-*O*-isobutyrylbritannilactone (CPD8), and 1-*O*-acetyl-6-*O*-isobutyrylbritannilactone (CPD9), have molecular formulas $C_{17}H_{22}O_4$, $C_{15}H_{20}O_3$, $C_{15}H_{20}O_4$, $C_{17}H_{24}O_5$, $C_{17}H_{24}O_6$, $C_{19}H_{26}O_7$, $C_{20}H_{28}O_5$, $C_{19}H_{28}O_5$, and $C_{21}H_{30}O_6$, with molecular weights of 290.1518, 248.1412, 264.1362, 308.1624, 324.1573, 366.1679, 348.1937, 336.1937, and 378.2042 Da, respectively. Simvastatin, with molecular formula $C_{25}H_{38}O_5$ and molecular weight of 418.2719 Da, was chosen as a comparative reference compound because of its clinical use and reported apoptosis-associated anticancer activity (Figure 1).

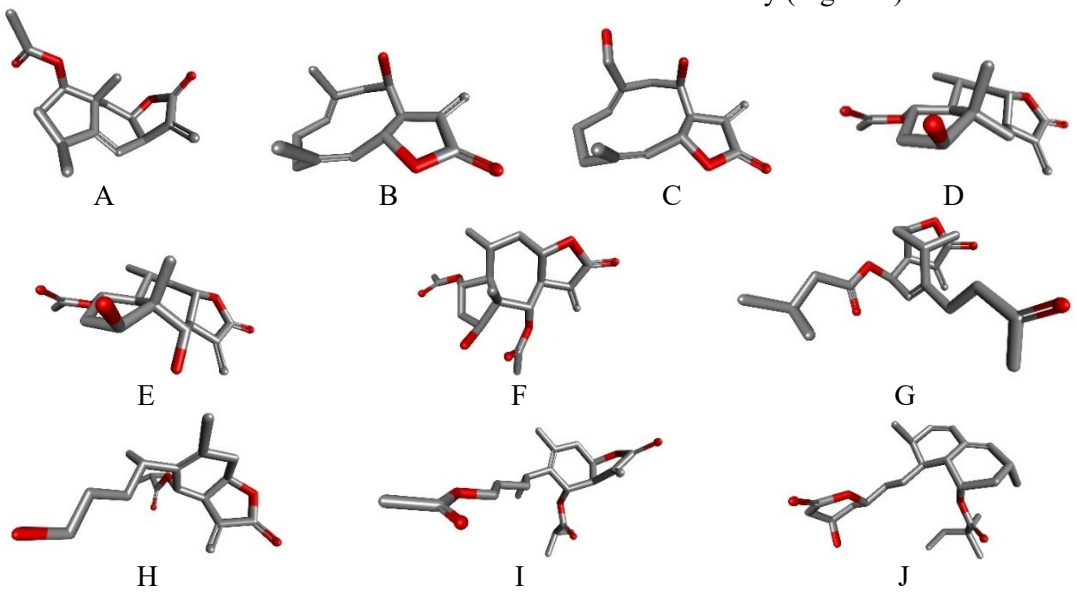


Figure 1. 3D Structures of selected ligands: (A) CPD1, (B) CPD2, (C) CPD3, (D) CDP4, (E) CPD5, (F) CPD6, (G) CPD7, (H) CPD8, (I) CPD9, and (J) Simvastatin.

Molecular docking analysis

Three-dimensional ligand conformations were prepared and exported in PDB format using BIOVIA Discovery Studio Visualizer. Polar hydrogen atoms were added, Gasteiger partial charges were assigned, and all rotatable torsions were defined as flexible. The structure of the anti-apoptotic target protein Mcl-1 (PDB: 6B4U) was obtained in PDB format from the RCSB Protein Data Bank [17]. Molecular docking was conducted with AutoDock Tools using a 60 × 60 × 60 grid box with a grid spacing of 0.375 Å. The docking region was centered at x = -2.774 Å, y = 16.913 Å, and z = 4.323 Å, following the binding-site coordinates reported for the 6B4U structure. The Lamarckian genetic algorithm guided conformational sampling and pose optimization to prioritize low-energy ligand-protein complexes with favorable intermolecular contacts. After docking, the highest-scoring binding mode was visualized and interpreted in Discovery Studio Client 2024, then evaluated against the docking profile of Simvastatin on the identical receptor as a reference standard to contextualize relative binding characteristics. Docking scores were interpreted as qualitative, within-protocol ranking metrics rather than quantitative measures of binding strength.

Molecular dynamics simulation

Molecular dynamics simulations were performed for the best-ranked docked complex with the 6B4U protein over 100 ns using GROMACS 2024.4 [18]. Before simulation, the protein model was curated in Swiss-PdbViewer to restore missing atoms and unresolved residues where applicable [19], while ligand parameters and topologies were generated with SwissParam [20]. The protein-ligand complex was solvated in a triclinic periodic box filled with Simple Point Charge (SPC) water and supplemented with 0.15 M NaCl to mimic physiological ionic strength and ensure overall charge neutrality. Energy relaxation was then carried out for 50,000 minimization steps to remove unfavorable contacts. Equilibration consisted of a 200 ps NVT (Number of particles, Volume, and Temperature) stage followed by a 200 ps NPT stage at 300 K and 1.0 bar. For each system, one 100-ns production run was executed using a 2-fs time step, and trajectory frames were recorded at 10 ps intervals. Simulation outputs were analyzed in Grace to extract core descriptors of structural stability and compactness, including root mean square deviation (RMSD), per-residue root mean square fluctuation (RMSF), radius of gyration (Rg), number of hydrogen bonds (Hbonds), and solvent-accessible surface area (SASA). Conformational stability of bound states was further examined by structural superposition in UCSF Chimera 1.13.3, aligning representative snapshots to evaluate whether ligand positioning within the active site remained consistent from 0 ns to 100 ns. Persistence of key contacts, including hydrogen bonding, van der Waals, and hydrophobic interactions, was inspected across the trajectory to characterize the durability and time-dependent evolution of ligand engagement throughout the 100 ns simulations.

Assay protocol for ADMET prediction

Early-stage ADMET profiling is integral to drug discovery because it can reveal pharmacokinetic liabilities and potential toxicities before costly downstream development, thereby reducing late-stage failures and facilitating the prioritization of compounds with more suitable developability. In the present work, the pkCSM web server was applied to predict ADMET-associated endpoints for CPD9 and Simvastatin. Using graph-based molecular signatures, pkCSM infers descriptors linked to absorption, distribution, metabolism, excretion, and toxicity, allowing a structured *in silico* comparison of these properties across the evaluated candidates.

Molecular mechanics generalized Born surface area (MMGBSA) analysis

Binding free energies for the CPD9-6B4U and Simvastatin-6B4U complexes were estimated using MMGBSA analysis implemented in gmx_MMPBSA under the CHARMM36 force field. In this framework, the generalized Born term was used to approximate the electrostatic contribution to solvation in an implicit solvent representation. In contrast, non-polar solvation was quantified from the solvent-accessible surface area. Energy components were extracted from the molecular dynamics trajectories using 125 uniformly distributed snapshots collected at 80 ps intervals over the 20-100 ns segment, corresponding to an 80 ns analysis window. Mean values derived from these frames were used to reflect within-trajectory temporal variability in ligand-protein coupling and to characterize relative MMGBSA energetic trends within the simulated environment. These endpoint estimates were interpreted as approximate within-protocol values rather than definitive experimental binding affinities or standalone criteria for lead superiority.

Quantum chemistry computation using the Density Functional Theory (DFT) method

Geometry optimization of CPD9 and Simvastatin was performed using the ORCA 6.1.0 quantum-chemistry suite. Molecular structures were first built in Avogadro and subsequently inspected, visualized, and subjected to orbital interpretation with IboView (v20211019). Density functional theory calculations were carried out at the B3LYP/6-31G(d,p) level to obtain reliable ground-state geometries and electronic-structure descriptions. Based on the optimized conformations, frontier orbital energies (HOMO and LUMO) were determined and used to estimate the energy gap (ΔE) and related reactivity descriptors, including chemical potential (μ), electronegativity (χ), hardness (η), softness (σ), and electrophilicity index (ω). These descriptors were derived through Koopmans-type relationships to support the comparative evaluation of the electronic characteristics of the investigated molecules [21, 22].

RESULTS AND DISCUSSION

Molecular docking analysis

Molecular docking supports structure-based screening by exploring ligand conformations and orientations inside a predefined binding pocket, followed by ranking with a scoring function that approximates binding propensity. Despite clear utility for prioritization, docking scores remain

model-dependent and sensitive to protein/ligand flexibility and parametrization; therefore, subsequent refinement by dynamics or end-point free-energy methods is commonly recommended [23]. Within apoptosis research, anti-apoptotic Bcl-2 family members are central regulators of mitochondrial cell-death control, and pharmacologic disruption of BH3-groove interactions has emerged as a validated anticancer strategy [24]. Before production docking, the protocol was validated by redocking the co-crystallized ligand and comparing the regenerated pose with the crystallographic conformation. This procedure yielded an RMSD of 0.9700 Å (Figure 2), indicating close pose reproduction. RMSD values below 2 Å are commonly used as a practical criterion for acceptable docking performance [25]. Following validation, candidate binding poses were ranked by docking score and the lowest-scoring conformations were selected for downstream interaction assessment.

The binding energies and key non-covalent contacts (hydrogen bonding, van der Waals, and hydrophobic interactions) observed between the docked ligands and the 6B4U protein were summarized in Table 1.

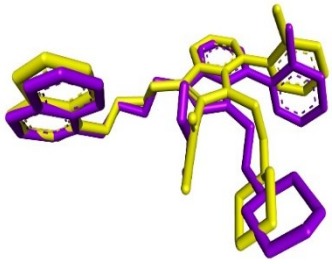


Figure 2. Superimposition of the docked and native ligands for validation of the molecular docking protocol on protein 6GL8 (violet = native, yellow = docked)

Table 1. Interactions between the docked ligands and the protein 6B4U.

Docked ligands	Binding energy (kcal/mol)	Hydrogen bond interaction	Van der Waals interaction	Hydrophobic interaction
CPD1	-8.20	-	Phe228, Met231, Leu235, Val249, Arg263, Thr266, Phe270	Met250, Val253, Phe254, Leu267
CPD2	-8.06	Leu246, Gly271	Leu235, Phe254, Ile294	Met231, Val249, Met250, Val253, Leu267, Phe270, Val274, Leu290
CPD3	-7.56	Leu267	Met231, Leu235, Ile237, Val249, Val253, Phe254, Thr266, Ile268, Gly271, Ile294	Leu246, Met250, Phe270, Val274, Leu290
CPD4	-8.73	-	Phe228, Leu235, Leu246, Phe254, Thr266, Val274, Leu290, Ile294	Met231, Val249, Met250, Val253, Leu267, Phe270
CPD5	-8.47	Leu267	Phe228, Leu235, Leu246, Val249, Phe254, Arg263, Thr266, Gly271, Val274, Leu290, Ile294	Met231, Met250, Val253, Leu267, Phe270
CPD6	-8.24	-	Ala227, Phe228, Leu235, Leu246, Phe254, Thr266, Gly271, Val274, Leu290, Ile294	Met231, Val249, Met250, Val253, Phe270
CPD7	-8.69	Met250	Ala227, Phe228, Met231, Leu235, Val249, Phe254, Thr266, Gly271, Val274, Leu290, Ile294	Leu246, Met250, Val253, Leu263, Phe270
CPD8	-8.35	Leu246, Leu267	Phe228, Leu235, Phe254, Arg263, Thr266	Ala227, Met231, Val249, Met250, Val253, Leu267, Phe270
CPD9	-8.84	-	Phe228, Met231, Leu235, Ile237, Leu246, Val253, Phe254, Arg263, Thr266, Gly271, Val274, Leu290, Ile294	Val249, Met250, Leu267, Phe270
Simvastatin	-8.80	Leu246	Ala227, Thr266, Ile294	Phe228, Met231, Leu235, Val249, Met250, Val253, Phe254, Arg263, Leu267, Phe270

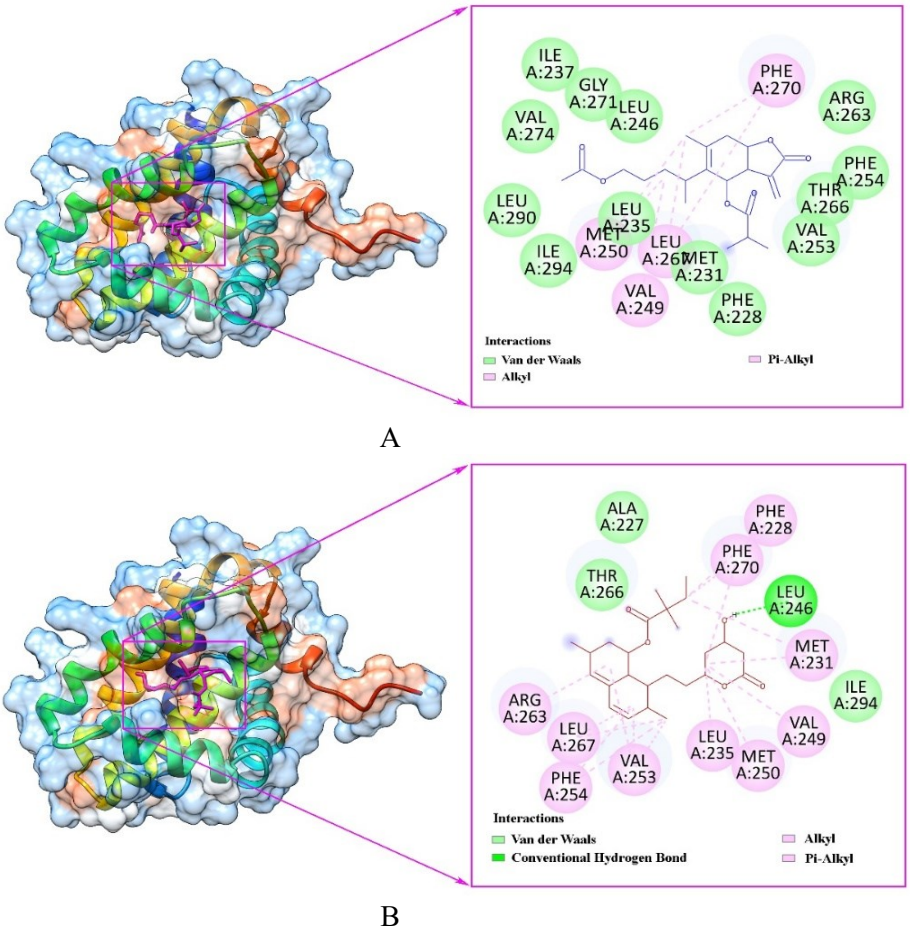


Figure 3. Molecular docking model and 2D interaction diagram of CPD9 (A) and Simvastatin (B) with 6B4U protein

Docking of CPD1-CPD9 against the 6B4U target indicated consistently favorable predicted affinities (-7.56 to -8.84 kcal/mol), with CPD9 presenting the most negative binding energy (-8.84 kcal/mol), which was essentially comparable to that of Simvastatin (-8.80 kcal/mol) rather than meaningfully superior. Because the difference between CPD9 and Simvastatin was only 0.04 kcal/mol, this small numerical gap was not interpreted as evidence of stronger binding. Instead, docking was used as a qualitative prioritization step based on score ranking, binding-site occupancy, and interaction patterns. Among the screened ligands, CPD9 occupied the canonical groove region delineated by Met250, Val253, Arg263, Thr266, Leu267, Phe270, and Gly271, indicating a well-positioned docking pose within a residue cluster repeatedly implicated in BH3-groove recognition and inhibitor optimization for MCL-1-like pockets (Figure 3A) [26]. Notably, CPD9 formed no hydrogen bond in the docking pose, suggesting that stabilization is dominated by close-range packing and non-directional contacts rather than a single polar anchor. A broad van der Waals network was predicted for CPD9, involving Phe228, Met231, Leu235, Ile237, Leu246, Val253, Phe254, Arg263, Thr266, Gly271, Val274, Leu290, and Ile294, accompanied by hydrophobic contacts with Val249, Met250, Leu267, and Phe270. The prevalence of hydrophobic and dispersion-driven interactions aligns with physical descriptions of protein-ligand stabilization in apolar grooves, where surface complementarity and burial of nonpolar areas can compensate for limited hydrogen bonding [27].

Simvastatin, used as a reference ligand, displayed a partially overlapping interaction footprint, with active-site involvement of Ala227, Met250, Val253, Arg263, Thr266, and Leu267 and a hydrogen bond to Leu246. Hydrophobic contacts spanned Phe228, Met231, Leu235, Val249, Met250, Val253, Phe254, Arg263, Leu267, and Phe270, while van der Waals contributions were noted for Ala227, Thr266, and Ile294. The overlap between CPD9 and Simvastatin at Leu246, Met250, Val253, Thr266, Leu267, Phe270 supports occupation of the same predicted pocket region, strengthening qualitative comparability of the docking poses across both systems (Figure 3B). In addition, Simvastatin has documented pleiotropic anticancer-relevant mechanisms in the literature, including modulation of apoptosis-related pathways, supporting suitability

as a benchmark compound in an anti-apoptosis-oriented computational workflow [28].

Across the remaining candidates, CPD4 (-8.73) and CPD7 (-8.69) also approached the reference score, whereas CPD3 showed the least favorable value (-7.56). Several ligands exhibited one or more hydrogen bonds (CPD2: Leu246 and Gly271; CPD3: Leu267; CPD5: Leu267; CPD7: Met250; CPD8: Leu246 and Leu267), yet the most negative docking score was associated with CPD9 in the absence of hydrogen bonding, reinforcing the possibility that pocket-filling hydrophobic, van der Waals complementarity can dominate predicted affinity in this binding site [29].

Based on the docking rank order among the screened sesquiterpenoids and the extensive, pocket-spanning contact pattern that substantially overlaps the Simvastatin interaction region, CPD9 represents the most justified choice for molecular dynamics simulations and downstream energetic validation, with Simvastatin retained as the comparator for stability and binding persistence analyses. This prioritization is consistent with contemporary guidance that docking-based triage benefits from follow-up sampling to assess conformational adaptation and interaction durability, particularly in Bcl-2 family grooves, where induced fit and contact reorganization can influence final rankings.

Molecular dynamics simulation

Molecular dynamics (MD) simulations were used to evaluate the time-dependent behavior of the CPD9-6B4U and Simvastatin-6B4U complexes in explicit solvent. Trajectory descriptors, including RMSD, RMSF, Rg, hydrogen bonds, and SASA, were analyzed to assess global stability, local flexibility, compactness, polar contacts, and solvent exposure [30]. Therefore, the evaluation systematically investigated these metrics to determine the stability, flexibility, and solvent exposure of the CPD9-6B4U and Simvastatin-6B4U complexes throughout the simulation timeframe.

Across 100 ns, backbone RMSD traces for the CPD9-6B4U and Simvastatin-6B4U complexes remained within a narrow sub-nanometer band, supporting preservation of the overall fold without a sustained deviation pattern compatible with large-scale destabilization [31].

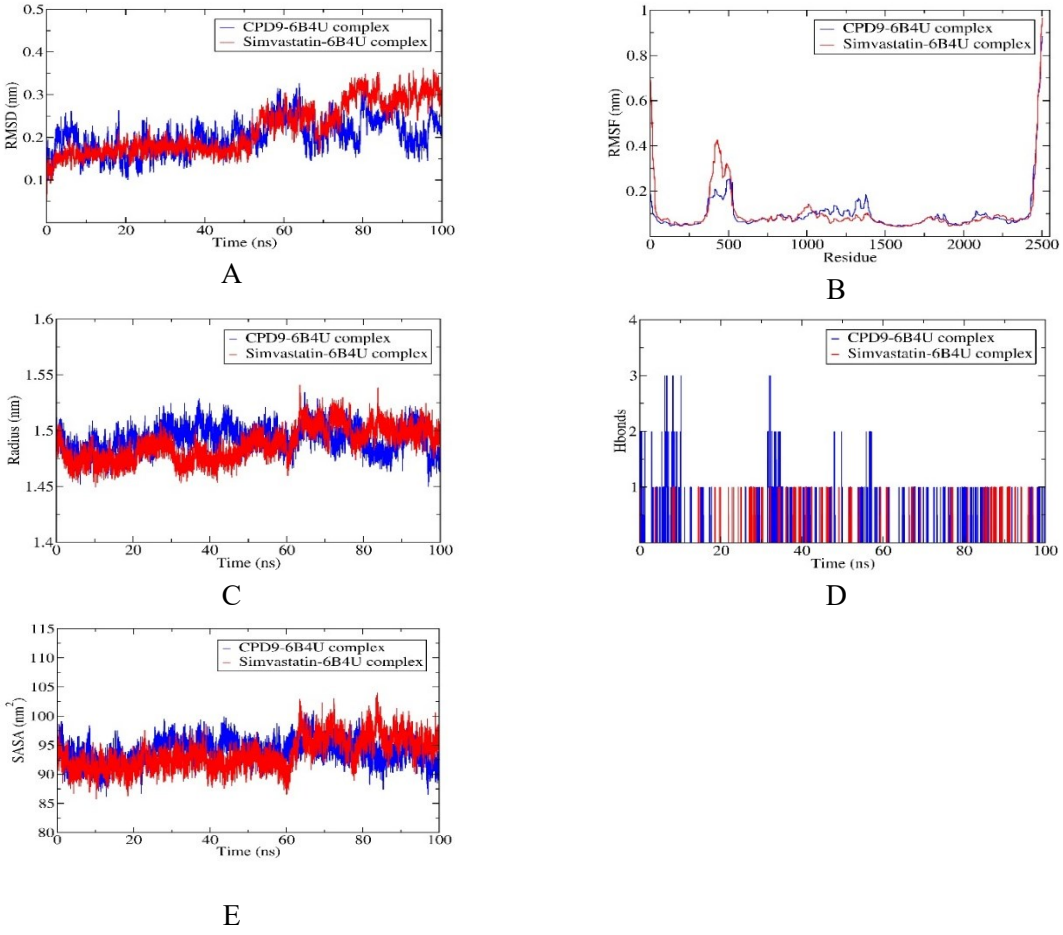


Figure 4. Results of MD simulation for the bindings of CPD9 (blue) and Simvastatin (red) with 6B4U protein: (A) RMSD, (B) RMSF, (C) Rg, (D) Hbonds, (E) SASA

After early equilibration and a modest increase around 50-70 ns, the Simvastatin-6B4U trajectory more frequently occupied a higher RMSD envelope after 70 ns, whereas CPD9-6B4U showed a lower late-stage deviation trend (Figure 4A).

Residue-level RMSF analysis over the Ser171-Glu325 segment showed low fluctuations for both complexes, with no sharp peaks or localized destabilization events (Figure 4B). Minor trace differences were observed, suggesting only subtle trajectory-level variation in local flexibility.

Rg profiles also showed broadly overlapping ranges, indicating comparable global compactness. However, Simvastatin-6B4U displayed a mild tendency toward higher Rg values after 60 ns, while CPD9-6B4U maintained a slightly tighter late-stage distribution (Figure 4C). Because Rg tracks mass distribution around the center of geometry, these patterns support a more expanded conformational ensemble for the Simvastatin-bound state in the late stage, alongside a comparatively compact ensemble under CPD9 [32].

Hydrogen-bond analysis showed sparse polar contacts in both complexes, with counts mostly fluctuating around 0-1. CPD9-6B4U displayed occasional short-lived spikes above 1, especially early in the trajectory, whereas Simvastatin-6B4U largely remained within the 0-1 range (Figure 4D). These transient changes likely reflect local rearrangements, water mediation, and side-chain reorientation rather than persistent polar anchoring [33].

SASA profiles further supported the late-stage differences between the two systems. Before 60 ns, both complexes overlapped mainly within the low-to-mid 90 nm^2 region. After 60 ns, Simvastatin-6B4U sampled higher SASA values more frequently and showed broader fluctuations, consistent with increased surface exposure and pocket-breathing behavior (Figure 4E). In contrast, CPD9-6B4U remained within a somewhat lower SASA band toward the end of the run, suggesting reduced solvent exposure in the final segment [34].

Overall, both complexes remained stable across the 100 ns trajectories. CPD9-6B4U showed a descriptive late-stage trend toward lower RMSD, slightly tighter compactness, and reduced solvent exposure, whereas Simvastatin-6B4U displayed modestly higher RMSD, Rg, and SASA variability after mid-simulation. These MD results were interpreted as single-trajectory descriptive observations supporting further energetic analysis, rather than as replicate-based statistical evidence of superior stability.

Free binding energy (MMGBSA) analysis

Molecular mechanics generalized Born surface area (MMGBSA) was used as an endpoint approach to estimate relative binding energetics from MD snapshots, complementing docking by incorporating conformational and implicit-solvent effects. In gmx_MMPBSA, the total binding estimate was decomposed into gas-phase interactions (ΔG_GAS = ΔVDW + ΔEEL) and solvation terms (ΔG_SOLV = ΔE_GB + ΔE_SURF), where ΔE_GB represents polar solvation and ΔE_SURF reflects nonpolar surface-area contributions [35]. As summarized in Table 2, both complexes displayed favorable mean MMGBSA totals, with Simvastatin-6B4U showing a more negative ΔTOTAL (-28.70 ± 2.35 kcal/mol) than CPD9-6B4U (-17.59 ± 3.59 kcal/mol), indicating a stronger MMGBSA-estimated binding profile for Simvastatin under the same protocol and sampling window. Accordingly, the MMGBSA result does not support interpreting CPD9 as the stronger-binding ligand relative to Simvastatin. Instead, it identifies binding-energy optimization, particularly improvement of van der Waals stabilization, as a key requirement for CPD9. The energetic difference was dominated by dispersion-driven packing: ΔVDW was substantially more favorable for Simvastatin (-37.01 ± 2.56 kcal/mol) than for CPD9 (-22.06 ± 3.42 kcal/mol), consistent with MMGBSA observations that hydrophobic shape complementarity and van der Waals contacts often contribute strongly to binding in apolar grooves. Electrostatics contributed modestly for both systems (ΔEEL = -3.01 ± 6.80 kcal/mol for Simvastatin; -3.85 ± 6.88 kcal/mol for CPD9), while polar solvation opposed complex formation more strongly for Simvastatin (ΔEGB = 15.94 ± 6.89 kcal/mol) than for CPD9 (11.44 ± 6.55 kcal/mol). Nonpolar solvation favored binding in both cases (ΔE_SURF = -4.61 ± 0.31 kcal/mol for Simvastatin; -3.12 ± 0.49 kcal/mol for CPD9), partially offsetting the generalized Born penalty and reinforcing a binding mode enriched in nonpolar burial [36].

Aggregated terms confirmed the same trend. Simvastatin showed more favorable gas-phase energy (ΔG_GAS = -40.02 ± 7.43 kcal/mol) than CPD9 (-25.91 ± 8.35 kcal/mol), whereas solvation opposed binding more strongly for Simvastatin (ΔG_SOLV = 11.33 ± 6.77 kcal/mol) than CPD9 (8.32 ± 6.34 kcal/mol). The smaller ΔTOTAL standard deviation for Simvastatin also suggests more consistent binding energetics across the analyzed snapshots compared with CPD9 [37].

Taken together, MMGBSA decomposition indicates that Simvastatin-6B4U achieves a stronger mean binding estimate primarily through enhanced

van der Waals stabilization and slightly more favorable nonpolar solvation, despite a larger polar-solvation penalty. CPD9-6B4U shows weaker overall MMGBSA favorability but benefits from a smaller generalized Born penalty and marginally more favorable electrostatics. Therefore, CPD9 was not interpreted as superior to Simvastatin in terms of MMGBSA binding energetics. Rather, CPD9 was retained as a prioritized sesquiterpenoid scaffold because it showed the most favorable docking score among the screened sesquiterpenoids, maintained acceptable single-trajectory MD behavior, and displayed several developability-relevant features in ADMET and DFT analyses. The less favorable ΔTOTAL and ΔVDW values of CPD9 are now explicitly treated as limitations and as targets for future structure-guided optimization.

ADMET prediction analysis

In silico ADMET profiling was conducted to contextualize developability-relevant pharmacokinetic behavior and safety flags for CPD9, compared with Simvastatin, using the pkCSM framework, which relies on graph-based molecular signatures for multi-endpoint prediction. Table 3 compiles the predicted absorption, distribution, metabolism, excretion, and toxicity outputs and enables an early-stage comparison of liabilities and strengths across both candidates within a consistent descriptor model.

Table 2. Free energy of binding obtained using MMGBSA calculations.

Energy component	Average (kcal/mol)		Standard deviation	
	CPD9-6B4U	Simvastatin-6B4U	CPD9-6B4U	Simvastatin-6B4U
ΔVDWAALS	-22.06	-37.01	3.42	2.56
ΔEEL	-3.85	-3.01	6.88	6.80
ΔEGB	11.44	15.94	6.55	6.89
ΔESURF	-3.12	-4.61	0.49	0.31
ΔGGAS	-25.91	-40.02	8.35	7.43
ΔGSOLV	8.32	11.33	6.34	6.77
ΔTOTAL	-17.59	-28.70	3.59	2.35

Table 3. Predicted ADMET properties of CPD9 and Simvastatin

ADMET properties	Unit	CPD9	Simvastatin
Water solubility	(Log mol/L)	-3.967	-5.239
Caco2 permeability	(Log Papp in 10^{-6} cm/s)	1.42	1.106
Intestinal absorption (Human)	(% Absorbed)	100	96.822
Skin permeability	(Log Kp)	-3.054	-3.547
P-glycoprotein substrate	Yes/No	No	Yes
P-glycoprotein I inhibitor	Yes/No	Yes	Yes
P-glycoprotein II inhibitor	Yes/No	No	Yes
VDss (Volume of distribution at steady state)	(Log L/kg)	-0.203	0.328
Fraction unbound (human)	(Fu)	0.198	0.196
BBB (Blood brain barrier) permeability	(Log BB)	-0.666	-0.304
CNS (Central nervous system) permeability	(Log PS)	-2.846	-2.262
CYP2D6 substrate	Yes/No	No	No
CYP3A4 substrate	Yes/No	Yes	Yes
CYP1A2 inhibitor	Yes/No	No	No
CYP2C19 inhibitor	Yes/No	No	No
CYP2C9 inhibitor	Yes/No	No	No
CYP2D6 inhibitor	Yes/No	No	No
CYP3A4 inhibitor	Yes/No	No	No
Total clearance	(Log ml/min/kg)	1.325	0.775
Renal OCT2 (Organic cation transporter 2) substrate	Yes/No	Yes	No
AMES toxicity	Yes/No	Yes	No
Maximum tolerated dose (human)	(Log mg/kg/day)	0.278	-0.164
Human Ether-a-go-go Related Gene (hERG) I inhibitor	Yes/No	No	No
hERG II inhibitor	Yes/No	No	Yes
Oral rat acute toxicity (LD50)	(mol/kg)	2.181	2.302
Oral rat chronic toxicity (LOAEL)	(Log mg/kg_bw/day)	1.812	1.251
Hepatotoxicity	Yes/No	No	No
Skin sensation	Yes/No	No	No
Tetrahymena pyriformis toxicity	(Log ug/L)	0.485	0.877
Minnow toxicity	(Log mM)	0.999	-0.215

Predicted aqueous solubility was higher for CPD9 than for Simvastatin (-3.967 *vs*. -5.239 log mol/L), suggesting a less pronounced solubility limitation for CPD9. Absorption-related descriptors also favored CPD9, including higher Caco-2 permeability (1.42 *vs*. 1.106 log Papp) and slightly higher intestinal absorption (100% *vs.* 96.822%) [38]. CPD9 was not predicted as a P-glycoprotein substrate, whereas Simvastatin was; however, both compounds were predicted as P-glycoprotein I inhibitors, and only Simvastatin was predicted as a P-glycoprotein II inhibitor [39].

Distribution descriptors showed higher VDss for Simvastatin than CPD9 (0.328 *vs*. -0.203 log L/kg), while fraction unbound values were nearly identical (0.198 *vs*. 0.196). Both compounds showed negative central distribution indices, although Simvastatin had less negative logBB and logPS values, suggesting relatively higher modeled CNS access than CPD9 within the same prediction scale [40]. For metabolism, both compounds were predicted as CYP3A4 substrates and CYP2D6 non-substrates. No inhibition was predicted for CYP1A2, CYP2C19, CYP2C9, CYP2D6, or CYP3A4, suggesting limited CYP inhibition-related interaction risk in this model [41]. CPD9 showed higher predicted total clearance than Simvastatin (1.325 *vs.* 0.775 log ml/min/kg) and was annotated as an OCT2 substrate, whereas Simvastatin was not. This indicates a possible renal transporter-related liability for CPD9 [42]. Safety predictions revealed the most important limitation of CPD9: it was AMES-positive, while Simvastatin was AMES-negative. Neither compound was predicted as an hERG I inhibitor, but Simvastatin was predicted as an hERG II inhibitor, unlike CPD9 [43]. Acute and chronic rodent toxicity values were broadly comparable, and both compounds were predicted negative for hepatotoxicity and skin sensitization. Ecotoxicity endpoints differed numerically, but these values were not extrapolated beyond the model outputs [44]. Both values exceed the toxicity threshold (> -0.5), indicating a positive flag for this endpoint in both candidates. Neither compound meets the high acute toxicity criterion (logLC50 < -0.3). This result was not treated as a minor toxicity flag, because an AMES-positive alert indicates potential mutagenic/genotoxic liability and can substantially limit the direct developability of a candidate compound. Although this in silico prediction does not confirm experimental genotoxicity, it identifies CPD9 as a scaffold requiring careful structural optimization before further advancement. Therefore, the favorable predicted absorption, Caco-2 permeability, solubility, and non-P-gp-substrate profile of CPD9 should be interpreted cautiously and cannot compensate for the predicted genotoxicity liability. Future work should prioritize removal or reduction of the structural features responsible for the AMES-positive alert, followed by experimental AMES testing and complementary genotoxicity assays.

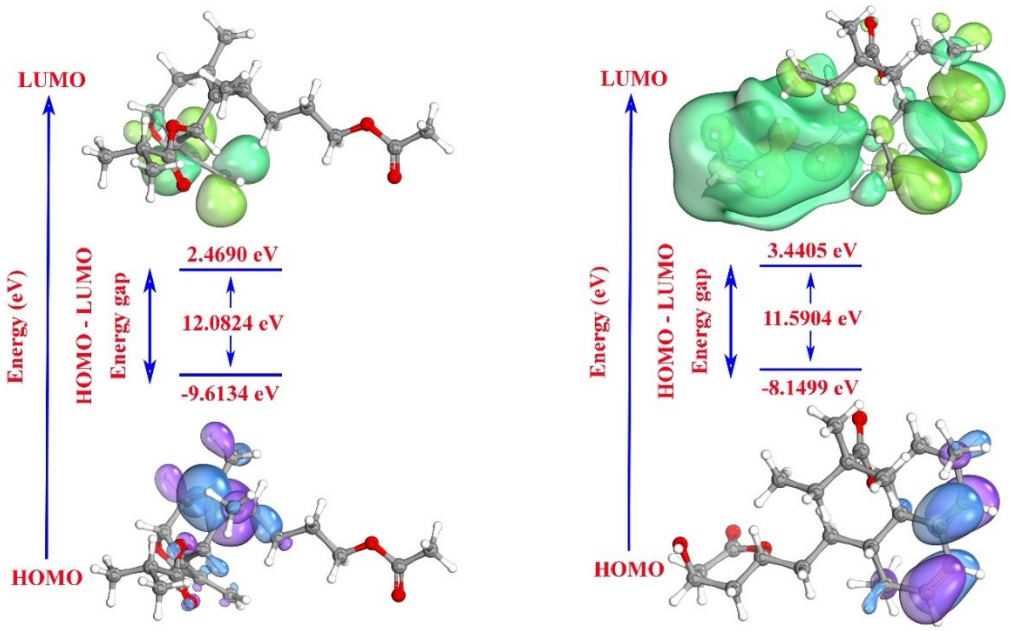
Collectively, pkCSM outputs suggest that CPD9 combines improved predicted solubility, permeability, and intestinal absorption with higher predicted clearance and an OCT2-substrate annotation. At the same time, Simvastatin shows stronger modeled tissue distribution and comparatively higher central distribution indices, along with an hERG II inhibition flag. The principal developability concern for CPD9 in this panel is the AMES-positive prediction, which typically warrants prioritization of confirmatory genotoxicity assessment or structural refinement during lead optimization.

Quantum chemistry computation using the DFT method

Density functional theory (DFT) descriptors were examined for CPD9 and Simvastatin to compare frontier-orbital characteristics and global conceptual-DFT reactivity indices derived from electronic structure analysis. Frontier orbital energies provide a compact proxy for charge-transfer tendencies, where lower EHOMO generally reflects reduced electron-donor propensity and lower ELUMO is commonly associated with enhanced electron-acceptor character within the same computational level [45]. As shown in Table 4, CPD9 exhibits a deeper EHOMO (-9.6134 eV) than Simvastatin (-8.1499 eV), consistent with CPD9's higher resistance to electron removal under the applied model. CPD9 also presents a lower ELUMO (2.4690 eV) than Simvastatin (3.4405 eV), indicating comparatively stronger electron-acceptor character for CPD9 in the same descriptor space.

Table 4. Quantum descriptors of CPD9 and Simvastatin. EHOMO: highest occupied molecular orbitals; ELUMO: lowest unoccupied molecular orbitals; ΔE: energy gap; μ: chemical potential; χ: electronegativity; η: hardness; σ: softness; ω: electrophilicity index.

Molecule	EHOMO (eV)	ELUMO (eV)	ΔE (eV)	μ (eV)	χ (eV)	η (eV)	σ (eV^{-1})	ω (eV)
CPD9	-9.6134	2.4690	12.0824	-3.5722	3.5722	6.0412	0.1655	1.0561
Simvastatin	-8.1499	3.4405	11.5904	-2.3547	2.3547	5.7952	0.1726	0.4784



A B

Figure 5. HOMO and LUMO surface diagrams of CPD9 (A) and Simvastatin (B)

The HOMO-LUMO gap (ΔE) is frequently used as a qualitative indicator of electronic responsiveness and kinetic stability, with larger gaps often aligning with greater global hardness [46]. CPD9 shows a slightly larger ΔE (12.0824 eV) than Simvastatin (11.5904 eV), suggesting modestly higher electronic rigidity for CPD9 (Figure 5). This trend agrees with the conceptual descriptors hardness (η) and softness (σ): CPD9 has higher η (6.0412 eV) and lower σ (0.1655 eV^{-1}) than Simvastatin (η = 5.7952 eV; σ = 0.1726 eV^{-1}), supporting a shift toward a globally harder profile for CPD9.

Charge-transfer descriptors further differentiate the molecules. Chemical potential (μ) and electronegativity (χ) are commonly interpreted as global measures of electron-escaping tendency and electron-attracting character, respectively, within conceptual DFT [47]. CPD9 displays a more negative μ (-3.5722 eV) and higher χ (3.5722 eV) than Simvastatin (μ = -2.3547 eV; χ = 2.3547 eV), consistent with a stronger overall electron-attracting character for CPD9 in this framework. The electrophilicity index (ω), a global descriptor derived from μ and η and often used to summarize electrophile strength, is higher for CPD9 (1.0561 eV) than for Simvastatin (0.4784 eV), indicating greater predicted electrophilic character for CPD9 under the same assumptions used to compute global indices from frontier-orbital energies [48].

Overall, the descriptor pattern supports an electronic profile for CPD9 characterized by deeper frontier orbital energies, a slightly larger gap, increased global hardness, and higher electrophilicity relative to Simvastatin. Such trends are frequently discussed as contributors to differential noncovalent recognition and stabilization propensities in biomolecular environments, yet remain dependent on the chosen functional/basis set and the approximations used to map orbital energies to conceptual descriptors.

CONCLUSION

This study presents an integrated *in silico* evaluation of sesquiterpenoids from *I. japonica* against the anti-apoptotic protein Mcl-1 (6B4U) in hepatocarcinoma. CPD9 showed the numerically most negative docking score among the screened sesquiterpenoids (-8.84 kcal/mol), which was essentially comparable to that of Simvastatin (-8.80 kcal/mol), fitting deeply into the canonical groove *via* large van der Waals and hydrophobic contacts. Over 100 ns MD, both complexes remained stable, while CPD9 showed tighter late-stage behavior (lower backbone deviation, less Rg/SASA drift) than Simvastatin. MMGBSA, however, favored Simvastatin overall (ΔTOTAL -28.70 ± 2.35 kcal/mol) over CPD9 (-17.59 ± 3.59 kcal/mol), mainly due to stronger van der Waals stabilization (-37.01 *vs.* -22.06 kcal/mol). Thus, CPD9 should not be interpreted as the stronger-binding ligand based on MMGBSA. Instead, its weaker ΔTOTAL and ΔVDW values highlight the need for structure-guided optimization to improve pocket packing and dispersion-driven stabilization. ADMET predictions suggested that CPD9 has better modeled solubility

and permeability and is not a P-gp substrate, but it carries a key concern with an AMES-positive flag. DFT descriptors further indicated that CPD9 is electronically harder and more electrophilic than Simvastatin. Overall, CPD9 remains a prioritized sesquiterpenoid scaffold for further optimization, but not a directly developable lead in its current form, because its weaker MMGBSA binding estimate and major AMES-positive genotoxicity liability must be addressed.

Despite these computational signals, experimental validation is required to confirm true target engagement and anti-cancer efficacy. Future work should prioritize biochemical binding assays, hepatocarcinoma cell assays (apoptosis/viability and mitochondrial-pathway markers), and confirmatory genotoxicity testing to resolve the AMES-positive prediction, alongside transporter studies (OCT2) and broader safety profiling. Structure-guided refinement should aim to strengthen binding energy while reducing predicted liabilities. If CPD9 sustains potency and safety in preclinical tests, it could justify progression toward translational development for Mcl-1-driven hepatocarcinoma.

REFERENCES

1. F. Bray, M. Laversanne, H. Sung, J. Ferlay, R. L. Siegel, I. Soerjomataram, A. Jemal, *CA. Cancer J. Clin.*, **74**, 229 (2024).
2. J. U. Marquardt, F. Edlich, *Front. Oncol.*, **9**, 1421 (2019).
3. D. Kaloni, S. T. Diepstraten, A. Strasser, G. L. Kelly, *Apoptosis*, **28**, 20 (2023).
4. V. V Senichkin, A. Y. Streletskaia, A. S. Gorbunova, B. Zhivotovsky, G. S. Kopeina, *Cell Death Differ.*, **27**, 405 (2020).
5. S. I. Tantawy, N. Timofeeva, A. Sarkar, V. Gandhi, *Front. Oncol.*, **13**, 1226289 (2023).
6. M. Michalski, M. Bauer, F. Walz, D. Tümen, P. Heumann, P. Stöckert, M. Gunckel, C. Kunst, A. Kandulski, S. Schmid, M. Müller, K. Gülow, *Biomedicines*, **11**, 1666 (2023).
7. P. Desai, S. Lonial, A. Cashen, M. Kamdar, I. Flinn, S. O'Brien, J. S. Garcia, N. Korde, J. Moslehi, M. Wey, P. Cheung, S. Sharma, D. Olabode, H. Chen, F. Ali Syed, M. Liu, J. Saeh, M. Andrade-Campos, T. M. Kadia, J. S. Blachly, *Clin. Cancer Res.*, **30**, 4844 (2024).
8. U. Rauh, G. Wei, M. Serrano-Wu, G. Kosmidis, S. Kaulfuss, F. Siegel, K. Thede, J. McFarland, C. T. Lemke, N. Werbeck, K. Nowak-Reppel, S. Pilari, S. Menz, M. Ocker, W. Zhang, K. Davis, G. Poncet-Montange, J. Roth, D. Daniels, V. K. Kaushik, B. Hubbard, K. Ziegelbauer, T. R. Golub, *Nat. Cancer*, **5**, 1479 (2024).
9. P. Dhyani, P. Sati, E. Sharma, D. C. Attri, A. Bahukhandi, B. Tynybekov, A. Szopa, J. Sharifi-Rad, D. Calina, H. A. R. Suleria, W. C. Cho, *Cancer Cell Int.*, **22**, 305 (2022).
10. T. Wang, T. Chen, Q. Zhang, Y. Cheng, C. Xie, Q. Zhang, Y. Ding, *Chem. Biodivers.*, **20**, e202300220 (2023).
11. Y. Ding, T. Wang, T. Chen, C. Xie, Q. Zhang, *Bioorg. Chem.*, **101**, 103973 (2020).
12. S. Forli, R. Huey, M. E. Pique, M. F. Sanner, D. S. Goodsell, A. J. Olson, *Nat. Protoc.*, **11**, 905 (2016).
13. M. S. Valdés-Tresanco, M. E. Valdés-Tresanco, P. A. Valiente, E. Moreno, *J. Chem. Theory Comput.*, **17**, 6281 (2021).
14. D. E. Pires, T. L. Blundell, D. B. Ascher, *J. Med. Chem.*, **58**, 4066 (2015).
15. F. Neese, *WIREs Comput. Mol. Sci.*, **15**, e70019 (2025).
16. X. D. Wu, L. F. Ding, W. C. Tu, H. Yang, J. Su, L. Y. Peng, Y. Li, Q. S. Zhao, *Phytochemistry*, **129**, 68 (2016).
17. M. Bruncko, L. Wang, G. S. Sheppard, D. C. Phillips, S. K. Tahir, J. Xue, S. Erickson, S. Fidanze, E. Fry, L. Hasvold, G. J. Jenkins, S. Jin, R. A. Judge, P. J. Kovar, D. Madar, P. Nimmer, C. Park, A. M. Petros, S. H. Rosenberg, M. L. Smith, X. Song, C. Sun, Z.-F. Tao, X. Wang, Y. Xiao, H. Zhang, C. Tse, J. D. Leverson, S. W. Elmore, A. J. Souers, *J. Med. Chem.*, **58**, 4089 (2015).
18. D. Van Der Spoel, E. Lindahl, B. Hess, G. Groenhof, A. E. Mark, H. J. C. Berendsen, *J. Comput. Chem.*, **26**, 1701 (2005).
19. N. Guex, M. C. Peitsch, *Electrophoresis*, **18**, 2714 (1997).
20. V. Zoete, M. A. Cuendet, A. Grosdidier, O. Michielin, *J. Comput. Chem.*, **32**, 2359 (2011).
21. J. Luo, Z. Q. Xue, W. M. Liu, J. L. Wu, Z. Q. Yang, *J. Phys. Chem. A*, **110**, 12005 (2006).
22. R. Das, J. L. Vigneresse, P. K. Chattaraj, *Int. J. Quantum Chem.*, **114**, 1421 (2014).
23. P. C. Agu, C. A. Afiukwa, O. U. Orji, E. M. Ezeh, I. H. Ofoke, C. O. Ogbu, E. I. Ugwuja, P. M. Aja, *Sci. Rep.*, **13**, 13398 (2023).
24. C. M. Croce, D. Vaux, A. Strasser, J. T. Opferman, P. E. Czabotar, S. W. Fesik, *Cell Death Differ.*, **32**, 1369 (2025).
25. H. Gohlke, M. Hendlich, G. Klebe, *J. Mol. Biol.*, **295**, 337 (2000).
26. A. Bolomsky, M. Vogler, M. C. Köse, C. A. Heckman, G. Ehx, H. Ludwig, J. Caers, *J. Hematol. Oncol.*, **13**, 173 (2020).
27. G. G. Ferenczy, M. Kellermayer, *Comput. Struct. Biotechnol. J.*, **20**, 1946 (2022).
28. C. Liu, H. Chen, B. Hu, J. Shi, Y. Chen, K. Huang, *Front. Pharmacol.*, **14**, 1188926 (2023).
29. R. Meli, G. M. Morris, P. C. Biggin, *Front. Bioinforma.*, **2**, 885983 (2022).
30. O. M. H. Salo-Ahen, I. Alanko, R. Bhadane, A. M. J. J. Bonvin, R. V Honorato, S. Hossain, A. H. Juffer, A. Kabedev, M. Lahtela-Kakkonen, A. S. Larsen, E. Lescrinier, P. Marimuthu, M. U. Mirza, G. Mustafa, A. Nunes-Alves, T. Pantsar, A. Saadabadi, K. Singaravelu, M. Vanmeert, *Processes*, **9**, 71 (2021).
31. R. Shukla, T. Tripathi, D. B. Singh, ed., Springer

Singapore, 2020, p. 133.
32. M. Y. Lobanov, N. S. Bogatyreva, O. V Galzitskaya, *Mol. Biol.*, **42**, 623 (2008).
33. M. A. Williams, J. E. Ladbury, Hydrogen bonds in protein-ligand complexes (Protein-ligand interactions), Wiley, 2003.
34. K. Konstantinidis, I. Karakasiliotis, K. Anagnostopoulos, G. C. Boulougouris, *Mol. Syst. Des. Eng.*, **6**, 946 (2021).
35. S. Genheden, U. Ryde, *Expert Opin. Drug Discov.*, **10**, 449 (2015).
36. G. Poli, C. Granchi, F. Rizzolio, T. Tuccinardi, *Molecules*, **25**, 1971 (2020).
37. [T. Simonson, C. Chipot, A. Pohorille, Free energy calculations: Approximate methods for biological macromolecules (Free energy calculations: Theory and applications in chemistry and biology), Springer, Berlin, 2007.
38. V. Acuña-Guzman, M. E. Montoya-Alfaro, L. P. Negrón-Ballarte, C. Solis-Calero, *Pharmaceuticals*, **17**, 750 (2024).
39. L. Bogaard, K. Tsoi, B. van de Steeg, E. F. A. Brandon, L. Geers, M. van Herwaarden, F. Jansman, D. Maas, M. Monster-Simons, D. S. Y. Ong, S. D. Borgsteede, *Front. Pharmacol.*, **15**, 1412692 (2024).
40. F. Lombardo, J. Bentzien, G. Berellini, I. Muegge, *J. Pharm. Sci.*, **110**, 500 (2021).
41. Y. Wei, L. Palazzolo, O. Ben Mariem, D. Bianchi, T. Laurenzi, U. Guerrini, I. Eberini, *Comput. Struct. Biotechnol. J.*, **23**, 3090 (2024).
42. A. C. Severance, P. J. Sandoval, S. H. Wright, *J. Pharmacol. Exp. Ther.*, **362**, 405 (2017).
43. Y. Jing, A. Easter, D. Peters, N. Kim, I. J. Enyedy, *Future Med. Chem.*, **7**, 571 (2015).
44. A. A. Toropov, A. P. Toropova, E. Benfenati, *Toxicol. Mech. Methods*, **30**, 605 (2020).
45. P. Geerlings, *Pharmaceuticals*, **15**, 1112 (2022).
46. Y. Li, M. Lin, M. Tian, G. Ye, X. Zhao, *J. Mol. Liq.*, **390**, 123059 (2023).
47. E. V. Gómez, N. A. Ramírez Guarnizo, J. D. Perea, A. S. López, J. J. Prías-Barragán, *ACS Omega*, **7**, 3872 (2022).
48. R. Pal, P. K. Chattaraj, *J. Comput. Chem.*, **44**, 278 (2023).

Bulgarian Chemical Communications, Volume 58, Issue 4 (pp. 504-514) 2026 *DOI: 10.34049/bcc.58.4.5757*

Advances in predictive toxicology for androgen receptor–mediated endocrine disruption

I. M. Tsakovska, A. G. Diukendjieva-Todorova, I. K. Pajeva*

Institute of Biophysics and Biomedical Engineering, Bulgarian Academy of Sciences, Acad. Georgi Bonchev Str., Block 21, Sofia 1113, Bulgaria

Received: March 16, 2026; Revised: June 01, 2026

This article provides an overview of the achievements and limitations of predictive toxicology approaches for assessing endocrine-disrupting chemicals (EDCs). It focuses on the androgen receptor (AR) as an important target of EDCs. AR is a nuclear receptor involved in numerous physiological processes related to male development and health, including sexual differentiation, reproductive function, as well as non-reproductive processes such as development of bones, muscles, and nervous system. Due to its significance, AR dysregulation by EDCs is a subject of strong scientific and regulatory interest. Research on AR-mediated toxicity has led to the development of several non-animal testing alternatives to traditional safety assessment, including *in silico*, *in chemico*, and *in vitro* methodologies (referred to as New Approach Methodologies or NAMs). The review offers insights into the current understanding of the functioning and classification of AR ligands, as well as advancements in high-throughput screening assays for assessing their effects. The primary focus is on existing computational models, particularly those utilizing data from programs and projects of the U.S. Environmental Protection Agency and the Organization for Economic Co-operation and Development. The reviewed studies illustrate the effectiveness of multiple methodologies, with machine learning algorithms dominating current research and consensus modeling strategies having the best predictive performance. Overall, AR-related toxicity prediction demonstrates that NAMs hold significant potential in supporting chemical safety evaluation, prioritizing compounds for experimental testing, and lowering the overall cost and time required for chemical risk assessment. Additionally, the need for integrating predictive tools into regulatory risk assessment frameworks is emphasized.

Keywords: Predictive toxicology, Endocrine-disrupting chemicals, Androgen receptor, Computational models, New approach methodologies.

INTRODUCTION

Endocrine-disrupting chemicals (EDCs) are xenobiotic compounds that interfere with the human endocrine system thus causing adverse effects such as reproductive dysfunction, metabolic disorders (incl. diabetes type 2), neurodevelopmental impairments (Alzheimer's disease), and increased risk of cancer (e.g. prostate cancer) or skin disorders [1]. They act through multiple mechanisms, including direct interaction with receptors responsible for hormonal signaling, like the androgen receptor (AR), estrogen receptors ERα or ERβ, thyroid receptors, and modulation of hormone receptor expression [2, 3].

EDCs are present in a wide range of everyday products, including certain cosmetics, food and beverage packaging, toys, and pesticides. Some chemicals used as flame retardants may also function as endocrine disruptors. Human exposure to these substances can occur *via* air, diet, skin contact, and water. Consequently, endocrine disruption (ED) is explicitly addressed in major regulatory frameworks including the Registration, Evaluation, Authorization and Restriction of Chemicals (REACH; No 1907/2006), the Biocides Regulation (BPR; Regulation (EU) No 528/2012), the Classification, Labelling and Packaging Regulation ([CLP; No 1272/2008) and the Endocrine Disruptor Screening Program (EDSP) of the United States Environmental Protection Agency (EPA; https://www.epa.gov/endocrine-disruption).

When assessing ED properties of chemicals, multiple types of information are integrated within a weight-of-evidence framework to support scientifically robust hazard identification. This process increasingly relies on predictive toxicology approaches that exploit fundamental knowledge of molecular structure, physicochemical properties, and chemical reactivity to anticipate biological effects. These methodologies provide the basis for non-animal testing strategies, now integral to both chemical safety assessment and regulatory decision-making.

Predictive toxicology integrates *in silico*, *in chemico*, and *in vitro* methodologies, collectively

* To whom all correspondence should be sent:
E-mail: *pajeva@biomed.bas.bg*

© 2026 Bulgarian Academy of Sciences, Union of Chemists in Bulgaria

referred to as New Approach Methodologies [4]. These approaches enable systematic evaluation of structure–activity and structure–reactivity relationships, linking molecular features such as functional groups, stereochemistry, lipophilicity, electronic properties and other structural descriptors to endocrine-related toxicity. *In silico* methods - including quantitative structure–activity relationship (QSAR), molecular docking, and cheminformatics-based screening - allow rapid prioritization of chemicals and identification of potential interactions with endocrine system-related targets. Complementary *in chemico* assays provide insight into intrinsic chemical reactivity, while *in vitro* assays translate these properties into measurable biological responses.

Predictive toxicology approaches support safety evaluation and risk assessment for a broad range of substances, including industrial chemicals, pharmaceuticals, and environmental contaminants. They form the backbone of next-generation risk assessment, which emphasizes human-relevant mechanisms, scalability across chemical space, and reduced reliance on animal testing. Together, these approaches enable chemists to contribute directly to more efficient, mechanism-driven, and ethically responsible assessment of endocrine-disrupting chemicals.

This review aims to provide an overview of the most recent approaches used to predict ED effects of chemicals, discussing their achievements and current limitations. We particularly focus on the AR as an important target of EDCs to offer researchers exemplifying studies utilizing approaches of the advanced predictive toxicology.

Androgen receptor, types of ligands, reference compounds

One of the main subjects of research in predictive toxicology is nuclear receptors, including the AR. The AR is a nuclear transcription factor of key importance for male health that regulates sexual differentiation, reproductive function, and spermatogenesis, as well as non-reproductive processes such as the development of bones, muscles, and the nervous system. The AR functions by binding androgen ligands (hormones). Upon ligand binding, a sequence of events is initiated, including conformational changes, dissociation from heat shock proteins (HSPs), and translocation from the cytoplasm to the nucleus (if not already localized there) (Figure 1). In the nucleus, the receptor interacts with specific DNA sequences known as androgen response elements, ultimately leading to the modulation of gene expression in target cells, including testicular cells. Representative AR target genes include *KLK3* (Prostate-Specific Antigen/PSA), *KLK2*, *FKBP5*, *NKX3-1*, *IGF1*, *MYC*, and *CCND1* (Cyclin D1). Activation of these and other involved genes promotes key biological responses such as cellular proliferation, differentiation, survival, metabolism, secretion, and tissue homeostasis, thereby reflecting the normal physiological functioning of AR signaling.

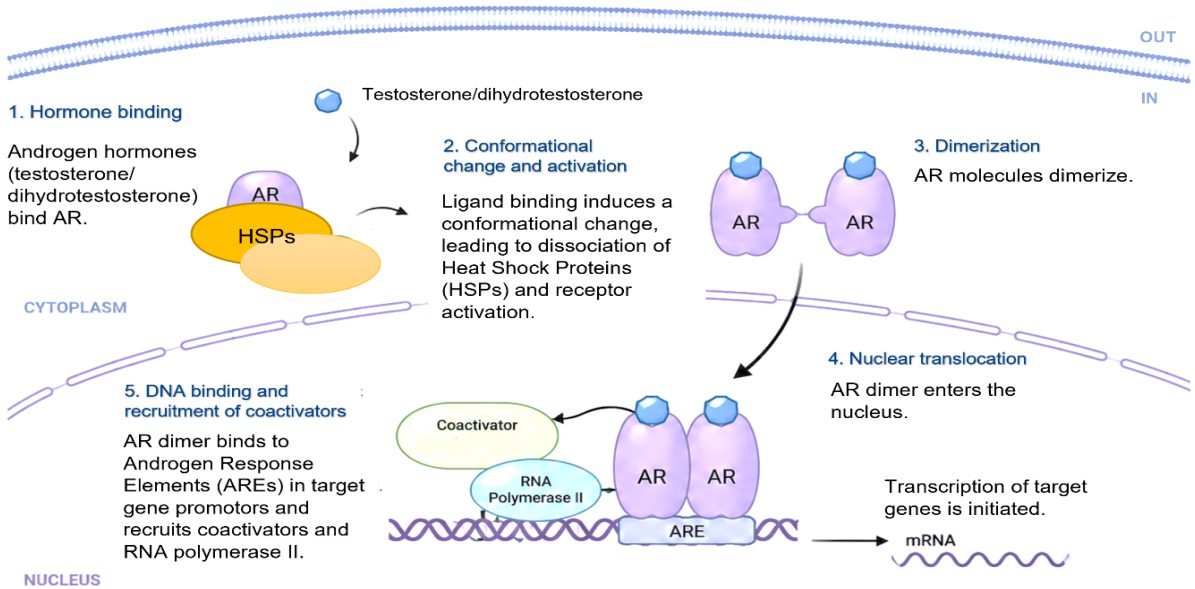
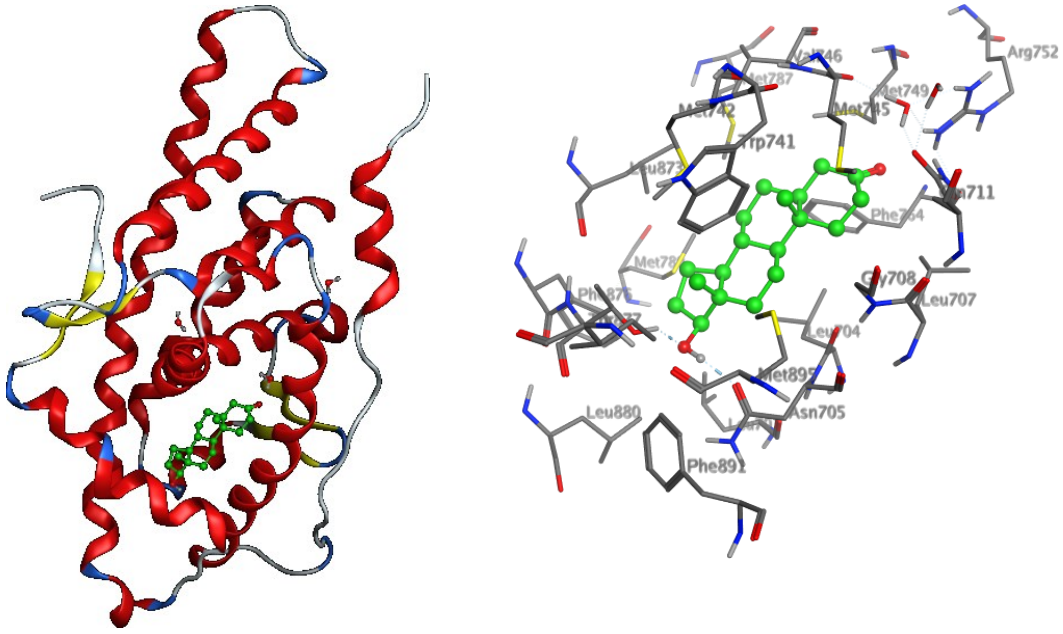


Figure 1. Schematic representation of AR signaling under normal conditions.



A B

Figure 2. A. 3D crystal structure (PDB ID 1T7T) of the androgen receptor ligand binding domain (the protein backbone rendered in ribbon) in complex with the agonist 5-alpha dihydrotestosterone (in green); B. Closer view of the active site with the amino acid residues forming the receptor binding pocket.

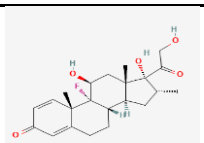
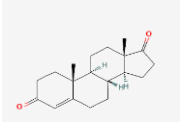
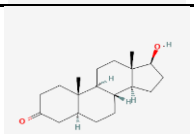
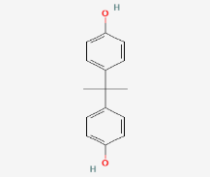
Disruptions in the AR function can result in severe reproductive disorders, ranging from complete androgen insensitivity syndrome to milder forms of impaired fertility. Due to its central role in androgen-dependent pathways that control male development and physiology, the AR is often described as a "master regulator" of these processes [5]. These factors also explain the strong scientific interest in the AR as a target of predictive toxicology research, alongside the estrogen receptors and other nuclear receptors involved in the regulation of essential physiological processes in the living organisms. The official symbol for the androgen receptor according to the HGNC (HUGO Gene Nomenclature Committee, https://www.genenames.org/) nomenclature is AR. Other symbols reported in the scientific literature include NR3C4 (nuclear receptor subfamily 3, group C, member 4), KD, AIS, AR8, TFM, DHTR, SBMA, HYSP1, SMAX1, HUMARA. Compounds that interact with AR are referred to as AR ligands and may be either endogenous (hormones) or exogenous (xenobiotics). AR is most commonly localized in the cytoplasm, where it forms a complex with heat-shock proteins. Activation of AR is initiated by binding to androgen hormones. Androgen-activated AR dissociates from heat-shock proteins and subsequently moves to the nucleus, where it mediates AR pathways [6]. Dihydrotestosterone is the most potent known endogenous ligand of the receptor. It binds to human AR with a dissociation constant (Kd) of 0.25–0.5 nM, which corresponds to an approximately 2–3-fold higher affinity than that of testosterone (Kd = 0.4–1.0 nM) and a 15–30-fold higher affinity than that of adrenal androgens. Fig. 1 illustrates the X-ray crystal structure of AR in complex with dihydrotestosterone retrieved from the Protein Data Bank (PDB; https://www.rcsb.org/). EDCs can mimic the interaction of the AR with its natural hormones, thereby interfering with its normal functions. The ability of EDCs to bind to AR and their specific mode of interaction represent the key molecular initiating event underlying the associated toxic effects. AR-targeting EDCs can disrupt the tightly regulated transcriptional processes controlled by AR signaling (Figure 2), leading to altered gene expression, epigenetic dysregulation, impaired reproductive development, endocrine dysfunction, and increased susceptibility to hormone-dependent diseases, including prostate cancer and infertility. Assessing these effects requires distinguishing between EDCs that act as agonists (activators) or antagonists (inhibitors) based on their ability to activate or inhibit transcription of AR target genes [7]. For example, bisphenol A is reported to antagonize AR signaling, alter the expression of *KLK3 (PSA)* and *NKX3-1* genes and is associated with reduced sperm quality, impaired male fertility, altered prostate development, endocrine dysfunction, and increased susceptibility to

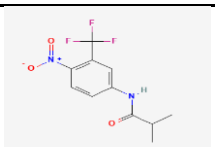
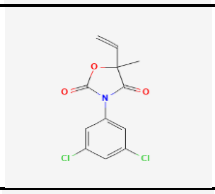
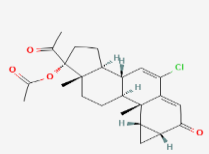
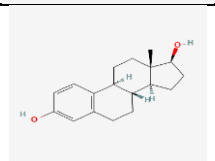
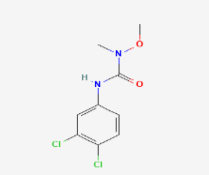
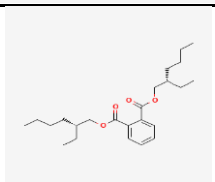
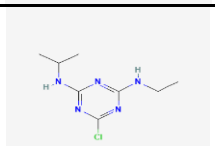
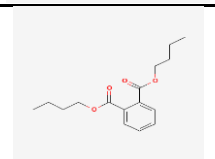
hormone-dependent cancers [8]. Similarly, vinclozolin metabolites function as AR antagonists, blocking androgen-dependent transcription and reducing expression of genes involved in male reproductive differentiation and steroidogenesis. Physiological consequences include cryptorchidism, hypospadias and impaired spermatogenesis [9].

A classic approach for distinguishing AR agonists from antagonists is based on evaluating their ability to induce N/C interactions—interactions between the NH_2-terminal (N-terminal) and the COO-terminal (C-terminal) of the receptor [10]. Using this criterion high-affinity AR agonists (e.g., dihydrotestosterone, mibolerone, testosterone, and methyltrienolone) have concentrations between 0.1 and 1 nM and induce the N/C interaction more than 40-fold. Agonists with lower affinity require concentrations of 10–100 nM for up to 23-fold induction of the N/C interaction (oxandrolone, fluoxymesterone). No N/C interaction is recorded for antagonists at concentrations up to 1 μM (hydroxytamoxifen, cyproterone acetate or RU56187, estradiol, progesterone, medroxyprogesterone acetate); each of these steroids inhibits the dihydrotestosterone-induced N/C interaction at concentrations of 1–500 nM. Kemppainen *et al.* [10] concluded that all ligands exhibited concentration-dependent AR agonist activity that corresponded with induction of the N/C interaction, while antagonists and weaker agonists did not trigger this interaction. Their results suggest that the N/C interaction enhances agonist potency at low physiological ligand concentrations, as shown by transcription, dimerization/DNA binding, and stabilization assays. However, at sufficiently high ligand concentrations, the N/C interaction is not required for agonist activity, and its inhibition does not necessarily indicate antagonist behavior.

The current classification of AR-targeting EDCs used in predictive toxicology deals with four main classes of activity: agonists, antagonists, selective AR modulators (SARMs), and inactive compounds [11]. SARMs are defined as small molecules that can act as agonists or antagonists with tissue-selective activities, which are their key characteristics. Table 1 illustrates this classification using 12 reference compounds for AR, reported in [10] and based on reports from the ICCVAM (Interagency Coordinating Committee on the Validation of Alternative Methods) [12] and the OECD (Organization of Economic Cooperation and Development) [13].

Table 1. Representatives of main activity classes of reference chemicals; SARM - selective androgen receptor modulator (according to Kleinstreuer *et al.* [11]).

Substance (product class)	CAS ref. no.	Chemical structure	Chemical class	Activity class
Dexamethasone (pharmaceutical)	50-02-2		Steroid, nonphenolic	AR agonist
4-Androstenedione (hormone)	63-05-8		Steroid, nonphenolic	Strong AR agonist
5α-Dihydrotestosterone (hormone)	521-18-6		Steroid, nonphenolic	Strong AR agonist
Bisphenol A (chemical intermediate)	80-05-7		Diphenylalkane bisphenol; Phenol	AR antagonist

Flutamide (pharmaceutical)	13311-84-7		Amide; Anilide; Nitrobenzene	AR antagonist
Vinclozoline (pesticide)	50471-44-8		Organochlorine; Cyclic imide; Carbamate	AR antagonist
Cyproterone acetate (pharmaceutical)	427-51-0		Nitrile; Diphenyl ether; Organochlorine	SARM
17β-Estradiol (hormone)	50-28-2		Steroid, phenolic; Estrene	SARM
Linuron (pesticide)	330-55-2		Urea	SARM
Diethylhexyl phthalate (used in a variety of customer products)	117-81-7		Phthalate	Inactive
Atrazine (pesticide)	1912-24-9		Aromatic amine; Triazine; Arylamine	Inactive
Di-*n*-butyl phthalate (plasticizer)	84-74-2		Phthalate	Inactive

ICCVAM published a list of 78 substances recommended for use in future validation studies of AR endocrine disruptors [12] with a summary of the available quantitative data on AR binding *in vitro* for each substance. Relative binding affinity (RBA) data are available for 33 (42%) of these 78 recommended substances.

Development and validation of new approach methodologies based on relevant toxicological data

- *The EPA's ToxCast and Tox21 programs for assessing the effects of chemicals on AR pathways (AR pathway model).* EPA has developed and maintains the Toxicity Forecaster (ToxCast) program, which was subsequently expanded under the Tox21 initiative (https://www.epa.gov/comptox-tools/exploring-toxcast-data). This program has generated data using *in vitro* high-throughput screening (HTS) assays measuring activity of chemicals at multiple points along the AR activity pathway (AR pathway model). The primary objective of ToxCast/Tox21 is to use these data to predict AR toxicity potential and prioritize testing of chemicals that pose the greatest risk to human health and the environment [14]. In practice, ToxCast/Tox21 provides the largest data for

evaluating the effects of chemicals on AR pathways. The data are collected from various sources, and a diverse range of chemical collections has been studied. A number of tests are used to assess AR activity, with a combination of HTS assays most often used to provide a more comprehensive evaluation of the potential toxic effects of the studied compounds.

The data from the HTS of ToxCast/Tox21 consist of approximately 9,500 substances that have been tested across roughly 1,400 assays. The ToxCast invitroDB v3.3 database (published in September 2020) is available at the following link: https://www.epa.gov/chemical-research/exploring-toxcastdata-downloadable-data [last accessed 11 March 2026]. The dataset includes AC_{50} values (the concentration at which 50% of the observed effect is achieved), binary codes representing activity (1) or inactivity (0) for each chemical–assay pair, and chemical-specific cytotoxicity scores.

Many aspects of AR activity have been investigated using a variety of assays. Most assess binding affinity together with agonistic and antagonistic activity, while some focus specifically on either antagonism or agonism. Transcriptional activation assays are also used to evaluate the ability of chemicals to stimulate AR-regulated gene transcription. These assays employ cell lines containing reporter genes under the control of AR-dependent promoters. Lynch and co-authors [15] screened the Tox21 library to identify AR activators using two reporter gene cell lines: AR β-lactamase (AR-bla) and AR luciferase (AR-luc). Seventy-five compounds identified in the primary assay were subsequently characterized as potential agonists or inactive compounds through confirmatory screening and secondary assays. Biochemical binding assays and AR nuclear translocation assays further confirmed the direct binding to and activation of AR by these compounds. Multiple AR activators were identified, including well-known AR agonists such as testosterone, as well as novel or less well-characterized compounds such as prulifloxacin [15].

One of the first comprehensive test collections includes a panel of nine high-throughput screening assays (five from ToxCast and four from Tox21). These tests evaluate receptor binding, cofactor recruitment, gene transcription, and protein production across multiple cell types, including eight human and one animal (chimpanzee) cell types [11]. The developed computational model assumes that the observed effect value (efficacy, A) at a given chemical concentration is a linear sum of contributions from the receptors being measured. It is based on the calculation of area under the curve (AUC) [11]. The model was initially trained using a set of 28 reference compounds, and subsequently tested on 1,846 ToxCast chemicals: 1,549 chemicals were inactive in the model; 115 chemicals were predicted to have strong effects as AR binders, either as agonists or antagonists; the remaining 182 chemicals showed results in an intermediate range.

In a subsequent study, Kleinstreuer *et al.* [16] expanded the panel from nine to eleven high-throughput assays by adding a rat AR binding assay (radioligand cell-free measurement). The list of unique reference compounds was also expanded from 28 to 44 to improve the evaluation and validation of the computational model. In one of the most recent studies conducted under the EPA's EDSP for endocrine disruptor screening, the assessment panel was further expanded to 14 high-throughput assays (Table 2) [17].

Table 2. List of assays used in models for assessing the effects of chemicals on AR pathways (14 assays) [17].

ToxCast name of the assay	Description of the assay (pathway)
NVS_NR_hAR	Receptor binding assay with human AR (antagonist and agonist pathway)
NVS_NR_cAR	Receptor binding assay with chimpanzee AR (antagonist and agonist pathway)
NVS_NR_rAR	Receptor binding assay with rat AR (antagonist and agonist pathway)
OT_AR_ARSRC1_ 0480	Coregulator recruitment assay at 8 h (antagonist and agonist pathway)
OT_AR_ARSRC1_ 0960	Coregulator recruitment assay at 16 h (antagonist and agonist pathway)
UPITT_HCI_U2OS_ AR_TIF2_ Nucleoli_Agonist	Nuclear translocation assay (antagonist and agonist pathway)
ATG_AR_TRANS_ up	Reporter gene assay (agonist pathway)
OT_AR_ARELUC_ AG_1440	Reporter gene assay (agonist pathway)
TOX21_AR_BLA_ Agonist_ratio	Reporter gene assay (agonist pathway)
TOX21_AR_LUC_ MDAKB2_Agonist	Reporter gene assay (agonist pathway)
ACEA_AR_ Agonist_80h	Real time impedance assay (agonist pathway)

UPITT_HCI_ U2Os	Nuclear translocation assay (antagonist pathway)
TOX21_AR_BLA_ Antagonist_ratio	Reporter gene assay (antagonist pathway)
TOX21_AR_LUC_ MDAKB2_ Antagonist_ 0.5nM_R1881	Reporter gene assay (antagonist pathway)

The aim of the study by Bever *et al.* [17] is to demonstrate a method for processing data to identify optimal minimal assay panels derived from a larger, comprehensive model, to provide a unified framework for evaluating the performance of future minimal panels, and to incorporate chemical cluster analysis into this evaluation. Although several of the assays used in the previously described AR pathway models are no longer available from the original provider, such an approach remains valuable for future evaluations of minimal assay models intended for prioritization and screening purposes. The authors compare two previously published models and report that the expanded 14-assay model shows higher sensitivity for antagonists, whereas the original 11-assay model demonstrates slightly higher sensitivity for agonists. They further analyze subsets of assays within the original AR pathway model to optimize overall testing strategies that reduce costs while maintaining sensitivity across a broad chemical space.

Analyses of model subsets derived from the 14-assay model identified three critical assays for predicting antagonism and two critical assays for predicting agonism. At least nine assays are required to predict both agonism and antagonism with high sensitivity (95%). The authors further demonstrate that testing workflows guided by chemical structure–based clustering can reduce the average number of assays required per chemical. In this approach, assay selection is informed by the probability that a chemical acts as an AR agonist based on its structural features. The results indicate that a multi-stage testing workflow can achieve 95% sensitivity while using only 48% of the resources needed to perform all assays included in the original full models. Resource use can be further reduced by incorporating *in silico* activity predictions. The main conclusion of the study is that integrating chemical clustering and the simultaneous evaluation of both antagonistic and agonistic mechanisms provides efficient approach to chemical screening. This strategy can minimize the total number of assays required to predict AR activity, thereby maximizing the number of chemicals that can be tested and supporting data-driven prioritization for further screening under the EDSP Universe of Chemicals list. The Universe of Chemicals list includes 10,272 compounds identified for potential screening (available at: https://www.epa.gov/sites/default/files/2015-07/documents/edsp_chemical_universe_list_11_12.pdf; last accessed 11 March 2026).

In their analysis of the 14-assay panel, Judson *et al.* [18] emphasize the importance of including AR homodimerization assays. However, they also note that not all AR assays are currently available from their original sources. Therefore, to apply subset models effectively, it may be necessary to identify existing assays or develop new ones that exhibit behavior similar to those selected for the optimal subsets. The authors further highlight that one of the major challenges in using *in vitro* data to predict *in vivo* outcomes is the limited representation of xenobiotic metabolism in *in vitro* systems.

To address the metabolic limitations of *in vitro* systems, the latest ToxCast strategic plan proposes the transfection of chemically modified mRNAs encoding human cytochrome P450 (CYP) enzymes into cells to induce intracellular CYP expression and functional metabolic activity [19, 20]. The study evaluated 2,165 ToxCast chemicals using an AR homodimerization assay conducted in parallel with 10 human liver CYP enzymes, with the aim of identifying antiandrogenic parent compounds and their metabolites. The authors conclude that the AR dimerization assay, when combined with metabolism testing, can detect chemicals that are either activated or deactivated by CYP-mediated metabolism. AR dimerization and CYP450 data are available for 131 agonists, 260 antagonists, and 128 tested compounds.

In 2023 OECD published a Test Guideline that established methods for identifying chemicals with androgenic properties. It exclusively addresses transcriptional activation and inhibition of an androgen-regulated reporter gene (Androgen Receptor TransActivation (ARTA) assays) and formulates the minimum standards for the performance of experimental controls and reference standards [21].

The *in vitro* assays developed under the ToxCast / Tox21 initiatives, and OECD guideline protocols, are designed to measure key components of the AR pathway. This pathway is activated through a series of well-characterized key events, beginning with receptor binding (molecular initiating event) and dimerization with cofactors, which subsequently modulate transcriptional activity, leading to the production of functional proteins and either stimulation or inhibition of downstream receptor responses. Studies have demonstrated that the

integration of multiple assays can quantitatively discriminate between AR-active and inactive substances [22]. The regulatory application of AR pathway–based methods is currently under consideration in several regulatory programs, for instance, EDSP.

- *Computational models used to predict the effects of chemical compounds on AR.* The overview of models presented below highlights recent *in silico* models to reflect current trends in *in silico* prediction of AR toxicity. The majority of these models are based on ToxCast/Tox21 data.

One of the earliest models utilizing ToxCast AR *in vitro* data are the OASIS QSAR models proposed by Bhhatarai *et al.* [23]. The authors rely on the OASIS methodology proposed by Mekenyan *et al.* [24] for the estrogen receptor by integrating molecular structure, metabolism, and mechanisms of action in QSAR models. OASIS QSAR AR models show high sensitivity (92–100%) and specificity (70–81%) for predicting AR binding. The authors recommended to apply a tiered screening approach for integrative testing and risk assessment.

The CoMPARA (Collaborative Modeling Project for Androgen Receptor Activity) project [25] brings together scientists specializing in computational toxicology from 25 research groups around the world. Using a variety of machine learning methods—Artificial Neural Networks (ANN), Support Vector Machines (SVM), Random Forest (RF), k-Nearest Neighbor (KNN), Decision Trees (DT), structural alerts, and others—the project enhances the statistical performance of the developed models. More than 90 predictive models have been developed, along with consensus models for predicting the binding, agonistic, and antagonistic activity of chemicals. In total 1,746 chemicals composed of a combined dataset based on the HTS panel of 11 *in vitro* assays from ToxCast™/Tox21 were included as a common training set. The predictive accuracy of the consensus models (on the evaluation set) is approximately 80%. The models have been implemented in the free, open-source OPERA application, enabling the screening of new chemicals with a defined applicability domain and accuracy assessment (https://ntp.niehs.nih.gov/whatwestudy/niceatm/comptox/ct-opera/opera; last assessed 11 March 2026). This implementation has been used to screen the entire EPA DSSTox database of approximately 875,000 chemicals. The predicted AR activities are available on the EPA CompTox Chemicals Dashboard and in the National Toxicology Program's Integrated Chemical Environment [26].

Maran *et al.* published classification QSAR models [27] based on the same dataset, used in CoMPARA project. The models were based on two datasets by the EPA's National Center for Computational Toxicology. The first dataset contains 1,688 compounds and was used to construct the training sets for model development. The second dataset, consisting of 5,273 compounds collected from multiple EPA sources, was used to evaluate the actual predictive accuracy of the models (test set). The developed classification models categorize compounds using the RF method into three activity groups: androgen-binding (binders), agonistic, and antagonistic activity. In addition, a multi-class approach was developed that simultaneously distinguishes between inactive compounds, agonists, and antagonists. For the test set, the classification models predict agonists with an accuracy of 80%, while the corresponding values for antagonists and binders are 72% and 78%, respectively. Combining agonists, antagonists, and inactive compounds in the multi-class approach results in a prediction accuracy of 64% for the evaluation set. Considering the size of the training datasets and their imbalance, the authors regard the achieved prediction accuracy as very good. The final classification models are available for study and prediction in the QsarDB repository [28].

The fingerprint model developed by Zron and co-workers [29] is based on invitroDBv3.1 summary files (EPA, U. EPA ToxCast & Tox21 Summary Files from invitrodb_v3.1. https://www.epa.gov/chemical-research/toxicity-forecaster-toxcasttm-data (April 16, 2019). From the initial dataset of 9214 substances 8645 substances were removed after curation (substances without structures, water samples, mixtures, incorrectly defined, polymers). "Coding" was performed using identifiers from two central sources, one for AC50 data from ToxCast/Tox21 and the other for AUC data (see section 2.1 above). The machine learning models use fingerprints with extended connectivity with a maximum diameter of 6, generated by the Chemistry Development Kit. Predictions are evaluated using a probability threshold, where a prediction of 0.5 or higher defines the chemical as active. Sets of nine agonist pathway analyses or seven antagonist AR pathway analyses were used for predictions: if more than half of the models in the group (i.e., at least five models for agonist pathway analysis or four models for antagonist pathway analysis) predict the compound as active, it is considered active. A limitation of this modelling is the consistent prediction of steroid chemicals as active, regardless of the test group, but this is a common limitation of

models that use fingerprints as molecular descriptors and may be overcome by analyzing other descriptors in future studies.

The model by Allen *et al.* uses an automated search for the maximum common substructure to generate 2D structural alerts from AR data from ToxCast. The model makes predictions based on 87 structural alerts for two receptors—AR and the glucocorticoid receptor (Glucocorticoid Receptor) — again using ToxCast data [30].

The models presented above were developed primarily using machine learning approaches, mainly quantitative structure–activity relationship (QSAR) classification methods. In the terminology of drug design and computational toxicology, these approaches are referred to as ligand-based methods [31]. However, models have also been developed using structure-based methods, primarily involving molecular docking of ligands in the active site of the receptor. The most significant of these models are described below.

The models of Trisciuzzi *et al.* [32] use a strategy based on the three-dimensional structure of the AR, selected from structures currently available in the Protein Data Bank (PDB; see Section 2.3 below for more information on the PDB dataset). From the nine initially selected structures, the one based on the complex with PDB ID 2PNU was identified as the best-performing structure-based classification model. The models were trained on a dataset of 1,689 curated compounds provided by the CoMPARA consortium and integrated with a two-stage applicability domain in order to reduce the number of false negatives. Three groups, each comprising 2,590 compounds extracted from the DUD-E collection (https://dude.docking.org/; last accessed 11 March 2026), were used to evaluate the model and the effectiveness of integrating the applicability domain. The model based on the 2PNU structure was subsequently applied to screen and prioritize two test groups of chemicals: A) a small set of 12 representative androgenic compounds that were accurately classified based on in-depth molecular-level analysis; and B) a large external set of 55,450 chemicals with potential for human exposure. In practice, this represents the largest external test set used in AR modeling studies.

The model of García-Sosa [33] applies deep neural networks (DNN) to molecular descriptors derived from docking (calculated protein–ligand binding), chemical fingerprint distances, and other statistical techniques, achieving good performance as indicated by AUC (0.87) and Matthews correlation coefficient (0.47). Another advantage of the model is the good interpretability of the descriptors and features used. The source code and data are publicly available on GitHub. In this publication, García-Sosa also provides a critical analysis of the training data used in the CoMPARA project, describing it as highly imbalanced, with a large number of non-binders (N = 1,468) compared with binders (N = 205). Such imbalances in datasets can strongly influence the performance of machine learning algorithms. Therefore, the author balances the training set in his model to ensure an equal number of compounds acting as binders and non-binders. The same author, together with Maran combined multivariate logistic regression, protein structural docking scores, extended connectivity fingerprints, and naïve Bayesians to predict compounds that bind to or disrupt the AR, improving model accuracy for toxicity prediction [34]. CoMPARA data set has been used also by Collins et al. [35] who applied RF method and developed models that predict androgen activity with high predictive capabilities (balanced accuracies of 93%, coverage of 89%).

Other models for predicting AR toxicity using different datasets and methodologies have also been described in the scientific literature. Wahl and Smiesko [36] used molecular dynamics to improve prediction of AR antagonist binding, but distinguishing between antagonists and agonists remained challenging. Gupta and Rana [37] developed a QSAR-based multilevel ensemble model to predict toxicity of small drug molecules binding to the AR, using a dataset of 10,273 molecules with feature selection and k-fold cross-validation. Banerjee *et al.* [38] utilized 2D-QSAR and chemical Read-Across models to predict AR binding affinity based on hydrophobicity, steroidal nucleus, bulkiness, and hydrogen bond donors and validated using stringent criteria and supported by pharmacophore mapping and molecular simulations. Ollitrault *et al.* [39] proposed QGexAR models to predict AR binding with a consensus balanced accuracy of 0.725 to 0.840 using gene expression profiles from LINCS (Library of Integrated Network-Based Cellular Signatures) database of NIH and machine learning algorithms.

The above analysis illustrates that the machine learning based approaches currently provide the most accurate predictions of chemical interactions with the AR. The CoMPARA project described above, and the consensus models generated within it using multiple machine learning algorithms, provide reliable predictions for thousands of compounds [40]. The integration of structure-based methods, such as molecular docking, further improves model performance [33, 41], particularly because structure-

based approaches offer easily interpretable models and represent a viable alternative for prediction in computational toxicology. Therefore, combining different computational approaches (ligand-based and structure-based) within a single framework significantly improves the predictive power of models and supports the development of consensus models for predicting AR toxicity.

CONCLUSIONS

Research on toxicity mediated through the AR highlights the biological and toxicological significance of this receptor. AR plays a key role in maintaining endocrine homeostasis and reproductive health, while also serving as a major molecular target through which numerous chemicals may exert adverse effects. Consequently, AR-mediated toxicity represents a well-established research field supported by extensive experimental and computational investigations.

A variety of computational approaches have been developed to predict AR-related toxicity, with consensus modeling strategies generally demonstrating the best predictive performance. The reviewed studies illustrate the effectiveness of multiple methodologies, with machine learning algorithms dominating current research. Approaches such as artificial neural networks, support vector machines, random forest models, k-nearest neighbor algorithms, and structural alert systems are widely applied to identify potential AR modulators. Among structure-based methods, molecular docking is commonly used to evaluate ligand–receptor interactions and predict binding affinity. In contrast, molecular dynamics simulations are applied less frequently due to their high computational cost, although they provide valuable mechanistic insight into receptor–ligand stability and conformational changes. Despite the availability of advanced computational techniques, the success of *in silico* modeling strongly depends on the availability of reliable and representative experimental data on AR-mediated toxicity. Current efforts focus on optimizing traditional *in vitro* high-throughput screening assays and complementing them with additional experimental approaches capable of capturing a broader range of biological responses across the signaling pathways associated with AR activity. The generation of cross-species toxicity data further contributes to improved understanding of endocrine mechanisms in both human and animal systems. Additionally, careful dataset curation and balancing remain essential to ensure adequate representation of chemical diversity and to improve model robustness.

However, despite the development of reliable predictive models for chemicals with potential ED activity, their regulatory implementation remains limited. By 2022, only a small number of pesticide active substances had been evaluated for endocrine-disrupting properties by EPA, and none had been formally classified as endocrine disruptors [41]. These findings emphasize the need for greater integration of predictive tools into regulatory risk assessment frameworks. In this context, new approach methodologies offer considerable potential to support chemical safety evaluation, prioritize compounds for experimental testing, reduce reliance on animal experiments, and lower the overall cost and time required for chemical risk assessment.

Acknowledgement: *The authors acknowledge the financial support by the project BG-RRP-2.017-0038-C02 "Web-based platform for in silico assessment of toxic effects of chemicals on human health and the environment" funded by the European Union through the NextGenerationEU instrument under the Recovery and Resilience Facility in implementation of investment C2I2: "Enhancing the innovation capacity of the Bulgarian Academy of Sciences in the field of green and digital technologies".*

REFERENCES

1. L. G. Kahn, C. Philippat, S. F. Nakayama, R. Slama, L. Trasande, *The Lancet Diabetes & Endocrinology*, **8,** 703 (2020).
2. O. Kucheryavenko, S. Vogl, P. Marx-Stoelting, in: Challenges in Endocrine Disruptor Toxicology and Risk Assessment (eds. A. Mantovani, A. Fucic), The Royal Society of Chemistry, 2020, p. 1.
3. D. A. Jiskoot, J. L. A. Pennings, W. J. G. M. Peijnenburg, G. J. P. Van Westen, W. Jespers, P. N. H. Wassenaar, *Trends in Endocrinology & Metabolism*, **37**, 584 (2026).
4. A. Najjar, N. Kramer, I. Gardner, T. Hartung, T. Steger-Hartmann, *Front. Pharmacol.*, **14**, 1257423 (2023).
5. T. Matsumoto, M. Sakari, M. Okada, A. Yokoyama, S. Takahashi, A. Kouzmenko, S. Kato, *Annu. Rev. Physiol.*, **75**, 201 (2013).
6. M. Kokal, K. Mirzakhani, T. Pungsrinont, A. Baniahmad, *Cancers*, **12**, 1833 (2020).
7. W. Gao, C. E. Bohl, J. T. Dalton, *Chem. Rev.*, **105**, 3352 (2005).
8. E. C. Brown, D. R. Hallinger, S. O. Simmons, *Front. Toxicol.,* **5**, 1134783 (2023).
9. G. R. Warner, V. E. Mourikes, A. M. Neff, E. Brehm, J. A. Flaws, *Molecular and Cellular Endocrinology*, **502**, 110680 (2020).
10. J. A. Kemppainen, E. Langley, C. Wong, K. Bobseine, W. R. Kelce, E. M. Wilson, *Molecular Endocrinology*, **13**, 440 (1999).

11. N. Kleinstreuer, D. Filer, M. Martin, K. Houck, D. Zang, D. Allen, W. Casey, R. Judson, NICEATM ToxCast Data Summit, Sept. 2014, Poster presentation, p. 1 (2014).
12. NIH Publication: ICCVAM Evaluation of In Vitro Test Methods for Detecting Potential Endocrine Disruptors: Estrogen Receptor and Androgen Receptor Binding and Transcriptional Activation Assays. May No. 03-4503, 2003, p. 79.
13. ICCVAM, Evaluation of In Vitro Test Methods for Detecting Potential Endocrine Disruptors, National Institute of Environmental Health Sciences (2003).
14. D. J. Dix, K. A. Houck, M. T. Martin, A. M. Richard, R. W. Setzer, R. J. Kavlock, *Toxicological Sciences*, **95**, 5 (2007).
15. C. Lynch, S. Sakamuru, R. Huang, D. A. Stavreva, L. Varticovski, G. L. Hager, R. S. Judson, K. A. Houck, N. C. Kleinstreuer, W. Casey, R. S. Paules, A. Simeonov, M. Xia, *Toxicology*, **385**, 48 (2017).
16. N. C. Kleinstreuer, P. Ceger, E. D. Watt, M. Martin, K. Houck, P. Browne, R. S. Thomas, W. M. Casey, D. J. Dix, D. Allen, S. Sakamuru, M. Xia, R. Huang, R. Judson, *Chem. Res. Toxicol.*, **30**, 946 (2017).
17. R. J. Bever, S. W. Edwards, T. Antonijevic, M. D. Nelms, C. Ring, D. Harris, S. G. Lynn, D. Williams, G. Chappell, R. Boyles, S. Borghoff, K. J. Markey, *Front. Toxicol.*, **6**, 1347364 (2024).
18. R. Judson, K. Houck, K. Paul Friedman, J. Brown, P. Browne, P. A. Johnston, D. A. Close, K. Mansouri, N. Kleinstreuer, *Regulatory Toxicology and Pharmacology*, **117**, 104764 (2020).
19. E. C. Brown, D. R. Hallinger, S. O. Simmons, *Front. Toxicol.*, **5**, 1134783 (2023).
20. S. O. Simmons, D. R. Hallinger, E. C. Brown, High-throughput Identification of Androgen Disrupting ToxCast Chemicals and CYP450 Metabolites, The United States Environmental Protection Agency's Center for Computational Toxicology and Exposure, 2024, p. 3153999.
21. OECD, Test No. 458: Stably Transfected Human Androgen Receptor Transcriptional Activation Assay for Detection of Androgenic Agonist and Antagonist Activity of Chemicals, OECD, 2023.
22. C. Johnson, S. Marty, M. Kim, K. Crofton, A. Roncaglioni, A. Bassan, T. Barton-Maclaren, A. Domingues, M. Frericks, A. Karmaus, S. Kulkarni, E. L. Piparo, S. Melching-Kollmuss, R. Tice, D. Woolley, K. Cross, *Computational Toxicology*, **35**, 100364 (2025).
23. B. Bhhatarai, D. M. Wilson, P. S. Price, S. Marty, A. K. Parks, E. Carney, *Environ. Health Perspect.*, **124**, 1453 (2016).
24. O. G. Mekenyan, *Toxicological Sciences*, **58**, 270 (2000).
25. S. Manganelli, A. Roncaglioni, K. Mansouri, R.S. Judson, E. Benfenati, A. Manganaro, P. Ruiz, *Chemosphere*, **220**, 204 (2019).
26. K. Mansouri, N. Kleinstreuer, A. M. Abdelaziz, D. Alberga, V. M. Alves, P. L. Andersson, C. H. Andrade, F. Bai, I. Balabin, D. Ballabio, E. Benfenati, B. Bhhatarai, S. Boyer, J. Chen, V. Consonni, S. Farag, D. Fourches, A. T. García-Sosa, P. Gramatica, F. Grisoni, C. M. Grulke, H. Hong, D. Horvath, X. Hu, R. Huang, N. Jeliazkova, J. Li, X. Li, H. Liu, et al., *Environ. Health Perspect.*, **128**, 027002 (2020).
27. G. Piir, S. Sild, U. Maran, *Chemosphere*, **262**, 128313 (2021).
28. G. Piir, S. Sild, U. Maran, *QDB archive #236*, QsarDB repository (http://qsardb.org/), (2020).
29. K. M. Zorn, D. H. Foil, T. R. Lane, W. Hillwalker, D. J. Feifarek, F. Jones, W. D. Klaren, A. M. Brinkman, S. Ekins, *Environ. Sci. Technol.*, **54**, 13690 (2020).
30. T. E. H. Allen, M. D. Nelms, S. W. Edwards, J. M. Goodman, S. Gutsell, P. J. Russell, *Environ. Sci. Technol.*, **54**, 7461 (2020).
31. I. Pajeva, I. Tsakovska, T. Pencheva, P. Alov, M. Al Sharif, I. Lessigiarska, D. Jereva, A. Diukendjieva, in: Research in Computer Science in the Bulgarian Academy of Sciences (ed. K. T. Atanassov), Springer International Publishing, Cham, 2021, p. 421.
32. D. Trisciuzzi, D. Alberga, K. Mansouri, R. Judson, E. Novellino, G. F. Mangiatordi, O. Nicolotti, *J. Chem. Inf. Model.*, **57**, 2874 (2017).
33. A. T. García-Sosa, *Molecules*, **26**, 1285 (2021).
34. A. T. García-Sosa, U. Maran, *IJMS*, **22**, 6695 (2021).
35. E. J. Collins, C. Bowyer, A. Tsouza, M. Chopra, *Biology*, **11**, 239 (2022).
36. J. Wahl, M. Smieško, *IJMS*, **19**, 1784 (2018).
37. V. K. Gupta, P. S. Rana, *J. Bioinform. Comput. Biol.*, **17**, 1950033 (2019).
38. A. Banerjee, P. De, V. Kumar, S. Kar, K. Roy, *Chemosphere*, **309**, 136579 (2022).
39. G. Ollitrault, M. Marzo, A. Roncaglioni, E. Benfenati, E. Mombelli, O. Taboureau, *Toxics*, **12**, 541 (2024).
40. F. Grisoni, V. Consonni, D. Ballabio, *J. Chem. Inf. Model.*, **59**, 1839 (2019).
41. M. V. Maffini, L. N. Vandenberg, *Front. Toxicol.* **4**, 908439 (**2022)**

Bulgarian Chemical Communications, Volume 58, Issue 4 (pp. 515-522) 2026 *DOI: 10.34049/bcc.58.4.5759*

Parametric optimization of ZK60 reinforced with ZrB_2 magnesium composites *via* Taguchi method

S. Suresh Kumar[1,2*], V. Mohanavel [3]

[*1]*Department of Mechanical Engineering, Bharath Institute of Higher Education and Research, Selaiyur, Chennai 600073, Tamil Nadu, India*

[2]*Department of Mechanical Engineering, PERI Institute of Technology, Mannivakkam, Chennai 600048, Tamil Nadu, India*

[3]*Centre for Sustainable Materials Research, Department of Mechanical Engineering, Academy of Maritime Education and Training (AMET), Deemed to be University, Kanathur, Chennai 603112, Tamil Nadu, India*

Received: April 17, 2026; Revised: June 17, 2026

The exploit of composite materials in many industrial usages is growing. By selecting the right materials, the composite could be customized to meet specific necessities as per suggestion of an engineer. Magnesium metal matrix composites (MMMCs) are a superior replacement for conventional alloys. By using the liquid metallurgy stir casting (SC) route to reinforce ZK60 with zirconium diboride (ZrB_2) particles, MMMCs were created. This study investigates the effect of ZrB_2 reinforcement (0, 4, 8 and 12) wt % (C1) on the wear and corrosion properties of composites produced. The wear examination was conducted at 20 N applied load (C2), 4 m/s sliding velocity (C3), 1500 m sliding distance (C4), 478 rpm speed for 1500 s. The variation of the wear loss in g for the different reinforcements was determined. The corrosion rate was determined using salt spray analysis. The wear and corrosion results showed that the 12 wt.% composite samples had lower wear loss and corrosion rate than those of ZK60 alloy. Furthermore, the Taguchi optimization process was adopted to investigate the parametric impact on the wear rate (WR), including C1, C2, C3 and C4. The primary effect plot shows that the least WR is achieved at 12 wt.% of ZrB_2 (C1), 5 N C2, 4 m/s C3, and 750 m C4. C1 is a notable variable for getting the least WR, with an impact of 43.34%, and next to it is C4 (21.21% impact). The factors C2 and C3 have smaller impacts according to the analysis of variance (ANOVA) data.

Keywords: ZK60, ZrB_2, stir casting, wear, Taguchi, optimization

INTRODUCTION

Composites are devised by blending multiple constituents that are exclusive in terms of material composition and properties. The two constituents that are most notable for their insoluble nature are the matrix and the reinforcing phase during the composite manufacturing process. The reinforcing phase often possesses higher degrees of strength and hardness than the matrix phase. The matrix materials and the reinforcing types, devised in the creation of composites, are the fundamental factors that determine the classification of these materials into a variety of distinct categories. The world's mechanical component manufacturing businesses are shifting toward the use of composites to cut weight without sacrificing the properties of the material [1, 2].

A combination of the material's own distinctive characteristics has been produced as a consequence of interaction. When mixed with different types of reinforcement materials, this unique material combination offers certain desirable qualities. It is widely employed in many different industries, including the maritime, automotive, and aerospace sectors.

The composite material can combine the most desirable properties of its components whilst suppressing less advantageous properties; this allows the composite material to display exclusive mechanical and physical properties. The creation of innovative materials and the deeper perception of the association between structure and qualities of the materials results in the development of novel composites [3, 4]. Metal matrix composites (MMCs) can be designed with desired properties by varying the type, shape, volume %, and distribution of ceramic reinforcing phases added to a metal matrix. Combining two or more materials that together have better qualities than either material alone yields metal-metal composites. Either a metal or an alloy based on metal makes up the matrix of this composite material. On the other hand, the majority of ceramics used for reinforcement are whiskers and particulates.

In order to meet the demanding and competitive quirements for particular material attributes, and the obsolescence of high-strength, lightweight

* To whom all correspondence should be sent: Email: *sandysureesh@gmail.com*

© 2026 Bulgarian Academy of Sciences, Union of Chemists in Bulgaria

materials, modern businesses are creating innovative manufacturing processes for reinforcing materials.

In this respect, MMCs are materials with good strength and low weight that are produced by a diversity of technical routes, including processing in liquid, solid, and vapor states. MMCs perform better than monolithic materials with respect to wear strength, stiffness, thermal conductivity and creep opposition [5, 6]. MMCs have improved qualities like wear resistance, tensile strength at room temperature and higher temperatures, hardness, and elastic modulus, together with important weight reserves over unreinforced metals. They are finding increased employment in airspace and automotive industries. Because of their special properties, MMCs have potential uses in a variety of contexts. These materials were created in response to the market need for materials with high levels of stiffness, wear resistance, and strength [7, 8].

Over the last few decades, there has been a rise in the use of magnesium in numerous distinct applications. This is because magnesium is the lightest metal and can replace aluminum. Magnesium is also capable of being used for a variety of other purposes. Owing to their exceptional cast ability, high stiffness, and strength, magnesium alloys are lightweight materials with diversified commercial applications. They have a high rate of recycling, are better at absorbing vibrations than steel and aluminum, are lighter and machine-friendly. They also provide a good substitute material for parts used in automobiles and aircraft. Light metals like magnesium are commonly utilized as the matrix in structural applications, providing strong support for the reinforcement. The matrix is implanted with the reinforcing substance. In addition to its primary function of reinforcing the material, reinforcement can also be utilized to modify physical qualities including wear opposition, friction coefficient, and thermal conductivity [9, 10].

Magnesium is less dense than typical metals, has better mechanical properties, is more resistant to corrosion and wear, and exhibits a lower thermal coefficient of expansion while mapped to customary materials. These days, more people are becoming aware of Mg and its alloys due to their good strength-to-weight ratio and low density. Because of their appealing biodegradation and mechanical qualities, Mg alloys and composites are employed as typical materials and have been regarded as viable alternatives of numerous alloys [11].

MMCs are a novel type of composites that are extensively used in the transportation sectors due to their lower density, greater mechanical properties, augmented opposition to corrosion and wear, compared to traditional metals and alloys. MMCs are interesting because, after being reinforced with metals and ceramics, they play a major role in a variety of lightweight applications. Over the last few decades, different efficient processes have been expanded to produce MMCs with uniformly dispersed reinforcements and strong interfacial bonding, ultimately leading to better performance [12, 13]. By incorporating several types of reinforcement, magnesium-matrix composites have been created to enhance the wear opposition of magnesium and its alloys. For many engineering applications, these MMMCs are the ideal option [14, 15]. Zirconium diboride (ZrB_2) is a member of the ultrahigh temperature ceramics material class. owing to its strong thermal and electrical conductivities, as well as its high melting temperature (over 3000 °C) [16, 17]. ZrB_2 is a great option for applications in harsh settings including elevated temperature electrodes, thermal guard systems and molten metal crucibles because of its unique set of characteristics. When set against alternative non-oxide structural ceramics, ZrB_2 has a good melting point, high strength, low density, and outstanding resistance to thermal shock and oxidation [18, 19].

For MMCs, a broad variety of manufacturing processes, both liquid-state and solid-state, have been studied. A multitude of processes, including squeeze casting, vapor deposition, stir casting, and powder metallurgy, have been developed to create MMCs. When compared to other fabrication techniques, stir casting is superior since it is simpler and can produce large quantities of composites. The stir cast (SC) fabrication route has numerous gains over other routes including accessibility, compliance, resourcefulness with other materials, and an inexpensive, elevated manufacture rate [20, 21]. The SC route is the most utilized commercial fabrication route because of its unique characteristics. SC creates MMCs by incorporating metallic or ceramic powders into a desired matrix. In SC, the powders are supplemented to the molten mix in a crucible and then agitated to achieve a fine circulation of the powders in the matrix.

The process creates a vortex in the liquid metal by means of a stirring mechanism. The easy integration of the particles with the few available types of stirring devices leads to a uniform dispersion. Stir casting has gained popularity because of its affordability, effortlessness of usage,

and capability to produce big quantities [22, 23]. When compared to other manufacturing methods, the SC process is simple to use, inexpensive, and appropriate for large-scale manufacture. The severe distortion during extrusion creates a very fine microstructure that improves the mechanical strength and hardness of the specimens. The increase in hardness is thought to be caused by adding harder granules to the structure, making it easier for grain boundaries to separate, and setting the ceramic particles out evenly [24, 25]. In mechanical terms, increasing the TiN content enhances the component's hardness and strength. At 12 wt % of TiN, the attained strength of the composites is 160 MPa and 80 HV. In salt spray and electrochemical assessments, elevated TiN amounts mitigated corrosion and mass loss. 12 wt.% of TiN offered the highest level of resistance [26]. New AZ91D/ZrB_2 composite study improved its mechanical characteristics. The addition of ZrB_2 particles to the AZ91D demonstrated favorable resultsthe composites is compared to earlier studies. This study produced AZ91D/ZrB_2 with different reinforcement weights using squeeze casting and AZ91D/12 wt.% by stir casting [27].

The authors of [28] optimized the influence of reinforcement weight percentages on the wear characteristics of Mg/TiC/MoS_2 composites and both reinforcements considerably enhanced the wear aversion of the produced composites compared to the Mg matrix. The authors of [29] analyzed the tribology parameters of Mg-3Al-5.6Ti composites and found that the inclusion of reinforcement particles enhances the wear resistance. The numerical examination of the wear behavior of Mg composites is reported in ref. [30]. In ref. [31] the wear parameter of Mg (5.6Ti+3Al)2.5 B_4C composites is studied. The authors of [32] explored the wear characteristics of AZ91E composites and determined that the conversion load increases as the amount of reinforcement enhances and the wear rate of the composite decreases relative to the alloy. The authors of [33] examined the wear characteristics of Mg armored with SiC. Under a lower load, the wear resistance of the composites is marginally better; however, at a higher load, the benefits of the SiC impregnation on wear are less clear. Girish *et al.* [34] probed the wear properties of AZ91-SiC-Gr composites and the findings demonstrate that, in the test conditions, the wear resistance of the composites was appreciably superior. The article [35] examined the wear behavior of TiC-, SiC- and fly ash-augmented Mg matrix and concluded that as the applied load rose, the wear rate and coefficient of friction increased for all samples. The research [36] explored the corrosion characteristics of Mg-SiC composites and found that the composites' SiC reinforcement and magnesium matrix did not considerably increase the rate of corrosion overall. The research [37] investigated the wear behavior of Mg-SiC-Gr composites and reported that because of the upright effect provided by both reinforcements, the resulting composites' wear resistance improved considerably more than the magnesium matrices. Amid the fabricated composites, the 5wt.% Gr-strengthened Mg-10SiC composites have good wear resistance.

The authors of [38] examined the corrosion and wear characteristics of a ZK60-10HA (hydroxyapatite) composite and stated that according to the findings, magnesium matrix composites that are biocompatible can effectively prevent corrosion and wear by utilizing HA particles as an inhibitor. The goal of this endeavor was to improve the ZK60 resistance to corrosion and to make it more durable. This was accomplished by incorporating micro-SiC and nano-AlN as fortifications into the material. The corrosion properties of the extrudates on both surfaces were evaluated while the extrusion process was in operation [39]. There is an increasing claim for materials that are both lightweight and sturdy, and as a result, the potential for magnesium composites has expanded in multiple sectors. In current decades, there has been an increase in the scope of potential applications for magnesium [40].

A limited selection of the available literature that have been offered in recent times is included in this study, which focuses on the fusion of reinforcements with various magnesium. However, no studies on the effect of ZrB_2 on ZK60 have been studied. Also, there is insufficient information accessible on the properties of ZK60 composites. Thus, our aim is to study the consequences of varying ZrB_2 reinforcement on the wear, and corrosion properties of the ZK60 composites and to focus on the optimization of wear parameters (WR) of MMMCs synthesized through stir casting.

EXPERIMENTAL

ZrB_2 particles were employed in the present work as reinforcements in a ZK60 alloy matrix. Through SC method, composites with different degrees of reinforcement including 0, 4, 8, and 12 % were used to synthesize the ZK60/0 wt.% ZrB_2, ZK60/4 wt.% ZrB_2, ZK60/8 wt.% ZrB_2, and ZK60/12 wt.% ZrB_2 composites and the raw material and fabricated sample is shown in Figure 1.



Figure 1. Raw material and prepared composite

In order to produce the composite specimen, the stir casting procedure was applied. This is due to the fact that it ensures a more equal dispersion of the reinforcing particles across the entirety of the specimen. The utilization of this technique allows for the manufacture of composites that contain particles to be achieved at the most cost-effective level feasible. The matrix alloy or matrix material was initially heated to a temperature that was higher than its melting point. In order to keep the matrix alloy in a semisolid state, the temperature was gradually lowered to a level that was lower than the liquid condition. This was done in order to maintain the matrix alloy. As soon as the temperature reached this level, the warmed reinforcement particles, at predetermined weight percentage were added to the slurry, and a stirrer was used to blend the particles. As the temperature of the composite slurry was being raised to a completely molten state, stirring was maintained at an average stirring speed while an argon gas shield provided an inert atmosphere for protection [41]. The entire process of fabrication with the processing parameters is shown in a flow chart (Figure 2).

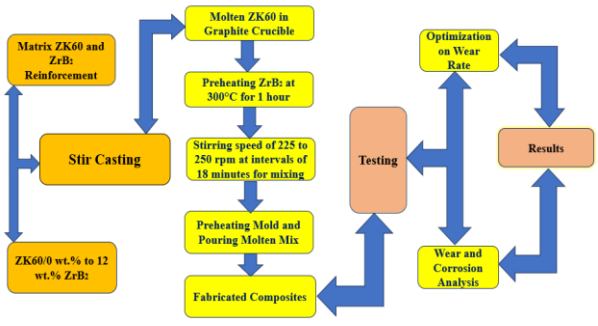


Figure 2. Entire work flow process of the research

The scheme of the casting setup is presented in Figure 3.

Initially, constants of 20 N (C2), 4 m/s (C3), and 1500 m (C4), sliding diameter of 40 mm, 478 rpm of sliding speed and 1500 s duration were used to conduct the wear test.

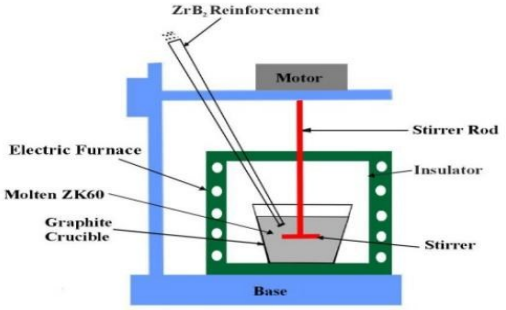


Figure 3. Scheme of the stir casting setup

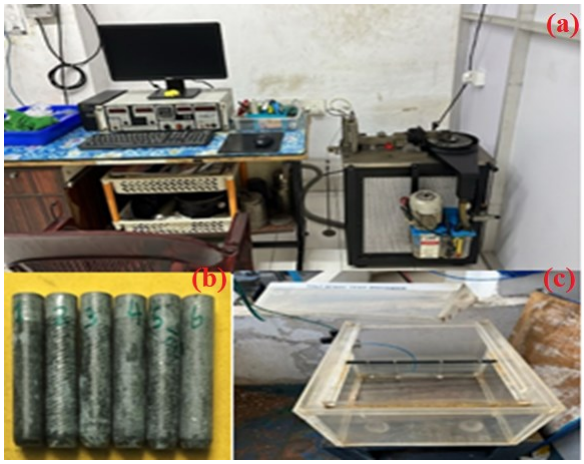


Figure 4. a) Wear tester (b) Wear sample (c) Salt spray

The wear tester is shown in Figure 4 (a). The machined samples are shown in Figure 4 (b). The salt spraying test is utilized and used weight loss methods to calculate the corrosion loss on composite samples with a size of 10×10×10 mm and the setup is shown in Figure 4 (c). It is carried out in compliance with ASTM B117. Wear examinations were performed utilizing the pin-on-disc (POD) tester on the composite specimens. As per ASTM G99, the specimens were made with size of 30 mm in length and 8 mm in diameter. Wear testing was performed at the room temperature at .

Taguchi's approach was applied to the experimentations. WR was considered as the output response in this study [42] and the four-level with four input components were chosen for experimentation which is displayed in Table 1.

Table 1. Parametric levels

Input parameters and their units	Levels			
	1	2	3	4
C1 (%)	0	4	8	12
C2 (N)	5	10	15	20
C3 (m/s)	1	2	3	4
C4 (m)	750	1000	1250	1500

RESULTS AND DISCUSSION

Wear analysis

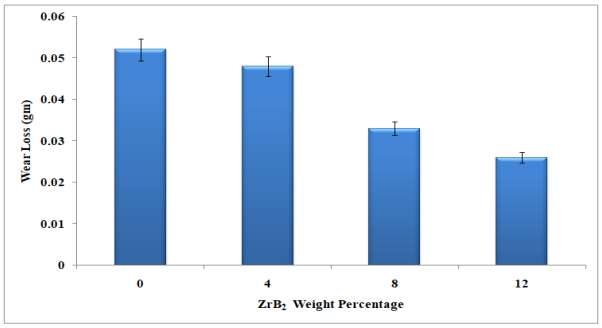


Figure 5. Weight percentage of reinforcement *vs.* wear loss

As seen in Figure 5, wear rate values fell as ZrB_2 weight percentage increased. The wear loss was significantly less than that of ZK60 alloy and ZK60/12wt.% ZrB_2 composites. Comparing the samples ZK60/8wt.% ZrB_2 and ZK60/4wt.%ZrB_2 to ZK60 alloy, a decrease in wear rate was also noted with a decline in values when reinforcement is increased. Nonetheless, the surface qualities are influenced by the weight fraction of the reinforcement.

Corrosion analysis

Figure 6 shows the weight loss for the ZK60 alloy, ZK60/4wt.% ZrB_2, ZK60/8wt.% ZrB_2, and ZK60/12wt.% ZrB_2 composite. The weight loss during the salt spray test is lessened by the increased ZrB_2 presence in the ZK60 alloy. When the wt.% of ZrB_2 added to the ZK60 matrix in increasing order, the corrosion rate also falls. For the fabricated composite samples, there is an improvement in corrosion resistance. This is because ZrB_2 is dispersed appropriately in the matrix's grain boundary, where it forms an appropriate passive layer that shields the surface from corrosion. It has been observed that raising the amounts of wt.% of particle in the ZK60 progressed the corrosion resistance.

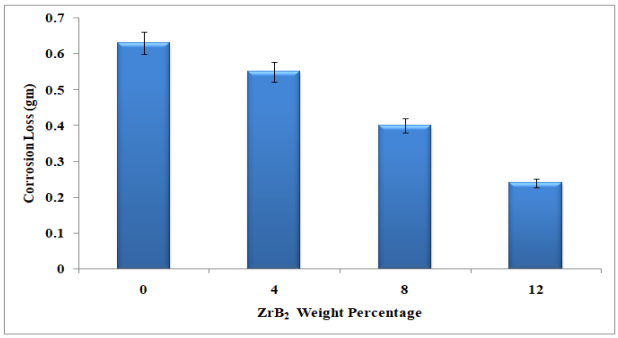


Figure 6. Weight percentage of reinforcement *vs.* corrosion loss.

Optimization for WR

Using a POD tester, produced ZK60/ZrB_2 composites' wear rate was assessed. The Taguchi approach [42] was utilized to optimize the variables for WR as optimization yields significant benefits, particularly in regard to cost savings. Industries may significantly minimize waste which greatly increases production. Since wear is an important parameter for any mechanical components this study is considered and the results are examined in as in Table 2.

Table 2. L_{16} orthogonal array

Exp. No	C1	C2	C3	C4	WR (mm^3/m)	S/N Ratio
1	0	5	1	750	0.044	27.1309
2	0	10	2	1000	0.047	26.5580
3	0	15	3	1250	0.050	26.0206
4	0	20	4	1500	0.053	25.5145
5	4	5	2	1250	0.044	27.1309
6	4	10	1	1500	0.053	25.5145
7	4	15	4	750	0.034	29.3704
8	4	20	3	1000	0.043	27.3306
9	8	5	3	1500	0.040	27.9588
10	8	10	4	1250	0.035	29.1186
11	8	15	1	1000	0.039	28.1787
12	8	20	2	750	0.034	29.3704
13	12	5	4	1000	0.021	33.5556
14	12	10	3	750	0.022	33.1515
15	12	15	2	1500	0.039	28.1787
16	12	20	1	1250	0.040	27.9588

Analysis of WR

Tables 3 and 4 display the WR - S/N ratio and WR mean for the produced ZK60/ZrB_2 composites. The tables show the response mean and the S/N ratio mean value for every intensity of control parameter. The arrangement of the important mechanism on the intended response value is demonstrated by a certain rank. Moreover, the tables demonstrate that the wt % of ZrB_2 particle (C1) has the biggest influence on WR, with the normal C4, C3, and C2 following in that order. This is explained by the ZrB_2 particles' contribution to the ZK60 composites which lowers the WR. Nonetheless, the wear rate is increased by C2. This is brought on by increased contact pressure between the disc surface and pin, which raises the WR.

Table 3. Response table for signal to noise of WR

Levels	C1	C2	C3	C4
1	-28.40	-29.20	-28.68	-29.45
2	-28.72	-29.08	-28.88	-29.18
3	-29.14	-28.92	-29.09	-28.80
4	-29.71	-28.79	-29.32	-28.55
Delta	1.31	0.41	0.64	0.90
Rank	1	4	3	2

Table 4. Response table for means

Levels	C1	C2	C3	C4
1	26.31	28.94	27.20	29.76
2	27.34	28.59	27.81	28.91
3	28.66	27.94	28.62	27.56
4	30.71	27.54	29.39	26.79
Delta	4.41	1.40	2.19	2.96
Rank	1	4	3	2

Figures 7 and 8 display the primary influence of WR through the S/N ratio and the mean value. The ideal level of each component and each one's impact on the WR of the tested ZK60/ZrB_2 composites are visible from the graphs. Figure 7 shows that the optimum levels of the following factors (12 wt.%), C2 (5 N), C3 (4 m/s), and C4 (750 m)—achieve the lowest WR. Figure 7 also makes it evident that as the weight percentage of ZrB_2 material is added, the WR steadily decreases.

The ZK60 composites reinforced with 12 wt.% ZrB_2 particles exhibit the lowest WR value of 0.021 mm3/m. It is evident that the WR increases in accordance with the Archard's law as the load increases. WR for the sliding velocity is largest at inferior speeds and diminishes with escalating speed. About the C4, more surface contact leads to a higher localized temperature, which in turn causes more metal loss. Therefore, as the sliding distance increases, so does the WR.

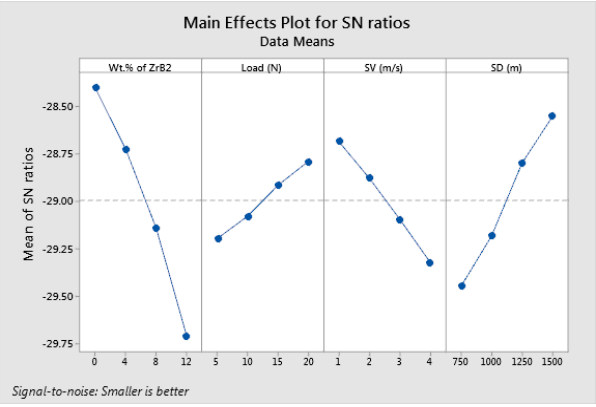


Figure 7. Main effects plot for S/N ratio of WR

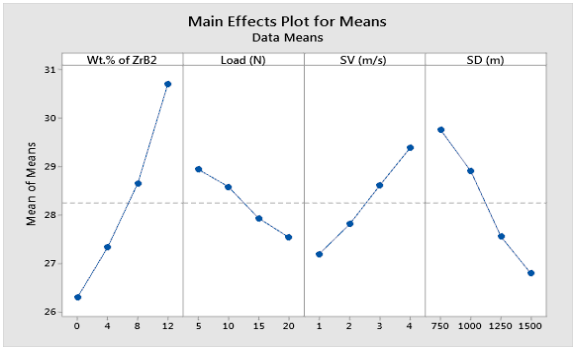


Figure 8. Main effects plot for means of WR

Contour plot analysis

The wear rate of ZK60/ZrB_2 composite is analyzed in Figure 9 (a–d) *via* contour plot analysis. Figure 9 (a) displays the WR of C1 *vs*. C2, Figure 9 (b) displays the WR of C2 *vs*. C3, Figure 9 (c) displays the WR of C3 *vs*. C4, Figure 9 (d) displays the WR of C1 *vs*. C4. It is evident from these plots that the weight percentage of ZrB_2 has a greater influence on the WR of the fabricated composites. However, a raise in load causes material wear because of the high contact pressure. This is because it is evident from the essentials of tribology that an augment in C4 results in an increase in wear volume, but the WR remains nearly constant. Overall, the contour plot analysis identifies the parameter regions that provide optimal and stable operating conditions, thereby facilitating process optimization and enhancing the robustness of the tribological performance.

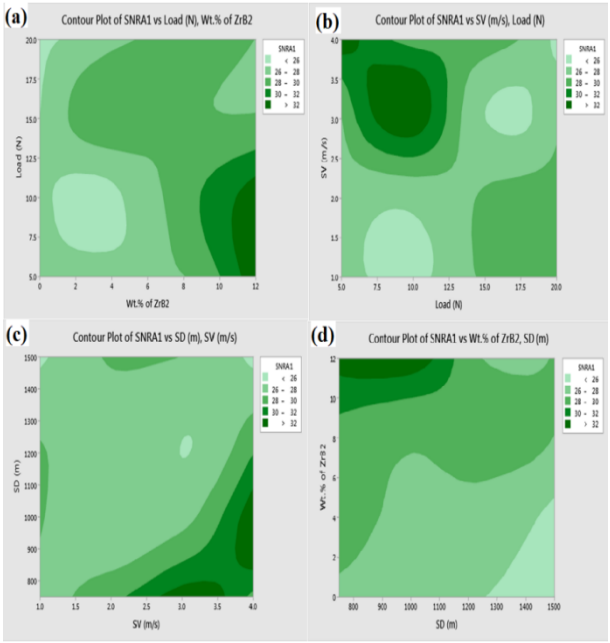


Figure 9. Contour plot for WR of (a) C1 *vs*. C2, (b) C2 *vs*. C3 (c) C3 *vs*. C4 (d) C1 *vs*. C4

Analysis of variance

ANOVA is an arithmetical design tool with an emphasis on least squares that is widely used to separate the individual effects from each of the control components. It is used to establish the order of factors in this study at a significance level of 5%. If a factor's P-value is less than 0.05, it is confirmed that the variables have an empirically noteworthy influence on the responses. Table 5 presents the WR of the ZK60/ZrB_2 composites that were created, as determined by an ANOVA and it could be witnessed that the P-values for C1 and C4 are less than 0.05, signifying that overall parameters encompass an important influence on WR. Moreover, the involvement of C1 had an effect of 43.34% and C4 had an effect of 21.21% on WR of the produced composites.

Table 5. ANOVA for WR

Source	DF	Adj SS	Adj MS	F-value	P-value
C1	3	43.344	14.4480	29.10	0.010
C2	3	4.765	1.5884	3.20	0.183
C3	3	10.952	3.6508	7.35	0.068
C4	3	21.217	7.0724	14.24	0.028
Error	3	1.490	0.4965		
Total	15	81.768			

CONCLUSIONS

In the current work MMCs are successfully synthesized using a stir casting method with different weight percentages of ZrB_2 particles (0, 4, 8, and 12 wt.%). This work focuses on the wear and corrosion properties of ZK60/ZrB_2 strengthened with various weight percentages of ZrB_2. Simultaneously, the ZK60/ZrB_2 underwent wear testing using a POD setup for finding the minimal wear rate in determining optimal parameter. The ZK60 alloy's wear and corrosion resistance significantly improved upon the addition of ZrB_2 particles up to a weight percentage of 12. The ZK60 alloy matrix composite containing 12 weight percent ZrB_2 showed excellent corrosion resistance, with corrosion loss of 0.242 gm. The Taguchi technique was used to identify the ideal parameters for the developed composites' wear rate in dry sliding circumstances, and their impact on the wear rate is assessed. The S/N ratio graph indicates that the ideal dry sliding parameters for the developed composites are 12 weight percent of ZrB_2 content, 5 N C2, 4 m/s C3, and 750 m C4. These values result in the least WR of 0.021 mm^3/m. According to the results of the ANOVA, the weight percentage of ZrB_2 content has a significant impact on wear rate, contributing 43.34% of the total.

Acknowledgement: *Not applicable.*
Author contributions: *S. Suresh Kumar has done the original draft, reviewing and editing. V. Mohanavel has supervised the research work.*
Conflict of interest: *On behalf of the authors, the corresponding author states that there is no conflict of interest.*
Research funding: *Not applicable.*
Data availability: *Not applicable.*

REFERENCES

1. P. Bharathi, T. Sampath Kumar, *Proc. Inst. Mech. Eng. Part E: J. Process Mech. Eng*., **237**, 1014 (2023).
2. M. P. Reddy, N. Alsaleh, S. Ataya, K. R. Gopal, A. M. A. Mohamed, *J. Mater. Res. Technol*., **39**, 8076 (2025).
3. S. Seetharaman, J. Subramanian, R. A. Singh, W. L. E. Wong, M. L. S. Nai, M. Gupta, *Technologies*, **10**, 32 (2022).
4. D. K. Ammisetti, S. H. Kruthiventi, S.Vinjavarapu, N. N.,Babu, J. R. Gandepudi, S. K. Battula, *J. Eng. Appl. Sci*., **71,** 60 (2024).
5. P. K. Gupta, A. K. Trivedi, M. K. Gupta, M. Dixit, *Proc. Inst. Mech. Eng. Part L: J. Mater. Des. Appl.,* **238,** 1827 (2024).
6. K. Pooja, N. Tarannum, P. Chaudhary, *Discov. Mater*., **5**, 35 (2025).
7. S. Jhamb, J. Matai, J. Marwaha, A. Goyal, A. Pandey, *Adv. Mater. Process. Technol*., **9**, 1249 (2023).
8. N. Gupta, M. Paramsothy, *JOM*, **66**, 862 (2014).
9. P. Emadi, B. Andilab, C. Ravindran, *J. Indian Inst. Sci.*, **102**, 405 (2022).
10. J. Tan, S. Ramakrishna, *Appl. Sci.,* **11**, 6861 (2021).
11. Y. Yang, X. Xiong, J. Chen, X. Peng, D. Chen, F. Pan, *J. Magnesium Alloys*, **9**, 705 (2021).
12. V. K. Bommala, M. G. Krishna, C. T. Rao, *J. Magnesium Alloys*, **7,** 72 (2019).
13. V. K. Murali, M. S. Starvin, *J. Chil. Chem. Soc*., **68**, 5911 (2023).
14. S. K. Rohit Singh, D. Tiwari, S. Sahu, V. B. Jadhav, A. K. Jain, K. K. Pandey, *Lect. Notes Mech. Eng., ICRAM 2025, Recent Adv. Mater. Manuf. Sci*., 2025.
15. J. Y. Ren, G. C. Ji, H. R. Guo, Y. M. Zhou, X. Tan, W. F. Zheng, Q. C. Jiang, *Materials*, **17**, 2454 (2024).
16. N. Mustafa, N. N. A. Basir, R. E. Ibrahim, M. M. Mahat, N. N. Bonia, M. Y. Sabrina, R. Rosmamuahamadani, *Int. J. Eng. Technol*., **7**, 406 (2019).
17. E. W. Neuman, M. Thompson, W. G. Fahrenholtz, G. E. Hilmas, *J. Eur. Ceram. Soc*., **42**, 4024 (2022).
18. H. Wang, C. A. Wang, X. Yao, D. Fang, *J. Am. Ceram. Soc*., **90**, 1992 (2007).
19. J. K. Sonber, A. K. Suri, *Adv. Appl. Ceram*., **110**, 321 (2011).

20. P. Sarmah, K. Gupta, *Materials*, **17**, 4635 (2024).
21. D. Srinivasan, M. Meignanamoorthy, A. Gacem, M. Vinayagam, T. Sathish, M. Ravichandran, H. L. Allasi, *J. Nanomater*., **2022**, 7840939 (2022).
22. K. Shivalingaiah, V. Nagarajaiah, C. P. Selvan, S. T. Kariappa, N. G. Chandrashekarappa, A. Lakshmikanthan, E. Linul, *Metals*, **12**, 1297 (2022).
23. R. S. Martins, I. Zimpel, V. K. De Barcellos, *Mater. Today Commun*., **43**, 111718 (2025).
24. C. Morsiya, S. Pandya, *Arch. Metall. Mater*., **68,** 1473 (2023).
25. A. Kumar, S. Kumar, N. K. Mukhopadhyay, *J. Magnesium Alloys*, **6**, 245 (2018).
26. H. Saravanan, D. Veeman, D. Srinivasan, M. Ravichandran, *Ceram. Int*., **51**, 7130 (2025).
27. S. Ayyanar, A. Gnanavelbabu, K. Rajkumar, P. Loganathan, K. Vishal, Proc. *Inst. Mech. Eng. Part C: J. Mech. Eng. Sci.*, **237**, 692 (2023).
28. N. Selvakumar, P. Narayanasamy, *Tribol. Trans*., **59**, 733 (2016).
29. S. Sathish, V. Anandakrishnan, S. Sankaranarayanan, M. Gupta, *J. Tribol*., **23**, 76 (2019).
30. M. S. Lee, C. G. Kang, J. S. S. Babu, *Metals*, **13**, 1418 (2023).
31. S. Sathish, V. Anandakrishnan, M. Gupta, *Ind. Lubr. Tribol*., **72**, 503 (2019).
32 C. Tarasasanka, K. Snehita, K. Ravindra, D. Sameerkumar, *Int. J. Eng. Sci. Technol*., **11**, 41 (2019).
33 C. Y. H. Lim, S. C. Lim, M. Gupta, *Wear*, **255**, 629 (2003).
34 B. M. Girish, B. M. Satish, S. Sarapure, D. R. Somashekar Basawaraj, *Tribol. Trans*., **58**, 481 (2015).
35 A. Singh, N. Bala, *Mater. Res. Express*, **6**, 1065H1 (2019).
36 S. Tiwari, R. Balasubramaniam, M. Gupta, *Corros. Sci*., **49**, 711 (2007).
37 K. S. Prakash, P. Balasundar, S. Nagaraja, P. M. Gopal, V. Kavimani, *J. Magnesium Alloys*, **4**, 197 (2016).
38 J. Su, J. Teng, Z. Xu, Y. Li, *Friction*, **10**, 31 (2022).
39 A. Sager, I. Esen, H. Ahlatçi, Y. Turen, *Materials*, **15**, 8582 (2022).
40 K. Chauhan, J. Karloopia, R. S. Walia, M. Dhanda, *Crit. Rev. Solid State Mater. Sci.,* **49**, 1 (2024).
41 S. S. Kumar, V. Mohanavel, *Matéria (Rio de Janeiro*), **29**, e20240264 (2024).
42 S. S. Kumar, V. Mohanavel, *Interactions*, **245**, 208 (2024).

Bulgarian Chemical Communications, Volume 58, Issue 4 (pp. 523-549) 2026 *DOI: 10.34049/bcc.58.4.5734*

Hydrogen as a strategic energy transition pathway: production technologies, cost dynamics, infrastructure, policy and India's statistical roadmap to 2030 and 2050

A. Gheewala*, H. Mistry, A. Solanki

Department of Electrical Engineering, Shroff S. R. Rotary Institute of Chemical Technology [SRICT], UPL University of Sustainable Technology, Vataria, Ankleshwar, Gujarat, India

Received: May 07, 2026; Revised: June 25, 2026

The transition toward green hydrogen is increasingly recognized as a key strategy for achieving deep decarbonization and long-term energy sustainability, particularly in developing and rapidly industrializing economies. This study presents a comprehensive review of hydrogen production technologies, techno-economic performance, sectoral applications, and policy frameworks associated with the emerging hydrogen economy. The analysis compares major hydrogen production pathways, including alkaline electrolysis (AWE), proton exchange membrane (PEM) electrolysis, and solid oxide electrolysis (SOEC), with respect to efficiency, operational flexibility, technological maturity, and economic feasibility.

The study further evaluates the levelized cost of hydrogen (LCOH) under different renewable energy integration scenarios and identifies the major factors influencing hydrogen production costs, such as electricity price, electrolyzer capital cost, system efficiency, and infrastructure availability. Current green hydrogen production costs remain higher than conventional fossil-fuel-based hydrogen pathways; however, significant cost reductions are expected due to advancements in renewable energy technologies, economies of scale, and improvements in electrolyzer performance.

Sectoral demand assessment indicates substantial future growth in hydrogen utilization across fertilizers, petroleum refining, steel manufacturing, chemical industries, power generation, and heavy transportation sectors. In addition, the review highlights major challenges related to hydrogen storage, transportation, infrastructure development, financing, and regulatory frameworks. The study also discusses the role of national policies, industrial investments, and research initiatives in accelerating hydrogen adoption. Overall, this work provides a generalized and integrated perspective on the technological, economic, and policy dimensions of the hydrogen transition and outlines key pathways for enabling large-scale deployment of sustainable hydrogen systems.

Keywords: Green hydrogen; Energy transition; Decarbonization; Levelized cost of hydrogen (LCOH); Electrolysis; Renewable energy integration; National green hydrogen mission (NGHM); Hydrogen economy; India; Carbon neutrality; Sectoral demand; Electrolyzer deployment

INTRODUCTION

The global energy system is undergoing one of the most profound structural transformations in recorded history. Escalating climate risks, geopolitical energy dependencies, and legally binding net-zero commitments are driving unprecedented investment in clean energy technologies. Within this landscape, hydrogen has emerged as a uniquely versatile energy carrier capable of decarbonizing sectors where direct electrification remains technically or economically constrained—including steel production, long-haul transport, fertilizer synthesis, and high-temperature industrial processes [2, 20, 60].

India occupies a particularly significant position in this global transition. As the world's most populous nation and fifth-largest economy, with energy demand projected to outpace all other major regions by 2040, India's energy choices carry global consequence. Currently, India annually consumes approximately 6–7 million tons *per annum* (MTPA) of hydrogen, almost entirely produced through grey pathways—steam methane reforming (SMR) and coal gasification—contributing an estimate of 57–65 million tons of CO_2 annually from hydrogen production alone [65, 67, 134].

The national green hydrogen mission (NGHM), launched on January 4. 2023 with an outlay of INR 19,744 crore (approximately USD 2.4 billion), is the most ambitious clean energy policy initiative in India's history. It targets 5 MTPA of green hydrogen production by 2030—with an ambition to reach 10 MTPA including exports—positioning India for approximately 10% of the projected global green hydrogen demand of 100+ MTPA by 2030 [86, 135, 155].

Despite rapid policy momentum, the academic literature lacks a unified, statistically grounded review that consolidates multi-dimensional data from government documents, international agency forecasts, and peer- reviewed research into

* To whom all correspondence should be sent: Email: *ankur.gheewala@upluniversity.ac.in*

© 2026 Bulgarian Academy of Sciences, Union of Chemists in Bulgaria

structured analytical framework. This review addresses that gap comprehensively—synthesising data across ten chart-illustrated quantitative dimensions and five creative process diagrams. This review integrates these dimensions within a unified analytical framework, constituting the most complete review of India's hydrogen transition available to date [31, 67, 109].

The hydrogen transition is structured across two strategic phases: Phase I (2023–2030) focuses on technology demonstration, policy activation, cost reduction, and initial industrial decarbonization; Phase II (2030–2050) targets large-scale commercial deployment, export leadership, and deep economy-wide decarbonization consistent with India's net-zero commitment for 2070 [67, 91, 135].

Despite the rapidly expanding body of literature on hydrogen energy systems, a critical gap persists in the integrated, India-specific assessment of hydrogen transition pathways, particularly in the context of long-term techno-economic feasibility, sectoral demand evolution, and policy-driven deployment frameworks. Existing reviews predominantly focus on global hydrogen trends, electrolyzer technologies, or isolated techno-economic aspects, often lacking a holistic, data-driven synthesis tailored to India's unique energy landscape [67, 109].

Several recent studies by international agencies such as IEA, IRENA, and NITI Aayog provide valuable projections; however, these analyses are typically fragmented across domains—technology performance, cost projections, infrastructure readiness, or policy frameworks—without offering a unified multi-dimensional evaluation. Furthermore, prior literature rarely integrates quantitative projections (2030–2050) with sector-wise hydrogen demand, infrastructure readiness, and investment trajectories in a single coherent framework. This creates a disconnect between strategic policy vision and implementable techno-economic pathways, particularly for emerging economies like India [106].

Another key limitation in existing reviews is the lack of comparative multi-criteria assessment of hydrogen production technologies (AWE, PEM, SOEC) under India-specific operating conditions, including renewable intermittency, cost sensitivity, scalability constraints, and infrastructure limitations. Additionally, limited attention has been given to the dynamic transition from grey to green hydrogen, especially in terms of cost convergence timelines, carbon reduction potential, and sectoral adoption thresholds [69].

Methodology of this review

This study employs a hybrid methodology combining systematic literature review (following PRISMA guidelines), bibliometric analysis, thematic synthesis, and statistical data consolidation [7, 8]. This PRISMA flow diagram, as shown in Figure 1, details the systematic literature selection process, starting with the initial identification of 731 records from comprehensive databases and alternative sources. After eliminating 96 duplicates, 635 unique records underwent a preliminary title and abstract screening, resulting in the exclusion of 339 irrelevant studies. The remaining 296 full-text articles were rigorously assessed for eligibility, where another 115 papers were excluded based on specific constraints such as lacking an India-focused scope or sufficient quantitative data. Ultimately, a refined cohort of 180 studies met all predefined criteria and was successfully synthesized. These final 180 papers were utilized across both the qualitative synthesis and quantitative statistical analyses for the study.

- *Literature search and data sources.* Databases searched include Scopus, Web of Science, ScienceDirect, and Google Scholar covering 2015–2025. Primary statistical data was sourced from: MNRE, NITI Aayog, NGHM mission documents, IEA global hydrogen review (2023), IRENA cost reports, IEEFA demand analyses, Bloomberg NEF hydrogen outlook, McKinsey global energy perspective, CEEW financing analyses, ORF America background papers, and Markntel Advisors market reports. Search terms included 'green hydrogen India statistics 2030-2050', 'NGHM targets', 'hydrogen demand forecast India', 'electrolyzer capacity India', and 'LCOH India' [7, 61, 67, 90, 135].
- *Statistical data consolidation.* Each quantitative data point presented in ten charts is cross-validated from at least two independent institutional sources. Where projections varied across sources, conservative central estimates are presented with source ranges noted. Data for charts 1–10 spans the period 2022–2050, covering demand, cost, capacity, investment, market size, CO_2 abatement, electrolyzer growth, renewable energy,

production mix, and CAPEX-LCOH correlation [61, 67, 109].

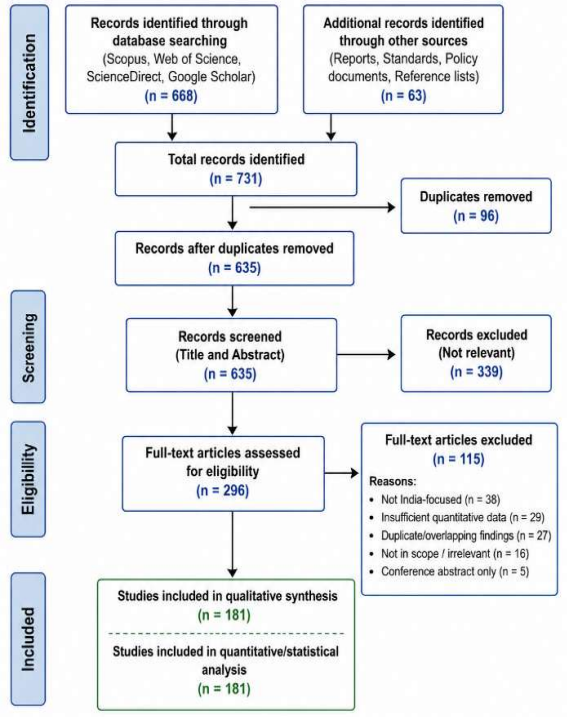


Figure 1. Methodology PRISMA framework of the review

Hydrogen energy fundamentals

Hydrogen (H_2) is the lightest and most abundant element in the universe yet does not occur freely in nature in significant quantities—it must be produced from compound forms such as water, natural gas, coal, or biomass. Its gravimetric energy content of 119.9–141.9 MJ/kg is 2–3 times higher compared to conventional hydrocarbon fuels, making it highly attractive for weight-sensitive applications such as aviation, shipping, and heavy-duty transport. However, its volumetric energy density at atmospheric pressure (10.7 MJ/m³) is lower by orders of magnitude than that of liquid fuels, necessitating compression to 350–700 bar or cryogenic liquefaction at −253°C for practical storage and transport [2, 9, 19]. Table 1 presents key thermodynamic and physical properties of hydrogen in comparison with conventional fuels.

Hydrogen functions as an energy carrier—not a primary source—analogous to electricity. When produced from renewable electricity *via* electrolysis, it enables seasonal and long-duration storage of intermittent solar and wind energy, and facilitates sector coupling across power, transport, and heavy industry. India's renewable energy capacity has grown from 35,850 MW (March 2014) to over 223,273 MW (March 2026)—a 6.2× increase in 12 years—providing an increasingly strong foundation for green hydrogen production [2, 9].

Table 1. Physical and thermodynamic properties of hydrogen *vs*. conventional fuels [2, 9, 19]

Property	Hydrogen	Methane	Gasoline	Diesel
Molecular weight (g/mol)	2.016	16.013	~110	~170
Boiling point (K)	20.3	111	298–488	453–633
Carbon content (mass%)	0	75	84	86
Higher heating value (MJ/kg)	141.9	55.5	47.3	44.8
Lower heating value (MJ/kg)	119.9	50.0	44.5	42.5
Auto-ignition temperature (K)	853	813	~623	~523
Volumetric energy (MJ/m³ STP)	10.7	33	33×10^3	35×10^3
Adiabatic flame temperature (K)	2,480	2,214	2,580	~2,300
Density (kg/m³ at 1 bar, 273 K)	0.089	0.720	730–780	830
Stoichiometric air/fuel ratio	34.4	17.2	14.7	14.5

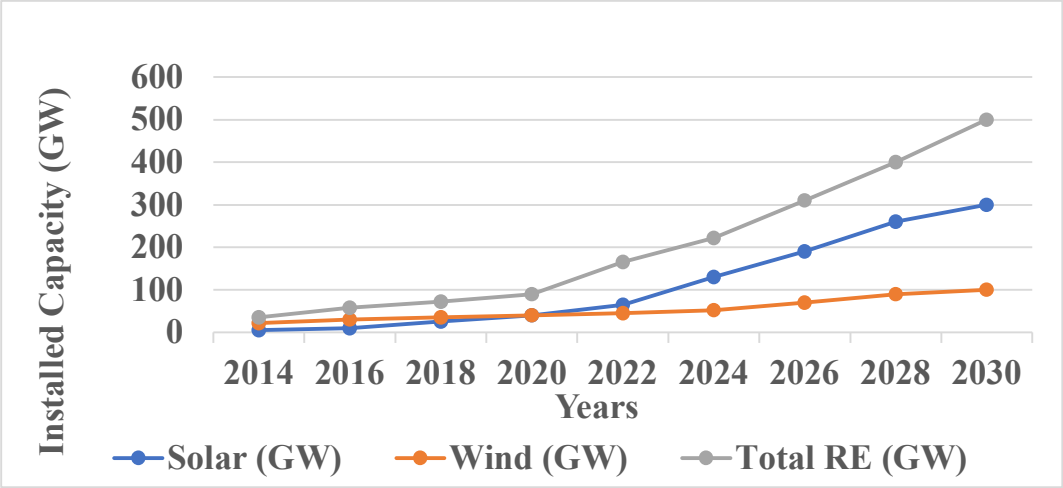


Figure 2. India's renewable energy installed capacity (GW) — historical & projected to 2030 [9, 105, 135, 153]

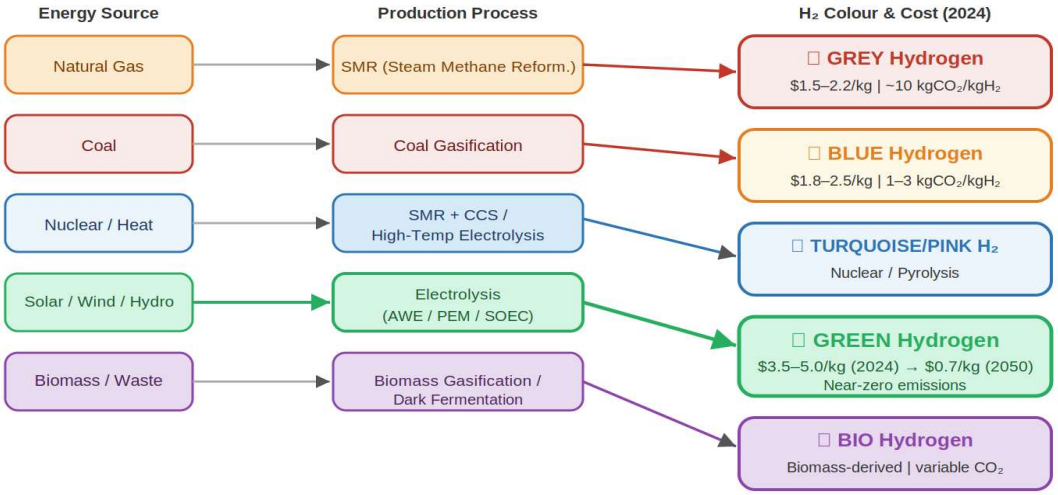


Figure 3. Hydrogen production pathways — color classification, processes & carbon intensity [11, 61, 109, 135]

The line graph in Figure 2, illustrates the growth and projected trajectory of renewable energy installed capacity in gigawatts (GW) from 2014 to 2030, categorized by solar, wind, and total renewable energy (RE) [105]. In the initial period between 2014 and 2020, both solar and wind capacities experienced steady but modest growth, with total RE capacity remaining under 100 GW. Post-2020, the trajectory accelerates sharply, driven primarily by a massive surge in solar capacity which overtakes wind power to become the dominant contributor [135]. By 2026, total RE capacity is shown tracking past 300 GW, with solar contributing roughly 190 GW and wind accounting for approximately 70 GW [153]. Looking forward to 2030, the aggressive upward trend is projected to continue, with total RE capacity targeting 500 GW, comprised of 300 GW from solar and 100 GW from wind [9].

Figure 3 provides a visual classification of all major hydrogen production pathways, their source materials, processes, environmental impact, and 2024 cost benchmarks. This figure replaces several paragraphs of descriptive text with a single-glance reference framework [11, 61, 109].

Hydrogen production technologies — technical assessment

Hydrogen production technologies broadly divide into conventional fossil-based routes and emerging renewable-based pathways. Technology selection determines carbon intensity, levelized cost of hydrogen (LCOH), scalability, and long-term strategic viability [109, 133].

Conventional methods

- *Steam methane reforming (SMR).* SMR accounts for approximately 48% of the global hydrogen production and is the dominant method in India, supplying hydrogen to fertilizer plants and petroleum refineries. Figure 4 illustrates the industrial process of producing high-purity hydrogen (H_2) *via* steam methane reforming (SMR), beginning with the endothermic reaction of natural gas and steam in a catalyst-filled reformer furnace (700-1000^0 C). The resulting synthesis gas (syngas) undergoes heat recovery and is fed into a two-stage water-gas shift (WGS) reactor to exothermically convert carbon monoxide and water into additional hydrogen and carbon dioxide. Following this shift, a purification system, such as pressure swing adsorption (PSA), separates the final high-purity hydrogen product from off-gas byproducts that are recycled back into furnace fuel. Economically, the process is highly advantageous due to its low production costs and well-established, globally dominant infrastructure. However, it carries a heavy environmental burden, generating significant carbon dioxide (CO_2) emissions that make it environmentally unsustainable without carbon capture and storage (CCS). SMR emits approximately 9–12 kg CO_2 per kg H_2 without CCS—making it the largest source of industrial CO_2 in the hydrogen sector. In India, SMR currently supplies ~40% of hydrogen demand in refining alone, producing ~47 Mt of CO_2 by 2050 under a business-as-usual scenario. [56, 133, 134].
- *Coal gasification.* Coal gasification partially oxidizes coal at 1,200–1,500°C (efficiency 55–65%) to produce synthesis gas, emitting 18–20 kg CO_2/kg H_2—the highest carbon intensity of any pathway. Figure:5 gives the details of the process of coal gasification, where a coal feed reacts with oxygen and steam via partial oxidation to generate syngas (H_2, CO, CO_2). The syngas undergoes pollutant removal and is fed into a water-gas shift (WGS) reactor before being purified (e.g., via PSA) to yield clean hydrogen (H_2). While the method economically leverages domestic coal and enhances energy security, it carries an optional integration for CCS to prevent high carbon emissions from bypassing geological storage. Without CCS, the process outputs create severe environmental liabilities, notably high CO_2 emissions that hinder a low-carbon transition. Furthermore, the overall process incurs a substantial environmental footprint through heavy air pollution (SO_2, NO_x, and particulates) alongside high water consumption. India's large domestic coal reserves make this a transitional option with CCS integration, though CCS at scale remains technically and economically challenging [24, 53].

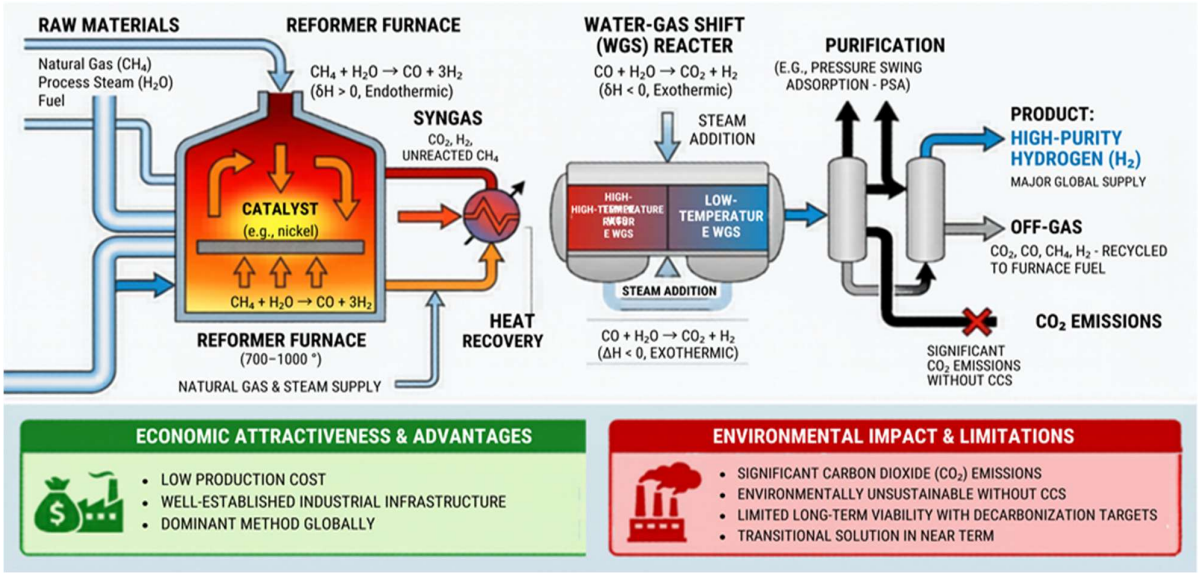


Figure 4. Steam methane reforming (SMR) process for hydrogen production

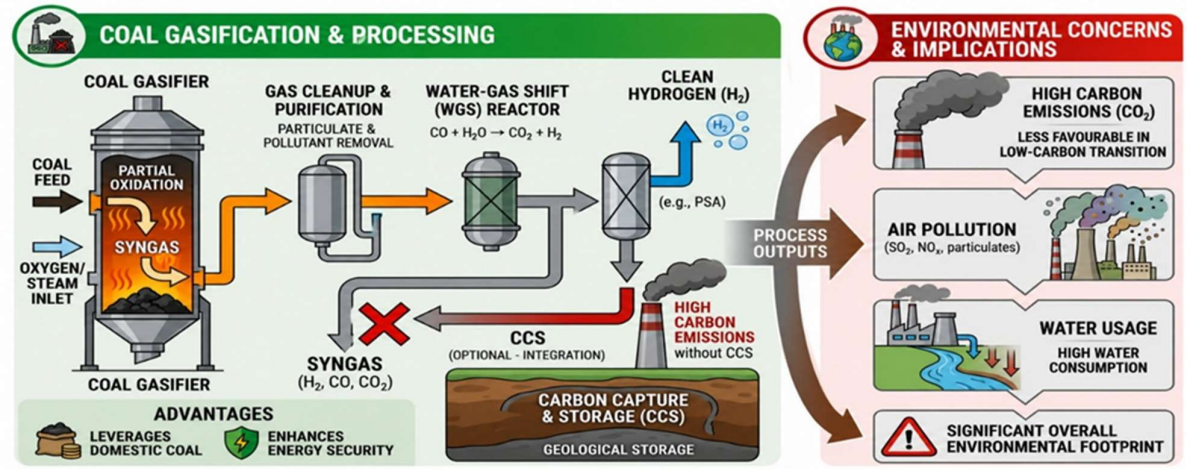


Figure 5. Coal gasification process for hydrogen production & environmental impact

Renewable-based methods

- *Alkaline water electrolysis (AWE).* AWE is the most commercially mature electrolysis technology with a global installed base exceeding 5 GW. Figure 6 presents an overview of alkaline water electrolysis (AWE) for hydrogen production, featuring its process schematic, industrial characteristics, and strategic application in India. The scheme depicts a DC power-driven cell operating at 60-90^0 C, where water (H_2O) splits to release hydrogen (H_2) at the cathode and oxygen (O_2) at the anode *via* hydroxyl (OH^-) ion transport across a porous separator. Industrially, AWE is highly advantageous due to being a mature, commercially established technology boasting long operational lifetimes and a relatively low capital cost. However, its primary operational limitation is a rigid design that offers limited flexibility for fluctuating power inputs and struggles with intermittent renewable sources. Strategically, its ideal deployment in India targets large-scale hydrogen production paired with stable, continuous renewable energy grids like utility-scale solar installations to ensure steady operation. The CAPEX of USD 500–1,100/kW (2024)—the lowest of any electrolysis option. Its primary restriction is limited dynamic response (<1% load change per sec), making it better suited to stable baseload renewable supply. In India, GAIL's 10 MW PEM plant at Vijapur and Indian Oil's solar-powered AWE station demonstrate both technologies at commercial scale [16, 41, 61, 150].
- *Proton exchange membrane (PEM) electrolysis*. PEM electrolyzers typically exhibit efficiencies of 70–90% based on the higher heating value (HHV) of hydrogen under optimized operating conditions. The upper end of this range generally represents stack-level performance achieved under controlled conditions. In practical industrial applications, overall system efficiency is often lower due to auxiliary power requirements, water purification systems, thermal management, gas compression, and balance-of-plant losses. Nevertheless, PEM technology remains highly attractive because of its rapid response, high current density, and compatibility with variable renewable energy sources [157]. Figure 7 depicts the details of the PEM electrolysis process, showcasing its operational mechanism, performance benefits, and future outlook. The simplified process schematic illustrates water (H_2O) split at the anode to produce oxygen (O_2), while protons (H^+) travel across a solid polymer electrolyte to the cathode to yield hydrogen (H_2). Performance advantages include higher efficiency and a rapid response to dynamic load conditions, making it ideal for seamless integration with variable renewable energy sources like wind and solar. On the downside, the technology faces key challenges, namely high capital costs and a critical dependence on scarce, expensive noble metal catalysts like platinum (Pt) and iridium (Ir). Despite these limitations, ongoing research in catalyst development and system optimization is expected to lower costs and enhance scalability, rendering PEM electrolysis a highly promising option for future clean hydrogen production in India. However, PEM requires platinum-group metal catalysts (iridium: 0.3–0.5 mg/cm²; platinum), driving CAPEX to USD 1,000–1,800/kW in 2024, declining to USD 300–700/kW by 2030. L&T's indigenously manufactured 1 MW ML-400 system at Hazira (March 2025) and GreenH's 100 MW Phase-1 facility at Jhajjar, Haryana (H2B2 partnership) are India's key PEM milestones [12, 61, 84, 179].

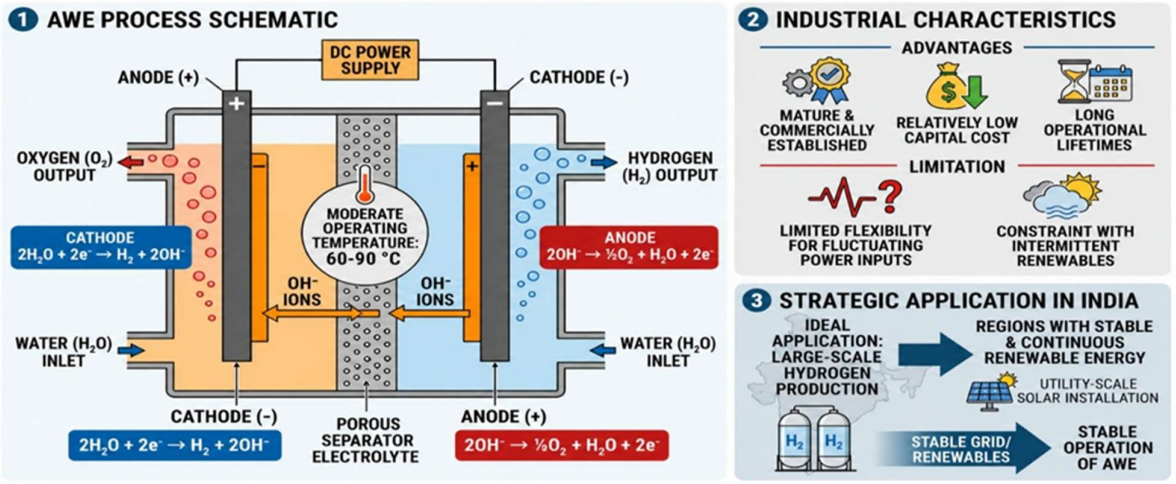


Figure 6. Alkaline water electrolysis

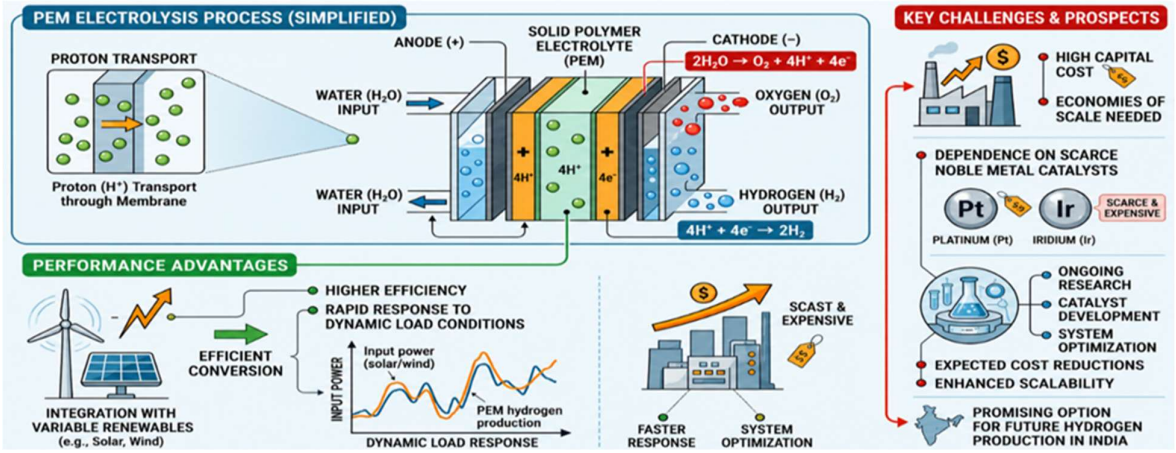


Figure 7. PEM electrolysis: technology, advantage and challenges

- *Solid oxide electrolysis cells (SOEC).* Figure 8 shows the SOEC technology which offers the highest efficiency among currently available electrolysis technologies, typically achieving electrical efficiencies of 85–95% under optimized operating conditions (600–1,000°C), incorporating waste heat from industrial processes. It also offers co-electrolysis of CO_2 and H_2O to produce syngas—a unique advantage. However, material degradation at elevated temperatures, slow start-up (>1 hour), and CAPEX of USD 2,000–3,000/kW (declining to USD 800–1,200/kW by 2030) limit near-term adoption. BARC's R&D program in Mumbai is actively developing SOEC membrane electrode assemblies for Indian industrial applications [32, 35, 61].
- *Biomass-based hydrogen production and their emerging routes.*

(i) Biomass-based hydrogen production. As shown in Figure 9, biomass-derived hydrogen offers a renewable pathway for hydrogen production while simultaneously utilizing agricultural residues, forestry waste, municipal solid waste, and other organic feedstocks [166, 169]. The most common production routes include biomass gasification, pyrolysis, and biological conversion processes. During gasification, biomass reacts with steam and oxygen at elevated temperatures (700–1000°C) to produce syngas, which can subsequently be processed through water–gas shift reactions to increase hydrogen yield [151]. India possesses substantial biomass resources from agriculture and agro-industrial sectors, making biomass-based hydrogen particularly attractive for decentralized and rural energy systems. However, feedstock variability, logistics, tar formation, and gas-cleaning requirements remain important challenges for large-scale deployment [151, 166, 169]. India generates approximately 500–700 million tons of agricultural residues annually, supporting biomass gasification

(efficiency 35–50%) for decentralized hydrogen production.

(ii) Biomass-based hydrogen production emerging routes. Microbial electrolysis cells (MECs) utilize electrochemically active microorganisms to generate hydrogen from organic substrates and wastewater. These systems offer simultaneous waste treatment and hydrogen production but currently face scalability and economic challenges [146, 151]. Photoelectrochemical (PEC) systems directly convert solar energy into hydrogen using semiconductor photoelectrodes. Recent advances in perovskite absorbers and nanostructured materials have improved solar-to-hydrogen conversion efficiencies, although stability and scalability remain key challenges [160]. Advanced cycles such as sulfur–iodine (S–I) and copper–chlorine (Cu–Cl) use high-temperature heat from nuclear or concentrated solar sources to split water into hydrogen and oxygen. Similarly, solar thermochemical processes employ metal oxide redox reactions to directly convert solar heat into chemical energy. Although these technologies exhibit high theoretical efficiencies, they remain at the demonstration stage [160]. Photocatalytic processes employ semiconductor catalysts such as TiO_2 and g-C_3N_4 to split water under solar irradiation. Despite significant progress in catalyst development, commercial-scale deployment remains limited by low conversion efficiencies [180]. Ongoing R&D at IIT Kharagpur, KPIT-Ankur (Vadodara), and TERI advances this route for agro-industrial clusters. PEC water splitting and dark fermentation remain at TRL 3–5 globally but hold promise for India's biomass-rich rural regions [1, 40, 62, 72, 117].

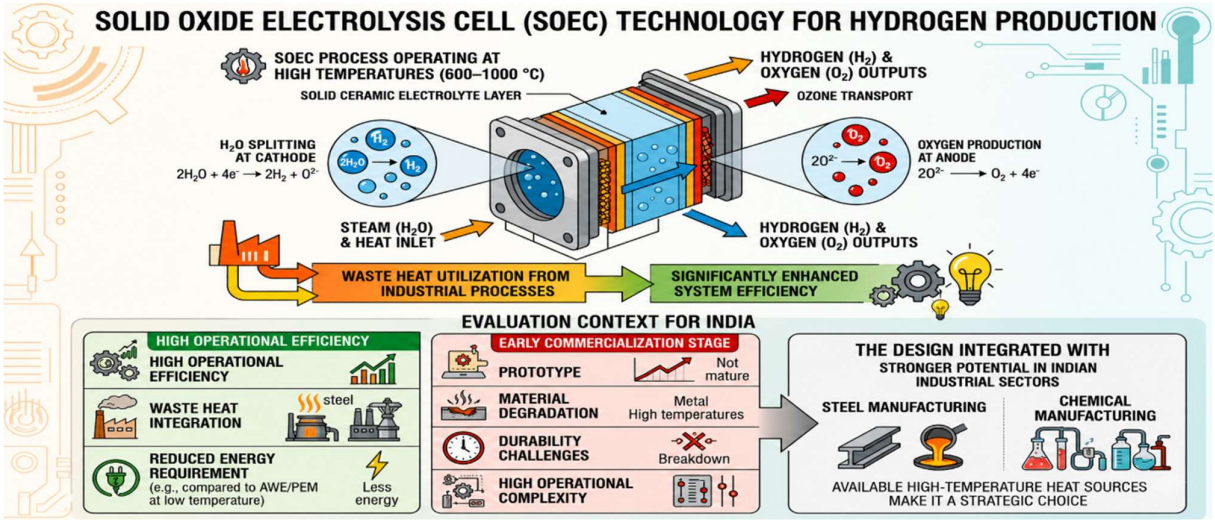


Figure 8. Hydrogen production by solid oxide electrolysis cell (SOEC) technology

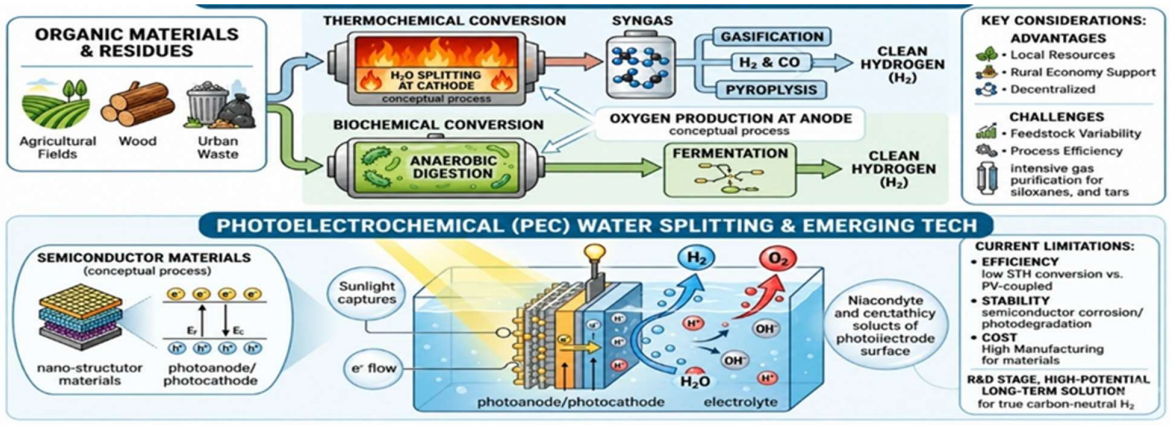


Figure 9. hydrogen production technologies (a) by conversion from biomass (b) by water splitting of photo-electro chemical (PEC)

Comparative electrolyzer analysis

Table 2. Comparative technical parameters of hydrogen production *via* electrolysis technologies [12, 16, 32, 61, 109]

Parameter	AWE	PEM	SOEC
Operating temperature (°C)	60–95	50–80	600–1,000
Current density (A·cm^{-2})	0.15–0.65	1.00–2.00	0.20–1.00
Electrolysis efficiency (%)	60–75	70–90	85–100
System efficiency (%)	51–60	46–60	76–81
Electrolyzer energy (kWh/Nm^3)	4.20–4.80	3.80–5.00	2.60–3.60
System energy (kWh/Nm^3)	5.00–5.90	5.20–5.90	3.70–3.90
Load flexibility (%)	20–100	0–120	−100 to +100
Cold start time	1–2 h	5–10 min	>1 h
Warm start time	1–5 min	<5 s	15 min
Industrial pressure (MPa)	0.1–3	0.1–5	0.1–1.5
CAPEX 2024 (USD/kW)	500–1,100	1,000–1,800	2,000–3,000
CAPEX 2030 target (USD/kW)	300–600	300–700	800–1,200
Commercial status	Mature / low CAPEX	Scaling / High CAPEX	Experimental

Table 2 presents a comparative assessment of the major electrolyzer technologies currently employed for hydrogen production. Alkaline water electrolysis (AWE) remains the most commercially mature and cost-effective technology, making it suitable for large-scale deployment [16]. Proton exchange membrane (PEM) electrolyzers offer higher hydrogen purity, rapid response characteristics, and better compatibility with intermittent renewable energy sources, albeit at higher capital costs [12]. Solid oxide electrolysis cells (SOECs) exhibit the highest theoretical efficiency due to their utilization of high-temperature heat; however, challenges related to material durability and commercial maturity continue to limit widespread deployment [32]. The comparison highlights the trade-offs between efficiency, cost, operational flexibility, and technological readiness among the different electrolyzer technologies [61].

Figure 10 illustrates the relative performance of AWE, PEM, and SOEC technologies with respect to efficiency, capital cost, operating temperature, and technology readiness level. The figure demonstrates that AWE currently dominates commercial installations because of its low cost and proven reliability, whereas PEM technology is increasingly preferred for renewable-energy-integrated hydrogen production due to its operational flexibility [24, 61, 133].

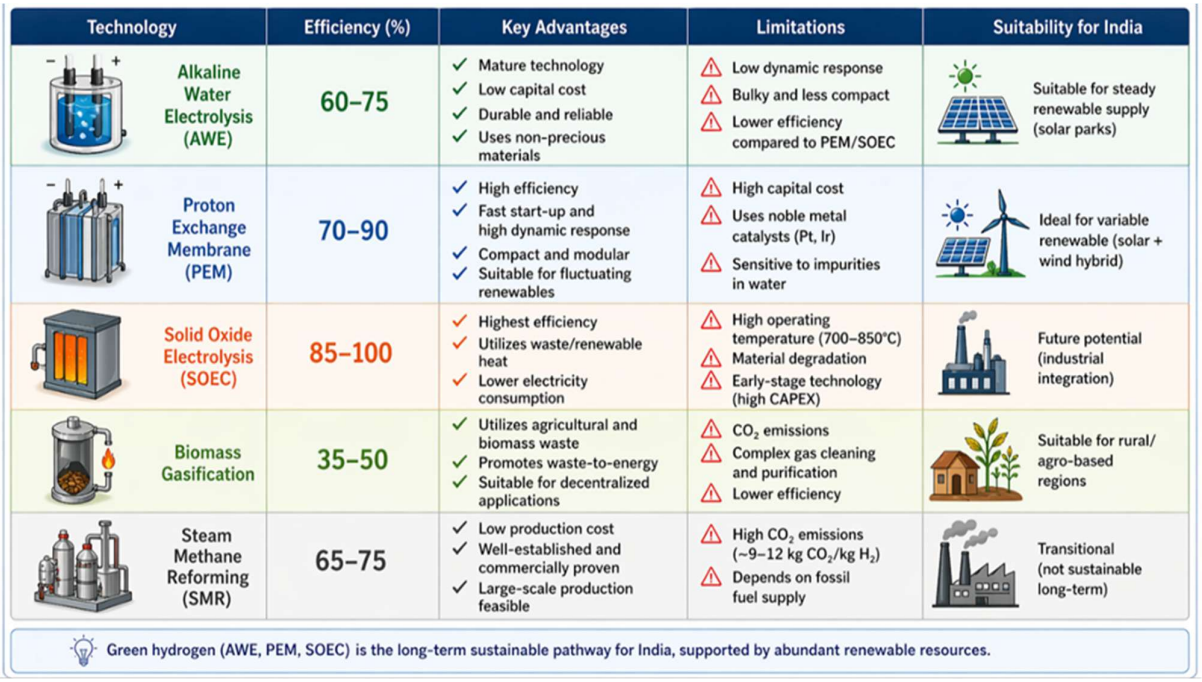


Figure 10. Comparison of different types of hydrogen production technologies

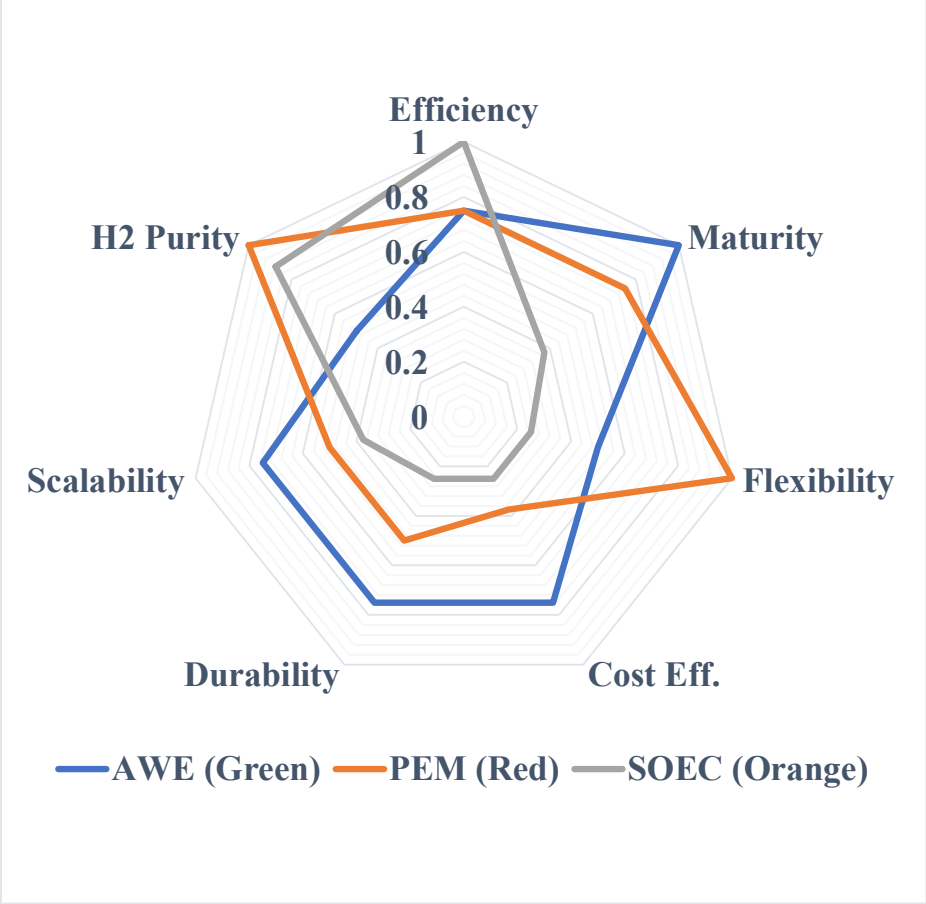


Figure 11. Electrolysis technology comparison — multi-criteria radar chart (normalized 0-1 scale) [12, 16, 32, 109].

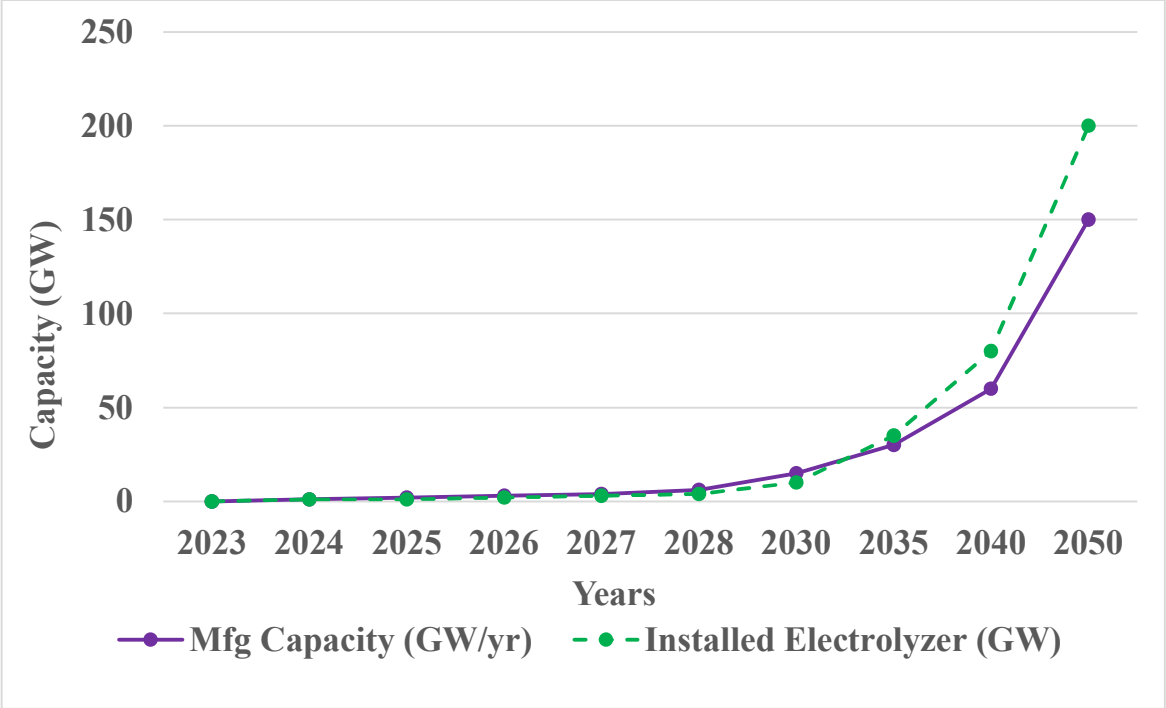


Figure 12. India's electrolyzer manufacturing & installed capacity forecast (GW) — 2023 to 2050 [106, 135, 156, 159]

Table 3. Hydrogen classification and cost analysis — India context [11, 39, 61, 135, 170].

Type	Production	CO_2 Emissions	Cost 2024 ($/kg)	Cost 2030 ($/kg)	Key Insight
Grey H_2	SMR / Coal Gasification	~10 $kgCO_2/kgH_2$	1.5–2.2	1.4–2.1	Cheapest; not net-zero compatible
Blue H_2	SMR + CCS	1–3 $kgCO_2/kgH_2$	1.8–2.5	1.6–2.3	Transitional bridge pathway
Green H_2	Electrolysis (RE)	<0.5 $kgCO_2/kgH_2$	3.5–5.0	2.0–3.5	Future dominant; cost falling fast

Although SOEC technology offers superior efficiency potential, further technological advancements and cost reductions are required before large-scale commercialization can be achieved [1, 16, 144]. The radar diagram in Figure 11 provides a visual multi-criteria comparison of AWE, PEM, and SOEC technologies across seven performance dimensions—efficiency, maturity, flexibility, cost-effectiveness, durability, scalability, and hydrogen purity—offering a single-glance strategic selection guide [12, 16, 32, 109].

The line graph as shown in Figure 12, projects the expansion of electrolyzer infrastructure from 2023 to 2050, tracking manufacturing capacity (GW/year) alongside cumulative installed electrolyzer capacity (GW). Between 2023 and 2030, both metrics remain exceptionally low, indicating a slow initial market ramp-up before accelerating significantly after 2035. By 2050, the sector experiences exponential growth, with manufacturing capacity surging to 150 GW/year and installed electrolyzer deployment climbing to a peak of 200 GW [106,135,156, 159].

Hydrogen cost dynamics and classification

The color-coded classification of hydrogen by production pathway and carbon intensity is the foundational framework for evaluating its role in decarbonization, market development, and policy design [11, 39, 61].

Figure 13 illustrates the projected decline in green hydrogen production costs as electrolyzer manufacturing scales up and renewable electricity prices continue to decrease. The most substantial cost reductions are expected after 2030, driven by economies of scale, technological learning, improved system efficiencies, and supportive policy interventions. This trend supports the growing competitiveness of green hydrogen relative to conventional fossil-fuel-based hydrogen production pathways.

Grey hydrogen: current dominance, declining future

Grey hydrogen produced *via* SMR dominates India's current production mix with an estimated 88% share in 2024 and production costs of USD 1.5–2.2/kg—the lowest of any pathway—supported by mature infrastructure. However, associated carbon emissions of 9–12 kg CO_2/kg H_2 are fundamentally incompatible with India's net-zero 2070 commitment. Under NITI Aayog projections, grey hydrogen's share is expected to decline from 88% (2024) to approximately 20% (2030) and near-zero by 2050 [67, 103, 134].

The pie chart of figure:14 illustrates the market share distribution of different hydrogen production methods. It clearly demonstrates that fossil-fuel-based grey hydrogen (Grey H_2) overwhelmingly dominates the global market, accounting for 88% of the total share. Low-emission alternatives remain comparatively marginal, with blue hydrogen (Blue H_2) and green hydrogen (Green H_2) capturing just 5% each, while alternative methods categorized under Other make up the remaining 2%

Green hydrogen: cost trajectory to competitiveness

As shown in Figure 15, Green H_2's production cost in India currently ranges from USD 3.5–5.0/kg (2024), driven primarily by electricity costs (60–70% of LCOH) and electrolyzer CAPEX. The pathway to cost competitiveness is multi-factorial: solar PV LCOE below USD 0.025/kWh at prime Indian sites; electrolyzer CAPEX declining from USD 1,100/kW (2020) to USD 380/kW (2030) to USD 120/kW (2050); improved capacity utilization through wind-solar hybrids (>50%); and WACC reduction from 9–11% to 5–7% through institutional finance mechanisms [61, 98, 144, 170]. NITI Aayog's optimistic scenario projects LCOH falling to approximately USD 1.60/kg by 2030 and USD 0.70/kg by 2050. The NGHM's own 2030 target is USD 2.0–3.5/kg. IRENA's global modelling suggests USD 0.7–1.6/kg by 2050 under a 1.5°C scenario [67, 61, 135, 159].

As shown in Figure16, the dual-axis line graph illustrates the projected cost reduction trajectories for green hydrogen infrastructure and production in India from 2020 to 2050.

Electrolyzer CAPEX (left axis): The capital expenditure for electrolyzers shows a steep decline from 1100 USD/kW in 2020 down to roughly 600

USD/kW in 2026, and is projected to hit a minimum of 130 USD/kW by 2050.

Levelized cost of hydrogen (LCOH, right axis): Mirroring the CAPEX trend, the LCOH (scaled by 100) drops consistently from an initial 700 units (7.00 USD/kg) in 2020 down to an estimated 70 units (0.70 USD/kg) by 2050.

Overall, the graph highlights a direct correlation where continuous technology maturity and scaling drastically lower both manufacturing capital costs and the final levelized price of hydrogen over the 30-year period.

INDIA'S TWO-PHASE HYDROGEN STATISTICAL ROADMAP: 2030 AND 2050

Based on consolidated data from the NGHM, NITI Aayog, IEA, IRENA, IEEFA, CEEW, ORF America, Markntel Advisors, and McKinsey, India's hydrogen transition is characterized across two strategic phases with distinct quantitative milestones [61, 67, 86, 97, 103, 135, 159]. Figure 17 presents a comprehensive timeline visual of these two phases, integrating all key milestones, capacity targets, investment flows, and impact metrics into a single navigable reference figure [135, 155].

PHASE I (2023–2030): FOUNDATION, SCALE-UP AND COST REDUCTION

The 2030 horizon is anchored by the NGHM's binding targets. Table 4 consolidates key 2030 objectives validated across multiple independent institutions [135, 155].

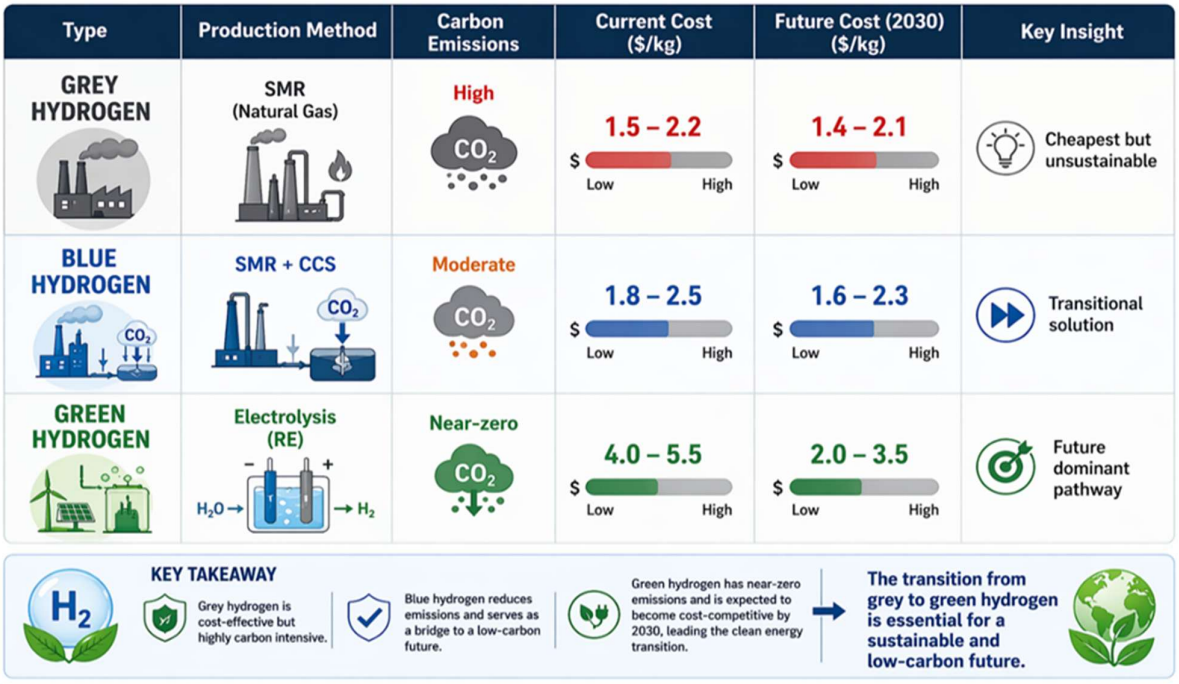


Figure 13. Comparison of different types of hydrogen: cost, emission and future outlook

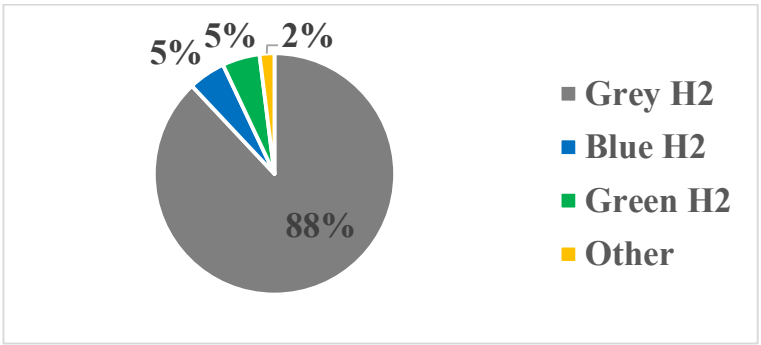


Figure 14. India's hydrogen production mix 2024 (% by source) — grey dominance *vs*. green target [MNRE 2023; IEEFA 2024; IEA 2024]

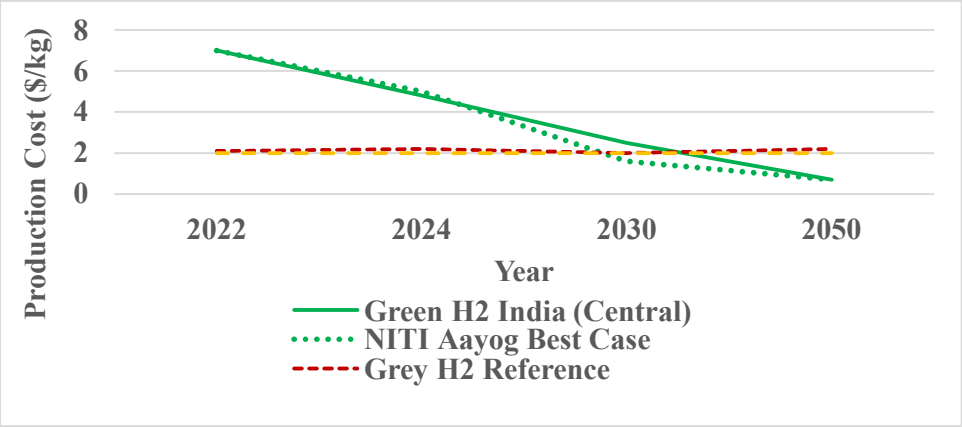


Figure 15. Green hydrogen production cost trajectory in India (USD/kg) — 2022 to 2050 [61, 67, 98, 144, 170]

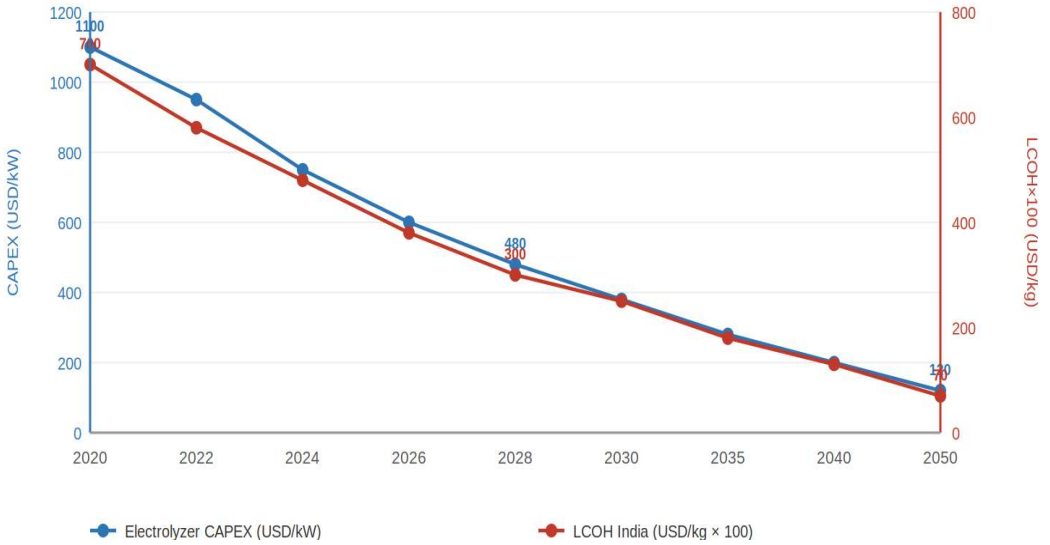


Figure 16. Electrolyzer CAPEX decline (USD/kW) & impact on LCOH (USD/kg×100) — 2020 to 2050 [44, 61, 98, 141]

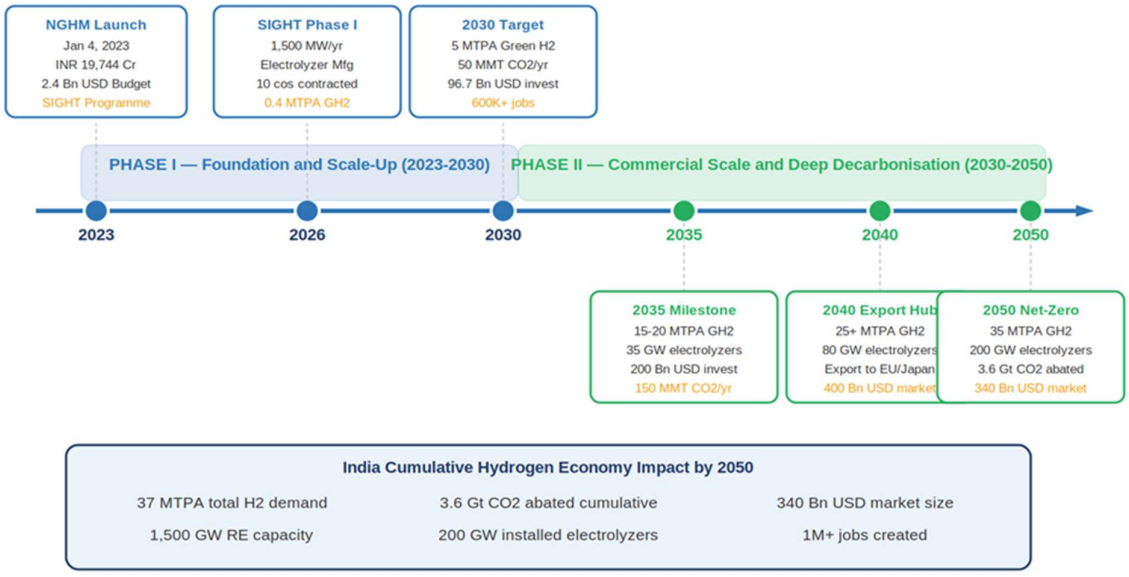


Figure 17. India's two-phase green hydrogen roadmap — key milestones 2023 to 2050 [67, 68, 86, 135, 155, 159]

As shown in Figure 18, key Phase I highlights: green hydrogen's share of total demand rises from ~5% (2024) to 25–33% (2030), corresponding to 3.5–5 MTPA of green production. The SIGHT program's electrolyzer manufacturing incentives (average USD 39.5/kW subsidy; USD 560 million total) will build 1,500 MW/yr capacity by 2026, scaling to 15 GW/yr by 2030. Annual CO_2 abatement reaches 50 MMTPA—equivalent to taking 10 million petrol cars off the road. Fossil fuel import savings of INR 1 lakh crore (USD ~12 billion) will reduce India's current account deficit [134, 144, 153, 154].

Table 4. Phase I (2030): India's green hydrogen mission — consolidated statistical targets [61, 671, 135, 144, 155, 156, 164, 170]

NGHM target (2030)	Projected value	Source
Green H_2 production	5 MTPA (up to 10 MTPA incl. exports)	MNRE NGHM 2023
Total investment mobilized	INR 8 lakh crore (~USD 96.7 Bn)	MNRE NGHM 2023
RE capacity addition (for H_2)	~125 GW additional	MNRE NGHM 2023
Annual CO_2 abatement	50 MMT per year	MNRE NGHM 2023
Fossil fuel import savings	INR 1 lakh crore (~USD 12 Bn)	MNRE NGHM 2023
Jobs created (direct + indirect)	>6 lakh (600,000+)	MNRE NGHM 2023
Electrolyzer manufacturing	≥1,500 MW/yr (Phase I) → 15 GW/yr (2030)	MNRE SIGHT 2023
LCOH target	USD 2.0–3.5/kg by 2030	IRENA 2023; CEEW 2024
Market value	USD 8 billion by 2030	Markntel Advisors 2024
Global market share target	~10% of global GH_2 market	NITI Aayog 2022

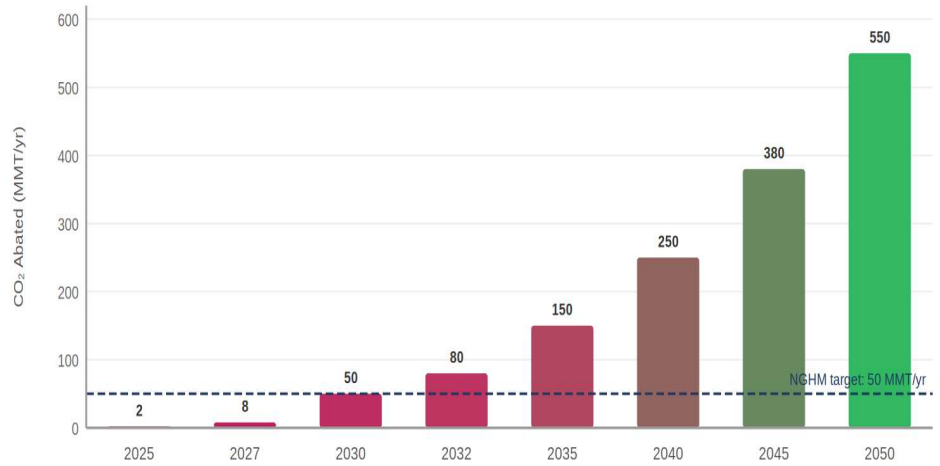


Figure 18. Annual CO_2 emissions abated *via* green hydrogen in India (MMTPA) — 2025 to 2050 [67, 134, 135]

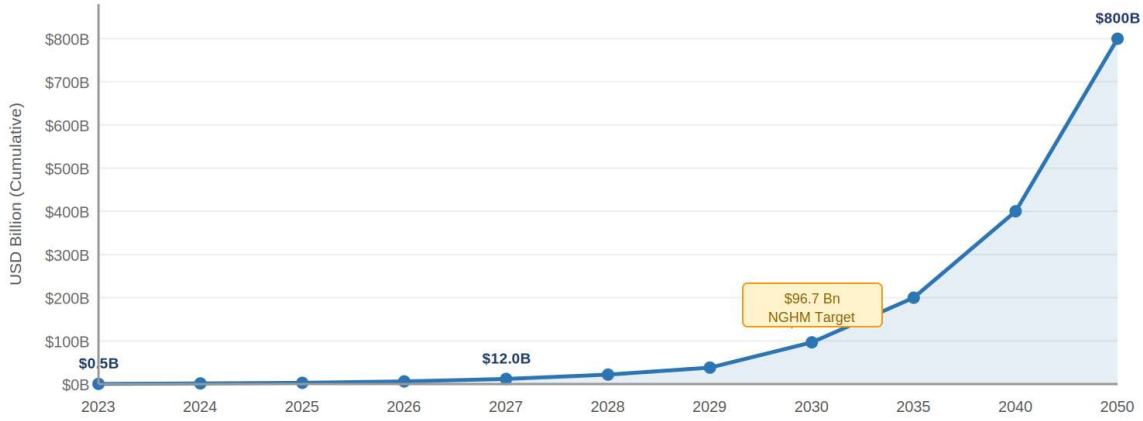


Figure 19. Cumulative investment in India's green hydrogen ecosystem (USD billion) — 2023 to 2050 [135, 143, 156, 164]

Table 5. Phase II (2050): India's green hydrogen long-term statistical projections [9, 67, 68, 69, 112, 134, 159, 164]

Indicator (2050 Horizon)	Projected value	Source
Total H_2 demand (India)	28–37 MTPA (4× vs 2024)	NITI Aayog 2022; IEEFA 2024
Green H_2 share	≥80% of total (22–30 MTPA)	NGHM 2023; IEA NZE Scenario
Green H_2 LCOH India	USD 0.70–1.60/kg (best case)	NITI Aayog 2022
Installed electrolyzer capacity	192–224 GW	FSR/EUI 2023; IRENA 2023
Total RE installed capacity	1,000–1,500 GW	IEA 2024; IRENA 2023
Cumulative CO_2 abated (2020–50)	3.6 Giga-tons	NITI Aayog 2022
Green H_2 market value (India)	USD 340 billion	Markntel Advisors 2024
Cumulative investment (2023–50)	USD 800 billion+	NITI Aayog; Bloomberg NEF 2023
Employment (H_2 sector)	Multi-million (direct + indirect)	NITI Aayog 2022
India net-zero target year	2070	GoI NDC 2022

The line graph in Figure19) charts a projected exponential growth curve for cumulative financial investments, measured in billions of US Dollars (USD Billion Cumulative) from 2023 to 2050. The timeline begins in 2023 with a modest baseline of $0.5B, rising slowly over the first few years to reach a cumulative total of $12.0B by 2027. An highlighted yellow callout box emphasizes the "NGHM Target" milestone of $96.7 Billion, which is projected to be achieved around the year 2030. Beyond 2030, the investment curve steepens dramatically, rapidly climbing from $200B in 2035 to approximately $400B by 2040. By the end of the projection period in 2050, the cumulative investment experiences a massive surge to reach an ultimate peak of $800B.

PHASE II (2030–2050): COMMERCIAL SCALE, EXPORT AND DEEP DECARBONIZATION

The 2050 horizon involves transformational change in India's energy system architecture, with hydrogen becoming a mainstream carrier across all hard-to-abate sectors [67, 68, 91].

Critical 2050 milestones

*A*s shown in Figure 20, total hydrogen demand reaches 28–37 MTPA (a fourfold increase *vs*. 2024), with green hydrogen comprising ≥80% of supply at 22–30 MTPA. IRENA's 1.5°C scenario requires global green hydrogen of 523 MTPA—India targeting 35 MTPA (10% share) requires 192–224 GW of installed electrolyzers, a 1,600-fold increase from 2024 levels. Cumulative CO_2 abatement reaches 3.6 Gt (2020–2050), equivalent to India's current five years of total energy sector emissions. The green hydrogen market in India alone reaches USD 340 billion—exceeding current total renewable energy investment [67, 71, 73, 112, 143].

As shown in Figure 21, this bar chart illustrates the projected exponential growth of a market size measured in billions of US dollars (USD Billion) from 2023 through 2050. According to Markntel Advisors (2024), the market is projected to expand at a robust compound annual growth rate (CAGR) of approximately 25.2% between the years 2026 and 2032. The market starts at a modest baseline of $0.3 B in 2023, climbing slowly through the decade to reach $8.0 B in 2030 and $14.0 B by 2032. Growth accelerates significantly after 2035 ($35.0 B), with the market size more than doubling by 2040 ($90.0 B) and doubling again by 2045 ($180.0 B). By the final year of 2050, the market experiences its most dramatic surge, peaking at an ultimate value of $340.0 B [156, 164, 170, 174].

SECTORAL HYDROGEN DEMAND — DETAILED STATISTICAL ANALYSIS

India's hydrogen demand is projected to grow from approximately 6.3 MTPA (2024) to 15 MTPA (2030) and 37 MTPA (2050), driven by both conventional demand growth and the emergence of entirely new hydrogen-consuming sectors [65, 67, 134, 154].

As shown in Figure 22, the projected demand trajectory indicates a substantial increase in hydrogen consumption between 2030 and 2050, primarily driven by the fertilizer, refining, steel, transportation, and power sectors. The results highlight the critical role of hydrogen in achieving long-term decarbonization objectives and underline the need for significant investments in production capacity, storage infrastructure, and transmission networks.

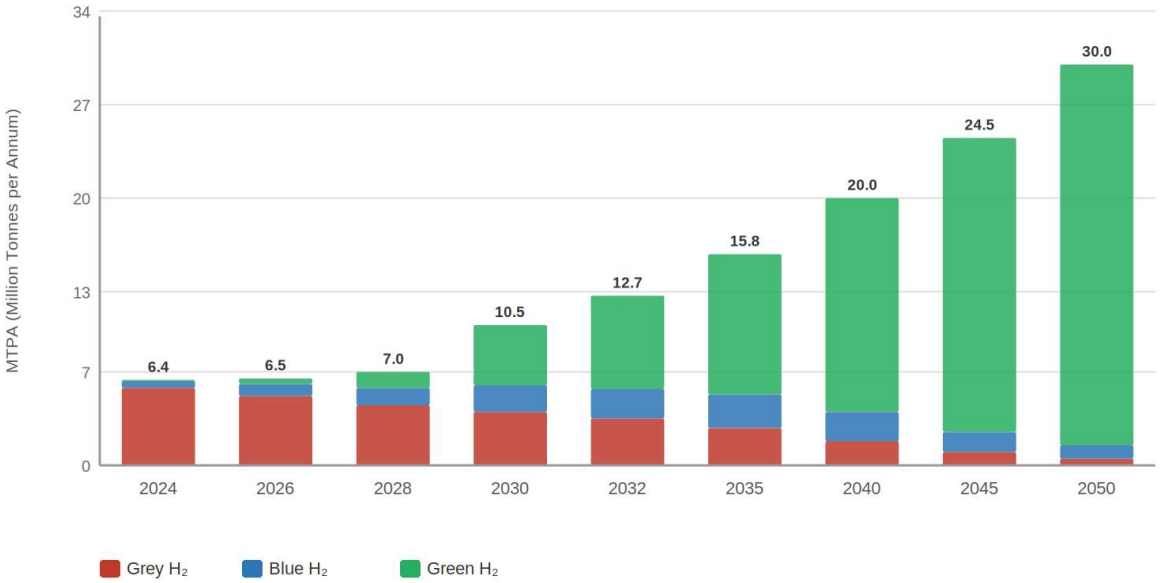


Figure 20. India's total hydrogen demand by type (MTPA) — 2024 to 2050, Stacked forecast [67, 103, 134, 135, 154]

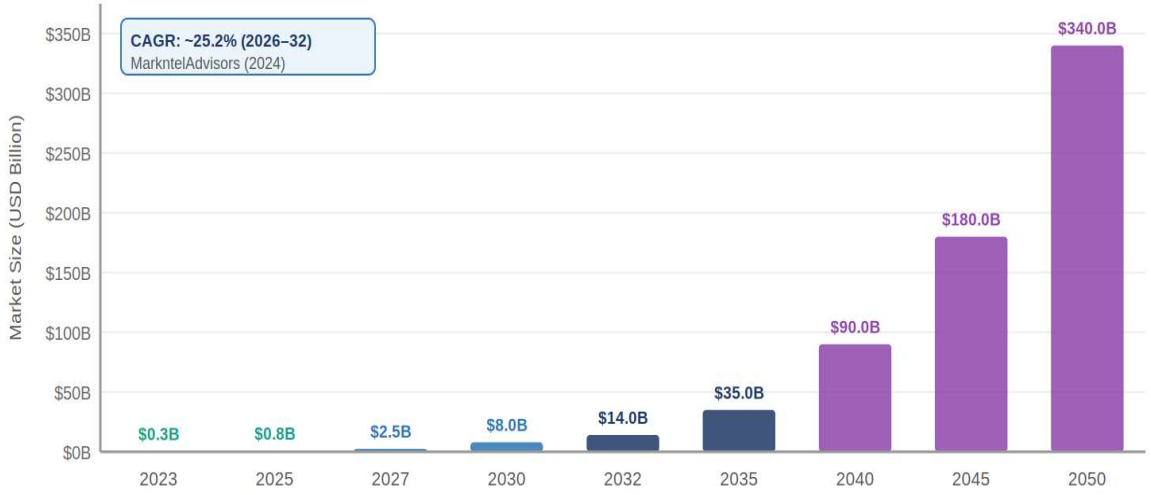


Figure 21. India's green hydrogen market size (USD billion) — 2023 to 2050 [156, 164, 170, 174]

Table 6. India's hydrogen sectoral demand and growth forecast — 2024, 2030 and 2050 [52, 54, 65, 67, 70, 74, 96, 134, 154]

Sector	2024 (MTPA)	2030 (MTPA)	2050 (MTPA)	Breakeven ($/kg)	Key driver
Fertilizer	3.0	6.1	8.0	1.7–2.1	Largest existing H_2 user; NH_3 synth.
Refining	2.5	4.5	6.0	1.7–2.1	Hydrocracking and desulfurization
Steel	0.3	1.0	8.0	<1.0	DRI green steel; biggest 2050 mkt
Mobility (road)	0.05	0.8	5.0	1.2–2.0	Trucks, buses, FCEVs
Shipping	0.05	0.6	3.0	1.7–2.0	Green NH_3/H_2 bunkering
Power & storage	0.1	0.5	3.0	—	Seasonal storage; grid balancing
Chemicals	0.4	1.5	4.0	—	Methanol, ammonia derivatives
TOTAL	~6.3	~15.0	~37.0	—	NGHM/NITI Aayog/IEA/IEEFA

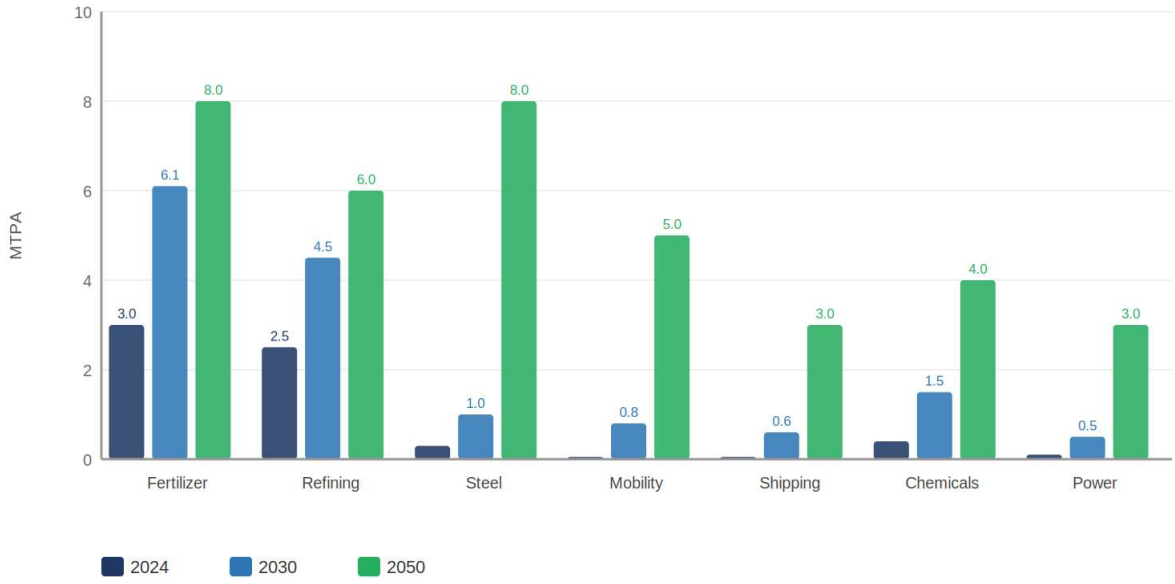


Figure 22. India's sectoral hydrogen demand by phase (MTPA) — 2024, 2030 and 2050 [52, 54, 67, 70, 74, 96, 134]

Fertilizer sector — early mover and largest consumer

India's fertilizer sector is the single largest hydrogen consumer with approximately 3.0 MTPA in 2024, projected to grow to 6.1 MTPA by 2030 and 8.0 MTPA by 2050, driven by rising food security demands. NITI Aayog projects green hydrogen uptake in fertilizers at 24% of sector demand by 2030 and near 100% by 2050, enabled by conversion of existing SMR-based ammonia plants and new green ammonia facilities. Cumulative CO_2 savings in this sector alone could reach 820 million tons between 2020 and 2050. The breakeven cost for green hydrogen adoption in fertilizers is USD 1.7–2.1/kg—achievable by 2030 under optimistic RE scenarios. [52, 67, 80, 134]

Refining — existing infrastructure advantage

India's refining capacity of ~250 Mt/year crude processing is the fourth-largest globally, with hydrogen demand of ~2.5 MTPA (2024), rising to 4.5 MTPA by 2030 and 6.0 MTPA by 2050. On-site SMR plants currently produce ~27 Mt of CO_2/year in this sector alone, rising to 47 Mt by 2050 without intervention. Green hydrogen uptake is projected at 24% of sector demand by 2030 and 100% by 2050 under NITI Aayog's efficient scenario, with a breakeven of USD 1.7–2.1/kg [54, 133].

Steel — largest long-term opportunity

India is the world's second-largest steel producer with current CO_2 emissions of 269 Mt/year (11% of India's total), projected to rise to 951 Mt/year by 2050 without decarbonization. Hydrogen-based DRI (direct reduced iron) can eliminate virtually all process emissions. India's DRI capacity of ~35 Mt/year (world's largest) provides an immediate retrofit opportunity. Tata Steel and JSW Steel have announced green steel roadmaps targeting 5 Mt/year of H_2-based production by 2030. NITI Aayog and RMI project steel and heavy-duty trucking together will drive 52% of India's hydrogen demand growth by 2050, reaching 8.0 MTPA—the largest sectoral demand by 2050 [69, 74, 99, 126, 132].

Mobility and transport

India's fuel cell vehicle (FCEV) market is growing rapidly. Key milestones include: IOCL's 15 green H_2 FCEV bus trials across Delhi, Haryana, and UP (September 2023); Indian Railways' Hydrogen for Heritage DEMU program—900 kW output from 8× Ballard FCmove-HD+ fuel cells with dynamic trials from 2025; and Amara Raja's 80 kg/day refuelling station in Leh, Ladakh (November 2024)—India's first H_2 refuelling station operating at 3,500 m altitude and temperatures from −20°C to +30°C. Mobility demand is projected to grow from negligible (2024) to 0.8 MTPA (2030) and 5.0 MTPA (2050). [70, 78, 123, 139, 157, 158, 172, 173].

Shipping, export and port hubs

India's strategic coastal geography positions it uniquely for green ammonia and hydrogen export. Priority maritime export hubs include Odisha (Paradeep, Gopalpur), Gujarat (Deendayal/Kandla, Hazira), Tamil Nadu (Tuticorin), and Maharashtra (JNPT). India targets 10% of the projected 100+ MTPA global green hydrogen market by 2030.

Shipping sector breakeven at USD 1.7–2.0/kg is relatively favorable due to existing high bunker fuel taxes [88, 96, 112, 131, 135, 147].

STATE-OF-THE-ART HYDROGEN INFRASTRUCTURE IN INDIA

Hydrogen infrastructure development is a prerequisite for realizing the NGHM's ambitious targets. Figure 23 maps the complete green hydrogen value chain from renewable energy source to end-use application, showing cost components, Indian milestones, and technology options at each stage [65, 135].

- *Renewable energy source (RE source):* Large-scale solar and wind power (~223 GW) provide low-cost renewable electricity, which serves as the primary energy input for green hydrogen production through AWE, PEM, or SOEC electrolyzers.
- *Electrolysis*: Water is split into hydrogen and oxygen using electricity, with hydrogen production costs estimated at approximately $3.5–5.0 per kg in 2024.
- *Purification*: The produced hydrogen is purified to 99.99% purity using technologies such as PSA, VPSA, or membrane separation, adding approximately $0.5–1.0 per kg to the cost.
- *Storage*: Hydrogen is stored either as compressed gas (around 350 bar) or in carriers such as LOHC and ammonia, with storage costs ranging from $1–2 per kg.
- *Transport*: Hydrogen is transported through pipelines, trucks, or ships, with additional logistics costs of approximately $0.5–1.5 per kg depending on distance and delivery method.
- *End use:* The delivered hydrogen is utilized in sectors such as fertilizers, steel manufacturing, mobility, and power generation, resulting in a total delivered cost of about $5–8 per kg in 2024, with projected reductions to $2–3 per kg by 2030 and $0.7–1.5 per kg by 2050.

Current production infrastructure

India's 6–7 MTPA hydrogen demand is currently served almost entirely by on-site SMR plants in the fertilizer (52% of consumption) and refining (46%) sectors. The western region accounts for 52.1% of total hydrogen demand due to the concentration of refining and petrochemical capacity in Gujarat and Maharashtra [32, 65, 67].

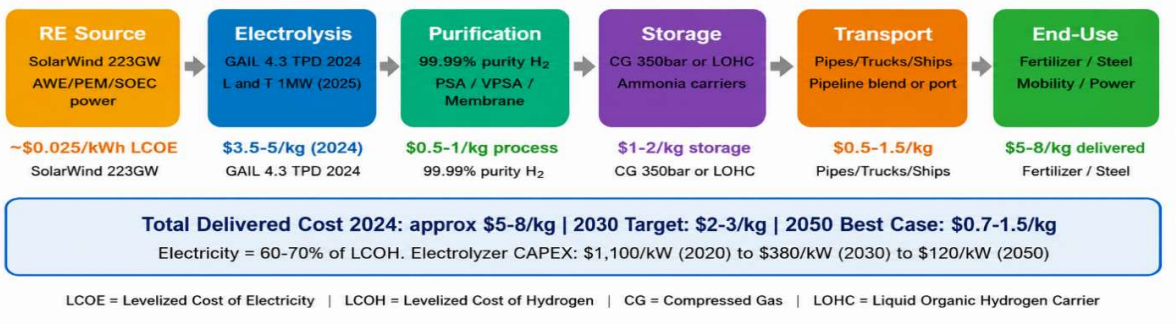


Figure 23. Green hydrogen value chain — stages, costs and Indian milestones [65, 110, 123, 135, 150, 179]

Regulatory framework

Table 7. Key regulatory agencies for hydrogen energy in India

Regulatory Agency	Role and Responsibilities
MNRE (Ministry of new and renewable energy)	Nodal agency; NGHM policy formulation; SIGHT programme [105]
PESO (Petroleum and explosives safety organization)	Regulation of H_2 storage, handling, and transport safety [115]
CEA (Central electricity authority)	National electricity planning; RE-H_2 grid integration [49]
BIS (Bureau of Indian standards)	H_2 safety standards, product certification frameworks [47]
PNGRB (Petroleum and natural gas regulation board)	Blending approval: 5% → 20% vol. H_2 in PNG networks [110]
Ministry of ports, shipping and waterways	Green shipping corridors; hydrogen bunkering regulation [96]

Green hydrogen pilot projects — statistical overview

GAIL's Vijapur plant (May 2024): 10 MW PEM; 4.3 TPD; 99.99% purity; powered by 20 MW co-located solar. L&T Hazira (March 2025): 1 MW indigenous ML-400 PEM; 200 Nm^3/hr; 300 MW/yr PLI allocation. NTPC Kawas (January 2023): 1 MW floating solar electrolysis; 5% vol./vol. PNG blending; PNGRB approved. Amara Raja Leh (November 2024): 80 kg/day; supports 5 NTPC fuel cell buses; India's first H_2 refuelling station [110, 139, 150, 152, 179].

Storage, transport and hydrogen hubs

India currently lacks a dedicated hydrogen pipeline network. The NGHM envisions utilizing India's 40,000 km natural gas pipeline network for hydrogen blending (approved at 5% vol./vol., roadmap to 20%) and eventual pure hydrogen transport. Underground geological storage feasibility is under assessment. The NGHM plans at least two green hydrogen hubs by 2026, with Odisha, Gujarat, Tamil Nadu, and Maharashtra identified as priority coastal hub locations. Co-locating production with consumption reduces delivered costs by 15–25% [27, 107, 112, 116, 131, 135, 147].

BARRIERS TO LARGE-SCALE DEPLOYMENT

Despite significant policy momentum, green hydrogen's large-scale deployment faces a complex web of technical, economic, infrastructural, and regulatory barriers—particularly acute in India's emerging market context [61, 144, 154].

Economic and cost competitiveness

Green hydrogen currently costs USD 3.5–5.0/kg versus grey hydrogen at USD 1.5–2.2/kg—a cost premium of USD 2–3/kg that must close to USD 0/kg by 2030 for competitiveness without subsidy. India's WACC for green hydrogen projects is 9–11% *vs.* 4–6% in Europe—adding approximately USD 1.0–1.5/kg to LCOH. Current NGHM production subsidies (USD 0.66/kg declining to USD 0.40/kg) cover only 10–20% of the cost gap, significantly below the US IRA's USD 3/kg production tax credit. An estimated USD 80–120 billion of new infrastructure investment is required by 2030, of which the government's INR 19,744 crore covers less than 5%. [48, 61, 135, 143, 144].

POLICY, GOVERNANCE AND R&D LANDSCAPE

NGHM governance architecture

Figure 24 provides a complete visual map of the NGHM's governance architecture, funding flows, and implementing agencies—from Union Cabinet to field-level executing organizations [135].

SIGHT program and financial incentives

The SIGHT program (INR 17,490 crore) provides: production-linked incentives of USD 0.66/kg (year 1) tapering to USD 0.40/kg (year 3); electrolyzer manufacturing support of average USD 39.5/kW (USD 560 million total); and a 25-year waiver on interstate transmission system (ISTS) charges for green hydrogen projects commissioned before 31 December 2030. By May 2024, eight companies secured contracts for 1,500 MW/yr electrolyzer manufacturing and ten companies contracted to produce 0.4 MTPA green hydrogen under Phase I [135, 156, 177].

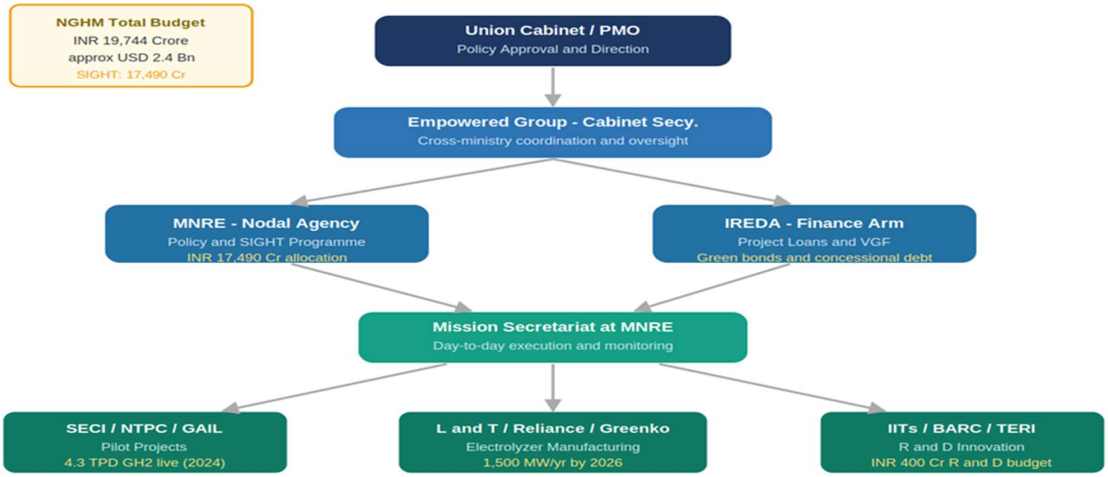


Figure 24. NGHM governance, funding and execution architecture [135, 156, 178]

Table 8. NGHM risk management framework [135]

Risk type	Risk category	Mitigation strategy
Strategic	Supply chain disruptions	Diversify supply chains; build domestic manufacturing
Technological	Technology disruptions	Technology-agnostic R&D funding; multiple parallel threads
Operational	Water availability constraints	Co-locate RE plants and H_2 production near water sources
Operational	Land availability constraints	State-level land banks for RE and H_2 deployment
Operational	Safety incidents	Rigorous standards enforcement; PESO oversight
Financial	Sustainable demand uncertainty	Demand creation through HPOs and blending mandates
Financial	Affordable RE access	Integrated planning of RE capacity addition
Financial	Electrolyzer availability	PLI incentives for domestic electrolyzer ecosystem
Financial	CAPEX overruns	Scale-up to achieve economies of scale
Financial	Credit access	Risk-sharing frameworks; FDI facilitation; bond markets

Table 9. NGHM governance bodies [135]

No.	Governing body	Primary function
1	MNRE (nodal agency)	Mission directives and policy oversight
2	IREDA (finance)	Financial assistance and project funding support
3	Empowered group (Cabinet secy.)	Cross-ministry implementation monitoring
4	Mission secretariat (MNRE)	Day-to-day execution and coordination

International collaborations

Table 10. India–EU collaborations in green hydrogen [55, 84, 113, 119, 145]

Sr.	Indian company	EU partner	Collaboration details
1	Reliance New Energy Ltd.	Stiesdal A/S (Denmark)	Low-cost HydroGen electrolyzer manufacturing in India [119]
2	GR Promoter / GreenH	H2B2 GreenH (Spain)	1,000 MW PEM plant; Phase-1 100 MW operational at Jhajjar, Haryana [84]
3	Greenko Group	John Cockerill (Belgium)	2 GW electrolyzer factory; USD 500 million investment [55]

Table 11. India–US hydrogen collaborations [59, 66, 102, 130]

Collaboration	Focus area	Year	Details
US-India hydrogen task force	H_2 R&D	2021	MNRE–US DOE partnership for technology development
SCEP (strategic clean energy partnership)	Safety and hubs	2024	Clean hydrogen cost reduction and safety priorities
Ohmium collaborations	Electrolyzer Mfg.	2024	US-based OEM building projects in South India
Hydrogen carriers (LOHCs and NH_3)	Transport tech.	2024	Joint LOHC and ammonia carrier development
H_2 transport infrastructure	Mobility	2024	Distribution network viability across Indian regions

State-level hydrogen policies

Six Indian states—Maharashtra, Uttar Pradesh, Andhra Pradesh, Rajasthan, Odisha, and West Bengal—have released dedicated green hydrogen policies with investment incentives, land allocation, and electricity tariff concessions. Andhra Pradesh targets 12,000 jobs per MTPA of green hydrogen production; Gujarat projects 1.8 lakh jobs from electrolyzer manufacturing; Uttar Pradesh has attracted INR 1.15 trillion in green hydrogen investments. [46, 121, 142]

Research and development landscape

India's R&D ecosystem for hydrogen is anchored by IITs, CSIR laboratories, BARC, ONGC Energy Centre, and TERI. MNRE's R&D roadmap (October 2023) allocated INR 400 crore under the NGHM with DST, DBT, and DRDO providing complementary funding [35, 106].

INDUSTRIAL APPLICATIONS AND KEY PILOT PROJECTS

GAIL India — Vijapur green hydrogen plant

Commissioned: 24 May 2024. Capacity: 4.3 TPD (1,569.5 t/yr). Technology: 10 MW PEM electrolyzer. Purity: 99.99%. Power source: 20 MW co-located solar plant. Significance: India's first commercial-scale dedicated green hydrogen plant, directly demonstrating NGHM Phase I objectives.

The plant provides real-world data on continuous PEM performance under Indian solar irradiance profiles [150, 156].

Larsen & Toubro — Hazira electrolyzer

Commissioned: 1 March 2025. Capacity: 1 MW; 200 Nm^3/hr. Technology: Two-stack ML-400 PEM system—India's first indigenously manufactured electrolyzer stack. PLI allocation: 300 MW/yr under NGHM. Strategic significance: establishes India's domestic electrolyzer manufacturing capability, critical for import substitution and achieving the SIGHT program's 1,500 MW/yr target by 2026. [161, 178]

Indian railways — hydrogen for heritage demu

India's Hydrogen for Heritage program retrofits 1600 HP diesel DEMU trains with hydrogen fuel cells, delivering 900 kW total power output (800 kW from 8× Ballard Power Systems FCmove-HD+ PEM fuel cells at 100 kW each, plus 400 kW battery backup). Hydrogen is stored as compressed gas at 350 bar in removable cylinders refillable in 45 minutes at Jind, Haryana. Dynamic trials are planned from 2025 covering 50,000 km; project cost is approximately INR 111.83 crore. India's 900 kW output surpasses Germany, France, Sweden, and China's existing hydrogen train deployments [100, 177].

Table 12. Key R&D Institutions in India's green hydrogen ecosystem

Institution	Location	Research focus
BARC	Mumbai	PEM MEA; AWE electrocatalysts; photoelectrochemical splitting [136]
ONGC EC – ICT Mumbai	Mumbai	Cu-Cl thermochemical cycle; molten salt thermal storage [114]
ONGC EC – IIT Delhi	Delhi	IS thermochemical cycle; 15-bar closed-loop metallic system [94]
ONGC EC – CSIR IIP	Dehradun	Open-loop I-S cycle; H_2 from H_2S in refineries [94]
Indian Oil R&D – IISc	Faridabad	Oxy-steam biomass gasification; VPSA H_2 separation [41]
Indian Oil R&D Centre	Faridabad	Solar-powered AWE/PEM/SOEC; 5,000 bar storage [41]
KPIT – Agharkar RI	Pune	Microbial dark fermentation from biomass and methane [40]
KPIT – Ankur Scientific	Vadodara	Woody biomass gasification for pure H_2 [40]
IIT Delhi	Delhi	Bunsen reactor; nanostructured H_2 materials [94]
IIT Madras	Chennai	Solar seawater electrolysis; photocatalysis [95]
IIT Guwahati	Guwahati	Biohydrogen from lignocellulosic biomass [57]
IIT Kharagpur	Kharagpur	Biological H_2 production from organic waste [42]
IIT Kanpur	Kanpur	Photoelectrochemical wastewater splitting [58]
IIT Hyderabad	Hyderabad	H_2S decomposition; CO_2 to syngas via plasma catalysis [43]
IIT Indore	Indore	Catalytic H_2 from methanol [148]
IIT BHU Varanasi	Varanasi	Ultra-pure on-site H_2; photocatalytic water splitting [45]
CSIR NEERI	Nagpur	Liquid organic hydride H_2 supply systems [50]
TERI	Gurgaon	Bio-hydrogen in closed-loop bioreactor [72]
NMRL – DRDO	Mumbai	Autothermal reforming; AIP for naval submarines [101]
SPRERI	Anand, Gujarat	Dual-fuel biomass gasification for H_2 [71]

Steel and green hydrogen integration

Tata Steel and JSW Steel are leading India's green steel transition, with hydrogen-based DRI production at demonstration scale. The world's largest hydrogen-based DRI plant (HYBRIT, Sweden) at 1.5 MTPA provides the commercial blueprint. India's 35 MTPA DRI capacity—the world's largest—constitutes a ready retrofit base. NITI Aayog projects steel sector hydrogen demand reaching 8.0 MTPA by 2050, making it the largest sectoral driver of India's long-term hydrogen economy [17, 69, 74, 99, 126, 132].

CROSS-SECTIONAL ANALYSIS AND STRATEGIC INSIGHTS

Technology–cost–scalability trade-offs

Synthesis of the preceding analysis reveals clear technology trade-offs: AWE offers optimal maturity, cost, and scalability for India's near-term (2024–2030) requirements; PEM is preferred for variable renewable coupling and high-purity applications; SOEC is the long-term bet for industrial waste-heat integration (2035–2050); biomass routes are most appropriate for decentralized rural applications. The radar diagram (Figure 11) visually captures these trade-offs across seven dimensions [1, 12, 16, 32, 61, 109].

India in global comparative context

Globally, the EU leads hydrogen policy ambition with EUR 470 billion committed through REPowerEU and IPCEI. Japan targets 3 MTPA of clean hydrogen by 2030 with USD 107 billion strategic investment. The US offer USD 3/kg production tax credits under the IRA and have committed USD 8 billion for hydrogen hubs. India's public investment of USD 2.4 billion (NGHM) is modest in absolute terms, but its renewable energy cost advantage—solar LCOE below USD 0.025/kWh at best sites—provides a structural competitive advantage that no European country has replicated [81, 86, 91, 130, 135, 175].

IRENA's 1.5°C scenario requires global green hydrogen of 125 MTPA by 2030 and 523 MTPA by 2050. India, targeting 5 MTPA (2030) and 35 MTPA (2050), would represent 4% and 7% of global production, respectively — a realistic and strategically important contribution [97, 159].

RESEARCH GAPS, FUTURE PATHWAYS AND POLICY RECOMMENDATIONS

Critical research gaps

Despite the rapidly expanding body of literature on hydrogen energy systems, a critical gap persists in the integrated, India-specific assessment of hydrogen transition pathways, particularly in the context of long-term techno-economic feasibility, sectoral demand evolution, and policy-driven deployment frameworks. Existing reviews predominantly focus on global hydrogen trends, electrolyzer technologies, or isolated techno-economic aspects, often lacking a holistic, data-driven synthesis tailored to India's unique energy landscape [67, 109].

Several recent studies by international agencies such as IEA, IRENA, and NITI Aayog provide valuable projections; however, these analyses are typically fragmented across domains—technology performance, cost projections, infrastructure readiness, or policy frameworks—without offering a unified multi-dimensional evaluation. Furthermore, prior literature rarely integrates quantitative projections (2030–2050) with sector-wise hydrogen demand, infrastructure readiness, and investment trajectories in a single coherent framework. This creates a disconnect between strategic policy vision and implementable techno-economic pathways, particularly for emerging economies like India [106].

Another key limitation in existing reviews is the lack of comparative multi-criteria assessment of hydrogen production technologies (AWE, PEM, SOEC) under India-specific operating conditions, including renewable intermittency, cost sensitivity, scalability constraints, and infrastructure limitations. Additionally, limited attention has been given to the dynamic transition from grey to green hydrogen, especially in terms of cost convergence timelines, carbon reduction potential, and sectoral adoption thresholds [69].

Future technology priorities

Priority R&D targets: non-noble metal PEM catalysts achieving >90% efficiency at >100,000 hours durability; solid-state hydrogen storage exceeding 6 wt% H_2 capacity at near-ambient conditions; wind-solar hybrid electrolysis achieving >60% capacity utilization; AI-enabled predictive maintenance for electrolyzer stacks targeting >99% uptime; and advanced membrane electrode assemblies for high-current-density PEM operation exceeding 3 A/cm².

To address these gaps, the present study introduces a comprehensive and integrated review framework that combines:

- Techno-economic analysis of hydrogen production pathways, including cost trajectories, efficiency, and CAPEX trends [106];

- Comparative multi-criteria evaluation of electrolyzer technologies using performance, scalability, and deployment-readiness indicators [62];
- India-specific hydrogen demand modelling (2024–2050) across key sectors such as fertilizers, refining, steel, mobility, and power [10];
- Policy and infrastructure assessment, aligned with the National green hydrogen mission (NGHM) and global decarbonization targets [10];
- Two-phase strategic roadmap (2030 and 2050) integrating production targets, investment flows, and emission reduction potential [4].

Strategic policy recommendations

Based on the comprehensive analysis, the following recommendations are proposed: (i) increase production subsidies to USD 1.5–2.0/kg, comparable to US IRA levels; (ii) introduce mandatory hydrogen purchase obligations (HPOs) for refineries (5% by 2027, 20% by 2030) and fertilizer plants (5% by 2028); (iii) implement carbon pricing at USD 20–50/tCO_2; (iv) standardize 10–15 year offtake agreements between government entities and green hydrogen producers; (v) develop hydrogen corridors connecting Gujarat, Rajasthan, and Tamil Nadu hubs to industrial consumers; (vi) harmonize state-level intrastate wheeling charge waivers; and (vii) establish an India Hydrogen Safety Institute to build inspection and certification capacity [48, 67, 69, 135, 142, 143, 144].

DISCUSSION

This review synthesizes evidence from 175 sources into a unified multi-dimensional analytical framework— a comprehensive assessment of India's hydrogen transition pathway integrating technological, economic, policy, infrastructure, and market dimensions. Three overarching insights emerge with particular strategic significance [38, 67, 90, 135].

First, the cost-sustainability trade-off is real but narrowing faster than base-case projections assumed. Green hydrogen in India has fallen from USD 7/kg (2022) to USD 3.5–5/kg (2024)—a 30–50% reduction in two years. NITI Aayog's best-case of USD 1.60/kg by 2030 and USD 0.70/kg by 2050 is technically achievable given observed solar cost trajectories (now below USD 0.025/kWh at prime sites), electrolyzer scale-up dynamics, and India's demonstrated manufacturing capability (L&T's ML-400 PEM system) [67, 98, 150, 179].

Second, infrastructure remains the most critical bottleneck. India's renewable energy base is growing at the required pace (223 GW in 2024, on track for 500 GW by 2030). The technology has been demonstrated at pilot scale. What is missing is connective tissue: hydrogen pipelines, storage hubs, refuelling stations, and port export terminals. An estimated USD 80–120 billion of infrastructure investment is required by 2030—10–15× the government's current NGHM outlay—underscoring the critical importance of private sector mobilization and multilateral financing [48, 87, 128, 135, 143].

Third, India's competitive advantage is structural, not cyclical. Solar LCOE below USD 0.025/kWh, abundant coastal land for export hubs, a large existing industrial hydrogen base, and an emerging domestic electrolyzer manufacturing capability together constitute a durable competitive position. However, realizing this advantage requires closing the WACC gap—reducing financing costs from 9–11% to 5–7%—through IREDA lending, multilateral development bank (ADB, World Bank, IFC) co-financing, green bond issuance, and credible long-term offtake frameworks that reduce project revenue risk [93, 118, 128, 143, 144, 179].

The interdependence of barriers deserves special emphasis. High production costs limit demand; limited demand delays infrastructure investment; insufficient infrastructure raises delivered costs; policy uncertainty deters private capital; slower investment prevents cost reduction—a reinforcing negative feedback loop. Breaking this loop requires simultaneous coordinated intervention across cost, infrastructure, and market dimensions. The NGHM represents precisely this kind of integrated intervention, but its financial scale currently lags peer programs in the US and EU by a factor of 10–40× [48, 118, 142, 143, 144].

CONCLUSION

This comprehensive review delivers a statistically supported and analytically structured assessment of hydrogen as a strategic energy transition pathway for India. Drawing on 175 references across government mission documents, international agency projections, peer-reviewed science, and industry analyses, and presenting ten quantitative charts and five creative process diagrams, it characterizes India's hydrogen trajectory across ten dimensions simultaneously — demand, cost, production mix, electrolyzer capacity, sectoral adoption, CO_2 abatement, investment flows, market size, renewable energy growth, and global positioning.

Core findings are unambiguous:

(i) Green hydrogen is on a steep cost reduction curve that will bring it to near cost parity with grey

hydrogen in India by 2030–2035 under favorable policy conditions;

(ii) The 5 MTPA NGHM target is technically achievable but requires a 3–5× amplification of current financial incentives to close the infrastructure gap;

(iii) Fertilizer and refining sectors offer the fastest near-term decarbonization payoffs, while steel, mobility, and shipping define the long-term market;

(iv) India's structural renewable energy advantage—already demonstrated in solar LCOE below USD 0.025/kWh—positions it as a credible candidate for 10% of the global green hydrogen market by 2030.

The cumulative impact is staggering in scale: 3.6 Gt CO_2 abated (2020–2050); a market valued at USD 340 billion by 2050; 600,000+ jobs by 2030; INR 1 lakh crore in fossil fuel import savings by 2030; and a pathway consistent with India's legally committed net-zero target of 2070. Realizing this opportunity—for India and for global climate stability—requires the urgency, scale, and coordinated application of policy, investment, technology, and international partnership that this review has comprehensively mapped.

REFERENCES

1. D. Das, T.N. Veziroğlu, *Int. J. Hydrogen Energy*, **26** (5), 437 (2001).
2. A. Züttel, *Nature*, **414** (6861), 353 (2003).
3. G. W. Crabtree, et al., *Physics Today*, **57** (12), 39 (2004).
4. J. A. Turner, *Science*, **305** (5686), 972 (2004).
5. M. Z. Jacobson, et al., *Science*, **308** (5730), 1901 (2005).
6. R. Kothari, et al., *Renew. Sustain. Energy Rev.,* **12** (8), 1909 (2008).
7. D. Moher, et al., *PLOS Medicine*, **6** (7), e1000097 (2009).
8. N. J. van Eck, L. Waltman, *Scientometrics*, **84** (2), 523 (2010).
9. E. Cetinkaya, et al., *Int. J. Hydrogen Energy,* **37** (3), 2071 (2012).
10. A. Ursúa, et al., *Proc. IEEE*, **100** (2), 410 (2012).
11. J. O. M. Bockris, *Int. J. Hydrogen Energy*, **38**, 2579 (2013).
12. M. Carmo, D. L. Fritz, J. Mergel, D. Stolten, *Int. J. Hydrogen Energy*, **38**, 4901 (2013).
13. C. Acar, I. Dincer, "Comparative assessment of hydrogen production methods", *Int. J. Hydrogen Energy*, **39**, 1–12 (2014).
14. H. W. Langmi, J. Ren, B. North, M. Mathe, D. Bessarabov, *Electrochim. Acta*, **128**, 368 (2014).
15. I. Dincer, C. Acar, *Int. J. Hydrogen Energy*, **40**, 11094 (2015).
16. M. Schalenbach, G. Tjarks, M. Carmo, W. Lueke, M. Mueller, D. Stolten, *J. Electrochem. Soc.*, **163**, F3197 (2016).
17. Ministry of Steel, Government of India, *National Steel Policy 2017*, New Delhi, 2017.
18. N. Muradov, in *Compendium of Hydrogen Energy*, Vol. 1, R. Basile, A. Basile, T. N. Veziroglu (Eds.), Woodhead Publishing, Cambridge, pp. 45–76 (2017).
19. P. Nikolaidis, A. Poullikkas, *Renew. Sustain. Energy Rev.*, **67**, 597 (2017).
20. P. Preuster, C. Papp, P. Wasserscheid, *Acc. Chem. Res.*, **50**, 74 (2017).
21. E. S. Hanley, J. P. Deane, B. P. Ó Gallachóir, *Renew. Sustain. Energy Rev.*, **82**, 3027 (2018).
22. J. O. Abe, A. P. I. Popoola, E. Ajenifuja, O. M. Popoola, *Int. J. Hydrogen Energy*, **44**, 15072 (2019).
23. P. Capros, D. Van Regemorter, L. Paroussos, P. Karkatsoulis, C. Fragkiadakis, S. Tsani, I. Charalampidis, T. Revesz, *Energy Policy*, **134**, 110960 (2019).
24. S. S. Kumar, V. Himabindu, *Mater. Sci. Energy Technol.*, **2**, 442 (2019).
25. G. Maggio, G. Nicita, G. Squadrito, *Int. J. Hydrogen Energy*, **44**, 11371 (2019).
26. J. W. Makepeace, T. He, C. Weidenthaler, T. R. Jensen, F. Chang, M. Vegge, P. Ngene, Y. Kojima, P. E. de Jongh, P. Chen, W. I. F. David, *Int. J. Hydrogen Energy*, **44**, 7746 (2019).
27. R. Moradi, K. M. Groth, *Int. J. Hydrogen Energy*, **44**, 12254 (2019).
28. E. Rivard, M. Trudeau, K. Zaghib, *Materials*, **12**, 1973 (2019).
29. I. Staffell, D. Scamman, A. V. Abad, P. Balcombe, P. E. Dodds, P. Ekins, N. Shah, K. R. Ward, *Energy Environ. Sci.*, **12**, 463 (2019).
30. A. Boretti, *Int. J. Hydrogen Energy*, **46**, 2367 (2021)
31. F. Dawood, M. Anda, G. M. Shafiullah, *Int. J. Hydrogen Energy*, **45**, 3847 (2020).
32. A. Hauch, S. D. Ebbesen, S. H. Jensen, M. Mogensen, *Science*, **370**, eaba6118 (2020).
33. S. E. Hosseini, B. Butler, *Int. J. Green Energy*, **17**, 13 (2020).
34. S. Krishnan, S. S. Kumar, V. Himabindu, *Energy Sources A: Recovery Util. Environ. Eff.*, **42**, 1351 (2020).
35. A. Nadar, S. S. Kumar, V. Himabindu, *Int. J. Hydrogen Energy*, **45**, 12691 (2020)
36. A. Pareek, S. S. Kumar, V. Himabindu, *Mater. Sci. Energy Technol.*, **3**, 319 (2020).
37. A. M. Elberry, M. A. Eldean, A. A. Elsayed, *Int. J. Hydrogen Energy*, **46**, 15671 (2021).
38. Hydrogen Insights 2021*,* Hydrogen Council, Brussels, 2021.
39. Hydrogen for Net Zero, Hydrogen Council and McKinsey & Company, Brussels, 2021.
40. *The Indian Express*, "Pune Labs: Hydrogen from Agri-Residue", 2021.
41. Indian Oil R&D Centre, Indian Institute of Science, Oxy-Steam Biomass Gasification, BioEnergy International, 2021.
42. Indian Institute of Technology Kharagpur, Hydrogen by Biological Routes, IIT Kharagpur Repository, 2021.

43. Indian Institute of Technology Hyderabad, H_2S Decomposition; CO_2 to Syngas via Plasma, IIT Hyderabad Repository, 2021.
44. Making Green Hydrogen a Cost-Competitive Climate Solution, *International Renewable Energy Agency (IRENA), Abu Dhabi, 2021.*
45. *The Telegraph*, "IIT-BHU: India's First Ultra-Pure On-Site H_2 Device", 2021.
46. Government of Andhra Pradesh, Andhra Pradesh Green Hydrogen Policy 2022, Amaravati, 2022.
47. Bureau of Indian Standards (BIS), Standards for Hydrogen Energy Systems, New Delhi, 2022.
48. Council on Energy, Environment and Water (CEEW), Boosting Investments for Domestic Green Hydrogen, New Delhi, 2022.
49. Central Electricity Authority (CEA), National Electricity Plan 2022–2032, New Delhi, 2022.
50. CSIR-National Environmental Engineering Research Institute (NEERI), Liquid Organic Hydrides for H_2 Supply, Nagpur, 2022.
51. Energy Transitions Commission (ETC), Making the Hydrogen Economy Possible, London, 2022.
52. Fertiliser Association of India (FAI), Annual Statistics 2021–22, New Delhi, 2022.
53. Global CCS Institute, Global Status of CCS 2022, Melbourne, 2022.
54. Bharat Petroleum Corporation Limited (BPCL), Sustainability Report 2021–22, Mumbai, 2022.
55. Greenko Group, Greenko–John Cockerill 2 GW Electrolyzer Factory, LiveMint report, 2022.
56. International Energy Agency (IEA), Hydrogen in Industry: Challenges and Opportunities, Paris, 2022.
57. Indian Institute of Technology Guwahati, Biohydrogen from Lignocellulosic Biomass, Guwahati, 2022.
58. Indian Institute of Technology Kanpur, PEC Wastewater Splitting and Fuel Cells, Kanpur, 2022.
59. Indian Register of Shipping, Provisional Guidelines – Fuel Cell Vessels, Mumbai, 2022.
60. IPCC, Climate Change 2022: Mitigation of Climate Change (AR6 WG-III), Cambridge University Press, Cambridge, 2022.
61. International Renewable Energy Agency (IRENA), Green Hydrogen Cost Reduction: Scaling Up Electrolysers, Abu Dhabi, 2022.
62. M. Kumar, A. Sharma, R. Singh, NPG Asia Mater., 14, 88 (2022).
63. J. Mathur, S. Mungla, Renew. Sustain. Energy Rev., 156, 112014 (2022).
64. McKinsey & Company, Decarbonising Shipping: All Hands on Deck, McKinsey Sustainability, 2022.
65. Ministry of New and Renewable Energy (MNRE), Government of India, National Hydrogen Energy Roadmap, New Delhi, 2022.
66. Ministry of Road Transport and Highways (MoRTH), AIS-157: Safety Requirements for Compressed H_2 Fuel Cell Vehicles, New Delhi, 2022.
67. NITI Aayog, Harnessing Green Hydrogen: Opportunities for Deep Decarbonisation in India, New Delhi, 2022.
68. NITI Aayog, Rocky Mountain Institute (RMI), India's Energy Transition Pathways 2030/2050, New Delhi, 2022.
69. Rocky Mountain Institute (RMI), NITI Aayog, Green Hydrogen in India: Opportunity and Pathways, New Delhi, 2022.
70. Society of Indian Automobile Manufacturers (SIAM), Hydrogen Roadmap for Automotive Sector in India, New Delhi, 2022.
71. Sardar Patel Renewable Energy Research Institute (SPRERI), Annual Report 2021–22: Biomass Gasification, Vallabh Vidyanagar, 2022.
72. The Energy and Resources Institute (TERI), Bio-Resources for Low-Carbon Bio-Hydrogen, New Delhi, 2022.
73. World Economic Forum (WEF), Hydrogen for Net Zero: India's Pathway, Geneva, 2022.
74. World Steel Association, Steel's Contribution to a Low Carbon Future, Brussels, 2022.
75. World Bank, Green Hydrogen in Developing Countries, World Bank Group, Washington, DC, 2022.
76. Adani New Industries Ltd., Green Hydrogen and Renewable Energy Investment Plan, Ahmedabad, 2023.
77. ACME Group, Green Ammonia and Hydrogen Projects, Gurugram, 2023.
78. Ashok Leyland Ltd., *Project HEMA:* Hydrogen Commercial Vehicles, Chennai, 2023.
79. BloombergNEF, Hydrogen Economy Outlook 2023, London, 2023.
80. Department of Fertilisers, Ministry of Chemicals and Fertilizers, Government of India, Annual Report 2022–23, New Delhi, 2023.
81. European Commission, REPowerEU: Hydrogen Import Strategy, Brussels, 2023.
82. Florence School of Regulation, The Green Hydrogen Economy: Insights from India, European University Institute, Florence, 2023.
83. Gujarat State Electricity Corporation Ltd. (GSECL), Renewable Energy-Powered Green Hydrogen Hubs in Gujarat, Vadodara, 2023.
84. GreenH Technologies, 1000 MW PEM Electrolyzer Plant in India, Bengaluru, 2023.
85. Greenko Energy Holdings, Green Hydrogen Production Targets, Hyderabad, 2023.
86. Hydrogen Council, Hydrogen Insights *2023*, Brussels, 2023.
87. India H_2 Alliance (IH2A), Industry Coalition for Net-Zero Hydrogen, New Delhi, 2023.
88. Indian Ports Association, Green Hydrogen Bunkering Infrastructure, New Delhi, 2023.
89. International Register of Shipping (IRS), Hydrogen Safety Codes for Maritime Applications, London, 2023.
90. International Energy Agency (IEA), *Global Hydrogen Review 2023*, Paris, 2023.
91. International Energy Agency (IEA), Net Zero by 2050: A Roadmap for the Global Energy Sector, Paris, 2023.

92. International Energy Forum (IEF), India's Green Hydrogen Mission: Economic Analysis, Riyadh, 2023.
93. Asian Development Bank (ADB), Accelerating the Hydrogen Economy in South and Southeast Asia, Manila, 2023.
94. ONGC Energy Centre, Indian Institute of Technology Delhi, *IS Thermochemical Cycle*, *SPGIndia Proceedings*, 2023.
95. Indian Institute of Technology Madras, Hydrogen from Seawater Using Solar Energy, Chennai, 2023.
96. International Maritime Organization (IMO), IMO's Work to Cut GHG Emissions from Ships, London, 2023.
97. International Renewable Energy Agency (IRENA), Global Hydrogen Trade to Meet the 1.5°C Climate Goal, Abu Dhabi, 2023.
98. International Renewable Energy Agency (IRENA), Renewable Power Generation Costs in 2022, Abu Dhabi, 2023.
99. JSW Steel Ltd., Sustainability Report 2022–23: Pathway to Green Steel, Mumbai, 2023.
100. Kochi Metro Rail Ltd. (KMRL), Hydrogen Train Feasibility Study, Kochi, 2023.
101. Larsen & Toubro, Defence Research and Development Organisation (DRDO), Air-Independent Propulsion for Indian Navy, Mumbai, 2023.
102. V. Jiman, *India*–US Green Hydrogen Collaboration Overview, LinkedIn article, 2023.
103. McKinsey & Company, Global Energy Perspective 2023: Hydrogen Outlook, New York, 2023.
104. McKinsey Global Institute, India's Turning Point: An Economic Agenda to Spur Growth and Jobs, New Delhi, 2023.
105. Ministry of New and Renewable Energy (MNRE), Government of India, National Green Hydrogen Mission Policy Document, New Delhi, 2023.
106. Ministry of New and Renewable Energy (MNRE), Government of India, R&D Roadmap for Green Hydrogen Ecosystem in India, New Delhi, 2023.
107. Ministry of Petroleum and Natural Gas (MoPNG), Government of India, Draft National Policy on Repurposing Gas Pipelines for Hydrogen, New Delhi, 2023.
108. Maharashtra State Electricity Distribution Co. Ltd. (MSEDCL), Green Hydrogen Integration with Grid: Maharashtra Roadmap, Mumbai, 2023.
109. R. Nagar, B. P. Vinayan, N. Rajalakshmi, S. Ramaprabhu, *Int. J. Hydrogen Energy*, **36**, 8822 (2011).
110. NTPC Ltd., India's First Green Hydrogen Blending in PNG, Press Release, 4 January 2023, New Delhi.
111. NTPC Renewable Energy Ltd., Green Hydrogen Strategy, New Delhi, 2023.
112. Odisha Renewable Energy Development Agency (OREDA), Green Hydrogen Hub Feasibility: Paradeep and Gopalpur, Bhubaneswar, 2023.
113. Observer Research Foundation (ORF), India–EU Green Hydrogen Partnership, New Delhi, 2023.
114. ONGC Energy Centre, Strides in Green Hydrogen Production, New Delhi, 2023.
115. Petroleum and Explosives Safety Organisation (PESO), Regulations for Storage and Handling of Hydrogen, Nagpur, 2023.
116. Petroleum and Natural Gas Regulatory Board (PNGRB), Technical Standards for Hydrogen–Natural Gas Blending, New Delhi, 2023.
117. S. A. Rawool, M. S. Akula, P. V. Korake, R. B. Mane, B. M. Thombare, S. B. Shrivastava, in: Handbook on Advanced Materials, A. K. Sharma, R. K. Mishra (eds.), Springer, 2023, p. 345.
118. Reserve Bank of India, Report on Currency and Finance 2022–23: Towards a Greener India, Mumbai, 2023.
119. Reliance Industries Ltd., New Energy – Stiesdal Partnership, Mumbai, 2023.
120. ReNew Power, *Green Hydrogen and Ammonia Projects Pipeline*, Gurugram, 2023.
121. Rajasthan Renewable Energy Corporation Ltd. (RRECL), Rajasthan Green Hydrogen Strategy and Incentive Policy, Jaipur, 2023.
122. Steel Authority of India Ltd. (SAIL), Sustainability Report 2022–23, New Delhi, 2023.
123. Indian Oil Corporation Ltd. (IOCL), First Green Hydrogen-Powered Bus in Delhi, Press Release, September 2023, New Delhi.
124. Shell International, Shell Hydrogen Study: Energy of the Future, The Hague, 2023.
125. Siemens Energy, Hydrogen Solutions for India, Erlangen, 2023.
126. P. Sun, Z. Yuan, Y. Zhang, J. Wu, *Energy Rep.*, **9**, 3612 (2023).
127. Ministry of Finance, Government of India, Union Budget 2023–24: Green Hydrogen and Clean Energy Allocations, New Delhi, 2023.
128. International Finance Corporation (IFC), World Bank Group, Financing Green Hydrogen in Emerging Markets, Washington, DC, 2023.
129. United Nations Development Programme (UNDP), Hydrogen Futures: Powering Sustainable Development in the Global South, New York, 2023.
130. U.S. Department of Energy, Technical Targets for PEM Fuel Cell Components, Washington, DC, 2023.
131. Tamil Nadu Energy Development Agency (TEDA), Green Hydrogen Hub: Tamil Nadu Coastal Policy, Chennai, 2023.
132. Tata Steel Ltd., Green Steel Roadmap: Hydrogen in DRI Production, Mumbai, 2023.
133. P. A. Thakar, V. Bhojak, Energy Fuels, **37**, 2896 (2023).
134. thyssenkrupp Uhde India Pvt. Ltd., Green Hydrogen: Benefits to Economy and Environment, Gurugram, 2023.
135. Government of India, Ministry of New and Renewable Energy, National Green Hydrogen Mission: Mission Document, New Delhi, 2023.
136. BP plc, BP Energy Outlook 2023: India Country Insights, London, 2023.

137. ABB Group, Electrification and Green Hydrogen: India Market Overview, Zürich, 2024.
138. ACME Solar Holdings Ltd., Annual Report 2023–24, Gurugram, 2024.
139. Amara Raja Energy & Mobility Ltd., India's First Hydrogen Refuelling Station – Leh, Ladakh, Press Release, November 2024.
140. Ballard Power Systems, FCmove-HD+ Technical Data Sheet, Burnaby, Canada, 2024.
141. BloombergNEF, Hydrogen Market Outlook 2024, London, 2024.
142. *Business Standard*, "UP Secures INR 1.15 Trillion Investment in Green Hydrogen", 2024.
143. CapstonesDC, India's Hydrogen Sector Primed for Foreign Investment, 2024.
144. Council on Energy, Environment and Water (CEEW), Boosting Investments for Domestic Green Hydrogen Financing, New Delhi, 2024.
145. CNBC TV18, India–EU Boost Ties with Extensive Green Hydrogen Roadmap, 2024.
146. F. Dawood, G. M. Shafiullah, M. Anda, *Energy Convers. Manage.*, **315**, 118856 (2024).
147. Deendayal Port Authority, Green Hydrogen Export Hub – Kandla, Gandhidham, 2024.
148. *The Economic Times*, "IIT Indore Catalyst for Hydrogen from Methanol", 2024.
149. Federation of Indian Petroleum Industry (FIPI), Hydrogen Market Report 2023, New Delhi, 2024.
150. GAIL (India) Ltd., Green Hydrogen Plant Commissioning, Press Release, 24 May 2024, New Delhi.
151. A. Ghimire, L. Frunzo, F. Pirozzi, E. Trably, R. Escudié, P. N. L. Lens, G. Esposito, *Bioresour. Technol.*, **399**, 130750 (2024).
152. GreenH Mobility, India's First Hydrogen Refuelling Station – Leh, Ladakh, Bengaluru, 2024.
153. Global Wind Energy Council (GWEC), India Wind Energy Market Outlook 2024–2028, Brussels, 2024.
154. Institute for Energy Economics and Financial Analysis (IEEFA), Enabling Sustainable Demand for Green Hydrogen in India, 2024.
155. National Green Hydrogen Mission (NGHM), Overview – Production Targets and Key Statistics, Ministry of New and Renewable Energy, New Delhi, 2024.
156. India Brand Equity Foundation (IBEF), Hydrogen Energy in India: National Green Hydrogen Mission Roadmap, New Delhi, 2024.
157. International Energy Agency (IEA), World Energy Investment 2024, Paris, 2024.
158. Indian Railways, Ministry of Railways, Hydrogen for Heritage: Hydrogen DEMU Specifications, New Delhi, 2024.
159. International Renewable Energy Agency (IRENA), Quality Infrastructure Roadmap for Green Hydrogen, Abu Dhabi, 2024.
160. K. Domen, Q. Wang, *Nat. Energy*, **9**, 112 (2024).
161. Larsen & Toubro Ltd., Annual Report 2023–24, Mumbai, 2024.
162. X. Li, J. Ogden, *Energy Policy*, **142**, 111498 (2020).
163. Mahindra Last Mile Mobility Ltd., Hydrogen Fuel Cell Commercial Vehicle Strategy, Mumbai, 2024.
164. MarkNtel Advisors, India Green Hydrogen Market 2026–2032, New Delhi, 2024.
165. National Renewable Energy Laboratory (NREL), Hydrogen and Fuel Cell Technologies Office Annual Progress Report 2024, Golden, CO, USA, 2024.
166. A. I. Osman, N. Mehta, A. M. Elgarahy, M. Hefny, A. Al-Hinai, A. H. Al-Muhtaseb, D. W. Rooney, *Environ. Chem. Lett.*, **22**, 1 (2024).
167. NTPC Ltd., Annual Report 2023–24, New Delhi, 2024.
168. Press Information Bureau (PIB), Government of India, India's Green Hydrogen Revolution: An Ambitious Approach, New Delhi, 2024.
169. Y. K. Salkuyeh, B. A. Saville, H. L. MacLean, *Renew. Sustain. Energy Rev.*, **193**, 114312 (2024).
170. R. Sawhney, Decoding India's Green Hydrogen Potential, ORF America Background Paper No. 20, Washington, DC, 2024.
171. Solar Energy Corporation of India (SECI), Tender for Green Hydrogen Production Units 2024, New Delhi, 2024.
172. Tata Motors Ltd., Hydrogen Fuel Cell Bus Programme, Pune, 2024.
173. The Hydrogen Energy, India's Hydrogen Train – Technical Details, 2024.
174. U.S. Commercial Service, India Green Hydrogen Market Intelligence, Washington, DC, 2024.
175. World Economic Forum (WEF), Green Hydrogen: Enabling Measures Roadmap for India, Geneva, 2024.
176. X. Wei, F. Song, J. Teng, J. Zheng, S. Zhu, K. Wang, X. Zhi, S. Bao, L. Qiu, *Int. J. Hydrogen Energy,* **109**, 67 (2025).
177. J.-H. Wang, Y.-F. Li, C.-M. Feng, *Renew. Energy,* **240**, 121982 (2025).
178. French Institute of International Relations (IFRI), India's Green Hydrogen Strategy in Action, Paris, 2025.
179. Larsen & Toubro Ltd., First Indigenously Manufactured Electrolyser at Hazira, Press Release, 1 March 2025.
180. Sustainable Future, Opportunities and Limits of India's Green Hydrogen Pursuit, *2025*.

Bulgarian Chemical Communications, Volume 58, Issue 4 (pp. 550-558) 2026 *DOI: 10.34049/bcc.58.4.5765*

Impact of polyvinylpyrrolidone as an additive to the positive electrolyte of a vanadium redox flow battery

P. Nikolov*, B. Mladenova, M. Matrakova, T. Stankulov, R. Boukoureshtlieva, L. Soserov

Institute of Electrochemistry and Energy Systems, Bulgarian Academy of Sciences, Acad. Georgi Bonchev Str., Block 10, 1113 Sofia, Bulgaria

Received: May 11, 2025; Revised: May 22, 2026

Charge and discharge reactions at the positive electrode of a vanadium redox flow battery involve intermediate protonation and deprotonation steps. Polyvinylpyrrolidone (PVP), added to the positive electrolyte of the battery, may function as a proton donor or acceptor and thereby modify the electrochemical reactions occurring at the positive electrode. Linear cyclic voltammetry measurements demonstrated that PVP with a molecular weight (MW) of 40 000 is more effective in increasing the oxidation and reduction peak current densities of vanadium ions than PVP with an MW of 360 000. Increasing the dosage level (from 0.0125 to 0.05 wt. %) of the PVP additive in the electrolyte does not lead to a proportional increase in the current associated with vanadium-ion oxidation and reduction reactions. The optimal PVP concentration is 0.025 wt.%. Electrical tests performed with a vanadium flow cell with an active area of 25 cm² and anion-exchange membrane demonstrated that the addition of 0.025 wt.% of PVP with an MW of 40 000 to the positive electrolyte results in enhanced discharge capacity, coulombic efficiency, and energy efficiency at various discharge-charge current densities (10–100 mA cm^{-2}) compared with a control cell without the additive. It was established that the PVP additive reduces the open-circuit voltage values of the test cell by 20–30 mV during both charge and discharge. This effect of PVP could be associated with active interactions of PVP polymer chains with VO^{2+}, VO_2^+, and protons (H^+). Volume imbalance in the electrolyte reservoirs was mitigated by a continuous electrolyte bridge connecting the positive and negative compartments. Prolonged constant-current (80 mA cm^{-2}) discharge and charge cycling of the test cells further proved that the beneficial effect of PVP is stable over time. The cell containing 0.025 wt.% of PVP achieved up to 98% utilization of electrolyte discharge capacity, compared with 94% for the control cell. The coulombic efficiency was greater than 98% for the PVP-containing cell and greater than 95% for the control cell.

Keywords: vanadium redox flow battery, VRFB, positive electrolyte, additive, polyvinylpyrrolidone, PVP.

INTRODUCTION

In recent years, vanadium redox flow batteries (VRFBs) have attracted increasing scientific and industrial interest. This is driven by the growing energy storage sector and the advantages of VRFBs over conventional electrochemical systems. VRFBs offer high energy efficiency, deep-discharge capability without significant degradation, and long service life. They also provide fast electrochemical kinetics, low self-discharge, and limited cross-contamination between electrolytes. These features make VRFBs attractive for large-scale storage and renewable energy integration [1-5]. Energy is stored through reversible changes in vanadium oxidation states in acidic electrolyte [6]. The main electrochemical reactions are [7]:

Positive electrode (V^{4+}/V^{5+}): $VO^{2+} + H_2O - e^- \leftrightarrow VO_2^+ + 2H^+$
Negative electrode (V^{2+}/V^{3+}): $V^{3+} + e^- \leftrightarrow V^{2+}$

Despite these advantages, VRFBs require further material and design optimization. Key limitations include low energy density, about 20–30 Wh L^{-1}, and a narrow electrolyte stability range [8]. System efficiency and durability depend on membranes with low vanadium permeability and high chemical resistance, as well as electrodes with high activity and limited side reactions [9]. Even with optimized components, electrolyte stability remains critical because vanadium ions may precipitate under specific temperature and concentration conditions. Therefore, additives are needed to improve solubility and suppress precipitation.

Various additive-based strategies have been reported to stabilize and improve vanadium electrolytes. Skyllas-Kazacos *et al.* [10] showed that suitable precipitation inhibitors can extend operational life and improve cycling stability. However, many organic additives are unstable in highly oxidizing V^{5+} media, requiring substances of higher chemical stability.

Li *et al.* [11] studied the effects of fructose, mannitol, glucose, and D-sorbitol on VRFB performance. D-sorbitol significantly reduced precipitation, improved electrochemical activity, and increased energy efficiency from 79.8% to 81.8%. Ding *et al.* [12] found that phosphate

* To whom all correspondence should be sent:
E-mail: *p_nikolov@iees.bas.bg*

© 2026 Bulgarian Academy of Sciences, Union of Chemists in Bulgaria

additives effectively suppress V(V) precipitation in the positive electrolyte.

Wen *et al*. [13] showed that controlling thermal stability and precipitation is critical for widening the operating temperature range and improving efficiency. Yu *et al.* [14] noted that additives can suppress precipitation, optimize viscosity, improve ionic conductivity, and limit corrosion. Increasing the concentration of vanadium ions using mixed electrolytes, and applying appropriate additives enhance the energy density and electrochemical performance of VRFBs while further improvements in stability, ionic conductivity, and control of active-species crossover are necessary for practical applications [15]. Zheng *et al.* [16] further demonstrated the role of polymer materials in vanadium systems, demonstrating that doping of membranes with polyvinylpyrrolidone (PVP) improves their stability and selectivity.

The electrochemical reactions occurring at the positive electrode of the vanadium flow cell involve proton participation in several intermediate protonation and deprotonation steps of vanadium ion species. Altering the properties of the electrode/electrolyte interface with the aim of influencing proton-involved reactions could result in improved battery performance. One class of suitable additives to the vanadium electrolyte that could modify the characteristics of the electrode /electrolyte interface includes substances exhibiting proton-acceptor or proton-donor properties. One such material is the polymer polyvinylpyrrolidone (PVP). The polymer chains of PVP may interact with both vanadium ions and protons, as well as adsorb on the surface of the carbon electrode. A very recent study [17] demonstrated that the addition of PVP with a molecular weight of 3 600 000, in combination with ammonium phosphate (50:50 wt.%), considerably suppresses the agglomeration of oxovanadium species and the detrimental formation of precipitates in solution at elevated temperatures (>40 °C), thereby having a positive impact on the cell's electrical characteristics.

In this study, the effect of polyvinylpyrrolidone (PVP) with different molecular weights as an additive to the positive electrolyte was evaluated, aiming to improve the overall electrical performance of a vanadium redox flow battery.

EXPERIMENTAL

Cells, electrodes, and peripheral accessories

A three-electrode cell configuration using a vanadium electrolyte (in-house modified ParaCell model, Gamry Instruments, USA) was employed for electrochemical measurements. In-house-made PTFE holders with inserted graphite electrodes (graphite rods, Gamry Instruments, USA) were used as the working electrode (area exposed to the electrolyte: 0.5 cm^2) and counter-electrode (area exposed to the electrolyte: 2.0 cm^2). The electrolyte volume was 120 mL. An in-house-made mercury/mercurous sulfate electrode (Hg/Hg_2SO_4/4.8 M H_2SO_4; -0.610 V *vs* SHE) served as the reference electrode.

Furthermore, electrical performance tests were conducted using laboratory-scale redox flow cells with an integrated flow field (A-Cell model, Redox-Flow B.V., Netherlands) and an active area of 5 cm × 5 cm (25 cm^2). Thermally activated AVCarb G280 graphite felt (AvCarb Specialty Materials LLC, USA), with a thickness of 2.8 mm, was used as the electrode material. This material was selected owing to its high specific surface area which facilitates redox reactions. The electrodes were mechanically compressed by 25–30% for the positive electrode and 20–25% for the negative electrode using appropriate gaskets to ensure optimal electrical contact and proper system sealing.

A Fumasep® FAPQ-330 anion-exchange membrane (Fumatech BWT GmbH, Germany), with a nominal thickness of 30 μm, was used to separate the half-cells. The electrolyte was continuously pumped through the positive and negative compartments of the test cell using PTFE tubes with an inner diameter (ID) of 1.6 mm and an outer diameter (OD) of 3.2 mm, together with a two-channel peristaltic pump (BT600L-YZ15T model, Redox-Flow B.V., Netherlands), at a flow rate of 20 mL min^{-1}. A small open-circuit voltage cell (OCV cell, Redox-Flow B.V., Netherlands) was connected in series before the main flow cell for electrode or full-cell potential measurements. The electrolyte reservoirs were 150 mL-capped glass bottles (Duran, Germany) containing appropriate tube fittings and adapters. The electrolyte volume for each measurement was 50 mL for both the positive and negative compartments.

Electrolyte and additives

In this study, an industrial vanadium electrolyte (Yinhui New Energy, China) was used. The main characteristics of the electrolyte were as follows: 0.80–0.85 mol L^{-1} V^{3+}, 0.80–0.85 mol L^{-1} V^{4+}, 2.15 mol L^{-1} H_2SO_4, total SO_4^{2-} = 4.3 mol L^{-1}, and density = 1.37 g cm^{-3}. The selection of a commercial product with established properties allowed precise monitoring of the effect of the applied additives.

Polyvinylpyrrolidone (PVP) with two different molecular weights — 40 000 and 360 000 — was obtained from Sigma-Aldrich, USA. The

experiments were conducted at various concentrations, with the additives pre-dissolved in the electrolyte before their introduction into the system.

Electrochemical measurements

The electrochemical screening tests were performed on a vanadium electrolyte, without initial pre-charge, using an Interface 1010E potentiostat/galvanostat (Gamry Instruments, USA). Cyclic voltammetry studies were carried out at a scan rate of 20 mV s^{-1}, and 20 voltammetric cycles were performed. The following working potential windows, relative to the Hg/Hg_2SO_4 reference electrode, were applied to evaluate the electrochemical behavior: 0.0 to +1.2 V for the positive electrode and −1.5 to −0.4 V for the negative electrode. The overall working potential window of the cell ranged from −1.5 V to +1.2 V. Before each measurement, the working graphite electrodes were mechanically polished with P800-grit emery paper and rinsed with ethanol (96%).

Electrical performance tests

The impact of the studied additives on the electrical performance characteristics of the vanadium redox flow cell was evaluated under constant-current discharge and charge conditions at currents of 0.25, 0.50, 1.00, 1.50, 2.00, and 2.50 A, corresponding to 10, 20, 40, 60, 80, and 100 mA cm^{-2}, respectively. For all measurements, the volumes of the positive and the negative electrolyte were 50 mL each. The calculated usable theoretical capacity of 50 mL of vanadium electrolyte was 1.10 Ah (1100 mAh). The initial pre-charge of the electrolyte was performed at a current of 1.0 A until the input charge capacity reached 2.20 Ah (2200 mAh). During the various testing profiles, the end-of-discharge cell voltage was limited to 0.80 V, and the upper charge voltage was limited to 1.60 V or until the input charge capacity reached 1100 mAh. Numerous electrical cell parameters were monitored, recorded, and calculated during discharge and charge testing, such as cell voltage, open-circuit voltage, positive and negative electrode polarization, Ah capacity, Wh energy, coulombic efficiency, and energy efficiency.

UV–Vis spectroscopy

The qualitative changes in the positive electrolyte after cycling were analyzed using UV–Vis spectroscopy (Shimadzu UV-1900i, Japan). The absorption spectra were recorded in the range of 300–900 nm. A 500 µL sample of the electrolyte was diluted in an acid solution with the same H_2SO_4 concentration as the electrolyte, after which the sample was analyzed in a quartz cuvette.

RESULTS AND DISCUSSION

Cyclic voltammetry measurements

As a preliminary screening study, the effects of PVP molecular weight and dosage level in the vanadium electrolyte on the discharge and charge reactions at the positive and the negative electrode were evaluated by cyclic voltammetry. Fig. 1a shows the recorded voltammograms after 20 cycles in the full potential window for the blank electrolyte solution and solutions containing 0.0125, 0.025, and 0.050 wt.% of PVP with a molecular weight of 360 000.

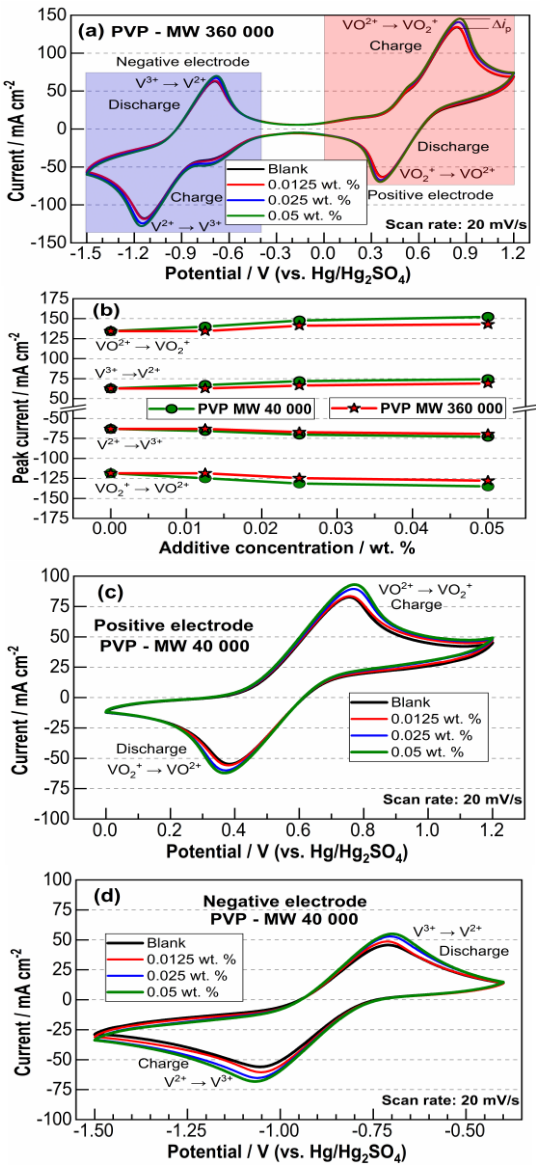


Figure 1. Cyclic voltammetry measurements at a scan rate of 20 mV s^{-1}: (a) Full-cell potential window; (b) Values of peak currents *vs.* PVP concentration in the electrolyte; (c) Negative-electrode potential window; (d) Positive-electrode potential window.

The profiles of the current–voltage curves indicate that the addition of PVP to the vanadium electrolyte results in increased current peak values compared with the blank electrolyte, which is associated with enhanced electrochemical reactions at both the positive and the negative electrode. The impact of the PVP additive with an MW of 360 000 is more pronounced on the charge reactions of the positive and the negative electrode. The increase in peak current is not proportional to the PVP dosage level. The addition of 0.0125% of PVP has no effect, whereas 0.025% of PVP results in a noticeable increase in current peaks. A further increase in the PVP dosage to 0.05% produces only a slight additional increase in peak current compared with the effect of 0.025%. Fig. 1b summarizes the effect of PVP dosage levels in the electrolyte and its molecular weight on reaction peak currents. It can be seen that the positive effect of PVP on the reactions occurring at the positive electrode is more pronounced, and the optimal concentration is 0.025 wt.%.

The influence of PVP on the peak currents of the positive and negative electrode reactions was quantified by calculating the change in peak current in the presence of the PVP additive relative to the control values (blank electrolyte) denoted as Δi_p. The calculated values for the additives under investigation are summarized in Table 1. The voltammetry measurements conducted in the potential windows of −1.5 to −0.4 V for the negative electrode and 0.0 to +1.2 V for the positive electrode are plotted in Figs. 1c and 1d, respectively. The current–voltage curves recorded at different concentration levels of PVP with a molecular weight of 40,000 confirm that in the presence of the studied additive the peak current values increase. Based on the obtained voltammetry data it can be concluded that the addition of PVP with a molecular weight of 40 000 or 360 000 to the vanadium electrolyte has a beneficial impact on the discharge and charge reactions at both the positive and the negative electrode. Based on the data listed in Table 1, it can be concluded that PVP with a molecular weight of 40 000 exhibits a stronger effect on the peak current values compared with its counterpart with a molecular weight of 360 000. The PVP 40 000 additive is more effective in enhancing the charge reactions of both the positive and the negative electrode.

Electrical performance testing

- *Approach to suppressing electrolyte imbalance.* In the present study, we employed an anion-exchange membrane. One of the major drawbacks of anion-exchange membranes used in vanadium redox flow batteries is the substantial volume imbalance between the positive and the negative electrolyte, which results in a decline in electrical performance characteristics [17]. This phenomenon is attributed to substantial water transfer through the anion-exchange membrane by osmosis and electroosmosis mechanisms, which causes an increase in volume of the negative electrolyte reservoir and a decrease in volume of the positive one.

To overcome this disadvantage of anion-exchange membranes, we designed an electrolyte bridge connecting the positive and the negative electrolyte reservoir, which operates on the principle of interconnected vessels (Fig. 2a). When electrolyte volume imbalance appears between the positive and the negative reservoir, it triggers liquid transfer until balanced electrolyte volumes are restored. The electrolyte bridge was constructed using a thin PTFE tube, with both ends submerged at different levels in the positive and the negative electrolyte reservoir, allowing a liquid flow predominantly from the negative to the positive compartment. Figure 2b shows the appearance of noticeable electrolyte imbalance after only 20 discharge-charge cycles.

Table 1. Changes in the voltammetric oxidation and reduction peak current densities for VO^{2+}, VO_2^+, V^{3+}, and V^{2+} in the presence of PVP additives with different molecular weights.

Additive	Amount, wt. %	Δi_p, mA cm^{-2} (current with additive *versus* control)			
		Positive electrode		Negative electrode	
		Charge	Discharge	Charge	Discharge
		$VO^{2+} \rightarrow VO_2^+$	$VO_2^+ \rightarrow VO^{2+}$	$V^{3+} \rightarrow V^{2+}$	$V^{2+} \rightarrow V^{3+}$
PVP MW 40 000	0.0125	+5.6	+2.6	+6.2	+4.4
	0.0250	+13.2	+7.2	+12.8	+9.2
	0.0500	+17.7	+10.0	+16.4	+11.6
PVP MW 360 000	0.0125	0.0	0.0	0.0	0.0
	0.0250	+6.8	+4.0	+6.0	+3.6
	0.0500	+8.4	+6.4	+9.2	+6.4

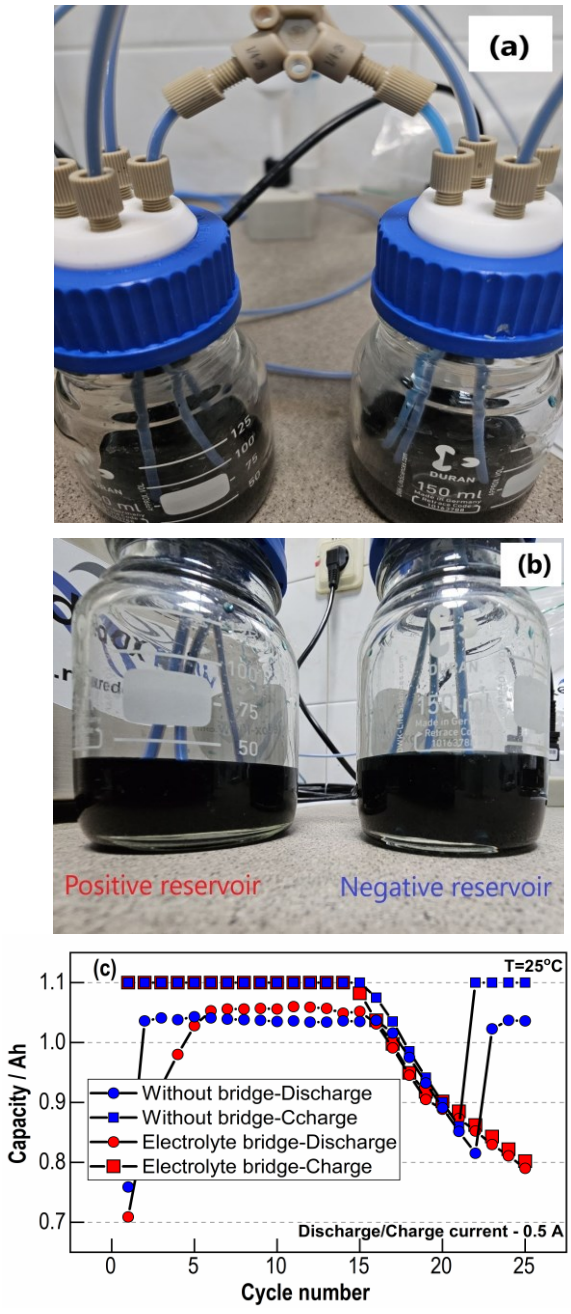


Figure 2. (a) Photograph depicting the electrolyte bridge connecting the reservoirs; (b) Photograph of vanadium flow-cell electrolyte reservoirs showing the appearance of volume imbalance; (c) Changes in discharge and charge capacity of the cell with and without an electrolyte bridge.

Fig. 2c compares the electrical performance of cells with and without an electrolyte bridge. It is evident that after 15 cycles the cell without an electrolyte bridge exhibits a decline in both discharge and charge Ah capacity. The cell with an electrolyte bridge initially follows the same trend; however, once a certain electrolyte volume imbalance is reached, liquid begins to transfer from the negative reservoir to the positive reservoir until the volumes are balanced. This results in a complete restoration of the cell discharge and charge Ah capacity to maximum values. The slightly lower discharge capacity of the cell with the electrolyte bridge compared with the cell without the bridge could be explained by a self-discharge process due to the continuous connection between the positive and the negative reservoir. All further studies were carried out using the electrolyte bridge.

- *Influence of PVP on the electrical characteristics of a vanadium flow cel.* The preliminary screening study by voltammetry technique revealed that PVP with a molecular weight of 40 000 exhibits a more pronounced positive effect on the electrochemical reaction at the positive electrode. Therefore, its effect on the electrical characteristics of vanadium flow cells was further investigated. Figure 3 summarizes the impact of 0.025 wt.% of PVP added to the electrolyte, compared with the blank sample, on the positive and the negative electrical characteristics of the cell during charge and discharge at a constant current of 1.0 A.

Fig. 3a shows that adding PVP shifts the cell-voltage profile downward by about 20 mV during both charge and discharge while slightly prolonging discharge duration. Comparison of Figs. 3a and 3b shows that the lower cell voltage does not negatively affect the discharge energy output or the charge energy input. The data collected from the open-circuit voltage cell during the charge and discharge processes indicate that the addition of 0.025 wt.% of PVP results in voltage values approximately 0.02 V (20 mV) lower than those of the control cell (blank). The downward shift in OCV by 20 mV could occur if the PVP additive:

(i) *complexes V(V) more strongly than V(IV)*. If it stabilizes VO_2^+, the effective activity of free VO_2^+ decreases, shifting the positive electrode potential to a lower value;

(ii) *changes proton activity*. As in the Nernst equation for the positive electrode potential, proton activity appears as a second-order term, small changes in acidity/activity can shift the potential value;

(iii) *changes activity coefficients*. Even if the concentrations of vanadium ions are unchanged, ionic strength or specific interactions can change vanadium-ion activities;

(iv) *adsorbs on the electrode surface*. This may shift the measured open-circuit potential through double-layer/interfacial effects, even without large bulk chemical changes.

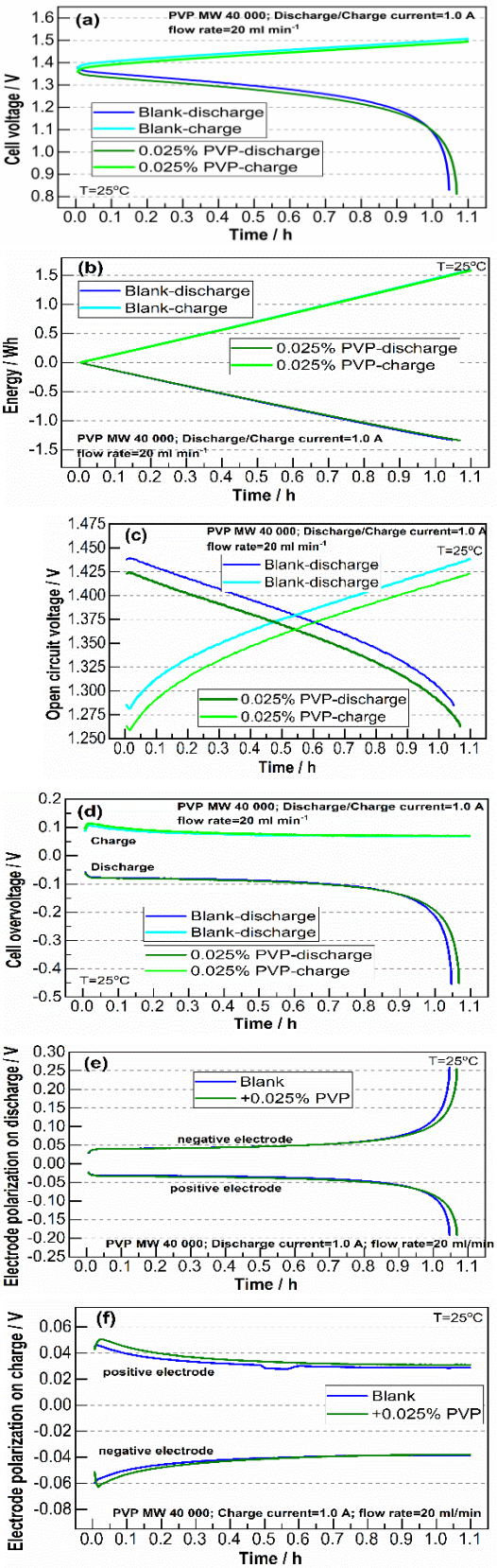


Figure 3. Changes in the electrical characteristics of a vanadium flow cell with PVP during discharge and charge: (a) Cell voltage; (b) Discharge and charge energy; (c) Open-circuit voltage; (d) Calculated cell overvoltage; (e) Electrode polarization during discharge; (f) Electrode polarization during charge.

The obtained experimental information is not sufficient to determine the dominance of one of the above-mentioned mechanisms. The cell overvoltage, calculated by subtracting the OCV values from the cell voltage under current and plotted in Fig. 3d, together with the respective positive and negative electrode polarizations (Figs. 3e and 3f), reveals that the addition of 0.025 wt.% of PVP has no effect on these electrical characteristics associated with the kinetics of the electrode reactions. The observed small increase in positive electrode polarization during charge for the cell with the 0.25 wt.% PVP additive compared with the blank cell could be attributed to the low open-circuit potential of the positive electrode.

The kink observed in the positive-electrode polarization profile of the blank cell after 0.45 h results from a small electrolyte transfer from the negative to the positive storage compartment through the electrolyte bridge. This transfer balances the electrolyte volume and composition. In conclusion, the PVP additive modifies the electrochemical properties of the positive electrolyte by shifting the open-circuit potential and slightly extending the discharge time.

The graphical plots in Fig. 4 summarize the influence of the 0.025 wt.% PVP additive on the integral electrical characteristics of cells tested at different discharge/charge current densities: 10, 20, 40, 60, 80, and 100 mA cm^{-2}.

The effect of the PVP additive on discharge capacity is shown in Fig. 4a. It is evident that for cycling at a current density of 10 mA cm^{-2}, the discharge-capacity values of the blank cell and the cell containing PVP in the positive electrolyte are highly scattered. The cycling data for discharge capacity at a current density of 20 mA cm^{-2} are almost identical for the cell with the 0.025 wt.% PVP additive and the control cell. The cycling results for discharge capacity obtained under current regimes of 40, 60, and 80 mA cm^{-2} clearly demonstrate that the addition of PVP has a noticeable positive impact on discharge capacity, but the beneficial effect decreases as the current density increases.

At a discharge current density of 80 mA cm^{-2}, the discharge capacity of the cell with the 0.025 wt.% PVP additive reaches stable peak values of 1080 mAh corresponding to 98% utilization, whereas the blank cell exhibits 1070 mAh corresponding to 97% utilization of vanadium ions. Although this difference appears small, it may become significant in practical systems using hundreds of cubic meters of electrolyte and operating over long periods.

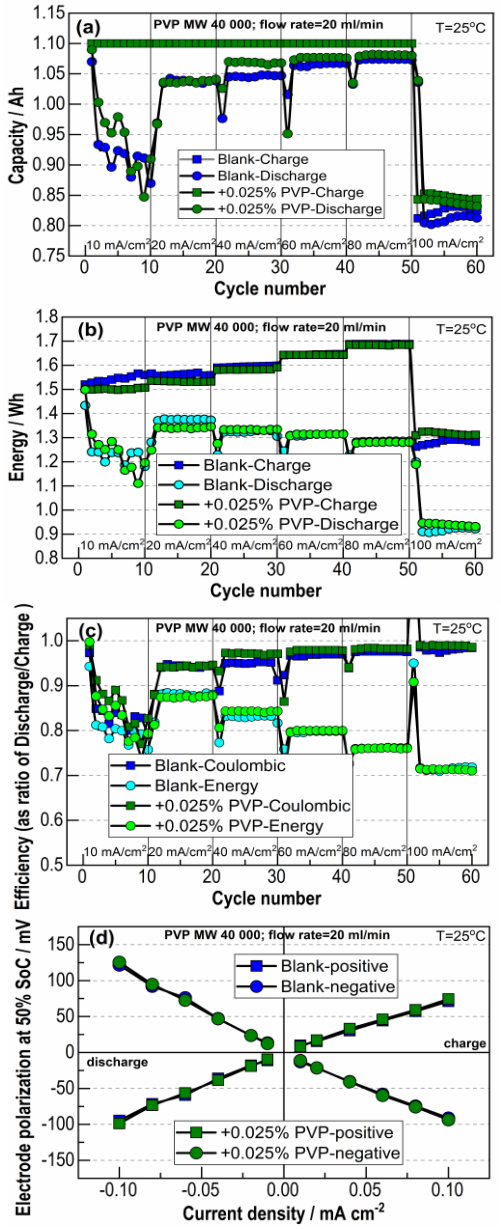


Figure 4. Influence of PVP in the positive electrolyte on the electrical characteristics of a vanadium flow cell measured at various current densities: (a) Discharge and charge capacity; (b) Discharge and charge energy; (c) Coulombic and energy efficiency; (d) Positive and negative electrode polarizations at 50% SoC during charge and discharge.

A further increase in discharge current density to 100 mA cm^{-2} causes a sharp drop in cell discharge and charge capacity to values of 800–850 mAh, but the cell with the PVP additive still demonstrates greater discharge capacity. This abrupt decline is associated with a considerable increase in internal resistance due to cell-design features such as electrode contact and electrolyte supply through the integrated flow field. Fig. 4b shows the recorded changes in discharge and charge energy as a function of current density for cells with and without PVP. PVP does not negatively affect the charge or discharge energy values. A slight decrease is observed only at 20 mA cm^{-2}, whereas a minor increase is registered at 100 mA cm^{-2}. Similarly, the coulombic efficiency and the energy efficiency, calculated as the ratio of the discharge to charge parameters, are plotted in Fig. 4c. The addition of PVP to the positive electrolyte improves coulombic efficiency, although the improvement ranges from noticeable to minor depending on the current density. This effect indicates that the PVP additive improves the reversibility of the processes related to the conversion of VO^{2+} to VO_2^+ and *vice versa*. The tendency of coulombic efficiency to increase at high current densities could be attributed to a decrease in charge and discharge time, thus minimizing the influence of undesired phenomena such as ion and liquid crossover through the membrane and reducing irreversible side reactions. The coulombic efficiency at a current density of 40 mA cm^{-2} is 95% for the blank cell and 97% for the cell with the PVP additive, while at 80 mA cm^{-2}, the blank cell yields 97.6% and the cell with the PVP additive yields 98.3%. Even small differences in this parameter could improve battery life and moderate capacity fading. The calculated values of energy efficiency at various current densities show that the 0.025 wt.% PVP additive in the positive electrolyte has no impact on this parameter. The positive and the negative electrode polarizations at 50% SoC during discharge and charge at various current densities, plotted in Fig. 4d, indicate that the PVP additive has no influence on this electrochemical parameter.

The impact of the PVP additive in the positive electrolyte on the cycling performance of a vanadium flow cell was evaluated during repetitive discharge-charge cycles at a constant current density of 80 mA cm^{-2}. The data obtained for various electrical characteristics of the test cell with the additive and the control cell are plotted in Figure 5.

The data in Fig. 5a clearly show that the addition of 0.025 wt.% of PVP to the positive electrolyte results in stable discharge capacity values of 1050 to 1080 mAh during all 250 cycles, whereas the control cell exhibits values of 1030 mAh in the first 100 cycles, which then drop to 950–1000 mAh. The cell with the PVP additive maintains the ability to accept full charge throughout all 250 cycles, while the control cell loses that ability after 100 cycles. Therefore, the addition of PVP with a molecular weight of 40 000 to the positive electrolyte ensures enhanced and stable cell discharge capacity. In terms of discharge energy (Fig. 5b), the cell with the PVP additive exhibits higher discharge-energy values than the control cell. The calculated values for

coulombic efficiency and energy efficiency, plotted in Fig. 5c, indicate that the PVP additive considerably improves and stabilizes coulombic and energy efficiency during the course of cell cycling. The observed abrupt variations in the cell's electrical characteristics were partially a consequence of liquid flow through the electrolyte bridge from the negative to the positive reservoir or *vice versa*.

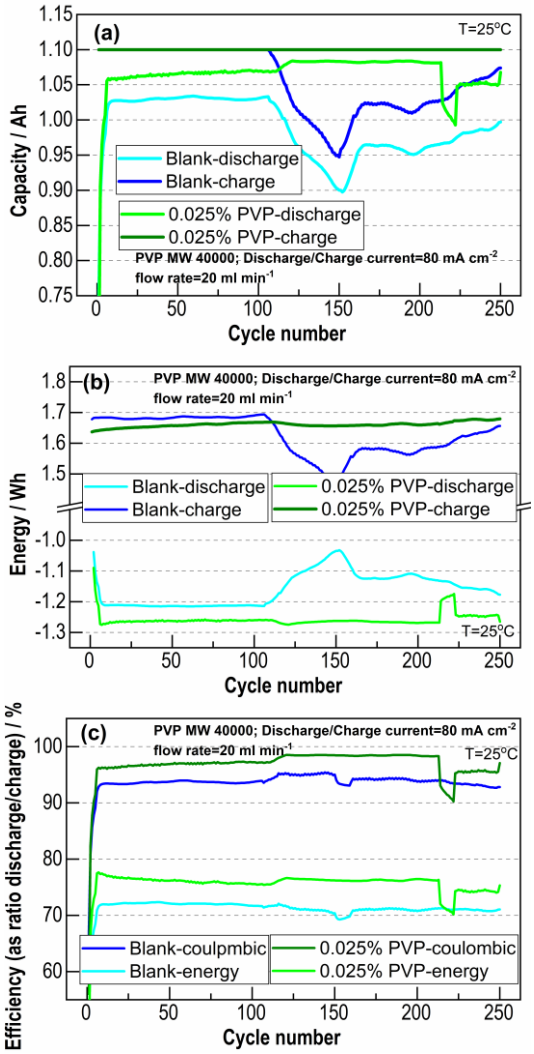


Figure 5. Impact of the PVP additive in the positive electrolyte on the evolution of cell electrical characteristics during discharge-charge cycling: (a) Discharge and charge capacity; (b) Energy; (c) Coulombic and energy efficiency.

To further understand the mode of action of the PVP additive during discharge and charge cycling, the cell-voltage and open-circuit-voltage profiles were compared for cycles 50 and 200 in Fig. 6. It can be seen that for the blank cell as cycling progresses, the cell voltage during charge (Fig. 6a) shifts to higher values, and the 1.60 V limit is reached earlier during the charge step. The cell voltage during charge for the cell with 0.025 wt.% of PVP remains stable during cycling and is lower than that of the blank cell. The cell voltage during discharge is less affected by the PVP additive. The trends of the open-circuit-voltage curves (Fig. 6b) reveal that the PVP additive acts to decrease the values by 20–30 mV. The impact of the PVP additive on open-circuit-voltage values is more distinct during charge than during discharge. Moreover, in the presence of PVP, the open-circuit-voltage values during charge are less affected by cycling than those of the blank cell.

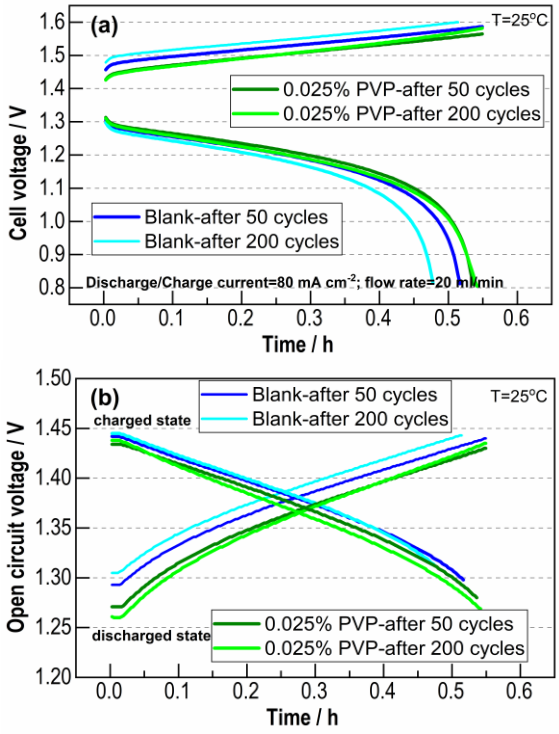


Figure 6. Comparison of voltage changes after 50 and 200 discharge-charge cycles for vanadium flow cells without and with the PVP additive in the positive electrolyte: (a) Cell voltage; (b) Open-circuit voltage.

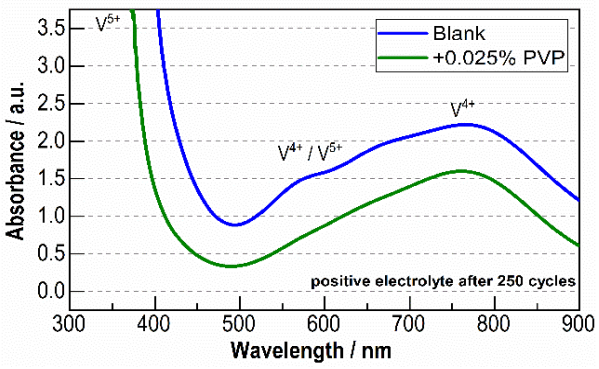


Figure 7. UV–Vis spectra of the positive electrolyte from vanadium flow cells with and without the PVP additive after 250 discharge-charge cycles.

The registered difference in open-circuit-voltage values indicates that an increase in the number of discharge and charge cycles provokes a variation in the ratio of V(V) and V(IV) ions, leading to a decline

in electrical performance. This phenomenon is suppressed by the PVP additive in the positive electrolyte. The PVP additive mainly affects the positive-electrode charge reaction, which involves H^+ ions (protons). Hence, the PVP polymer, as a pronounced proton-donor or proton-acceptor substance, is readily involved in the intermediate elementary processes of protonation and deprotonation occurring at the positive electrode.

Fig. 7 compares the UV–Vis absorption spectra of vanadium electrolyte samples taken from the positive reservoir at the end of cycling, with and without PVP.

A broad absorption band with a maximum at approximately 765 nm is observed, characteristic of VO^{2+} (V(IV), vanadyl), along with a weak shoulder around 580 nm, which is attributed to additional charge-transfer transitions in the VO^{2+}/VO_2^+ (V(IV)/V(V)) system. In the samples with added PVP, the positions of the characteristic absorption maxima are preserved, which indicates that the added polymer does not significantly affect the electronic structure of the vanadium species. At the same time, a significant decrease in the intensity of the absorption bands is observed along with the disappearance of the shoulder at 580 nm. These effects can be attributed to interactions between PVP and vanadium ions, which increase ion stabilization in solution and suppress ionic aggregation [18, 19]. The UV–Vis measurements support the conclusion that the improved electrical characteristics of the test cell result from close interactions between PVP polymer chains and vanadium ions in the positive electrolyte.

CONCLUSIONS

In summary, cyclic voltammetry tests showed that the addition of polyvinylpyrrolidone (PVP) alone to the vanadium electrolyte has a positive impact on the electrochemical reactions occurring at the positive and the negative electrode of a vanadium redox flow cell. PVP with a molecular weight of 40 000 exhibits a more pronounced beneficial effect than PVP with a molecular weight of 360 000, with an optimal dosage level of 0.025 wt.%. Electrical tests conducted with flow cells demonstrated that adding 0.025 wt.% of PVP with a molecular weight of 40 000 to the positive electrolyte provides a stable, long-term enhancement of cell discharge capacity and energy while also improving coulombic efficiency compared with a control cell without the additive. Open-circuit voltage measurements during discharge and charge tests revealed that in the presence of PVP the voltage values shifted downward by 20–30 mV which results in better cell charging. This shift could be attributed to active interactions between the polymer chains, vanadium ions, and protons.

Acknowledgement: *This research was carried out with the financial support of the National Recovery and Resilience Plan of the Republic of Bulgaria, co-funded by the European Union NextGenerationEU, under Project No. BG-RRP-2.011-0048 Improved Electrolyte for Vanadium Flow Batteries.*

REFERENCES

1. J. Zhang, L. Li, Z. Nie, B. Chen, M. Vijayakumar, S. Kim, W. Wang, B. Schwenzer, J. Liu, Z. Yang, *J. Appl. Electrochem*., **41**, 1215 (2011).
2. T. M. Tseng, R. H. Huang, C. Y. Huang, C. C. Liu, K. L. Hsueh, F. S. Shieu, *J. Electrochem. Soc*., **161**, A1132 (2014).
3. H. Kaneko, K. Nozaki, Y. Wada, T. Aoki, A. Negishi, M. Kamimoto, *Electrochim. Acta*, **36**, 1191 (1991).
4. A. Shibata, K. Sato, *Power Eng. J.,* **13**, 130 (1999).
5. L. Cao, M. Skyllas-Kazacos, C. Menictas, J. Noack, *J. Energy Chem*., **27**, 1269 (2018).
6. L. Li, S. Kim, W. Wang, M. Vijayakumar, Z. Nie, B. Chen, J. Zhang, G. Xia, J. Hu, G. Graff, J. Liu, Z. Yang, *Adv. Energy Mater*., **1**, 394 (2011).
7. J. Martin, K. Schafner, T. Turek, *Energy Technol*., **8**, 2000522 (2020).
8. D. S. Aaron, Q. Liu, Z. Tang, G. M. Grim, A. B. Papandrew, A. Turhan, T. A. Zawodzinski, M. M. Mench, *J. Power Sources*, **206**, 450 (2012).
9. T. Jirabovornwisut, A. Arpornwichanop, *Int. J. Hydrog. Energy*, **44**, 24485 (2019).
10. M. Skyllas-Kazacos, L. Cao, M. Kazacos, N. Kausar, A. Mousa, *ChemSusChem*, **9**, 1521 (2016).
11. S. Li, K. Huang, S. Liu, D. Fang, X. Wu, D. Lu, T. Wu, *Electrochim. Acta*, **56**, 5483 (2011).
12. C. Ding, X. Ni, X. Li, X. Xi, X. Han, X. Bao, H. Zhang, *Electrochim. Acta*, **164**, 307 (2015).
13. Y. Wen, Y. Xu, J. Cheng, G. Cao, Y. Yang, *Electrochim. Acta*, **96**, 268 (2013).
14. Z. Yu, X. Jia, Y. Cai, R. Su, Q. Zhu, T. S. Zhao, H. Jiang, *Energy Storage Mater*., **69**, 103404 (2024).
15. X. Wu, J. Liu, X. Xiang, J. Zhang, J. Hu, Y. Wu, *Pure Appl. Chem.*, **86**, 1035 (2014).
16. L. Zeng, T. S. Zhao, L. Wei, Y. K. Zeng, Z. H. Zhang, *J. Power Sources*, **327**, 374 (2016).
17. T. D. Nguyen, A. Whitehead, N. Wai, G. G. Scherer, A. N. Simonov, Z. J. Xu, D. R. MacFarlane, *Small*, **20**, 2311771 (2024).
18. N. H. Choi, S. Kwon, H. Kim, *J. Electrochem. Soc*., **160**, A973 (2013).
19. D. N. Buckley, X. Gao, R. P. Lynch, N. Quill, M. J. Leahy, *J. Electrochem. Soc*., **161**, A524 (2014).

Bulgarian Chemical Communications, Volume 58, Issue 4 (pp.559-564) 2026 *DOI: 10.34049/bcc.58.4.5762*

One-pot synthesis of pyrano chromene carbonitriles catalyzed by $NiFe_2O_4$ nanoparticles and their anticancer potential

K. Takankhar*, A. Durrani

Department of Chemistry, Dr. Rafiq Zakaria College for Women, Chhatrapati Sambhajinagar-431001, Maharashtra, India

Received: April 18, 2026; Revised: July 31, 2026

In the present paper, a rapid, clean, and highly efficient method was developed for the preparation of 2-amino-4-(2,4-alkylphenyl)-5-oxo-4,5-dihydropyrano [3,2-*c*]-3-carbonitrile and its derivatives by one-pot condensation of a three-component system consisting of malononitrile, 4-hydroxycoumarin and various aromatic aldehydes, using a novel $NiFe_2O_4$ nanocrystalline catalyst. The latter was synthesized by a simple sol-gel method. The obtained nanoparticles were characterized by spectroscopic methods such as SEM, XRD, TEM, a. o. The nanocatalyst is highly efficient and environmentally friendly. Some novel 2-amino-4-(2,4-alkylphenyl)-5-oxo-4,5-dihydropyrano [3,2-c] chromene carbonitrile derivatives were prepared by the described synthetic method and were analyzed by $_1$HNMR,$_{13}$CNMR, FTIR, mass spectroscopy, a. o. Anticancer activity of the synthesized compounds was checked against MCF-7 breast cancer cell line using the MTT assay.

Keywords: $NiFe_2O_4$ NPs, Three-component reactions, EtOH, Chromene carbonitriles, Anticancer activity

INTRODUCTION

The research is devoted to nanomaterials, including nanoparticles, nanofillers, nanowires, and various nanocomposites, owing to their distinctive chemical, optical, magnetic, and electrical properties [1]. Among these, spinel ferrites such as nickel ferrite ($NiFe_2O_4$) nanoparticles (NPs) have attracted considerable attention due to their intrinsic magnetic characteristics, which confer high electrical resistivity and excellent thermal stability. These properties render $NiFe_2O_4$ NPs highly suitable for a broad spectrum of technological applications, including magnetic sensors, power transformers, temperature-dependent magnetic devices, heterogeneous catalysts, gas sensing and microwave communication systems [2-5].

Nickel ferrite ($NiFe_2O_4$) is a well-known spinel-type magnetic material that has been widely investigated for its unique physicochemical properties. In the present study, $NiFe_2O_4$ NPs were synthesized using the sol–gel method. The precursors employed included nickel nitrate, ferric nitrate and citric acid. This synthesis route is advantageous due to its simplicity, cost-effectiveness and mild reaction conditions, which facilitate the formation of homogeneous nanocrystalline powders. The resulting $NiFe_2O_4$ NPs exhibit several benefits, including uniform particle distribution, high crystallinity and economic feasibility of production [6].

The primary objective of this work is to establish a reliable, efficient, and environmentally sustainable strategy for the preparation of highly crystalline $NiFe_2O_4$ NPs. Such materials are expected to display desirable physicochemical characteristics, making them promising candidates for advanced applications in catalysis, biomedical fields, and other emerging technologies.

Chromenes represent a significant class of oxygenated heterocyclic compounds with broad biological importance. Among these, pyrano [3,2-c] chromene carbonitrile derivatives have gained notable interest in recent years due to their broad pharmacological potential. These molecules are reported to possess multiple biological activities, including anti-anaphylactic, anticoagulant, anticancer, antispasmodic, and diuretic effects, highlighting their relevance in heterocyclic drug discovery **[7]**. The pyrano [3,2-c] chromene carbonitrile scaffold is particularly attractive for investigation because of its ease of synthesis, structural versatility, and promising therapeutic applications. The present protocol provides a simple, sustainable and environmentally safe synthesis of pyranochromene carbonitrile derivatives [8].

Numerous studies on the synthesis of these compounds have been stimulated by the special qualities and wide-range applications of pyrano coumarins and the nanoparticles were tested for their catalytic effectiveness [9]. In this way not only a novel route to highly efficient synthesis of this series of heterocyclic compounds was

* To whom all correspondence should be sent:
E-mail: *takankharkomal99@gmail.com*

© 2026 Bulgarian Academy of Sciences, Union of Chemists in Bulgaria

introduced, but also the scope of these medicinally important products was broadened [10]. The utilization of magnetic nanoparticles is an exponentially expanding domain in the pursuit of sustainable and environmentally friendly methodologies [11]. Chromene is recognized as a privileged structure and a useful template for the design of novel compounds with potential pharmacological interest especially in the field of neurodegenerative, inflammatory and infectious diseases [12]. In this study, particular emphasis was placed on the synthesis of pyrano [3,2-c] chromene carbonitrile derivatives using $NiFe_2O_4$ NPs as a catalytic system. The target compounds were obtained *via* a three-component condensation reaction involving 4-hydroxycoumarin, aldehydes, and malononitrile. Although several catalysts such as DABCO [13], $Mg(ClO_4)_2$ [14], and MNPs@Cu [15] have previously been employed in this reaction, these methods often suffer from limitations including low product yields, reliance on toxic solvents, high operational costs, elevated reaction temperatures, and need for specialized equipment. To overcome these drawbacks, $NiFe_2O_4$ NPs were applied as an efficient and environmentally benign catalyst. This approach provided a simple, cost-effective, and eco-friendly route to pyrano [3,2-c] chromene carbonitriles, with the resulting compounds demonstrating notable biological, pharmacological, and therapeutic potential.

EXPERIMENTAL

Materials and methods

Chemicals of analytical grade were used. Aromatic aldehyde, 4-hydroxy coumarin, and malononitrile were purchased from Sigma Aldrich. Ethanol, n-hexane, and pet ether were acquired from a local provider and purified by a standard procedure. $NiFe_2O_4$ NPs (10 mol %) and 3 ml of EtOH were mixed; TLC was used for checking reaction progress. The solvent system used was hexane/ethyl acetate (8:2). After completion of the reaction the catalyst was separated by using an external Nd magnet, the residue was used as recovered catalyst. Open capillary tubes were used for melting point determination. All synthesized products were analyzed by SEM, TEM, XRD, IR, $_1$HNMR and $_{13}$CNMR spectral data.

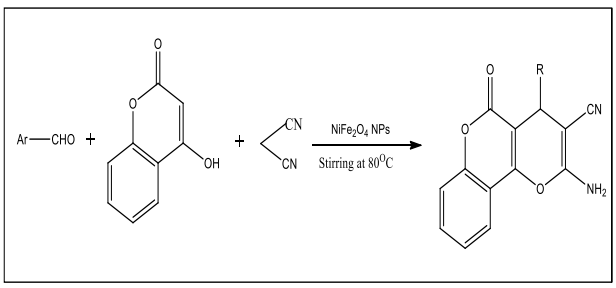
General procedure for obtaining $NiFe_2O_4$ NPs

$$4\ Fe(NO_3)_3.9H_2O + 2\ Ni(NO_3)_2.6H_2O + 2\ C_6H_8O_7 \longrightarrow 2\ NiFe_2O_4 + 12\ CO_2 + 56\ H_2O + 8\ N_2 + 11\ O_2$$

Nickel ferrite ($NiFe_2O_4$) NPs were prepared using a sol–gel synthesis route under ambient conditions. The starting materials consisted of iron nitrate nonahydrate [$(FeNO_3)_3.9H_2O$], nickel nitrate hexahydrate [$(Ni\ (NO_3)_3.6H_2O$] and citric acid [$C_6H_8O_7.H_2O$]. A molar ratio of 1:2 was maintained between the metal nitrates and citric acid. The precursors were dissolved in distilled water in stoichiometric proportions and stirred magnetically on a hot plate to obtain a uniform solution. The pH of the solution was adjusted to 7 by dropwise addition of ammonia under continuous stirring. The mixture was then heated at 80 °C for 3 h under constant stirring. The resulting solution was dried in a hot-air oven at 120 °C for 12 h, which led to gel formation. The dried gel was ground with a mortar and pestle and subsequently calcined at 600 °C for 4 h in a muffle furnace. After cooling to room temperature, $NiFe_2O_4$ NPs were obtained. The latter were utilized as catalysts in the synthesis of pyrano [3,2-c] chromene carbonitrile derivatives.

General procedure for obtaining pyranochromene carbonitrile compounds

As shown in Scheme 1, the reaction mixture was prepared by combining aromatic aldehyde (1 mmol), 4-hydroxycoumarin (1 mmol), malononitrile (1.2 mmol), and ethanol (3 mL) in a round-bottom flask. Nickel ferrite ($NiFe_2O_4$) NPs (10 mol%) were introduced as a catalyst, and the mixture was magnetically stirred at 80 °C. Under these conditions, the reaction proceeded to completion within 30 min. Progress was monitored by TLC using hexane/ethyl acetate (8:2) as the mobile phase. Upon completion of the reaction the catalyst was separated using an external Nd magnet. The reaction mixture was then cooled to room temperature, the crude product was collected and recrystallized from hot ethanol (10 ml) to afford the pure pyrano [3,2-c] chromene carbonitrile derivative. The purified product was filtered and dried in an oven at 60 °C.



Scheme 1. Synthesis of pyranochromene derivatives catalyzed by $NiFe_2O_4$ NPs.

RESULTS AND DISCUSSION

The synthesized pyranochromene carbonitrile derivatives were obtained in very good yields Obtained spectral data confirmed the successful formation of the products. All the details are shown in Tables 1 and 2.

SEM analysis

The microstructure of the nickel ferrite sample and its chemical composition were analyzed using SEM. The SEM analysis confirmed the formation of $NiFe_2O_4$ NPs. The particles were uniformly distributed but showed significant agglomeration due to magnetic interactions and high surface energy. The average particle size was estimated to be in the range of 40-100 nm as shown in Fig. 1. The rough, porous surface texture suggests the presence of fine crystallites forming clustered aggregates. Overall, the microstructure is characteristic of spinel ferrite nanomaterials and supports the successful synthesis of nanosized $NiFe_2O_4$.

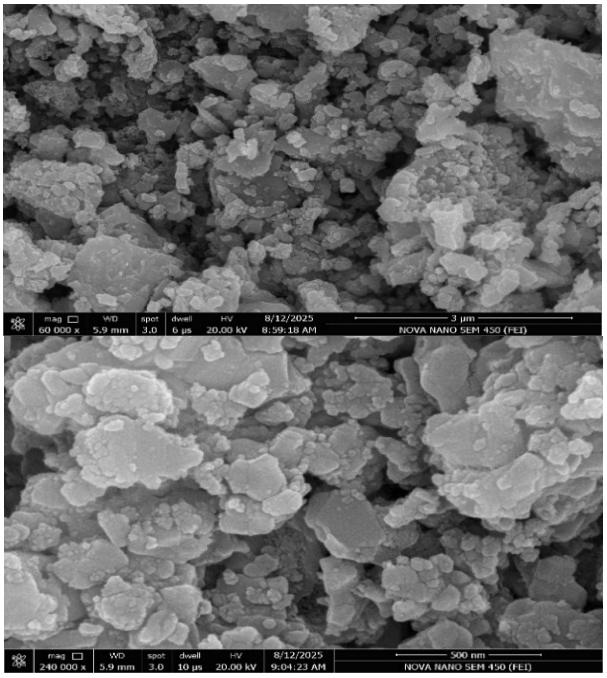


Figure 1. SEM images of the synthesized $NiFe_2O_4$ NPs

XRD analysis

The synthesized $NiFe_2O_4$ nanoparticles exhibit excellent diffraction peaks at 2θ values coordinating with (111), (220), (311), (222), (400), (511) and (440) crystallographic planes, as shown in Fig. 2. The standard JCPDS data for cubic spinel ferrite $NiFe_2O_4$ confirmed the formation of single-phase nickel ferrite because reflections were perfectly matched. The most intense peak. referred to a (311) plane. indicates high crystallinity of the prepared nanoparticles. The absence of extra peaks suggests phase purity without any detectable secondary phases. The peak broadening confirms the nanocrystalline nature of the material.

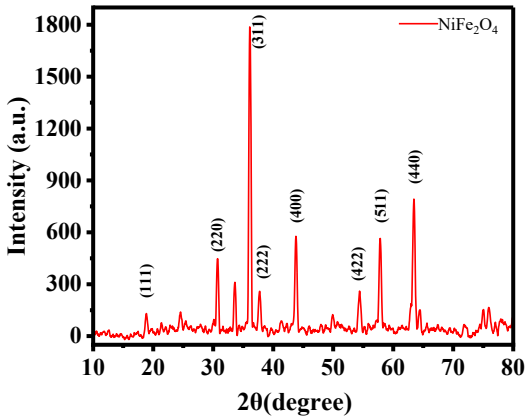


Figure 2. XRD spectrum of the $NiFe_2O_4$ NPs

TEM analysis

The TEM micrograph of the $NiFe_2O_4$ nanoparticles reveals the formation of nearly spherical to irregularly shaped particles with noticeable agglomeration as shown in Fig. 3, The particle size varies from 28 nm to 45 nm with a regular size around 35-40 nm, The observed aggregation is attributed to strong magnetic dipole interactions and high surface energy of ferrite nanoparticles. The uniform contrast and well-defined particle boundaries confirm the formation of crystalline $NiFe_2O_4$ nanoparticles.

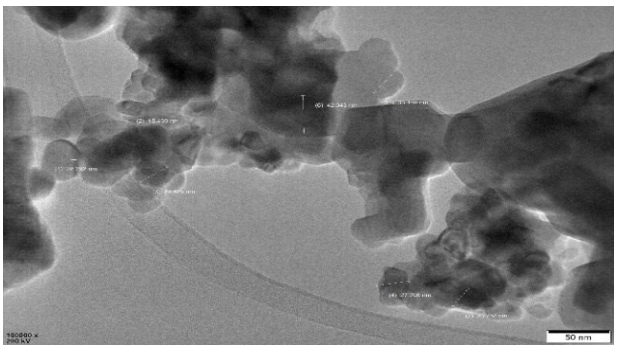


Figure 3. TEM image of the synthesized $NiFe_2O_4$ NPs

Spectral data of pyrano chromene carbonitrile derivatives. (supplementary information ^{1}HNMR,^{13}C NMR & mass spectrometric graphs)

(1) 2-Amino-4-(2,6-dichorophenyl)-5-oxo-4,5-dihydropyrano [3,2-c] chromene-3-carbonitrile

Yield 0.90 g (88 %), color white, m. p. 235–238°C; IR spectrum ν, cm^{-1}: 756 (C-Cl), 1246 (C-O-C), 1602, 1514 (C=C), 1684 (C=O), 2223 (C≡N), 2924 (C-H), 3062 (Ar-CH), 3421, 3328 (NH_2); ^{1}H NMR spectrum δ, ppm: 5.52 (s,1H, CH) 6.90 (s, 1H,

pyran-H), 7.45-7.35 (d, 2H, Ar-H), 7.70-7.30 (m, 4H, Ar-H), 7.90-7.75 (d, 2H, Ar-H); ^{13}CNMR spectrum δC, ppm 38.7 (CH_3), 78.5, 104.3, 133.8, 131.6, 129.4, 128.7, 126.9, 124.8, 123.5, 121.9. 137.9, 136.4, 158.6, 154.2, 162.8(C=O); Mass spectrum *m*/*z* 384.

(2) 2-Amino-4-(2,4-dimethoxyphenyl)-5-oxo-4,5-dihydropyrano [3,2-c] chromene-3-carbonitrile

Yield 0.90 g (89 %), color yellow, m. p. 234-239 °C. IR spectrum, ν, cm^{-1}: 1134 (C–C), 1435 (C–N), 1542 (C–O), 1632 (C–O), 1747 (C=O), 2242 (C≡N), 3189 (=C–H), 3284 and 3381 (NH_2); ^{1}H NMR spectrum δ, ppm 3.24 s (6H, CH_3O), 5.02 s (1H, 4-H), 7.44 d (2H, *J* = 8.0, 7.2 Hz,), 7.85 d (2H, *J* = 8.0, 7.2 Hz), 9.79 s (2H, NH_2); ^{13}C NMR spectrum, δC, ppm: 35.6 (CH3), 103.6, 110.5, 112.8, 112.9, 116.2, 118.3, 120.2, 122.6, 124.6, 132.2, 136.2, 140.2, 142.8, 152.3,157.2, 162.6, 172.2 (C=O); Mass spectrum *m*/*z* 378.23.

(3) 2-Amino-4-(4-methoxyphenyl)-5-oxo-4,5-dihydropyrano [3,2-c] chromene carbonitrile

Yield 0.98 g (91%), color whitish yellow, m. p. 242-246°C, IR spectrum ν, cm^{-1}; 832, 1032 (C-O-C), 1178(C-O), 1251 (C-O-C), 1360 (C-O), 1718 (C=O), 2218 (C≡N), 3452 (N-H); ^{1}H NMR δ, ppm (DMSO-d6): d 3.73 (s, 3H, OCH_3), 4.41 (s, 1H, CH), 6.72-8.33 (m, 10H, Ar, NH_2); ^{13}CNMR spectrum δ C, ppm 55.10 (OCH_3), 116.43, 135.27, 113.69, 158.28, 157.78, 152.95, 151.9, 159.40 (C=O); MS (ESI) m/z 346 (MC).

(4) 2-Amino-4-(3,5-dibromo-4-hydroxy-phenyl)-5-oxo-4,5-dihydropyrano[3,2-c] chromene-3-carbonitrile

Yield 0.89 (87%), color white, m. p. 222-226°C; IR spectrum ν, cm^{-1} 592, 528 (C-Br), 1268 (C-O), 1604,1512 (C=C), 1708 (C=O), 2224 (C≡N), 3062 (C-H), 3356 (NH_2), 3428 (O-H); ^{1}H NMR δ, ppm (400 Hz, DMSO-d6): 3.32(br s, 2H, NH_2), 4.45 (s, 1H, H-4), 7.1-7.3 (m, 2H, ArH), 9.88 (s, 1H, NH);

^{13}C NMR spectrum δ C, ppm: 55.69 (-CH), 104.53, 103.34, 119.31 (-CN), 132.54, 129.69, 124.51 (C-Br), 159.16, 158.01, 155.92, 153.61 (Ar-CH), 159.61 (C=O); MS (ESI): m/z: 490.

(5) 2-Amino-4-(3-iodophenyl)-5-oxo-4,5-dihydropyrano [3,2-c] chromene-3-carbonitrile

Yield 0.91 g (89%), color whitish, creamy, m. p. 260-265°C; IR spectrum ν, cm^{-1}: 856 (C-H), 1068 (C-O-C), 1159 (C-I), 1358 (C-O), 1527 (CN), 1632 (C=C), 1725 (C=O), 2221 (C≡N), 3348 (N-H); ^{1}H NMR, δ, ppm (400 Hz, DMSO-d6): 4.62 (s,1H), 7.28 (m,2H),7.45 (m,2H),7.68 (d, J=8.0 Hz, 2H), 7.92 (d,J= 8.0 Hz, 2H); ^{13}CNMR spectrum δ C ppm: 38.6 (CH2), 112.4, 115.7, 119.3, 121.9, 124.2, 126.4, 128.6, 129.8, 139.1, 147.6 (Ar-CH), 155.8 (C-O), 159.4 (C=O); MS (ESI): m/z 346.

(6) 2-Amino-4-(4-chlorophenyl)-5-oxo-4,5-dihydropyrano [3,2-c] chromene-3-carbonitrile

Yield 0.98 g (91%), color dark yellow, solid, m. p. 266–269°C; IR spectrum ν; cm^{-1}: 775 (C–Cl), 1044 (C–O), 1234 (C–O), 1600 (C=C), 1652 (C=C), 1735 (C=O), 2242 (C≡N), 3120 (=C–H), 3216 and 3312 (NH_2); ^{1}H NMR spectrum δ, ppm: 4.96 s (1H, 4-H), 7.46 d (2H, *J* = 8.4, 7.2 Hz),7.8 d (2H,*J* = 8.2, 7.4 Hz), 9.78 s (2H, NH_2); ^{13}C NMR spectrum, δC, ppm: 105.5, 114.6, 115.8, 115.9, 116.8, 118.6, 121.3, 124.3, 122.8, 133.3,134.4, 138.9,143.9, 152.9, 156.4, 161.8, 173.3 (C=O); Mass spectrum: *m*/*z* 351.28.

(7) 2-Amino-4-(4-nitrophenyl)-5-oxo-4,5-dihydropyrano [3,2-c] chromene-3-carbonitrile

Yield 0.90 g (90%), color dark yellow, solid, m. p. 255–257°C; IR spectrum ν, cm^{-1}:1032 (C–O), 1246 (C–O), 1340 (NO_2), 1655 (C=C), 1736 (C=O), 2258 (C≡N), 3219 (=C–H), 3328 (NH_2), 3415 (NH_2); ^{1}H NMR spectrum δ, ppm: 5.10 s (1H, 4-H), 7.46 d (2H, *J* = 8.0, 7.2 Hz), 7.87 d (2H, *J* = 8.0, 7.6 Hz, Harom), 8.49 s (2H, NH_2); ^{13}C NMR spectrum, δC, ppm: 101.3, 112.6, 114.4, 114.6, 117.2, 120.8, 122.4,124.6,127.6, 130.4,132.5, 137.6, 148.7, 158.9, 160.8, 163.2, 176.8 (C=O); Mass spectrum: *m*/*z* 363.43.

(8) 2-Amino-4-(3-nitrophenyl)-5-oxo-4,5-dihydropyrano [3,2-c] chromene-3-carbonitrile

Yield 0.91 g (89%), color yellow, solid, m. p. 258–260°C; IR spectrum, ν, cm^{-1}: 986 (C–C),1045 (C–C), 1230 (C–O), 1346 (NO_2),1608 (C–O), 1636(C–O), 1732 (C=O), 2249 (C≡N), 3127 (=C–H), 3325 (NH_2), 3492 (NH_2); ^{1}H NMR spectrum δ, ppm: 4.80 s (1H, 4-H), 7.44 d (2H, *J* = 8.2, 7.5 Hz,), 7.56 d (2H, *J* = 8.2, 7.2 Hz,), 9.96 s (2H, NH_2); ^{13}C NMR spectrum δC, ppm: 105.5, 110.6, 112.8, 116.8, 118.8, 121.8,122.7, 124.6, 127.9, 134.3, 138.6, 140.2, 142.6, 154.5, 156.6, 164.2, 174.7 (C=O); Mass spectrum: *m*/*z* 363.28.

(9) 2-Amino-4-(4-methylphenyl)-5-oxo-4,5-dihydropyrano [3,2-c] chromene-3carbonitrile

Yield 0.84 g (80%), color white, solid, m. p. 266–269°C; IR spectrum ν, cm^{-1}: 1159 (C–O), 1236 (C–C), 1608(C–O), 1636 (C–O), 1746 (C=O), 2236 (C≡N), 3298 (=C–H), 3314 (NH_2); ^{1}H NMR spectrum δ, ppm:1.6 s (3H, CH_3), 4.96 s (1H, 4-H), 7.36 d (2H, *J* = 8.2, 7.4 Hz), 7.62 d (2H*J* = 8.2, 7.4 Hz), 6.74 s (2H, NH_2); ^{13}C NMR spectrum δC, ppm: 21.4 (CH_3), 106.6, 113.9, 116.7, 116.8, 118.6, 121.6, 122.8, 126.8, 128.2, 132.7, 136.4, 140.9, 142.4, 152.8, 158.8, 164.2, 176.6 (C=O); Mass spectrum: *m*/*z* 332.23.

(10) 2-Amino-4-(4-hydroxyphenyl)-5-oxo-4,5-dihydropyrano [3,2-c] chromene-3-carbonitrile

Yield 0.88 g (86%), color white, solid, m. p. 260–265°C; IR spectrum ν, cm^{-1}: 854 (C–H), 1125 (C–C), 1222 (C–C), 1444 (C–O),1636 (C–O), 1738 (C=O), 2236 (C≡N), 3182 (=C–H), 3292 and 3384 (NH_2); ^1H NMR spectrum δ, ppm: 5.20 s (1H, 4-H), 7.46 d (2H, J = 8.1, 7.3 Hz), 7.74 d (2H, J = 8.1, 7.3 Hz), 6.84 s (2H, NH_2); ^{13}C NMR spectrum δC, ppm: 104.6, 109.1, 110.4, 111.8, 112.4, 116.1, 118.6, 120.4, 122.2, 122.8, 126.1, 128.8, 139.4, 146.3, 152.2, 156.2, 176.5 (C=O); Mass spectrum *m*/*z* 334.62.

Anticancer activity

The MTT assay of the synthesized pyrano chromene carbonitrile derivatives against MCF-7 (human breast cell line) showed that all tested samples: 2-amino-4-(4-dichlorophenyl)-5-oxo-4,5-dihydropyrano [3,2-c] chromene-3-carbonitrile, 2-amino-4-(2,4-dimethoxyphenyl)-5-oxo-4,5-dihydropyrano [3,2-*c*] chromene-3-carbonitrile, and 2-amino-4-(4-3,5-dibromo-4-hydroxyphenyl)-5-oxo-4,5-dihydropyrano [3,2-c] chromene-3-carbonitrile exhibited dose-dependent cytotoxic activity. [2-Amino-4-(2,4-dimethoxyphenyl)-5-oxo-4,5-dihydropyrano [3,2-*c*] chromene-3-carbonitrile showed the strongest anticancer activity with lowest IC_{50} value (58.80 µg/ml) and significant reduction in cell viability. Compound (4) showed moderate activity, while (1) exhibited the least cytotoxic effect overall. Compound (2) gave the best result, as shown in Figs. 4 and 5.

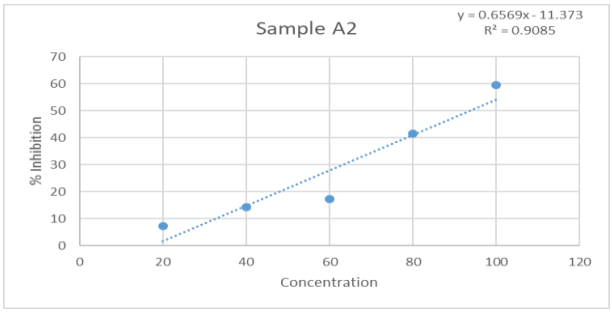


Figure 4. Concentration-dependent anticancer activity of sample (2) against MCF-7

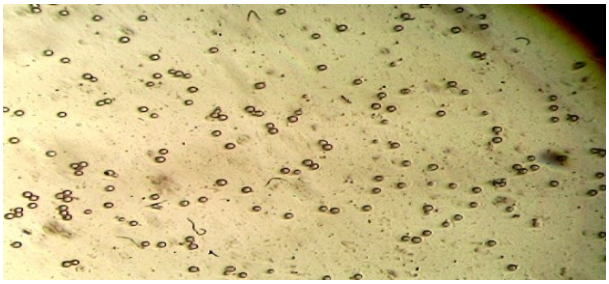


Figure 5. Cell morphology images against MCF-7

Table 1. Preparation of substituted pyrano [3,2-*c*] chromene carbonitrile derivatives (1-10) (ethanol, reflux) using $NiFe_2O_4$ catalyst

Compound	Time (min)	Yield (%)	M. p. (°C)
(1) 2,6-(Cl)$_2$C$_6$H$_4$ CHO	25	88	235-238
(2) 2,4-(OMe)$_2$ C$_6$H$_4$ CHO	27	89	234-239
(3) 4-OMe C$_6$H$_4$ CHO	20	92	242-246
(4) 3,5(Br)$_2$, 4-OH C$_6$H$_4$ CHO	30	87	222-226
(5) 3- I C$_6$H$_4$ CHO	20	89	260-265
(6) 4-Cl C$_6$H$_4$ CHO	20	91	266-269
(7) 4-NO$_2$ C$_6$H$_4$ CHO	20	90	255-257
(8) 3-NO$_2$ C$_6$H$_4$ CHO	30	89	258-260
(9) 4-Me C$_6$H$_4$ CHO	28	80	266-269
(10) 4-OH C$_6$H$_4$ CHO	35	86	260-265

Table 2. Preparation of pyrano [3,2-*c*] chromene carbonitriles compared with other catalysts

S. No.	Catalyst	Time (min)	Yield (%)	Ref.
1	DABCO	30	87	8
2	$Mg(ClO_4)_2$	35	85	9
3	MNPs@Cu	40	80	10
4	$NiFe_2O_4$	20	92	Present work

CONCLUSION

Nickel ferrite ($NiFe_2O_4$) NPs were successfully synthesized *via* the sol–gel method. The catalyst was comprehensively characterized using XRD, SEM, and TEM. The analytical data confirmed the successful formation of well-defined $NiFe_2O_4$ NPs. These nanoparticles were subsequently employed in the synthesis of 2-amino-4-arylphenyl-5-oxo-4,5-dihydro-pyrano [3,2-c] chromene-3-carbonitrile and its derivatives. The structures of the obtained compounds were verified through IR spectroscopy, ^1H NMR, ^{13}C NMR, and mass spectrometry, all of which provided consistent and reliable results. Cytotoxicity assays demonstrated that the pyrano [3,2-c] chromene carbonitrile derivatives exhibited promising anticancer potential, underscoring their relevance in medicinal chemistry. The methodology offers several advantages, including short reaction times, high product yields, and excellent purity (90–93%). The use of the nanocatalyst provides a highly

efficient and sustainable approach for the synthesis of bioactive heterocyclic compounds.

Acknowledgement: *The authors are thankful to the Principal, Dr. Rafiq Zakaria College for Women Chhatrapati Sambhajinagar-431001, Maharashtra, India, for providing the research facilities.*

Conflict of interest: *The authors declare that they have no conflict of interest.*

Author contributions: *All authors contributed to editing, reviewing, and sanctioning the finished version for publication.*

ORCID IDs: *Komal V. Takankhar https://orcid.org/0009-0007-6847-4201*

A. N. Durrani https://orcid.org/0009-0000-8384-2446

REFERENCES

1. A. M Abu-Dief, I Nassar, W. H. Elsayed. *Appl. Organomet. Chem.,* **30** (11) 917 (2016)**.** DOI: https://doi.org /10.1002/aoc.3521
2. M. Pardavi-Horvath, *J. of Magn. and Magn. Mater.,* 215 171 (2000). DOI; https://doi.org/10.1016/S0304-8853(00)00106-2
3. M. C. Tanasoiu, C. Miclea, C. F. Gheorghiu, A. V. Tanasoiu. *J. of Magn. and Magn. Mater.,* **290**, 1506 (2005). DOI:https://doi.org/10.1016/j.jmmm.2004.11.561
4. N. Rezlescu, N. Iftimie, E. Rezlescu, C.Doroftei, P. D. Popa. *Sens. and Act. B: Chemical*, **114** (1), 427 (2006). DOI: https://doi.org/10.1016/j.snb.2005.05.030
5. Z. Gao, F. Cui, S. Zeng, L. Guo, J. Shi, *Micro- Meso-Mater.*, **132** (1-2), 188 (2010). DOI:10.1016/j.micromeso.2010.02.019
6. N. Rezlescu, N. Iftimie, E. Rezlescu, C. Doroftei, P. D. Popa. *Sens. and Actuators B: Chem.,* **114** (1), 427 (2006). DOI: https://doi.org/10.1016.j.matpr.2015.07.165
7. Y. R Shelke, V. D. Bobade, D. R. Tope, J. A. Agashe, A. V. Borhade. *Russ. J. Org. Chem.,* **59** (4)**,** 663 (2023) DOI:https://doi./org/10.1134/S1070428023040152
8. K. Pradhan. *Iran. J. of Catal.,* **13** (4), (2023). DOI: https://doi.org./ 10.30495/IJC.2023.1993771.2041
9. D. B. Wahul, S. S. Katkar. *Curr. Org. Synth.*, **21 (**1), 20 (2024) DOI: https://doi.org/ 10.2174/1570179420666230327144202
10. Pourshojaei, F. Z. Yaghoub, E. Khalil, M. Talebi, M. Laleh, A. Mahnaz, A. Khodadadi, R. Shamsimeymandi, E. Faghih-Mirzaei. *J. of Nanosci. and Nanotech.,* **20** (5), 3206 (2020). DOI: https://doi.org/ 10.1166/jnn.2020.17396
11. M. Chadha, A. Garg, A. Bhalla, S. Berry. *Tetrahedron,* **150,** 133741 (2024). DOI: https://doi.org/10.1016/j.tet.2023.133741.
12. J. Reis, A. Gaspar, N. Milhazes, F. Borges, *J. of Medic. Chem.,* **60** (19), 7941 (2017). DOI: https://doi.org/10.1021 /acs.jmedchem.6b01720
13. H. Emtiazi, M. A. Amrollahi, *Bulg. Chem. Commun.*, **49** (2), 478 (2017).
14. W. Ma, A. G. Ebadi, M. S. Sabil, R. Javahershenas, G. Jimenez, *RSC Adv.,* **9** (23), 12801 (2019). DOI: https://doi/.org/10.1039/ C9RA01679A
15. A. T. Khan, M. Lal, S. Ali, M. M. Khan, *Tetrahedron Lett.*, **52** (41), 5327 (2011). DOI: https://doi./org./10.1016.j.tetlet.2011.08.019

Instructions about Preparation of Manuscripts

General remarks: Manuscripts are submitted in English by e-mail. The text must be prepared in A4 format sheets using Times New Roman font size 11, normal character spacing. The manuscript should not exceed 15 pages (about 3500 words), including photographs, tables, drawings, formulae, etc. Authors are requested to use margins of 2 cm on all sides.

Manuscripts should be subdivided into labelled sections, e.g. INTRODUCTION, EXPERIMENTAL, RESULTS AND DISCUSSION, etc. **The title page** comprises headline, author(s)' names and affiliations, abstract and key words. Attention is drawn to the following:

a) **The title** of the manuscript should reflect concisely the purpose and findings of the work. Abbreviations, symbols, chemical formulae, references and footnotes should be avoided. If indispensable, abbreviations and formulae should be given in parentheses immediately after the respective full form.

b) **The author(s)'** first and middle name initials and family name in full should be given, followed by the address (or addresses) of the contributing laboratory (laboratories). **The affiliation** of the author(s) should be listed in detail (no abbreviations!). The author to whom correspondence and/or inquiries should be sent should be indicated by an asterisk (*) with e-mail address.

The abstract should be self-explanatory and intelligible without any references to the text and containing up to 250 words. It should be followed by keywords (up to six).

References should be numbered sequentially in the order, in which they are cited in the text. The numbers in the text should be enclosed in brackets [2], [5, 6], [9−12], etc., set on the text line. References are to be listed in numerical order on a separate sheet. All references are to be given in Latin letters. The names of the authors are given without inversion. Titles of journals must be abbreviated according to Chemical Abstracts and given in italics, the volume is typed in bold, the initial page is given and the year in parentheses. Attention is drawn to the following conventions: a) The names of all authors of a certain publications should be given. The use of "et al." in the list of references is not acceptable; b) Only the initials of the first and middle names should be given. In the manuscripts, the reference to author(s) of cited works should be made without giving initials, e.g. "Bush and Smith [7] pioneered...". If the reference carries the names of three or more authors it should be quoted as "Bush et al. [7]", if Bush is the first author, or as "Bush and co-workers [7]", if Bush is the senior author.

Footnotes should be reduced to a minimum. Each footnote should be typed double-spaced at the bottom of the page, on which its subject is first mentioned. **Tables** are numbered with Arabic numerals on the left-hand top. Each table should be referred to in the text. Column headings should be as short as possible but they must define units unambiguously. The units are to be separated from the preceding symbols by a comma or brackets. Note: The following format should be used when figures, equations, etc. are referred to the text (followed by the respective numbers): Fig., Eqns., Table, Scheme.

Schemes and figures. Each manuscript should contain or be accompanied by the respective illustrative material, as well as by the respective figure captions in a separate file. As far as presentation of units is concerned, SI units are to be used. However, some non-SI units are also acceptable, such as °C, ml, l, etc. Avoid using more than 6 (12 for review articles) figures in the manuscript. Since most of the illustrative materials are to be presented as 8-cm wide pictures, attention should be paid that all axis titles, numerals, legend(s) and texts are legible.

The authors are required to submit the text with a list of three individuals and their e-mail addresses that can be considered by the Editors as potential reviewers. Please note that the reviewers should be outside the authors' own institution or organization. The Editorial Board of the journal is not obliged to accept these proposals.

The authors are asked to submit **the** final text (after the manuscript has been accepted for publication) in electronic form by e-mail. The main text, list of references, tables and figure captions should be saved in separate files (as *.rtf or *.doc) with clearly identifiable file names. It is essential that the name and version of the word-processing program and the format of the text files is clearly indicated. It is recommended that the pictures are presented in *.tif, *.jpg, *.cdr or *.bmp format. The equations are written using "Equation Editor" and chemical reaction schemes are written using ISIS Draw or ChemDraw programme.

EXAMPLES FOR PRESENTATION OF REFERENCES

REFERENCES

1. D. S. Newsome, Catal. Rev.–Sci. Eng., 21, 275 (1980).
2. C.-H. Lin, C.-Y. Hsu, J. Chem. Soc. Chem. Commun., 1479 (1992).
3. R. G. Parr, W. Yang, Density Functional Theory of Atoms and Molecules, Oxford Univ. Press, New York, 1989.
4. V. Ponec, G. C. Bond, Catalysis by Metals and Alloys (Stud. Surf. Sci. Catal., vol. 95), Elsevier, Amsterdam, 1995.
5. G. Kadinov, S. Todorova, A. Palazov, in: New Frontiers in Catalysis (Proc. 10th Int. Congr. Catal., Budapest (1992), L. Guczi, F. Solymosi, P. Tetenyi (eds.), Akademiai Kiado, Budapest, 1993, Part C, p. 2817.
6. G. L. C. Maire, F. Garin, in: Catalysis. Science and Technology, J. R. Anderson, M. Boudart (eds.), vol. 6, Springer Verlag, Berlin, 1984, p. 161.
7. D. Pocknell, GB Patent 2 207 355 (1949).
8. G. Angelov, PhD Thesis, UCTM, Sofia, 2001, pp. 121-126.
9. JCPDS International Center for Diffraction Data, Power Diffraction File, Swarthmore, PA, 1991.
10. CA 127, 184 762q (1998).
11. P. Hou, H. Wise, J. Catal., in press.
12. M. Sinev, private communication.
13. http://www.chemweb.com/alchem/articles/1051611477211.html.

Texts with references which do not match these requirements will not be considered for publication!!!

AUTHOR INDEX

Abdollahi, A., See Toshev et al. 209
Abu Sayeed, M., Sultan, Md. Z., Mehedi Masud, M., Rashid, M. A., Akhter Simo, H., Gatifloxacin metal complexes: spectroscopic, thermal, and X-ray structural analysis with antimicrobial evaluation 461
Acknowledgement to Reviewers for vol. 57 120
Adsul, V., See Gaikwad et al. 74
Agova, N. V., See Toshev et al. 209
Akdemir, K., Gonultas, H., Isik, B. K., Tugrul, N., Synthesis and characterization of eco-friendly edible films based on pistachio shell 331
Akhter Simo, H., See Abu Sayeed et al. 461
Akyol, E., See Saleha et al. 315
Akyol, E., See Simsek et al. 310, 382
Aleksandrova, D., See Idakiev et al. 30
Al-Mahmoud, S. M., Electrode shape modification for efficient dye removal using electrocoagulation 129
Amir, B., See Tusseyev et al. 103
Amran, F., See Rahaman et al. 482
Anbumeenakshi, C., See Kumutha et al. 93
Angelova, D. S., See Zheleva et al. 218
Aslan, S. K., See Çolak et al. 291
Athare, A. E., See Deshpande et al. 442
Authors index 565
Awari, S. M., Vikhe, V. V., Vikhe, V. K., Gadhave, A. G., Uphade, B. K., $NiFe_2O_4$@Cellulose-PEG nanocomposite: A novel reusable catalyst for straightforward one-pot synthesis of benzopyran derivatives 154
Bahçeci, D., See Demir et al. 286
Baizhumanov, K. D., See Tusseyev et al. 103
Balabanov, A., See Boyanova et al. 23
Balakumar, M., See Kumutha et al. 93
Bektaş, T. E., See Yiğit et al. 364
Benhebal, H., See Rabiaa et al. 136
Bondartsev, D. Yu., See Genbach et al. 109
Boukoureshtlieva, R., See Nikolov et al. 550
Boyanova, P., Chavdarova, A., Dobreva, V., Gradinarska, D., Goranov, B., Balabanov, A., Slavova, V., Impact of polyols on microbiological viability and sweetness perception in frozen yogurt 23
Boye, G., See Idakiev et al. 30
Cagliyan, Y., Ozyalcin, Z. O., Kipcak, A. S., Freeze drying of manila clam: drying kinetics and mathematical modelling 247
Catal, T., See Hayrat et al. 37
Çetin, B., See Çolak et al. 291
Chavdarova, A., See Boyanova et al. 23
Çolak, E., Çetin, B., Kurçin, H. C., Aslan, S. K., Ünlü, D., Nigiz, F. U., Synthesis and characterization of polydopamine-modified MOFs for polymer electrolyte membranes 291
Çorbacıoğlu, B. D., See Özgündüz et al. 320
Demir, A. B., Bahçeci, D., Özer, S., Şahin, Ö. Y., Şakar, D., Preparation and analysis of an herbal extract solution having potential restorative effects against radiation dermatitis 286
Demir, K., See Tumtum et al. 391
Derun, E. M., See Uygunoz et al. 297, 303
Deshmukh, S. S., See Deshpande et al. 442
Deshpande, M. S., Sonawane, D. V., Deshmukh, S. S., Athare, A. E., Photocatalytic degradation of azo dye (Congo red) using aluminum-doped cadmium oxide nanoparticles 442
Dimitrova, T. L., See Yari Dramane et al. 16
Dinesh Kumar, V., Sammaiah, P., Hemadri, V. B., Advancements in polylactic acid (PLA) biocomposites: a review on reinforcement, additive manufacturing, and prospects for a sustainable future 476
Dishliev, A., See Georgieva et al. 52, 59
Diukendjieva-Todorova, A. G., See Tsakovska et al. 504
Dobreva, A. M., See Nenova et al. 66
Dobreva, V., See Boyanova et al. 23
Dökmeci, A. H., See Eren et al. 261
Durrani, A., See Takankhar et al. 559
Enisoglu Atalay, V., See Hayrat et al. 37
Ercan, O., Ozyalcin, Z. O., Kipcak, A. S., Rehydration characteristics of freeze-dried mussel, shrimp and squid 254
Eren, B., Dökmeci, A. H., Degradation mechanisms of selected aminopolycarboxylic acid molecules by DFT method 261
Eren, B., See Sabudak et al. 386
Ergul, C., Kurumoglu, S., Yalcin Gurkan, Y., Brain penetration in CNS and non-CNS drugs using molecular electronic parameters 377
Eswara Rao, M., See Gnaneswara Reddy et al. 85
Farcy, A., See Rabiaa et al. 136
Först, P., See Idakiev et al. 30
Gadhave, A. G., See Awari et al. 154
Gaikwad, S. A., Khatiwora, E., Adsul, V., Torane, R., Uttam Pandit, V. R., Parthibavarman, M., Comparative account of biosynthesized zinc oxide nanomaterials from Cassia tora for biomedicament 74
Gavrilov, I., Petrin, S., Mileva-Petrova, P., Radeva, G., Valchev, I., Temperature-time and concentration dependences of mild dilute acid hydrolysis 189
Gavrilov, I., See Petrin et al. 185
Genbach, A. A., Bondartsev, D. Yu., Georgiev, A. G., Investigation of capillary-porous coatings made of mineral media 109
Georgiev, A. G., See Genbach et al. 109
Georgieva, M., Kozhukharov, S., Girginov, Ch., Dishliev, A., Petkov, P., Comparison between ortho- and meta-phosphoric acid containing phosphate potential buffering systems 59
Georgieva, M., Kozhukharov, S., Girginov, Ch., Dishliev, A., Petkov, P., Potential buffers based on borax, orthophosphoric and metaphosphoric acid 52
Georgieva, S. F., See Toshev et al. 209

Georgieva, S., See Stancheva et al. 200
Gheewala, A., Mistry, H., Solanki, A., Hydrogen as a strategic energy transition pathway: production technologies, cost dynamics, infrastructure, policy and India's statistical roadmap to 2030 and 2050 523
Girginov, Ch., See Georgieva et al. 52, 59
Gnaneswara Reddy, M., Kiranmaiye, S., Eswara Rao, M., Stefan blowing and chemical reaction influences on non-Darcian flow of Casson nanofluid over a stretched surface..... 85
Gonultas, H., See Akdemir et al. 331
Goranov, B., See Boyanova et al. 23
Gradinarska, D., See Boyanova et al. 23
Gürakin, H. K., See Şakar et al. 281
Gurkan, B., See Kemanci et al. 370
Hayrat, N., Kilinc, B., Yilmaz, B., Kul, A., Tarbiat, Sh., Enisoglu Atalay, V., Catal, T., Investigation of antioxidant activities of *Ganoderma* mushroom..... 37
Hemadri, V. B., See Dinesh Kumar et al. 476
Idakiev, H., Aleksandrova, D., Boye, G., Först, P., Vorhauer-Huget, N., Impact of drying techniques on protein denaturation in *Tenebrio molitor*: A thermal analysis via differential scanning calorimetry 30
Idrish Khan, A., See Kumutha et al. 93
Ilaiyavel, S., See Kumutha et al. 93
Iliev, I. R., See Toshev et al. 209
Iliev, I., See Stancheva et al. 200
In Memoriam Dedicated to the memory of Prof. DSc Dimitar Mehandzhiev (1933-2026)..... i
İpsalalı, Ö., Okyay, B., Nigiz, F. U., From orange peel to sustainable biocomposite: production and characterization of pectin/CMC films with matcha tea extract 336
Isik, B. K., See Akdemir et al. 331
Isik, B. K., See Menekse et al. 269
Işık, Ö., See İşman et al. 341
İşlek, D. S., Kiriş, E., Şen Yılmaz, A., Köse, E., Forensic identification of pen ink pigments using dual-wavelength Raman spectroscopy combined with chemometrics..... 276
Ismaili Uka, D., See Özbakiş et al. 396
İşman, N., Işık, Ö., Terzioğlu, P., Orhan, M., Effect of tannic acid concentration on structural, mechanical, and antibacterial properties of polyvinyl alcohol/chitosan/pomegranate peelbased biocomposite films..... 341
Kadi, S., See Rabiaa et al. 136
Kahraman, S., Özbey, E., Uzun, S., Nigiz, F. U., Production and characterization of a doublelayered wound dressing containing electrospun polylactic acid and hypericum-infused alginate hydrogel 358
Kahraman, S., See Yiğit et al. 364
Kalinov, K. N., See Nenova et al. 66
Karabekiroğlu, S. N., See Kocaoğlu et al. 351
Katirci, A., Nigiz, F. U., Production of desalination membranes from recycled PVDF polymers..... 241
Kemanci, B., Kurumoglu, S., Gurkan, B., Investigation of the correlation between skin permeation and global reactivity descriptors in phenolic antioxidants: a comparative DFT and ADMET study 370
Keyf, S., See Özgündüz et al. 320
Khatiwora, E., See Gaikwad et al. 74
Kilinc, B., See Hayrat et al. 37
Kipcak, A. S., See Cagliyan et al. 247
Kipcak, A. S., See Ercan et al. 254
Kıpçak, E., Comparative evaluation of infrared and microwave drying of berries: kinetics, diffusivity, and modeling approaches 401
Kiranmaiye, S., See Gnaneswara Reddy et al. 85
Kiriş, E., See İşlek et al. 276
Kocaoğlu, M., Karabekiroğlu, S. N., Activated carbon from gypsophila roots: a sustainable adsorbent for dye removal..... 351
Köse, E., See İşlek et al. 276
Kozhukharov, S., See Georgieva et al. 52, 59
Kucuk, İ., See Simsek et al. 382
Küçük, İ., See Tavlıbıyık et al. 325
Kul, A., See Hayrat et al. 37
Kumutha, R., Ilaiyavel, S., Sudhakar, B., Udhayakumar, K., Balakumar, M., Anbumeenakshi, C., Idrish Khan, A., Suresh, K., Enhanced wear resistance of AISI steel via sequential nitriding, laser texturing, and TiN coating..... 93
Kurçin, H. C., See Çolak et al. 291
Kurumoglu, S., See Ergul et al. 377
Kurumoglu, S., See Kemanci et al. 370
Kurumoglu, S., See Tumtum et al. 391
Kuzeva, S., See Petrin et al. 185
Lambert, S. D., See Rabiaa et al. 136
Lellou, S., See Rabiaa et al. 136
Lozanov, I. I., See Stamenov et al. 431
Madjarova, G. K., See Petkova et al. 193
Mahy, J. G., See Rabiaa et al. 136
Mathiarasu, A., Suresh Kumar, S., Senthil, R., Pandian, R.,Chemical characterization and performance analysis of post-modified microwave pyrolyzed karanja seed bio-oil..... 5
Matrakova, M., See Nikolov et al. 550
Mehedi Masud, M., See Abu Sayeed et al. 461
Menekse, A., Isik, B. K., Tugrul, N., Utilization of sugar beet pulp as an agricultural by-product in vegan leather production 269
Merdzhanova, A., See Stancheva et al. 200
Mijakov, I., See Petkova et al. 193
Mileva-Petrova, P., See Gavrilov et al. 189
Mileva-Petrova, P., See Petrin et al. 185
Mistry, H., See Gheewala et al. 523
Mladenova, B., See Nikolov et al. 550
Mohanavel, V., See Suresh Kumar et al. 515
Muniyappan, A., See Samraj Selvaraj et al. 173
Navgire, M. E., See Padol et al. 436
Nedeva, D. A., See Nenova et al. 66
Nenova, R. H., Nedeva, D. A., Dobreva, A. M., Shimazaki, T. I., Kalinov, K. N., A comparative study of the chemical composition of oil–bearing

Rosa damascena Mill. cultivated in Bulgaria and in Japan 66
Nguyen, H. D., Computational modelling of limonoids from *Melia azedarach* as potential inhibitors of leukemia 162
Nguyen, H. D., Integrated *in silico* discovery of anti-apoptotic sesquiterpenoid candidates from *Inula japonica* against hepatocarcinoma 451
Nguyen, H. D., Unveil mechanism of action of parthenolide-9-one as an inhibitor for human erythroleukemia via molecular modeling, ADMET and MMGBSA analysis 44
Nguyen, H. D., Unveiling breast cancer therapeutics of bufadienolides from *Helleborus foetidus* through molecular docking, molecular dynamics, and MMGBSA computations 492
Nguyen, H. D., Unveiling mechanisms of action of isoquinoline alkaloids from *Hylomecon japonica* as promising inhibitors of breast cancer through computational modelling 143
Nigiz, F. U., See Çolak et al. 291
Nigiz, F. U., See İpsalalı et al. 336
Nigiz, F. U., See Kahraman et al. 358
Nigiz, F. U., See Katirci et al. 241
Nikolov, P., Mladenova, B., Matrakova, M., Stankulov, T., Boukoureshtlieva, R., Soserov, L., Impact of polyvinylpyrrolidone as an additive to the positive electrolyte of a vanadium redox flow battery 550
Okyay, B., See İpsalalı et al. 336
Orhan, M., See İşman et al. 341
Özbakiş, M., Ismaili Uka, D., Terzioğlu, P., Sicak, Y., Sustainable and bioactive chitosan/PVA hydrogels incorporating allantoin for wound healing applications 396
Özbey, E., See Kahraman et al. 358
Ozcelik, C., See Sabudak et al. 386
Ozdemir, R., Unlu, D., Synthesis and characterization of boron-containing benzoxazine resins for advanced thermal protection systems 347
Özer, S., See Demir et al. 286
Özgündüz, H. İ., Çorbacıoğlu, B. D., Keyf, S., Modıfıcatıon of bıtumen by addıng reactıve terpolymer, polyolefin elastomer and thermoplastic 320
Ozyalcin, Z. O., See Cagliyan et al. 247
Ozyalcin, Z. O., See Ercan et al. 254
Padol, A. R., Navgire, M. E., Raut, M. A., Design and biological evolution of La_2O_3-ZnO mixed metal oxide nanomaterials for anticancer activity against MCF-7 cell lines 436
Pajeva, I. K., See Tsakovska et al. 504
Pandian, R., See Mathiarasu et al. 5
Parthibavarman, M., See Gaikwad et al. 74
Petkov, P., See Georgieva et al. 52, 59
Petkova, J. N., Mijakov, I., Simeonova, E. P., Madjarova, G. K., Quantum chemical insights into porous s-triazine and tri-s-triazine carbon nitrides 193
Petrin, S., Kuzeva, S., Gavrilov, I., Radeva, G., Mileva-Petrova, P., Valchev, I., Kinetic study of softwood cooking for bleached pulp production 185
Petrin, S., See Gavrilov et al. 189
Rabiaa, H. N. E., Benhebal, H., Sebbah, O., Kadi, S., Lellou, S., Farcy, A., Mahy, J. G., Lambert, S. D., Zn-doped $SrBi_2O_4$ nanopowders prepared by sol-gel method and their photocatalytic properties 136
Radeva, G., See Gavrilov et al. 189
Radeva, G., See Petrin et al. 185
Rahaman, T. F., Amran, F., Zaini, M. A. A., Fitting and interpretation of equilibrium and kinetic models, and two-stage adsorber design of condensate-based adsorbents for methylene blue removal 482
Rashid, M. A., See Abu Sayeed et al. 461
Raut, M. A., See Padol et al. 436
Sabudak, T., Eren, B., Ozcelik, C., Determination of the chemical composition of the essential oil of the Rubia tinctorum plant 386
Şahin, Ö. Y., See Demir et al. 286
Şakar, D., Gürakin, H. K., Removing disperse orange 30 dye from simulated wastewater using formaldehyde-stabilized quince leaf powder bioadsorbent 281
Şakar, D., See Demir et al. 286
Saleha, N. A., Akyol, E., Sustainable heavy metal ion detection of waste-based carbon quantum dots 315
Sammaiah, P., See Dinesh Kumar et al. 476
Samraj Selvaraj, A., Sanmugam, A., Muniyappan, A., Optimization and performance evaluation of hydroxyapatite–magnesium oxide coatings on UHMWPE for improved tribological and antibacterial behavior in orthopaedic applications 173
Sanmugam, A., See Samraj Selvaraj et al. 173
Sebbah, O., See Rabiaa et al. 136
Şen Yılmaz, A., See İşlek et al. 276
Sengor, I., See Uygunoz et al. 297, 303
Senthil, R., See Mathiarasu et al. 5
Sharipkhanov, A. B., See Tusseyev et al. 103
Shimazaki, T. I., See Nenova et al. 66
Sicak, Y., See Özbakiş et al. 396
Simeonova, E. P., See Petkova et al. 193
Simeonova, G. V., Trifonova, T. P., Chelation reaction vs. isotope exchange for production of effective receptor-targeted radiopharmaceuticals 226
Simsek, S., Akyol, E., Kucuk, İ., Comparison of the effects of cellulase, pectinase, and xylenase enzymes on the total flavonoid content of *Helichrysum arenarium* extract obtained by enzymatically pre-treated Soxhlet extraction 382
Simsek, S., Usoğlu, O. Y., Akyol, E., Evaluation of the inhibitory effects of phenolic compoundson calcium oxalate crystallization 310
Slavova, V., See Boyanova et al. 23
Slavova, V., See Yari Dramane et al. 16
Solanki, A., See Gheewala et al. 523
Sonawane, D. V., See Deshpande et al. 442
Soserov, L., See Nikolov et al. 550

Stamenov, N., Lozanov, I. I., UV-Vis spectrometer from scratch: a budget do-it-yourself solution to a growing problem..... 431
Stancheva, R., Iliev, I., Merdzhanova, A., Georgieva, S., Computational evaluation of COX-1 binding by EPA, DHA, and AA using blind and flexible docking approaches..... 200
Stankulov, T., See Nikolov et al..... 550
Sudhakar, B., See Kumutha et al..... 93
Sultan, Md. Z., See Abu Sayeed et al. 461
Suresh Kumar, S., Mohanavel, V., Parametric optimization of ZK60 reinforced with ZrB_2 magnesium composites via Taguchi method 515
Suresh Kumar, S., See Mathiarasu et al..... 5
Suresh, K., See Kumutha et al. 93
Suthagar, S., Tamilselvan, K. S., Comparing odor-active compounds of South Indian mangoes by odor uproot blend analysis and the natural aroma instantaneous input to the sniffing port method for evaluating odor interactions 421
Takankhar, K., Durrani, A., One-pot synthesis of pyrano chromene carbonitriles catalyzed by $NiFe_2O_4$ nanoparticles and their anticancer potential 559
Tamilselvan, K. S., See Suthagar et al..... 421
Tarbiat, Sh., See Hayrat et al. 37
Tavlıbıyık, O., Küçük, İ., Effect of hemp filler on the mechanical and physical properties of PLA/PBAT composite films..... 325
Terzioğlu, P., See İşman et al..... 341
Terzioğlu, P., See Özbakiş et al. 396
Torane, R., See Gaikwad et al..... 74
Toshev, N. A., Iliev, I. R., Agova, N. V., Abdollahi, A., Georgieva, S. F., Computational evaluation of bexarotene alkyl esters through DFT and molecular docking..... 209
Trifonova, T. P., See Simeonova et al. 226
Tsakovska, I. M., Diukendjieva-Todorova, A. G., Pajeva, I. K., Advances in predictive toxicology for androgen receptor–mediated endocrine disruption 504
Tugrul, N., See Akdemir et al. 331
Tugrul, N., See Menekse et al. 269
Tumtum, G., Demir, K., Kurumoglu, S., Yalcin Gurkan, Y., Reactivity and ecotoxicity of the next-generation herbicide flufenauxirim: a density functional theory (DFT) and quantitative structure-activity relationship (QSAR) study with reference to aminocyclopyrachlor..... 391
Tusseyev, T., Baizhumanov, K. D., Zhumanov, M. A., Amir, B., Sharipkhanov, A. B., Photoadsorption processes on the surface of silicon dioxide..... 103
Udhayakumar, K., See Kumutha et al. 93
Uğur Nigiz, F., See Yiğit et al..... 364
Ünlü, D., See Çolak et al. 291
Unlu, D., See Ozdemir et al. 347
Uphade, B. K., See Awari et al. 154
Usoğlu, O. Y., See Simsek et al. 310
Uttam Pandit, V. R., See Gaikwad et al..... 74
Uygunoz, D., Sengor, I., Derun, E. M., Biomass energy production from sunflower plant 303
Uygunoz, D., Sengor, I., Derun, E. M., Natural pigments doped polymer films synthesis by solution casting method and characterization..... 297
Uzun, S., See Kahraman et al..... 358
Valchev, I., See Gavrilov et al. 189
Valchev, I., See Petrin et al..... 185
Vikhe, V. K., See Awari et al..... 154
Vikhe, V. V., See Awari et al..... 154
Vorhauer-Huget, N., See Idakiev et al..... 30
Yalcin Gurkan, Y., See Ergul et al. 377
Yalcin Gurkan, Y., See Tumtum et al. 391
Yari Dramane, T., Slavova, V., Yasar, A., Dimitrova, T. L., Discrimination of radish seed cultivars using fluorescence spectroscopy and advanced machine learning algorithms 16
Yasar, A., See Yari Dramane et al..... 16
Yiğit, S., Bektaş, T. E., Kahraman, S., Uğur Nigiz, F., Synthesis and in vitro characterization of quercetin-loaded alginate-keratin composite hydrogels for enhanced wound healing applications..... 364
Yilmaz, B., See Hayrat et al..... 37
Zaini, M. A. A., See Rahaman et al..... 482
Zheleva, D. I., Angelova, D. S., Deposition of zinc nanoparticles on woolen substrates in footwear 218
Zhumanov, M. A., See Tusseyev et al. 103

SUBJECT INDEX

acid value 303
activated carbon 352
additive 550
additive manufacturing 476
ADMET 371, 378
adsorption 482
adsorption kinetics and isotherms 281
AISI 52100 93
alginate hydrogel 359
alkyl esters 209
allantoin 396
Aloe vera 286
aluminum 442
aminocyclopyrachlor 391
aminopolycarboxylic acids (APCA) 261
androgen receptor 504
anti-apoptosis 143, 162, 492
antibacterial assay 173
antibacterial modification 218
anticancer activity 436, 559
anti-inflammatory potential 200
antimicrobial activity 461
antioxidants 27, 371
apoptosis 44, 451
AutoDock 4.2 200
azo dye 442
Bcl-2 ..... 143, 451
Bcl-xL 162
benzopyran 154
benzoxazine 348
Bexarotene 209
Bifidobacterium spp. 23
bilayer wound dressing 359
bio-based filler 325
biodegradable 269, 476
biodegradable packaging 331
biodegradable polymers 297
biodiesel 303
bio-material 269
biosynthesis 74
bitumen modification 320
blanching 247
bleachability 185
bleached pulp 185
blind rigid-body docking 200
blood–brain barrier 378
blueberry 401
borate and phosphate compositions 52
breast cancer 143, 451
bufadienolides 451
buffering capacity 52
buffering capacity 59
cadmium oxide (CdO) nanoparticles 442
Calcium oxalate (CaOx) 310
carbon neutrality 523
carbon nitrides 193
carbon quantum dots (CQDs) 315
caspase-3 44
Cassia tora 74
Casson nanofluid 85
cellulase 383
Centella asiatica (gotu kola) 286
chemical reaction 85
chemistry education 431
chitosan 342, 396
chromene carbonitriles 559
Cistus (*Cistus creticus*; laden) 286
CNS drugs 378
coatings 109
combustion chamber 109
computational chemistry 27
computational models 504
Congo red 136
cooking 185
curved electrode 129
cyclooxygenase-1 (COX-1) 200
decarbonization 523
degree of polymerization 189
dehydroxylation 103
density functional theory (DFT) 143, 162, 193, 209, 261, 371, 378, 391, 492
dental activity 74
desalination 241
diesel engine 5
differential scanning calorimetry (DSC) 30, 461
dip-coating 173
disodium monohydrogen phosphate 59
disperse orange 30 dye 281
doping 136
DPPH 27
drug release 365
DTPA 261
dye 352
dye removal yield 281
E. coli bacteria 173
edible film 331
EDS 442
EDTA 261
elastomeric terpolymer 320
electrochemical energy storage 291
electrocoagulation 129
electrode modification 129
electrolysis 523
electrolyzer deployment 523
electronic descriptors 209
electronic reactivity 371, 378
electrospinning 291, 359
emulsification 5
endocrine-disrupting chemicals 504
energy transition 523
environmental 352
environmental engineering 482
enzyme-assisted extraction 383
Eriochrome black T 129
essential oil 387
EtOH 559

^{18}F 226
flavonoids 310
flavor dilution (FD) factor 421
flexible docking 200
flufenauxirim 391
fluorescence intensities 315
fluorescence spectroscopic techniques 16
footwear 218
forensic chemistry 276
formaldhyde stabilised quince leaves bioadsorbent 281
free radical scavenging 74
freeze-drying 30
frozen yogurt 23
FT-IR 461
^{68}Ga 226
Ganoderma lucidum 27
gas chromatography 387
gas separation membranes 193
gatifloxacin-metal complexes 461
GC–FID 66
GC-MS 387
golden berry 401
green hydrogen 523
Gypsophila spp. 352
heat protection 109
heat transfer 109
heavy metal contamination 315
Helichrysum arenarium 383
Helichrysum arenarium extract 310
hepatocarcinoma 492
HEPTA 261
heterogeneous catalyst 303
human erythroleukemia 44
hydrogel 365, 396
hydrogen economy 523
hydroxyapatite 173
Hylomecon japonica 143
Hypericum perforatum extract 359
in silico toxicology 391
India 523
infrared drying 401
inquiry-based learning 431
IR spectra 103
isoquinoline alkaloids 143
Karanja bio-oil 5
keratin 365
kidney stone 310
kinetics 185, 189
La_2O_3–ZnO nanocomposite 436
lactic acid bacteria 23
laser surface texturing 93
leukemia inhibitor 162
levelized cost of hydrogen (LCOH) 523
light intensity 103
limonoids 162
LogBB 378
low-cost spectrophotometric teaching equipment 431
lyophilization 247, 254
machine learning techniques 16
magnesium oxide 173
Matcha tea 337
mathematical modelling 401
MCF-7 cells 436
Mcl-1 492
mealworm 30
mechanical properties 325
Melia azedarach 162
membrane distillation 241
metal-organic framework 291
metaphosphoric acid 59
methylene blue 482
MHD 85
microcrystalline cellulose 189
microwave drying 401
microwave pyrolysis 5
mild acid hydrolysis 189
mineral media 109
mixed metal oxide 436
modelling 247, 254
molecular docking 209, 451
molecular modeling 44, 492
NAIIS 421
nano-CaO 303
nanocomposite 154
nanotechnology 436
national green hydrogen mission (NGHM) 523
natural fibers 476
natural pigments 297
new approach methodologies 504
$NiFe_2O_4$ NPs 559
$NiFe_2O_4$@Cellulose-PEG 154
nitriding 93
non-biodegradable 476
nozzle 109
nut waste 331
odor-active components 421
omega-3 fatty acids 200
one-pot multicomponent synthesis 154
optimization 515
orange peel 337
orthophosphoric acid 59
OUBA 421
oven drying 30
packaging materials 297
paired binomial proportion test 66
palm oil condensate 482
parthenolide-9-one 44
PBAT (poly-butylene adipate-co-terephthalate) 325
peanut oil 331
pectin 337
pectinase 383
penetration value 320
pH buffers 52
pH ranges 52, 59
phenolic compounds 310
phenolic resin 348
phenylboronic acid 348
photocatalysis 136
photoluminescence quenching 315

photosorption 103
pigment analysis 276
pin-on-disc 173
pistachio shell 331
PLA (polylactic acid) 325
Plantago lanceolata (allantoin) 286
polydopamine 291
polylactic acid 359, 476
polymeric films 297
polyolefin elastomer 320
polyols 23
polysaccharide-based 337
polyvinyl alcohol 297, 342, 396
polyvinylpyrrolidone 550
pomegranate peel powder 342
positive electrolyte 550
powder X-ray diffraction (PXRD) 461
predictive toxicology 504
pre-treatment temperature 103
principal component analysis (PCA) 276
prostate cancer 226
protein denaturation 30
proton-exchange membrane 291
PSMA 226
PVDF 241
PVP 550
QSAR 391
quantitative surface descriptors 371
quercetin 365
radiopharmaceuticals 226
Radish seeds 16
Raman spectroscopy 276
reactive 320
recyclable catalyst 154
recycling 241
renewable energy integration 523
rose oil 66
Rubia tinctorum 387
RXRα 209
seafood 247, 254
sectoral demand 523
self-led exercise 431
SEM 442
sensory profile 23
sesquiterpenoids 492
shell 247
silicon dioxide 103
skin permeation 371
sodium alginate 365
softening point 320
softwood 185
sol-gel 136
solvent-free 154
South Indian mangoes 421
Soxhlet extraction 383
$SrBi_2O_4$ 136
Stefan blowing 85
stir casting 515
sugar beet pulp 269
sulfonated poly(phenylene sulfone) 291
sunflower oil 303
sustainable 269
sustainable protein source 30
swelling 254
Taguchi 515
tannic acid 342
Tenebrio molitor 30
thermal efficiency 5
thermal properties 348
thermal radiation 85
three-component reactions 559
TiN coating 93
total flavonoid content 383
transesterification 303
tribology 93
ultrasonication 254
vanadium redox flow battery 550
vegan leather 269
VRFB 550
wastewater treatment 352, 482
wear 93, 515
wool 218
wound care 365
wound healing 396
xylanase 383
ZK60 515
ZnO nanoparticles 218
ZrB_2 515

CONTENTS

S. Suthagar, K. S. Tamilselvan, Comparing odor-active compounds of South Indian mangoes by odor uproot blend analysis and the natural aroma instantaneous input to the sniffing port method for evaluating odor interactions……..… 421
N. Stamenov, I. I. Lozanov: UV-Vis spectrometer from scratch: a budget do-it-yourself solution to a growing problem…….. 431
A. R. Padol, M. E. Navgire, M. A. Raut, Design and biological evolution of La_2O_3-ZnO mixed metal oxide nanomaterials for anticancer activity against MCF-7 cell lines…… 436
M. S. Deshpande, D. V. Sonawane, S. S. Deshmukh, A. E. Athare, Photocatalytic degradation of azo dye (Congo red) using aluminum-doped cadmium oxide nanoparticles……. 442
H. D. Nguyen, Integrated *in silico* discovery of anti-apoptotic sesquiterpenoid candidates from *Inula japonica* against hepatocarcinoma…….. 451
M. Abu Sayeed, Md. Z. Sultan, M. Mehedi Masud, M. A. Rashid, H. Akhter Simo, Gatifloxacin metal complexes: spectroscopic, thermal, and X-ray structural analysis with antimicrobial evaluation…….. 461
V. Dinesh Kumar, P. Sammaiah, V. B. Hemadri, Advancements in polylactic acid (PLA) biocomposites: a review on reinforcement, additive manufacturing, and prospects for a sustainable future…….. 476
T. F. Rahaman, F. Amran, M. A. A. Zaini, Fitting and interpretation of equilibrium and kinetic models, and two-stage adsorber design of condensate-based adsorbents for methylene blue removal……. 482
H. D. Nguyen, Unveiling breast cancer therapeutics of bufadienolides from *Helleborus foetidus* through molecular docking, molecular dynamics, and MMGBSA computations… 492
I. M. Tsakovska, A. G. Diukendjieva-Todorova, I. K. Pajeva, Advances in predictive toxicology for androgen receptor–mediated endocrine disruption…… 504
S. Suresh Kumar, V. Mohanavel, Parametric optimization of ZK60 reinforced with ZrB_2 magnesium composites *via* Taguchi method…… 515
A. Gheewala, H. Mistry, A. Solanki, Hydrogen as a strategic energy transition pathway: production technologies, cost dynamics, infrastructure, policy and India's statistical roadmap to 2030 and 2050…… 523
P. Nikolov, B. Mladenova, M. Matrakova, T. Stankulov, R. Boukoureshtlieva, L. Soserov, Impact of polyvinylpyrrolidone as an additive to the positive electrolyte of a vanadium redox flow battery……. 550
K. Takankhar, A. Durrani, One-pot synthesis of pyrano chromene carbonitriles catalyzed by $NiFe_2O_4$ nanoparticles and their anticancer potential…… 559
Authors index…… 565
Subject index…… 569
INSTRUCTIONS TO AUTHORS…… 572